SISSA
Scuola
Internazionale
Superiore di
Studi Avanzati

Physics Area - PhD course in
Astroparticle Physics

Testing the gravitational phenomenology of compact objects: superradiance, scalarization and screening mechanisms

Candidate:
Alexandru Dima

Advisor:
Enrico Barausse

Academic Year 2020-21

Declaration of Authorship

I, Alexandru DIMA, declare that this thesis titled, "Testing the gravitational phenomenology of compact objects: superradiance, scalarization and screening mechanisms" and the work presented in it are my own. I confirm that:

- This work was done wholly or mainly while in candidature for a research degree at this University.
- Where any part of this thesis has previously been submitted for a degree or any other qualification at this University or any other institution, this has been clearly stated.
- Where I have consulted the published work of others, this is always clearly attributed.
- Where I have quoted from the work of others, the source is always given. With the exception of such quotations, this thesis is entirely my own work.
- I have acknowledged all main sources of help.
- Where the thesis is based on work done by myself jointly with others, I have made clear exactly what was done by others and what I have contributed myself.

Signed: _____

Date: _____

"Come se dixe a Bojon, qua bisogna imparare a rajonare."

Prof. G. Zampieri

SCUOLA INTERNAZIONALE SUPERIORE DI STUDI AVANZATI

Abstract

Testing the gravitational phenomenology of compact objects: superradiance, scalarization and screening mechanisms

by Alexandru DIMA

In the last decades, an interesting variety of extended models of gravity has been proposed with the goal of capturing cosmological effects such as the accelerated phases of expansion and/or the so-called "dark sector" of our universe. In parallel, the quest for a full-fledged theory of quantum gravity proceeds by investigating the low-energy limit of candidate models. Many of these modified gravity models might leave imprints in the physics of compact objects and with gravitational-wave astronomy we have the unprecedented opportunity to test them against data with improving accuracy. A popular class of models (scalar-tensor theories) extends the field content of general relativity with an additional scalar field. These theories provide multiple examples where black hole and neutron star physics deviates from general relativity and can be constrained with observations. In this sense, superradiance and spontaneous growth of scalar fields around black holes and neutron stars are potentially detectable signatures of new physics. Screening mechanisms can in principle hide scalar effects, but their effectiveness in the strong-field regime is still largely unmodeled. In this thesis I briefly review the traditional tests of gravity, from the weak-field observations to gravitational-wave tests, before moving to discuss in details a collection of personal contributions in modeling the aforementioned scalar effects.

List of publications

The research presented in this thesis was conducted mainly in SISSA (International School for Advanced Studies) between November 2017 and October 2021, and was the product of scientific collaborations that resulted in the following publications:

- Chapter 3:
  Title: Numerical investigation of plasma-driven superradiant instabilities.
  Journal: Class.Quant.Grav. 37 (2020) 17, 175006, e-Print: 2001.11484 [gr-qc].
  Authors: A. Dima, E. Barausse.

- Chapter 4:
  Title: Spin-induced black hole spontaneous scalarization.
  Journal: Phys. Rev. Lett. **125** (2020), 231101, e-Print: 2006.03095 [gr-qc].
  Authors: A. Dima, E. Barausse, N. Franchini, T. Sotiriou.

- Chapter 5:
  Title: Dynamical Chameleon Neutron Stars: stability, radial oscillations and scalar radiation in spherical symmetry.
  Journal: Submitted to Phys. Rev. D, e-Print: 2107.04359 [gr-qc].
  Authors: A. Dima, M. Bezares, E. Barausse.

Acknowledgements

In più momenti durante questi quattro anni di dottorato ho avuto modo di realizzare quanto il percorso che mi ha portato fino a qui sarebbe stato infinitamente più arduo senza tutte le persone che hanno dato un senso a tutta questa esperienza. E per questo, non posso ora che soffermarmi ancora una volta e provare ad esprimere a parole la mia profonda gratitudine per quello che ciascuno di voi mi ha donato.

Senza timore di esagerare, posso ora affermare che sono stato molto fortunato nell'avere Enrico come guida durante questi ultimi anni. In primo luogo, gli sono grato per tutte le volte che mi ha mostrato con pazienza dove imparare le cose che ancora non sapevo o come correggere gli errori che ingenuamente commessi. GLi sono grato per ogni volta che mi ha offerto pazienza, empatia e supporto nell'affrontare anche i più piccoli ostacoli incontrati durante il dottorato. Gli sono grato per aver mantenuto un costante, ininterrotto ed aperto dialogo, cosa che si è scoperta non scontata e quantomai preziosa in periodi complicati come quelli recenti. Infine, gli sono grato per tutto quello che ho avuto l'opportunità di imparare da lui, sulla Fisica e sul modo di fare Scienza.

In secondo luogo, voglio ringraziare i postdoc e i dottorandi del gruppo in cui ho lavorato per gli innumerevoli consigli e per gli stimolanti scambi di idee avuti con loro: Marco, Mario, Miguel, Sebastian, Nicola, Memo, Lotte e Mateja. Devo però un ringraziamento speciale a Miguel, senza il quale molti dei propositi e progetti fatti durante il mio dottorato non si sarebbero mai concretizzati.

E non posso non dedicare un pensiero speciale a tutti i miei "compagni di merende": Uriel, Paolo, Shani, Ale, Warren, Lollone, Alfredo e tutti coloro che sono passati per la Vineria; ancora Miguel, Nicola e Memo; Dario, Antonio e tutti gli assidui frequentatori della casa in Viale. Con tutti voi ho condiviso più memorabili aneddoti di quanti riuscirò mai a riportare per iscritto, e forse anche ricordare. La vostra amicizia è sicuramente la cosa più bella che ho scoperto qui a Trieste, e mi fa ora rimpiangere che questo dottorato non duri almeno altri quattro anni. In particolare, sarò sempre grato a Paolo per avermi insegnato ad apprezzare la molestia, la palestra, la carne, la politica di destra e l'atletica leggera, tra le molte cose. Ad Uriel, per "le vinerie trankis", per le struggenti canzoni latinoamericane cantate assieme, e per essere sempre stato pronto ad ascoltare i turbamenti del mio animo. Ringrazio Dario e Antonio per le immancabili amatriciane e le sontuose carbonare, le eccessive grigliate in lockdown, per avermi fatto conoscere la pesca (poca) in apnea e per le lunghe notti passate a parlare davanti a una bottiglia di rum. Aggiungerò qui uno speciale ringraziamento anche alla piccola Mr. Pickles, per avermi rallegrato con la sua dolcissima compagnia felina ogni volta che ne sentivo il bisogno.

Sono molto felice di avere avuto Marta al mio fianco in questi ultimi anni. A lei sono grato per avermi fatto scoprire e coltivare lati di me sconosciuti o dimenticati. Per il tuo affetto, per la tua dolcezza e per la tua pazienza nel supportarmi fino a qui, io ti ringrazio.

Infine, vorrei concludere ringraziando la mia famiglia, i miei genitori e i miei nonni. Vi sarò eternamente grato per tutte le scelte che avete fatto ponendomi in primo piano, per tutto il prezioso tempo e le energie che mi avete dedicato, per i sacrifici incondizionati e l'infinito amore che mi regalate. Inoltre, dovrei ringraziare ciascuno di voi per innumerevoli motivi, ma spenderò solo qualche parola su quelli che per me sono più significativi. Sono tanto grato a mia madre per la sua accentuata sensibilità e capacità d'empatia, che spero di aver assorbito almeno in parte, e per quella che potrei chiamare "sana dose di follia", su cui spesso faccio affidamento e di cui spero di non abusare. Sono molto grato a mio padre per la caparbietà

e la determinazione, che temo di aver fatte mie nel bene e nel male, e per avermi fatto per primo apprezzare il fascino della Narrazione, dalla quale è breve il passo al Sogno e alla Poesia. Sono infinitamente grato a mio nonno per avermi insegnato a ridere, a cantare e ad affrontare la vita e tutti i suoi accidenti con maggiore serenità e stoicismo. Sono enormemente grato a mia nonna per essere stata il mio primo Maestro; per avermi donato il rigore, il metodo e la disciplina; per avermi insegnato ad imparare; per avermi per prima mostrato come coltivare la mia curiosità e trasformarla in Scienza. Tutti gli obiettivi da me raggiunti finora e i risultati futuri avranno sempre segretamente anche la sua firma, subito accanto alla mia.

Contents

List of Figures

List of Tables

A Marta

Chapter 1

General relativity: theory and tests

1.1 The Theory of Gravitation

1.1.1 The Equivalence Principle

Physical intuition moves under the guiding light of fundamental principles, that historically marked the path towards the greatest results and most successful theories. In the development of the theory of gravitation a fundamental role was played by the principle of equivalence in its various incarnations, from the original Newtonian formulation to the Einsteinian interpretation. In particular, the latter lies at the foundation of the Einsteinian logic that built the theory of general relativity. Nowadays, the equivalence principle not only has an undoubted historical and pedagogical importance, but represents a powerful tool in the classification of the large number of alternative theories of gravity. Here I will borrow this illuminating perspective from influential works from the past [1–3]: a hierarchy between the different equivalence principles can be established, based on the sophistication of their requirements. In this regard, this series of nested definitions determine an incremental specialization in the space of gravitational theories that abide them, until general relativity is singled out as the theory satisfying the most restrictive formulation.

The Newtonian Equivalence Principle identifies, based on empirical evidence first elaborated by Newton [4], the concept of *inertial mass*, appearing in the fundamental laws of dynamics, with the *gravitational mass*, the physical quantity that sources the gravitational attraction between bodies. In practice, the Newtonian Equivalence Principle is satisfied by all theories that recover Newtonian gravity when restricting to "weak" gravitational fields and slow motion of sources (i.e., the Newtonian limit). Although typically identified with the previous, the Weak Equivalence Principle is a separate formulation that encodes the empirical notion of universality of free-fall, as old as the work of Galileo Galilei at least: test bodies (i.e. backreaction on the surroundings and self-gravity effects are negligible) all respond with a universal behavior under the effect of solely gravitational forces, independently of their properties. There is a natural temptation to interpret the universality of free-fall as due to a geometric effect of spacetime, but to do so on the basis of the Weak Equivalence Principle alone only an affine connection is strictly necessary for determining the rules for parallel-transport on the spacetime manifold [3]. The need of a metric tensor that mediates gravity is required only when invoking the Einstein Equivalence Principle, which includes the weak formulation with the addition of local Lorentz and position invariance. The latter identifies "metric theories of gravity", in which gravity is geometric and encoded in the spacetime curvature of the metric-compatible Levi-Civita connection. Finally, the Strong Equivalence Principle is the most stringent formulation of the family of equivalence principles. It requires the validity of local Lorentz and position invariance of all experiments, even the ones

gravitational in nature, together with the extension of Weak Equivalence Principle to bodies with non-negligible self-gravity. As it turns out, general relativity is the only known theory in four dimensions that satisfies the Strong Equivalence Principle, although there is a notable exception represented by Nordström gravity [5] that abides the principle but is ruled out by observations (i.e. does not predict the bending of light) [6].

1.1.2 General relativity

The Strong Equivalence Principle actually selects the class of "Lanczos-Lovelock" theories [7–9], which is the unique class of Lorentz-invariant theories in D dimensions that satisfy the requirements of the equivalence principle and feature second order field equations and thus propagate only two physical degrees of freedom associated to a massless graviton. A consequence of Lovelock's theorem [10] the unique realization of Lanczos-Lovelock gravity in four dimensions is general relativity, described by the *Einstein-Hilbert* action [11]

$$S_{EH} = \int d^4x\sqrt{-g}\frac{M_{\rm pl}^2}{2}\left[R - 2\Lambda\right] + S_m[g_{\mu\nu};\Psi]\,, \tag{1.1}$$

where g is the determinant of the metric tensor $g_{\mu\nu}$; R is the Ricci scalar, constructed from an appropriate combination of second derivatives of the metric and $M_{pl} = 1/\sqrt{8\pi G}$ is the reduced Mass Planck in natural units, $\hbar = c = 1$. In action (1.1) a term proportional to the cosmological constant, Λ, has been included to describe the most general four-dimensional theory compatible with Lovelock's theorem. The matter sector is introduced via the action $S_m[g_{\mu\nu};\Psi]$, which is here kept as a generic action of the matter fields, all collected together under the symbol Ψ, coupled to the spacetime metric $g_{\mu\nu}$. In general relativity, the matter fields are universally and minimally coupled to the metric through the covariant volume element $d^4x\sqrt{-g}$, but alternative theories might give different prescriptions as we will see in the following sections. From (1.1) one can derive the Einstein field equations,

$$G_{\mu\nu} + \Lambda g_{\mu\nu} = 8\pi G T_{\mu\nu}\,, \tag{1.2}$$

where $G_{\mu\nu} \equiv R_{\mu\nu} - 1/2 g_{\mu\nu}R$ is the Einstein tensor, $T_{\mu\nu} \equiv -2/\sqrt{-g}\,(\delta S_m/\delta g^{\mu\nu})$ is the matter stress-energy tensor. As a consequence of Bianchi identities, the Einstein tensor is divergence-free, fact that together with the Einstein equations enforces the weak equivalence principle (i.e. matter test field move along spacetime geodesics) and the covariant conservation of the matter stress-energy tensor, $\nabla_\mu T^{\mu\nu} = 0$. Alternative theories of gravitation can be found when generalizing on the assumptions underlying the Lovelock theorem, for instance by admitting additional gravitational degrees of freedom other than the standard massless graviton.

1.2 Tests of gravity

In this section I will give a brief review of the main probes of the gravitational interaction available to date. I will start from the classical weak-field tests (bending of light, orbital precession, general-relativistic time-delay, Nordtvedt effect) and the post-Newtonian bounds that can be hence extracted. From here, I will then move to discuss more thoroughly the observations that allow us to pierce the veil of the previously forbidden strong-gravity realm, focusing first on the novel tests

with gravitational-wave observations and then reviewing the other main sources of strong-field constraints.

1.2.1 Weak-field tests

The standard framework to compare the predictions of different theories of gravity in the weak-field regime and test them against observations is the parametrized post-Newtonian (PPN) formalism [12–17]. This is a powerful tool to parametrize the deviations from general relativity in the limit of slowly-moving, $v/c \ll 1$, and weakly-gravitating bodies, $GM/Rc^2 \ll 1$, where the latter can be regarded as the ratio between the gravitational (Schwarzschild) radius of the system with typical mass scale, M, and size R. To be more precise, the PPN framework is based on the post-Newtonian (PN) expansion of the metric around flat Minkowski space with expansion parameter $\epsilon \sim GM/rc^2 \sim v^2/c^2$. In general, the post-Newtonian corrections to the metric are controlled by ten post-Newtonian parameters. However, for conservative metric theories of gravity such as the scalar-tensor theories considered in this thesis, the relevant parameters are only two: γ, which quantifies the amount of spatial curvature induced by a unit mass; and β, controlling the nonlinearity of the gravitational potential at first post-Newtonian order. In this case, the PPN metric, up to second order corrections, outside a (spherically symmetric) body of mass M at distance r reads

$$g_{00} = -1 + 2\frac{GM}{r}(1 - \beta\frac{GM}{r}), \quad g_{0i} = 0, \quad g_{ij} = (1 + 2\gamma\frac{GM}{r})\delta_{ij}. \tag{1.3}$$

The full expression including higher post-Newtonian orders, together with a more detailed treatment of the topic can be found in [1, 2, 18]. As already mentioned, the PPN formalism is perfect to parametrize general relativistic corrections in the gravitational field of non-relativistic stars like our Sun. The PPN framework can be extended to capture also to alternative theories of gravity, such as scalar-tensor theories involving higher-order derivative operators in the action (see [19]). In particular, several observations in the Solar System already delivered precise measurements of the lowest order PPN parameters and allow to put tight contraints on physics beyond general relativity. On this point, here follows a brief summary of the main results.

Deflection of light

The bending of light as a consequence of the spacetime curvature around massive objects is perhaps the most famous predictions of general relativity and certainly the first to receive observational confirmation thanks to the fascinating results obtained by Sir Arthur Eddington in 1919 [20]. The angular deflection of a light ray traveling from a distant source and reaching the Earth after passing the Sun at a distance b (at the point of its trajectory closest to the Sun) can be computed in the PPN framework to be:

$$\delta\theta = (\frac{1+\gamma}{2})\frac{M_\odot}{b}(1 + \cos\Phi), \tag{1.4}$$

where γ is the relevant PPN parameter, $M_\odot$ is the mass of the Sun and Φ is the angular separation between the undeflected trajectory of light and the Sun-Earth distance. The bending of light is a prediction shared by all theories satisfying the Weak Equivalence Principle: if the trajectory of test bodies are independent on their

mass, the "Newtonian" deflection of light can be computed by considering the photons as test bodies in the limit $v \to c$. GR, however, predicts an additional $\gamma/2$ contribution, with $\gamma = 1$, due to the curvature of space around massive objects. Different theories predict different values of γ, e.g. Nördstrom scalar gravity predicts $\gamma = -1$ and is thus ruled out. The most relevant and tightly constraining observations available nowadays are obtained through very-long-baseline (radio) interferometry (VLBI) techniques, which offer data on the light emitted by distant quasars and bent by our Sun. Most recent analysis of such data [21] offer a constraint $\gamma - 1 = (-1.6 \pm 1.5) \times 10^{-4}$ [21]. On kiloparsec scales, constraints on γ come from observations of the lensing effect around elliptic galaxies [22]: while not being compatitive with solar-system bounds, the constraints (at 10% level) produced with these techniques are still interesting since they probe light-deflection on larger galactic scales. In the near future, the GAIA mission [23] promises to deliver accurate astrometric data of Solar-System objects, thanks to which a one-order-of-magnitude improvement in the current bounds on γ will hopefully be achieved [24].

Shapiro time-delay

In passing a massive body, light (or, equivalently, a photon) is not only deflected but also slowed down in terms of coordinate speed (although locally free-falling observers would always measure $c = 1$). In practice, the echoes of a signal sent from Earth and bouncing off a planet in the Solar System would be detected back after a delay in time given by (in the special case of a Sun-grazing light ray) [25]

$$\delta t = 2(1+\gamma) M_\odot \ln\left(\frac{4 d_\odot d_p}{R_\odot^2}\right), \tag{1.5}$$

where $M_\odot$ and $R_\odot$ are the mass and radius of the Sun and d_p ($d_\odot$) is the distance of the Sun to the planet (Earth). Note that formula (1.5) contains a Newtonian contribution (i.e., it can be derived from Newtonian gravity with the requirement of EEP), and the one induced by curvature of space, proportional to γ [26]. The astronomer Irwin Shapiro was the first to discover this effect and observe it thanks to radio pulses reflected back at Earth from Mercury and Venus [27, 28]. More recent experiments make use of artificial satellites that actively retransmit the radar signals (as opposed to planets, used as passive reflectors) and, in fact, from the measurement of the Shapiro time-delay of radio signals retransmitted by the Cassini spacecraft provide $\gamma - 1 = (2.1 \pm 2.3) \times 10^{-5}$, which are the most stringent bounds up to date on the γ post-Newtonian parameter [29].

Orbital precession

Another classical test of gravity consists in the prediction of the perihelion precession of Mercury. Historically the orbital precession of Mercury has been an open problem for a long time, until the famous calculation by Einstein [30] that contributed largely to his fortune and provided the very first successful prediction of GR. In the PPN framework, the computation of the orbital precession of a body of mass m_2 gravitating around a heavier body of mass m_1 delivers an advance (in arcseconds) per orbit of

$$\delta\omega = \frac{6\pi\mu}{a(1-e^2)}\left(\frac{1}{3}(2+2\gamma-\beta) + \frac{JR^2}{2\mu a(1-e^2)}\right), \tag{1.6}$$

where a and e are the semi-major axis and eccentricity measure of the orbit, $\mu = M_1 + M_2$ is the sum of the masses and J is the (dimensionless) quadrupole moment of the heavier body. The measurement of Mercury's perihelion advance obtained by the Messenger spacecraft [31], combined with the Cassini bound on γ yields a constraint on $\beta = 1 + (-0.2 \pm 2.5) \times 10^{-5}$. Improvements in this constraint are typically bounded by accuracy to which γ and the Sun quadrupole moment are measured. Nonetheless, the BepiColombo spacecraft launched in 2018 could offer improvements in the future in this constraint [32].

Nordtvedt effect

Many alternative metric theories of gravitation can predict violations of the Weak Equivalence Principle for gravitating objects (sometimes referred to as the Gravitational Weak Equivalence Principle or Gravitational Weak Equivalence Principle). The violation of the equivalence of inertial and gravitational mass is called "Nordvedt effect" [33], and is realized, for instance, in scalar-tensor theories where the gravitational constant is varying depending of the position in space [34]: in the Newtonian limit, the acceleration induced in a massive object by an external gravitational potential Φ can be parametrized as

$$\mathbf{a} = (1 - \eta_N \frac{E_g}{M}) \nabla \Phi \,, \tag{1.7}$$

where M and E_g are the mass and gravitational self-energy of the object. The PPN parameters enter in $\eta_N = 4\beta - \gamma - 3$ ($\eta_N = 0$ in GR) when preferred-frame effects typical of non-conservative theories have been neglected. A classic test of the Nordvedt effect consists in continuous monitoring of the Earth-Moon distance by precise measurements of the round-trip travel times of laser pulses sent from Earth and reflected from a mirror placed on the surface of the Moon during the Apollo 11 mission. Recent analysis [35] of the data obtained with Lunar Laser Ranging [36, 37] offer a constraint on the Nordvedt parameter of $|\eta_N| < 2.9 \times 10^{-4}$. The Nordvedt effect can also be tested in the strong-field regime of triple systems composed of a pulsar and two white dwars [38, 39] from which one can place a bound on $\Delta = \eta_N (E_g/M) = (0.5 \pm 1.8) \times 10^{-6}$ at 95% of confidence level. Given that roughly $E_g/M \sim 0.1$ for a relativistic star, one can deduce that $|\eta_N| \lesssim 10^{-6}$.

1.2.2 Strong-field tests

Binary pulsars

The first (isolated) radio pulsar was discovered in 1968 [40]: radio pulsars are rapidly rotating and highly magnetized neutron stars that emit radio pulses at each rotation due to a magnetic dipole misaligned with the rotation axis, following the standard "lighthouse model" [41–43]. A large part of the population of radio pulsars consists in "young" neutrons stars rotating with periods 30–500 ms, that are the remnants of supernovae explosions (e.g. like [44]). In 1982 with the observation [45] of the first fast rotating pulsars with periods $\lesssim 30$ ms, hence the name *millisecond pulsars*, evidence was provided for the existence of a population of "older" rotating neutron stars (also referred to as *recycled pulsars*) that have been spun up by accretion from a companion star [46–48]. In addition to their shorter periods, millisecond pulsars also appear to be more stable in their rotation as their secular change in period are typically smaller than standard pulsars. In practice, the time of arrival of radio pulses

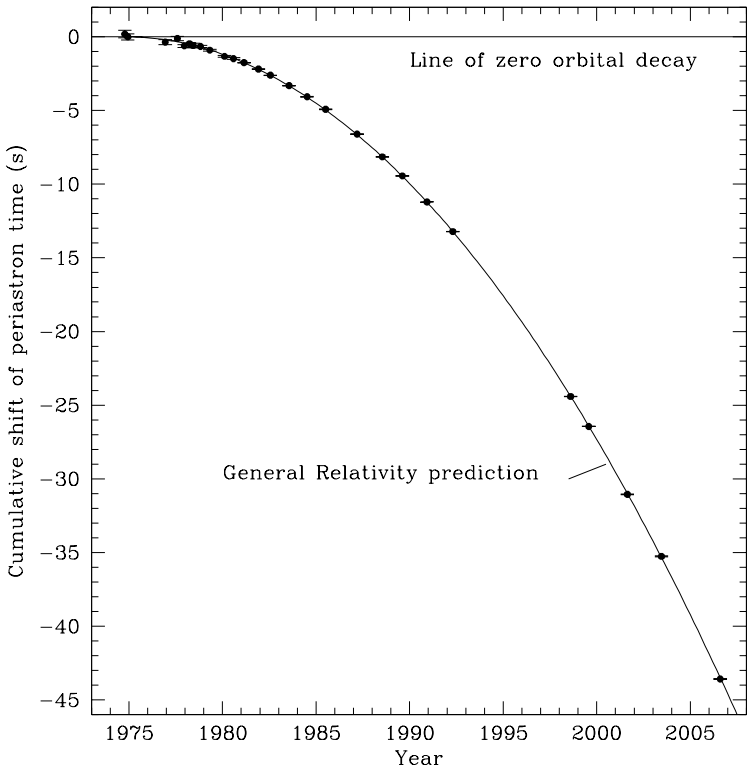

FIGURE 1.1: *Comparison of the expected shift of periastron time according to general relativity (parabola) with measurements from PSR B1913+16.* Credit: [66]

coming from these very precise "pulsar clocks" is measured by radio telescopes on Earth over time scales of several years.

A true gamechanger for gravitational physics was the discovery of the first binary pulsar system in 1974 by Russell Hulse and Joseph Taylor [49]. Not only the measurement of the decrease of orbital period provided the first indirect confirmation of the existence of gravitational waves, but it also opened an entirely new avenue for testing gravity with strongly-gravitating bodies [50]. With *pulsar timing* techniques, any deviation from general relativity predictions can be constrained with great precision by fitting with accurate models the relativistic effects due to the orbital motion of the binary, time dilation and time delays in the signal [47, 51, 52]. The two-body problem in general relativity generally does not admit an analytical solution: the orbital dynamics of binary systems must be solved either numerically or within the post-Newtonian framework under the slow-motion and weak-field assumptions. The equations describing the relative motion in the general relativistic post-Newtonian approximation have been worked out to high post-Newtonian orders [53–56] and have been extended also to describe orbital motion and gravitational-wave emission of binaries in alternative theories of gravity [57–65].

The *parametrized post-Keplerian* (PPK) formalism [67] is an alternative way of testing gravity with strongly-gravitating binary objects, which extends its scope beyond the

weak-field and slow-motion limitations of the PPN framework. Building on the earliest results in this direction [68–70] the PPK approach consists in a phenomenological modeling of the pulsar timing data with five Keplerian parameters: the orbital period, P_b, the eccentricity of the orbit, e, the projected semi-major axis of the orbit, x, the epoch of periastron passage, T_0, the longitude of the periastron, ω. On top of that, up to 19 post-Keplerian parameters can be considered in order to account for the quasi-stationary evolution of the binary system. Among these, we shall just mention the secular damping of the orbital period due to gravitational-wave emission, $\dot{P}_b$, the periastron advance due to the relativistic precession of the orbit, $\dot{\omega}$, and the parameter controlling the time-dilation in the pulses due to a sum of gravitational and dynamical effects, $\tilde{\gamma}$.

The post-Keplerian parameters can be related to the masses of the pulsar and its companion and to the Keplerian parameters, but each gravitational theory can predict largely different functional forms and direct dependence on the (additional) fundamental parameters of the theory. Independent measures of at least two parameters can be combined in general relativity to obtain several estimates of pulsar and companion masses, which can be then compared to do consistency checks for general relativity predictions. Historically, the first of such tests was possible only some years after the discovery of the first binary pulsar PSR B1913+16. After the binary system masses could have been determined thanks to measurements of $\tilde{\gamma}$ and $\dot{\omega}$, a measurement of the orbital decay rate proved the general relativity predictions correct up to one part in 10^{12} [66, 71]. The gravitational-wave-induced orbital period damping can be tested to even grater accuracy with double pulsar systems like [72, 73].

Largely asymmetric systems like PSR J1738+0333 [74], which is composed by a pulsar and a white-dwarf companion, are the best source of constraints for theories that violate the strong equivalence principle and predict dipolar gravitational-wave emissions as the latter, in fact, is typically proportional to the square of the difference of the additional "gravitational charges" [75] and is maximized when the companion is a weakly gravitating body like in PSR J1738+0333 [76].

Black-hole X-ray observations

The strong-field regime of gravity can be also tested through observations of the electromagnetic radiation emitted by infalling matter in accretion disks around astrophysical black holes. Such tests are sensitive to the interactions between gravity and matter, the geodesic motion of the latter and, thus, probe the Eistein equivalence principle. In this sense, they are complementary to gravitational-wave tests (see next subsection), which are directly sensitive to the Einstein equations (1.2) and to potential deviations from them. The sketch of the system consists in a black hole surrounded by accreting matter distributed in two main structures: a cold, geometrically-thin and optically-thick disk; and a hot, lower-density and quasi-spherical "corona". The disk can locally be approximated as a system at thermal equilibrium that emits a black-body spectrum, which is typically peaked in the X-ray band for stellar-mass black holes (or in the optical/UV for supermassive black holes). The disk temperature is expected to change with the distance from the black hole, so that the sum of all radial contributions will give a multi-temperature black-body spectrum. A part from this thermal radiation, *disk-corona model* (sometimes referred to as "lamppost" model) predicts electromagnetic emissions with two additional components: thermal photons that, after emission from the disk, Compton-scatter off the

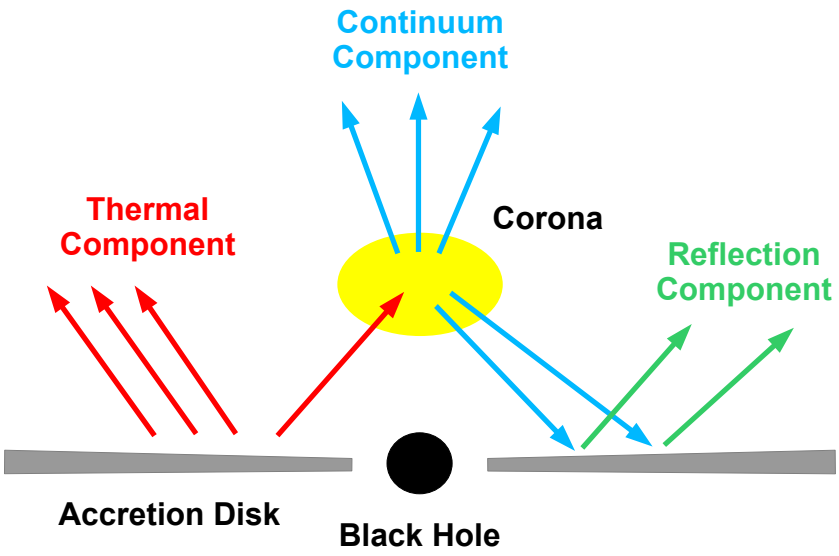

FIGURE 1.2: *Sketch of the black hole-corona-accretion disk model.* Credit: [77]

hot electron corona; and photons that, after Compton-scattering in the corona, get are reflected off by the disk [78].

The field of *X-ray reflection spectroscopy* deals with analyzing observational data of the reflected component with accurate astrophysical models, from which one can extract information about the properties of the accreting black hole and, potentially, test fundamental theoretical assumptions [79]. In particular, the reflected radiation spectrum contains two relevant features: the fluorescence emission lines left by the elements of the cold disk when illuminated by the hot corona and a characteristic Compton "hump" around energies of 20 – 30 keV. Information about the curved spacetime region where the radiation was produced is encoded in relativistic effects that distort these features (gravitational redshift, Döppler beaming and light bending). In general relativity these effects depend mainly on the spin of the spacetime at the innermost stable circular orbit (ISCO), assumed to coincide with the inner boundary of the disk; thus, naturally the iron-line fitting technique has been mainly used to estimate the spin parameter in X-ray binaries or active galactic nuclei [80–83].

An alternative approach consists in fitting the continuous multi-temperature spectrum due to thermal radiation, method called *continuum fitting* [84, 85]. However, contrary to the latter, the continuous spectrum depends on five parameters: the mass, M, and spin, a, of the black hole, the accretion rate, $\dot{M}$, the distance of the source, D, and the viewing angle of the disk, ι. In addition to that, the effects of these parameters are largely degenerate and independent estimates of a subset of the parameters (typically, M, D and ι thanks to optical observations) are required to break the degeneracy.

Recently, however, increasing effort has been devoted to model numerically the

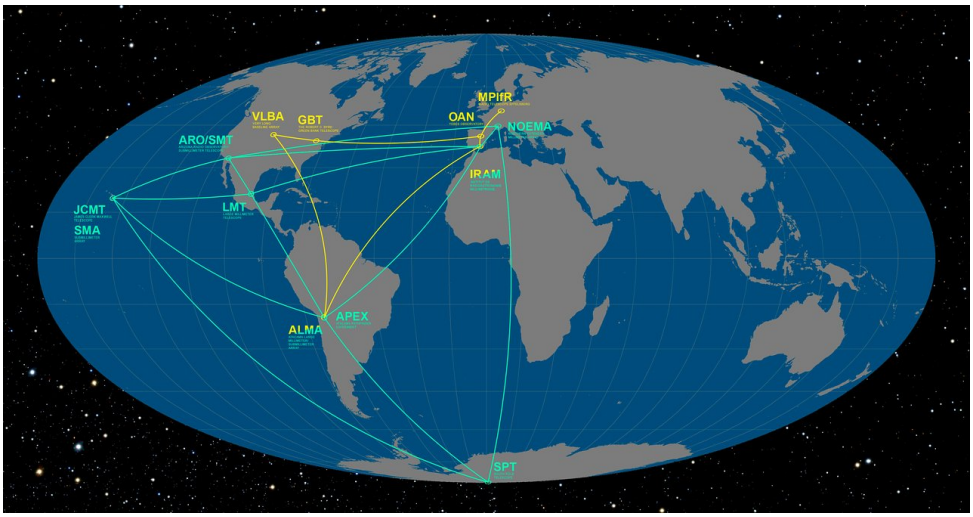

FIGURE 1.3: *Array of observatories of the Event Horizon Telescope collaboration.* Credit:ESO/O. Furtak, [101]

X-ray emissions from accretion disks in non-Kerr spacetimes modeled with parametric black-hole metrics, which contain an infinite sum of parameters controlling possible deviations from the Kerr metric (e.g.: *Johansen metric* [86] or *Rezzolla-Zhidenko metric* [87]). The results are then compared with X-ray reflection observations, either to conduct null-tests in order to verify that the data are compatible with vanishing non-Kerr parameters [88–90] or to conduct model-specific tests [91–95]. Tests of gravity with the continuum-fitting technique have been considered [96–98] but are limited because of a degeneracy between spin and nnon-general-relativistic deformations effects [79].

In addition to these two methods, a promising new probe of the strong-field regime around astrophysical black holes consists in the quasi-periodic oscillations (QPOs) that have been observed in the time series of X-ray emissions of black holes [99]. Once a robust astrophysical model for their mechanism will be found, QPOs promise to become a new source for stringent bounds on deviations from the Kerr paradigm [100].

In conclusion, although many systematics still have to be taken into account and astrophysical models need improving before being able to provide strong-field constraints that are competitive with the ones coming from gravitational-wave observations [88], these techniques for probing gravity are only relatively recent and the development is proceeding in parallel with the roaring growth of gravitational-wave astronomy.

Black Hole shadows

In 2017 the Event Horizon Telescope collaboration (EHT) announced the successful reconstruction of the first horizon-scale image of a supermassive black hole [102, 103], which added a brand new observational probe of the strong-gravity region surrounding astrophysical black holes. Most galaxies host at their center very bright regions that, in the case of quasars [104–106], represent some of the most luminous sources of electromagnetic emissions in the observable universe. The mechanism behind these intense emissions is believed to be high-rate accretion of supermassive black holes from matter distributed in a cold, geometrically-thin and optically-thick

disk [107]. Some galaxies instead, including the Milky Way [108–110] and M87 [111, 112], host at their center supermassive black holes accreting at low rates from hotter, geometrically-thick and optically-thin disks [113–115]. In these low-luminosity active galactic nuclei (LLAGN) the accretion flow and/or the relativistic plasma jets launched from the near-horizon region contribute via synchrotron radiation to electromagnetic emissions in the radio and far-infrared bands [114–118]. Because of the optical transparency of the medium in which LLAGNs are immersed, such systems are optimal candidates for observations of horizon-scale features with VLBI techniques [119] at $\sim$ 1.3 mm wavelengths. But what features can a distant observer resolve in such systems? Black hole spacetimes typically feature a photon capture radius, R_c, that marks the critical impact parameter for which photons approaching from infinity are captured and plunge into the black hole: for a Schwarzschild spacetime [120] the corresponding photon capture radius is $R_c = 3\sqrt{3}r_g$, where $r_g \equiv GM/c^2$ is the characteristic scale of the black hole. Note how the photon capture radius is more than two times larger than the Schwarzschild radius, $R_s = 2r_g$, which determines the size of the (spatial section) of the event horizon. Thus, the EHT cannot access directly the "image of the event horizon" but only the lensed image of the "photon ring", i.e. the unstable circular orbit of photons with impact parameter exactly equal to R_c. For rotating black holes, described in general relativity by the Kerr metric [121], the latter may not be circular anymore as the shape of the cross section depends now on the orientation of the light ray with respect to the spin angular momentum of the black hole [122–124]. In particular, when the latter is surrounded by a geometrically-thin and optically-thick disk simulations have shown that the system would appear to a distant observer as a combination of a thin emission ring and a lensed image of the thin disk [125]. In the case of LLAGNs, instead, the expected image consists in a darker region ("shadow") surrounded by a bright ring-shaped emission region that, due to spin and relativistic effects, can appear to have a "crescent" shape [119, 126–129]. The size of the observed emission ring is proportional to the photon capture radius, R_c, and encodes information regarding the strong gravitational field of the central object. However, in addition to the dependence on the black-hole parameters (mass, spin and spin orientation), the shape and size of the observed shadow strongly depends on the instrumental resolution and on the details of the astrophysics of the hot, turbulent and magnetized emitting region. By modeling the latter with advanced general-relativistic numerical simulations [130] and by combining independent mass and mass-to-distance ratio estimates [111] with the radio observations obtained with VLBI [131], the EHT collaboration was able to provide an estimate of the emission ring of M87* that is compatible with the lensed photon capture radius of a general relativistic black hole within 17% error at 68% confidence level [103].

The idea of using this observation to extract information about the underlying theory of gravity has been developing for many years now [133–135], and several predictions for the size and shape of alternative objects [136–140] or of black holes in extended models of gravity [141–149] are now available for comparison with observational data. Tests of strong-gravity with black hole shadow measures follow mainly two directions. The first one consists in employing the shadow measurement in the theory-agnostic framework of deformed metrics [86, 87], in order to constraint the deformation parameters and test multiple spacetimes alternative to general relativity black holes at a time. An example of this approach is given by [150], in which an attempt to constraint higher order terms in post-Newtonian expanded

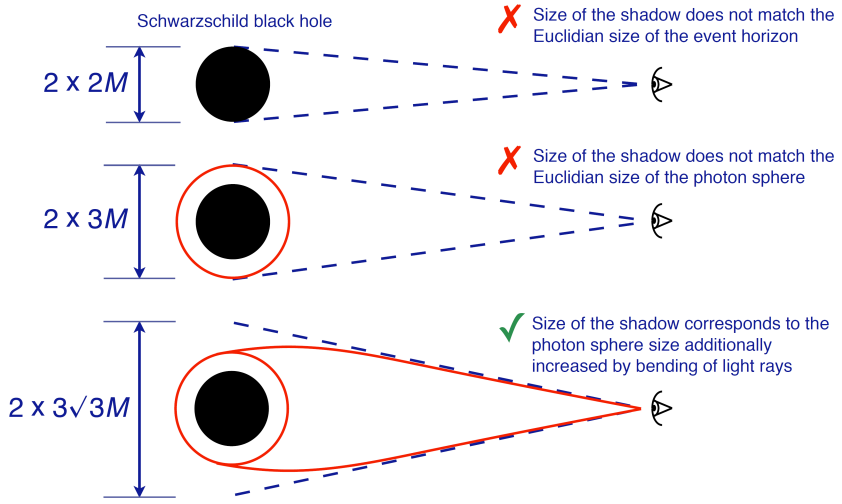

FIGURE 1.4: *Shadow size in the case of a Schwarzschild black hole.* Credit: [132]

deformed metric. Note however that the approachs used in this work raised several critiques, from the validity of the post-Newtonian expansion in strong-field regimes to the unjustified *a priori* assumptions made on the different post-Newtonian parameters [151]. Indeed, the main problems in parametric tests with one black-hole shadow measurement is that, naively, with only one data point available only combinations of the deformation parameters can be constrained. Furthermore, the deformed parameters are not directly connected to the fundamental parameters of the alternative compact object/extended theory, thus making immediate physical interpretations more difficult. The alternative approach consists in constraining directly physical properties of the modified horizon-scale geometry, i.e. angular momentum, electric charge and/or extra (scalar) charges [150, 151]: such model-specific tests obviously loose in scope but gain in robustness and tightness of the constraints, allowing to probe fundamental aspects of the theory like no-hair and *cosmological censorship conjecture* [150] or the Kerr hypothesis, when future measurements will improve in precision down to the level of observable spin effects.

In conclusion, black-hole shadow measurements are not yet capable of providing bounds on alternative spacetimes that are comparable with the ones coming from gravitational-wave observations, but are nonetheless an important probe of the strong-field regime of gravity in the scale of masses typical of supermassive black holes.

1.2.3 Gravitational-wave tests

The prediction that accelerating masses with a varying quadrupole moment can radiate gravitational waves dates back to the early days of general relativity. However, the physical interpretation of gravitational radiation was debated for many years: its very existence and/or observability was initially critically questioned by Einstein himself [153, 154]. The first indirect observational confirmation of the existence of gravitational waves came with the measurement of the orbital period damping in the

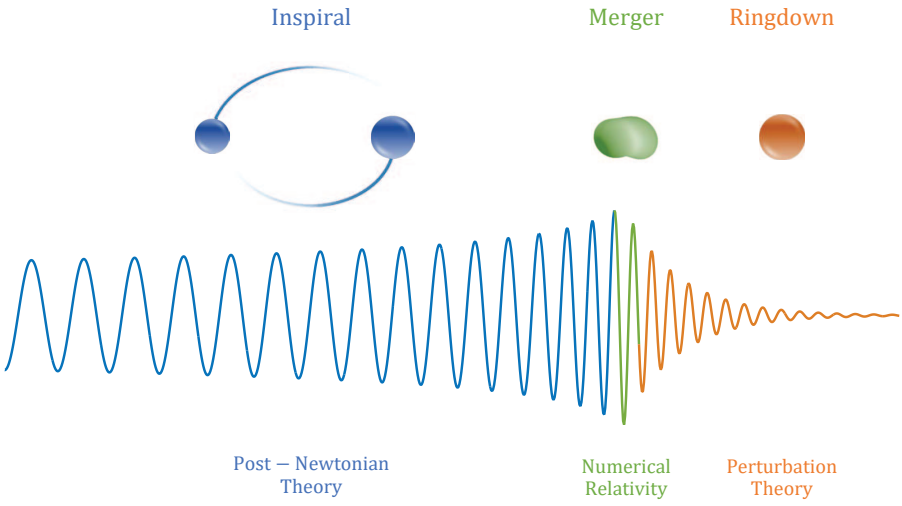

FIGURE 1.5: *Stages of the coalescence of a binary system of compact objects.* Credit: [152]

Hulse-Taylor pulsar [49], while the first direct detection of a gravitational wave produced during the merger of a distant black-hole binary system came in 2015 [155]. Since then the number of observed gravitational-wave events grew significantly and the current catalog of detections includes numerous binary black-hole mergers, two binary neutron stars [156, 157] and two black hole-neutron star events [158]. Currently all the gravitational-wave observations come from the Laser Interferometer Gravitational-Wave Observatory (LIGO) Scientific Collaboration [159] and the VIRGO Collaboration [160] thanks to the three L-shaped ground-based interferometers respectively located in Livingston and Hanford (US) and Cascina (Italy). Since 2020 the array of gravitational-wave antennae has been extended as the Kamioka Gravitational Wave Detector (KAGRA) [161] became operational and plans to join LIGO–VIRGO in the fourth observational run are currently under discussion. Meanwhile, *third-generation* ground-based interferometers like the Einstein Telescope [162] and Cosmic Explorer [163] are currently under planning and share the ambition of reaching $\sim$ 100 times higher sensitivities than the older generation. The realization of space-based interferometric experiments is prospected for the mid 2030s. Such space-bourne gravitational-wave telescopes are completely unaffected by standard (i.e. seismic and anthropic) noise sources that instead affect the sensitivities of ground-based experiments; and thanks to the very large design arm-lengths they are devised to be sensitive to sub-Hertz signals that are not accessible by current interferometers. Currently, the proposed future missions include the realization of the Laser Interferometric Space Antenna (LISA) [164, 165], TianQin [166] and the Deci-Hertz Interferometer Gravitational-wave Observatory (DECIGO) [167, 168]. An interesting approach in alternative to laser interferometry given by *Pulsar Timing Array* (PTA) techniques: a gravitational wave in passing will leave tiny fluctuations in the otherwise extremely regular periodic signals emitted from pulsars [169, 170], which could be detected by computing the time residuals in the measured time of arrival of radio pulses from a correlated array of known stable (millisecond) pulsars [171]. Observational efforts implementing the PTA program consists in the monitoring of 25 pulsars by the Parkes Pulsar Timing Array [172], 45 pulsars by the North American Nanohertz Observatory for Gravitational Waves (NANOGrav) [173] and 42 pulsars by the European Pulsar Timing Arrays (EPTA) [174], which together constitute the

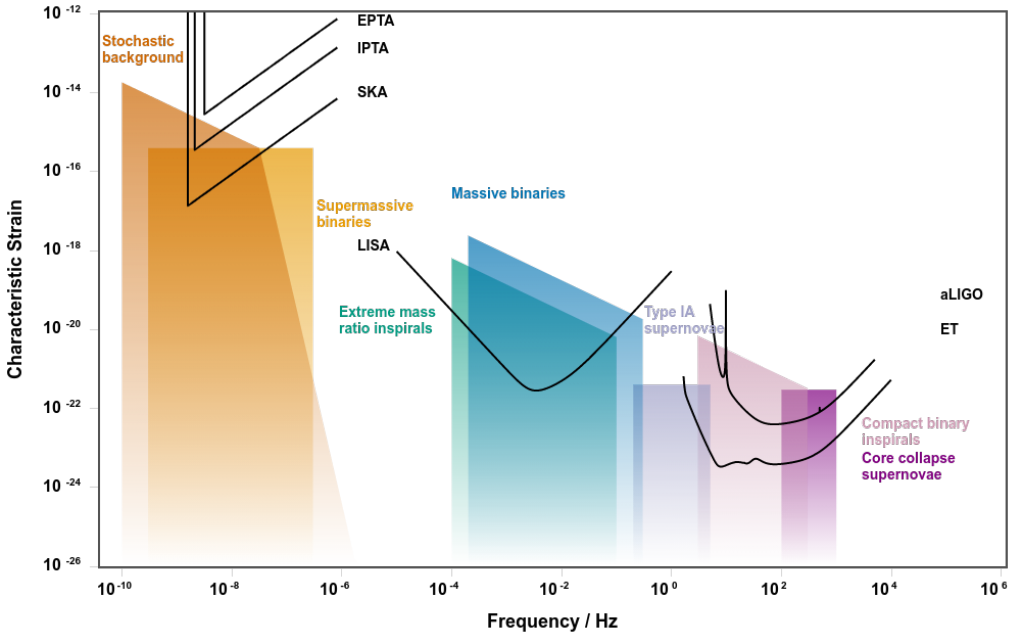

FIGURE 1.6: *Gravitational-wave sources and detector sensitivity curves.* Credit: [176]

International Pulsar Timing Array (IPTA) [175] monitoring a total of 65 independent millisecond periodic radio sources.

Gravitational-wave signals can be divided into four categories based on their origin and properties: bursts, stochastic gravitational waves, continuous periodic signals and chirps from the coalescence of compact binaries. At the end of their life-cycles, red giant stars and/or white dwarfs accreting from a companion are believed to undergo gravitational collapse to a black hole or neutron star remnant. Such cataclysmic events can produce supernovae (respectively of Type II and Type I) associated with emissions of (mainly) neutrinos, electromagnetic radiation and, depending on the geometry of the collapse, also gravitational-wave bursts which can carry away a significant part of the binding energy of the original system (see [177, 178] for reviews). Because of the complexity of the problem the most of the details of the mechanism that ignites the supernovae explosion are still unknown [179]. Such fascinating extreme phenomena are mainly investigated with numerical simulations [177], although incorporating consistently all relevant physics (e.g. general relativity, magneto–hydrodynamical turbulence, neutrino transport) is still an open challenge [178]. On the observational side, much effort has been put to detect signals from collapsing stars [180], neutron-star excitations [181, 182] and other more exotic sources of short-duration gravitational-wave transients [183, 184]. However, only upper bounds on the source-rates have been put so far [185].

Because of conservation of mass and total angular momentum, rotation of spherically symmetric or axisymmetric objects does not generate gravitational waves in general relativity. However, rapidly rotating NS that feature even a tiny asymmetry in their geometry [186] could in principle produce periodic and continuous gravitational-wave signals analogous to the radio pulses produced by pulsars [187, 188]. So far, none of such continuous gravitational-wave signals has been detected by the LIGO–VIRGO collaboration [189–191].

The incoherent sum of unresolved signals produced throughout the history of the Universe will constitute a random gravitational-wave field of astrophysical origin [192]. Analogously to the cosmic microwave background, a cosmic gravitational-wave background is predicted to be composed of relic gravitational radiation from early universe processes [193]. These are the astrophysical and cosmological components of the stochastic gravitational-wave background that is the object of modern sky-surveys conducted by the LIGO–VIRGO collaboration [194, 195] and PTA survey [196]. Recently, the NANOGrav collaboration claimed the observation of strong evidence for stochastic process that could be interpreted either as a gravitational-wave background due to an early-universe phase-transition occuring at temperatures below the electro-weak scale; or as the astrophysical contribution due to unresolved coalescences of supermassive black holes [197, 198].

All events detected so far by the LIGO–VIRGO collaboration fall in the category of compact binary coalescence. A binary system of coalescing compact objects emits gravitational waves throughout the three stages of its dynamical evolution: inspiral, merger and post-merger ringdown of the remnant (see Fig. 2.1). During the inspiral the orbits decay dynamically because of the energy lost through gravitational-wave emission. As the two objects come closer, their orbital velocities increase until reaching a significant fraction of the speed of light during the last orbit before the violent merger. As a consequence, the frequency and amplitude of the gravitational waves emitted also increase, producing the typical "chirp-like" signal. After the merger, while relaxing to a stable axisymmetric configuration, the remnant emits a ringdown signal composed of characteristic frequencies that contain information about the properties of the object. Mergers of two neutron stars can form, as an intermediate stage, a supramassive or hypermassive neutron star that exceeds the maximum mass limits, which eventually collapse to a black hole. Current ground-based interferometers are sensitive to gravitational waves in the frequency range $O(10)$–$O(1000)$ Hz being mainly limited by seismic and thermal noise in the low-frequency end. This translates in a limited window of masses for the detectable binary systems, which coincides exactly with stellar-origin black holes and neutron stars. The characteristic frequency, f, of a binary system can be estimated via the Kepler law $GM \sim R^3 f$, where G is the Newton constant, M and R are the characteristic mass and length scale of the system. For an order of magnitude estimate, M can be chosen to be the total mass of the binary and R the gravitational radius of the system $R = GM/c^2$. The final estimate yields a typical gravitational-wave frequency that is inversely proportional to the characteristic mass of the binary $f \sim 1/M$: intermediate-mass black hole binaries (typical masses in the ballpark of 100 to 10^4 solar masses) or supermassive black hole binaries (up to 10^6–10^7 solar masses) will be observable at low frequencies (from deci-Hertz down to micro-Hertz), which will be the future operativity range in frequencies of third generation detectors and/or space-bourne interferometers. Finally, binaries composed of a compact object orbiting closely around an intermediate or supermassive black hole (respectively called *intermediate* and *extreme mass ratio inspirals*) are an additional potential source of low-frequency gravitational waves that is predicted to be relevant for instrument like LISA [199].

Waveform modeling can be very challenging already in general relativity, and is typically even more so when trying to include extensions/modifications thereof. The problem of computing the gravitational waveforms is naturally connected to solving the dynamics of a system of N bodies interacting gravitationally. In particular, the two-body gravitational problem admits an analytical solution only in Newtonian gravity and already in general relativity it requires resorting either to numerical

methods or approximated analytical techniques. Historically, the first contributions in the latter direction started shortly after the publication of the theory of general relativity [200–203], although the seminal works that constitute the foundation of the modern post-Newtonian formalism appeared only decades later [204–208]. At zero order in the post-Newtonian expansion, the Newtonian contribution to gravitational waves is given by the Einstein quadrupole formula [200, 202]

$$h_{ij} = \frac{2G}{c^4 r}\frac{d^2 Q_{ij}}{dt^2}(t - r/c) + O(\epsilon)\,, \tag{1.8}$$

where Q_{ij} is the quadrupole moment of the source evaluated at the retarded time, $t - r/c$. The quadrupole formula has been proven successful when compared with observations (see section 1.2.2) and modern day post-Newtonian formalism has evolved to include also higher-order relativistic corrections to the Newtonian contribution [56]. Although being a very powerful tool for analytical solutions of gravitational waves, the weak-field and slow-motion approximations on which the post-Newtonian expansion relies are known to break down in interesting systems. For instance, in the coalescence of compact objects these are strictly valid only in the early inspiral phase and results obtained with this method become unreliable at small separations. Numerical realtivity is the key tool for exploring the otherwise unaccessible nonlinear strong-field regime of gravity [209–212]. For instance, in the merger and post-merger phases one has to resort to accurate numerical simulations to decode the coalescence of compact binaries and, in particular, to model the gravitational waveforms [213–221]. Finally, the black-hole perturbation theory framework is typically employed to describe the characteristic ringdown of the remnant (for reviews,see [222, 223]). Combining the results obtained with the three different methods to produce a single waveform that is consistent throughout the whole coalescence stages requires sophisticated techniques based on the *effective-one-body formalism* [224].

In the following sections I will give a summarized introduction to the type of tests that have been conducted with gravitational-wave events detected by the LIGO–VIRGO collaboration [225–228].

Consistency tests

In practice, the easiest tests one can conduct with gravitational-wave observations consists in evaluating how well does the general relativity waveform template fit the data and analyze the residuals in search for new physics that one might have missed. Typically gravitational-wave signals originated from the coalescence of compact objects are buried in noise and must be "dug out" via *match-filtering* techniques, which consist in correlating the times series coming from the detector with parametrized template waveforms until a threshold in the *signal-to-noise ratio* is reached. The latter is a quantity introduced to estimate the probability of detection of the signal and, as the name suggests, is a function of the signal over noise power spectral densities (for more details see, for instance, [229] for a pedagogical review). The best-fitting template is only the waveform that most likely explains the data. If there were significant residual power in the data stream, then it would mean that the parametrized templates is not suited to explain all the physical features of the signal. This could happen for several reasons, for instance because either the signal is actually composed of several independent gravitational waves that are superimposed; because of non-negligible modeling systematic errors or the signal is better described by non-general-relativistic waveforms. The first simple test that is

conducted on detected signals consists in analysis of the *residuals*, which is done by looking for physical features in the signal after subtraction of the best-fitting waveform, i.e. ones that are not correlated with the instrumental noise [225–228]. The analysis of the residuals can tell how well do general relativity templates fit the observed signals and whether there are some physical effects that one is missing by assuming general relativity as the fundamental theory of gravity.

A more refined way to check that the assumption of general relativity fits well the observed data consists in conducting consistency checks between the physical properties of the system as deduced from different portions of the signals. For instance, by comparing the mass and spin estimates obtained from the inspiral, merger and ringdown signal phases any statistically relevant inconsistency between the different estimates would signal the presence of non-general-relativistic effects [230–233]. This technique is referred to as inspiral-merger-ringdown (IMR) consistency check, and recent examples of its application typically are implemented within a parametrized framework [234] (see, instead, [235] for model-specific forcasted bounds). Moreover, with the same spirit one can test the validity of Hawking's "area law" [236] by elaborating estimates of the event horizons areas in the pre-merger and post-merger phases [237].

Parametrized tests: wave generation

The first theory-agnostic frameworks attempted to incorporate phenomenological modifications to the general relativity waveforms at each post-Newtonian order [18, 230, 238, 239]. Metric theories of gravity that have a well-defined Newtonian limit can also fit in the parametrized post-Newtonian framework. For instance, the dynamics of binary sources and analytical waveforms in scalar-tensor theories are now available up to third [64, 65] and second post-Newtonian order [61–63] respectively. Tests of post-Newtonian gravity with parametrized inspiral waveforms with this approach have been proposed [56, 240, 241] and later the formalism was extended to what is now known as the parametrized post-Einsteinian (PPE) formalism [242], which was built to capture generic non-general-relativistic effects entering at any post-Newtonian order. In the frequency-domain such parametrized waveforms for quasi-circular inspiral read

$$h(f) = h_{GR}(f)(1 + \alpha\, u^a)e^{i\delta\Psi}\,, \qquad \delta\Psi = \beta u^b\,, \tag{1.9}$$

where h_{GR} is the (frequency-domain) general relativity waveform, $u = (\pi\mathcal{M}f)^{1/3}$ is the effective relative velocity of the binary components (with $\mathcal{M}$ the chirp mass) and f the gravitational-wave frequency. The gravitational-wave phase modifications are introduced via the factor $\delta\Psi$. The post-Einsteinian parameters (α, β) and (a, b) determine, respectively, the amplitude of the deviations and post-Newtonian order at which they appear. Each alternative model of gravity predicts different values for these parameters and dictionaries between the PPE and fundamental parameters can be constructed [243, 244]. The parametrized post-Einsteinian framework has been since generalized to include dipole radiation [245], other polarizations and higher harmonics [246]. Thanks to the currently available mass of data from gravitational-wave events, several bounds on the post-Einsteinian parameters can be placed [227, 228] and compared, for instance, with the post-Newtonian bounds from binary pulsars [233, 247, 248].

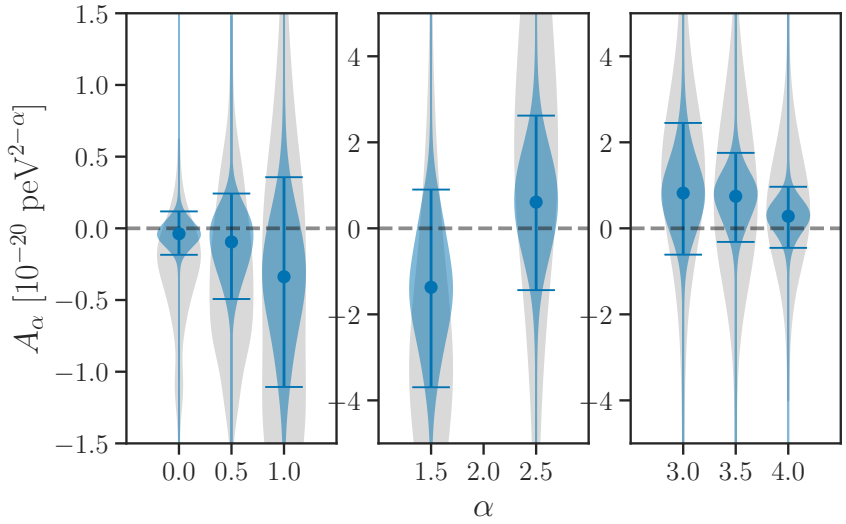

FIGURE 1.7: *Violin plots of the posteriors on the dispersion relation phenomenological parameters.* Credit: [228]

Parametrized tests: wave propagation

Parametrized tests of the gravitational-wave propagation are employed to constrain a set of phenomenological parameters, A_α and α, introduced to account for power-law deviations from the gravitational-wave dispersion relation [249]:

$$E^2 = p^2c^2 + A_\alpha p^\alpha c^\alpha \tag{1.10}$$

where E and p are the gravitational-wave energy and momentum, c is the speed of light. While the general-relativistic relation is trivially reobtained when $A_\alpha = 0$ for all α, a variety of alternative (typically Lorentz-violating) theories have a (leading-order) correspondence with the phenomenological corrections [250–253]. With the available gravitational-wave data stringent bounds have been placed on the deviations in the gravitational-wave dispersion relation [227, 228] (see Fig. **??**). Of particular interest is the correction $\alpha = 0$, which corresponds to the effects due to a graviton mass $m_g = A_0^{1/2}/c^2$ [254]. Current bounds from the collection of data in the first and second observing runs of the LIGO–VIRGO collaboration put a tight upper bound on the graviton mass, i.e. $m_g < 1.76 \times 10^{-23}\ eV/c^2$ [228]. The terms with $\alpha = 2$ correspond to a frequency-independent correction to the speed of propagation of gravitational waves. In general relativity the latter is equal to the speed of light, but in other metric theories deviations from this paradigm are in principle allowed, depending on the structure of the gravitational field equations. For instance, simple massless scalar-tensor theories maintain this property while theories with higher derivative operators can easily predict subluminal or even superluminal propagation of gravitational waves without incurring in causality violations [255–257]. The first constraints on the speed of propagation of gravitational waves have been placed by analyzing the times of arrival of signals to widely separated detectors [258, 259]. As we will see in the next subsection the tightest bounds available on the speed of gravitational waves comes from multi-messenger events.

Multi-messenger observations

Mergers of binary neutron stars not only produce emissions in the gravitational-wave channel, but also observale radiation across the electromagnetic spectrum, in particular prompt gamma-ray bursts and long-lived x-ray afterglows. The multi-messenger nature of these events offer a treasure of data that would not be accessible through the each individual channel alone, creating an incredible opportunity for testing alternative models of gravity.

In 2017 the LIGO–VIRGO Collaboration detected a gravitational-wave event compatible with the coalescence of two neutron stars [156]. A nearly simultaneous gamma-ray burst event (GRB170817A) was detected by the network of gamma-ray observatories [260] and later on an optical counterpart was identified [261]. The direct comparison of the times of arrival of the gravitational radiation and of the gamma-ray burst (assuming nearly simultaneous emission) allows to place the tightest bounds to date on the speed of gravitational waves, which matches the speed of light up to an impressively small error of few parts in $\sim 10^{15}$ [260]. The presence of an electromagnetic counterpart in GW170817 also allowed the first direct confirmation of binary neutron star mergers as (one possible) source of short gamma-ray bursts [226], in addition to other improved constraints on deviations from general relativity, such as in the polarization content (see next subsection).

Gravitational-wave polarizations

As a consequence of the fact that the theory propagates only two degrees of freedom associated to the massless graviton, in general relativity there are only two physical and independent gravitational-wave polarizations. In the appropriate (traceless-transverse) gauge they are typically referred to as *cross*, $h_\times$, and *plus*, h_+, polarizations. Other metric theories of gravity can predict up to six independent polarization states: one additional transverse "breathing" mode and three additional longitudinal modes, including a "streching" mode along the direction of propagation [262, 263]. A detector's response to different gravitational-wave polarizations is determined by the antenna pattern functions [2, 264] and a network of at least five detectors should in principle be able to do a complete analysis of the polarization content of a gravitational-wave signal [228]. However, the currently available network of three antennae can test the hypothesis of pure tensor polarization against purely-scalar or purely-vector alternatives [265–267], the latter two being strongly disfavored by the collection of data from the second catalog of gravitational-wave transients by the LIGO–VIRGO collaboration [228]. Because of the detection of an electromagnetic counterpart a more accurate sky-localization was possible with GW170817, fact that helped placing the tighest bounds on alternative polarization contents [226]. In the future, as the array of detectors is expected to enlarge the sky-localization of observed events is expected to improve significantly and test with mixed-polarization states will be available.

Black-hole spectroscopy

In the framework of general relativity the most general stationary black hole spacetime is described by the Kerr-Newman family of solutions of the Einstein equations, as stated by *no-hair theorems* [268–270]. From an astrophysical perspective, the *no-hair conjecture* maintains that dynamical processes (e.g. gravitational collapse)

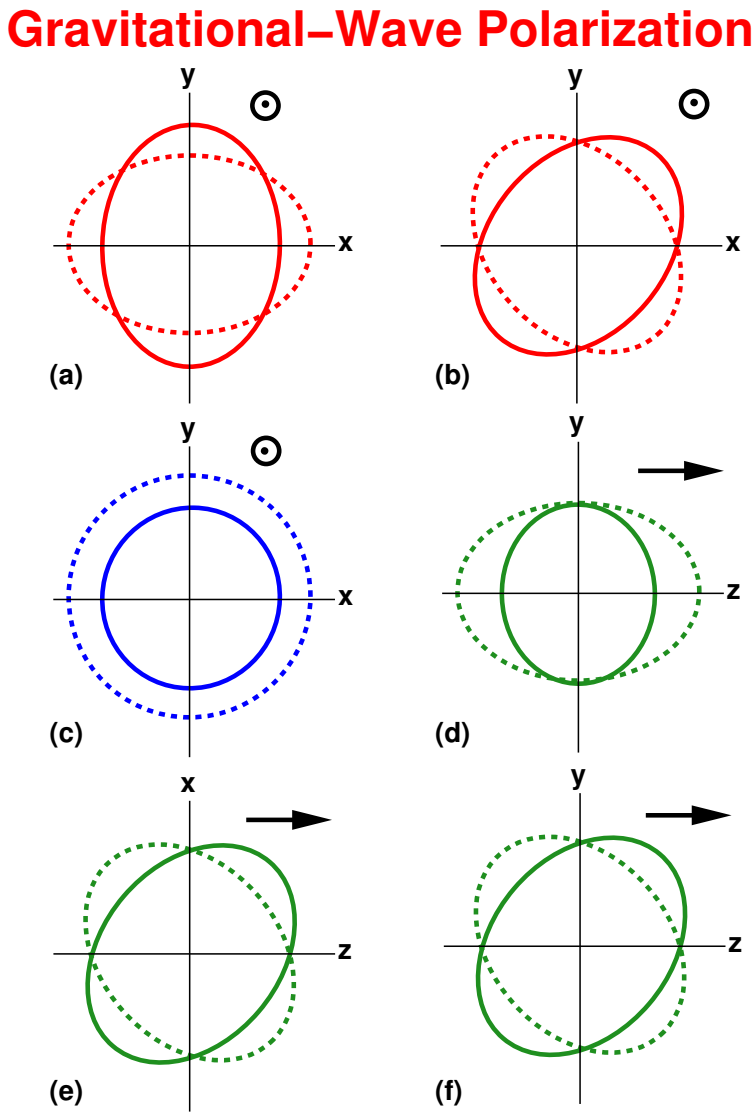

FIGURE 1.8: *Gravitational-wave polarizations.* Effect of the passage of a gravitational wave on a circle of test masses. Credit: [1]

will lead to axisymmetric Kerr(-Newman) spacetimes regardless of the details and field content of the process. The coalescence of two black holes lead to a third perturbed black hole that eventually relaxes to a stable axisymmetric state after a ringdown phase. During this transient, the higher multipole moments of the remnant are dissipated away through the emission of gravitational waves with specific frequencies. The *quasi-normal modes* [271–273] of the remnant object are characteristic modes corresponding to dampened sinusoidal oscillations with complex frequencies, ω_{lmn}, labeled by two angular quantum numbers l, m, and one overtone number $n = 0, 1, 2, ...$ As a consequence of no-hair theorems, the quasi-normal mode frequencies of Kerr black holes are parameterized entirely by the black-hole mass and spin. For astrophysical black-holes, the electric charge is expected to be suppressed to irrelevant values because of Schwinger pair-production, accretion of matter and interaction with the magnetic fields of accretion disks [274–278]).

This is the so-called *Kerr paradigm* that in the era of gravitational-wave astronomy can be tested via *black-hole spectroscopy* [279–285], which consists in the determination

of the remnant properties from the analysis of the ringdown part of gravitational-wave signals. The spectrum of quasi-normal mode frequencies is completely determined by the mass and spin of the final black-hole but the relative amplitude of the excited quasi-normal modes depends on the properties of the progenitor system, e.g. individual spins and mass ratio [286–290]. In particular, the dominant mode in ringdown signals is the fundamental mode corresponding to $l = m = 2$ [291], followed by the $l = m = 4$ mode in non-spinning, equal-mass binaries [286, 287] or by a very loud $l = m = 3$ mode for unequal-mass black-hole binaries or neutron-star black-hole mergers [288–290]. For black-hole spectroscopy to achieve sufficient precision to test the no-hair theorem it is necessary the detection of at least two quasi-normal modes with accurate damping times and frequencies measurements: in practice, these requirements translate in lower bounds on the signal-to-noise ratio of the ringdown signal for such tests [280, 292].

From analyzing the ringdown signal of the first (and loudest) gravitational-wave event detected to date, GW150914 [155], and by including in the analysis not only the fundamental mode $l = m = 2$ but also its first overtone the authors in [282] managed to provide the first constraints on the validity of no-hair theorems. Very recently a new spectroscopic study analyzed the ringdown signal of the event GW190521 [284], which is compatible with the merger of an asymmetric system of two intermediate-mass black holes [293]. The detection and analysis of the fundamental mode and the subdominant $l = m = 3$ mode allowed to test the Kerr hypothesis with a higher precision than the one achieved with the overtone analysis in [282], finding results that are compatible with a general-relativistic Kerr black hole up to a $\lesssim 10\%$ uncertainty and allowing to disfavor alternative explanations of GW190521 in terms of merger of more exotic objects [294]. Recently a parametrized framework for testing the quasinormal ringdown of black holes has been developped [295, 296] and the prospected constraints from future observations have been analyzed in [297].

Parametrized vs model-targeted tests

There are some limitations to the type of tests reviewd so far. Consistency tests can only give a quantitative estimate of how well general-relativistic predictions fit the observational data, but cannot exclude the possibility that a competitive theory could yield better fits. The parametrized tests listed above are in essence null tests of gravity that assume general relativity as a null hypothesis and are capable of placing bounds on the phenomenological parameters that control deviations thereof [227, 228]. In practice, however, it is sometimes hard to translate such bounds into *tight* constraints on the fundamental parameters of a particular theory, as the former typically correspond to combinations of the latter. Parametrized approaches might just not be the best option to capture strong-field effects that can produce large deviations from general relativity.

An alternative and complementary approach consists in direct tests of theories beyond general relativity. These consist in model-dependent searches for strong-field signatures of new physics. In the following chapter I will review a relevant subset of scalar-tensor theories of gravity on which my research has recently focused. Then in section 2.2, I will give a brief introduction to three strong-gravity effects that can produce (or hide) large deviations from general relativity and that can serve as interesting testing grounds for modified gravity.

Chapter 2

Scalar fields beyond General Relativity

2.1 Scalar-tensor theories

2.1.1 Minimal coupling

One of the simplest extensions of General Relativity that can be considered consists in extending the number of dynamical degrees of freedom to include an additional scalar field. When the scalar field is minimally coupled to the metric it will essentially count as some sort of exotic matter appearing in the right hand-side of the Einstein equations. The action of a minimally coupled scalar field reads

$$S_g = \int d^4x \sqrt{-g} \frac{M_{\rm pl}^2}{2} \left[R - 2g^{\mu\nu}\partial_\mu\phi\partial_\nu\phi - V(\phi) \right] . \tag{2.1}$$

All the key properties of the scalar field are enclosed in the potential, which can vary wildly depending on the desired applications. Historically, such simple models were first applied in Cosmology as *quintessence* models of dynamical dark energy or inflation [298, 299]; and models of scalar (or "fuzzy") dark matter [300–304].

2.1.2 Bergman-Wagoner

The classic example of non-minimal coupling is given by Fierz-Jordan-Brans-Dicke theory [305–307], which was first introduced as a theory in where the gravitational constant, G, is promoted to a dynamical scalar field φ. The corresponding action can be formulated as:

$$S_{FJBD} = \int d^4x \sqrt{-\tilde{g}} \frac{M_{\rm pl}^2}{2} \left[\varphi\tilde{R} - \frac{\omega_{BD}}{\varphi}\tilde{g}^{\mu\nu}\partial_\mu\varphi\partial_\nu\varphi \right] + S_m[\tilde{g}_{\mu\nu};\Psi] , \tag{2.2}$$

where "standard" matter, represented collectively under the symbol Ψ, is minimally coupled to the $\tilde{g}_{\mu\nu}$ metric; and all quantities with a tilde are constructed from the metric $\tilde{g}$. The natural generalization of this model is given by the Bergman-Wagoner formulation of scalar-tensor theories [308, 309], described by the action

$$S_{BW} = \int d^4x \sqrt{-\tilde{g}} \frac{M_{\rm pl}^2}{2} \left[\varphi\tilde{R} - \frac{\omega(\varphi)}{\varphi}\tilde{g}^{\mu\nu}\partial_\mu\varphi\partial_\nu\varphi - U(\varphi) \right] + S_m[\tilde{g}_{\mu\nu};\Psi] , \tag{2.3}$$

which promotes the constant ω_{BD} to a function of φ and endows the scalar field with a self-interaction potential $U(\varphi)$. Through the conformal transformation of the

metric $g_{\mu\nu} = \varphi\tilde{g}_{\mu\nu}$ and a scalar field redefinition $\varphi(\phi) \equiv A(\phi)^{-2}$ and $3 + 2\omega(\varphi) \equiv \alpha(\phi)^{-2}$, where $\alpha(\phi) \equiv d\ln A(\phi)/d\phi$, the action (2.3) can be recast into the form

$$S_{ST} = \int d^4x\sqrt{-g}\frac{M_{\rm pl}^2}{2}\left[R - 2g^{\mu\nu}\partial_\mu\phi\partial_\nu\phi - V(\phi)\right] + S_m[A(\phi)^2 g_{\mu\nu}; \Psi]\,, \tag{2.4}$$

where the potential has been redefined as $V(\phi) \equiv A(\phi)^4 U(\varphi(\phi))$. The two actions (2.3) and (2.4) describe the same theory in two different but equivalent frames called, respectively, *Jordan* and *Einstein* frame. In the first, the scalar field is manifestly an additional gravitational degree of freedom because of its non-minimal coupling to the metric. This is sometimes referred to as the "physical" frame since test particles and matter fields in general propagate on geodesics of the Jordan-frame metric, $\tilde{g}_{\mu\nu}$. Nonetheless, it is often more convenient to solve problems (e.g. finding solutions in vacuum) in the Einstein frame, in which the metric and scalar field are disentangled and the field equations are treatable with the same approach used in general relativity.

2.1.3 Horndeski and beyond

Several generalizations of the models described above have been considered in the literature so far. The class of Horndeski theories is the most general formulation of scalar-tensor theories that yields second order field equations [310] described in terms of the following action:

$$S_g + S_m = \int d^4x\sqrt{-g}\sum_{i=2}^{5}\mathcal{L}_i[g_{\mu\nu}, \phi] + S_m[g_{\mu\nu}; \Psi], \tag{2.5}$$

where the gravitational sector, S_g, is given as a linear combination of the Lagrangians:

$$\mathcal{L}_2 \equiv G_2(\phi, X), \tag{2.6a}$$
$$\mathcal{L}_3 \equiv G_3(\phi, X)\Box\phi, \tag{2.6b}$$
$$\mathcal{L}_4 \equiv G_4(\phi, X)R - 2G_{4X}(\phi, X)\left[(\Box\phi)^2 - \phi^{\mu\nu}\phi_{\mu\nu}\right] + \tag{2.6c}$$
$$+F_4(\phi, X)\epsilon^{\mu\nu\rho}{}_\sigma\epsilon^{\mu'\nu'\rho'\sigma}\phi_\mu\phi_{\mu'}\phi_{\nu\nu'}\phi_{\rho\rho'}, \tag{2.6d}$$
$$\mathcal{L}_5 \equiv G_5(\phi, X)G_{\mu\nu}\phi^{\mu\nu} + \frac{1}{3}G_{5X}(\phi, X)\left[(\Box\phi)^3 - 3\Box\phi\phi_{\mu\nu}\phi^{\mu\nu} + 2\phi_{\mu\nu}\phi^{\mu\sigma}\phi^{\nu}{}_{\sigma}\right] \tag{2.6e}$$
$$+ F_5(\phi, X)\epsilon^{\mu\nu\rho\sigma}\epsilon^{\mu'\nu'\rho'\sigma'}\phi_\mu\phi_{\mu'}\phi_{\nu\nu'}\phi_{\rho\rho'}\phi_{\sigma\sigma'}\,. \tag{2.6f}$$

The notation used in (**??**) is standard, denoting derivatives of the scalar field with multiple greek indices, i.e. $\phi_\mu \equiv \partial_\mu\phi$ and $\phi_{\mu\nu} \equiv \nabla_\mu\partial_\nu\phi$; the laplacian of the scalar field is denoted with $\Box\phi \equiv g^{\mu\nu}\nabla_\mu\partial_\nu\phi$ and the symbol $X \equiv -1/2 g^{\mu\nu}\phi_\mu\phi_\nu$ was introduced as a short notation for the canonical kinetic term of the scalar field. Terms with coefficients G_i with $i = 2, ...5$ strictly belong to the Horndeski class. Instead, terms proportional to F_4 and F_5 belong to the so-called "beyond Horndeski" or Gleyzes-Langlois-Piazza-Vernizzi theories which, although yielding third-order equations of motion, do not propagate undesired extra degrees of freedom (except the scalar one) [311, 312]. This fact is possible thanks to the imposition of special constraints, or *degeneracy conditions*, that prohibit the propagation of ghosts: such degeneracy conditions can be employed to identify the most general degenerate higher-order

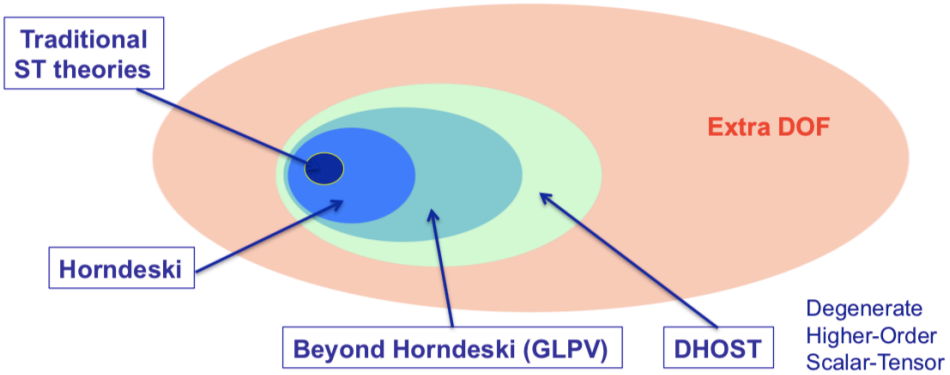

FIGURE 2.1: *Space of scalar-tensor theories.* Credit: [315]

scalar-tensor theory (DHOST) featuring higher-order derivative operators but propagating only one extra scalar mode [313–316].

2.1.4 Quadratic gravity

General Relativity considered as a quantum theory of gravity is known to be non-renormalizable, as it receives additional contributions proportional to higher curvature invariants at each loop order [317, 318]. It was soon realized, however, that extending the Einstein-Hilbert action to include from the start one-loop quantum corrections proportional to quadratic curvature-invariants was enough to obtain a renormalizable theory [319]. Inclusion of higher-derivative operators in the action, however, inevitably introduces so-called *Ostrogradski ghosts*, unwanted modes with unbounded negative energy that destabilize the theory [320], thus renormalizability is achieved at the cost of introducing problems with unitarity. One simple way out of this impasse is to adopt an effective field theory perspective and to treat higher-curvature quantum corrections as small perturbations that remain under control up to energies comparable with the Planck scale [321, 322]. Many attempts to solve the ghost problem of quadratic gravity outside of the EFT approach (e.g. [323–327]) but no flawless solution has been found yet. Two quadratic curvature invariants are of particular interest namely the Gauss-Bonnet term, $\mathcal{G} \equiv R^2 - 4R_{\mu\nu}R^{\mu\nu} + R_{\mu\nu\rho\sigma}R^{\mu\nu\rho\sigma}$, and the Chern-Simons term, $({}^*RR) \equiv 1/2 R_{\mu\nu\rho\sigma}\epsilon^{\nu\mu\lambda\tau}R^{\rho\sigma}_{\lambda\tau}$, which arise in the low-energy limit of quantum gravity theories [328–331]. In four dimensions these curvature scalars do not contribute to the field equations when included alone in the action, because their integrals over the four-dimensional volume element are actually topological invariants. For this reason, they are typically considered coupled to

a dynamical field, e.g. a scalar field in the simplest case. The most general action for a scalar field coupled to quadratic curvature operators can be written as [332, 333]

$$S_g = \int d^4x\sqrt{-g}\frac{M_{\rm pl}^2}{2}\left[R - 2g^{\mu\nu}\partial_\mu\phi\partial_\nu\phi - V(\phi) + \right.$$
$$\left. +\alpha_1(\phi)R^2 + \alpha_2(\phi)R_{\mu\nu}R^{\mu\nu} + \alpha_3(\phi)R_{\mu\nu\rho\sigma}R^{\mu\nu\rho\sigma} + \alpha_4(\phi)({}^*RR)\right] . \qquad (2.7)$$

Action (2.7) describes a generalization of the ghost-plagued quadratic gravity, which corresponds to the functions $\alpha_i(\phi) =$ constant for $i = 1, 2, 3, 4$, and is generally also prone to develop Ostrogradski instabilities. The only known sub-class of quadratic gravity models that avoids propagation of ghosts correspond to Einstein-Scalar-Gauss-Bonnet gravity, defined by the choice $\alpha_1 = -4\alpha_2 = \alpha_3 = f(\phi)$, $\alpha_4 = 0$ and $V(\phi) = 0 = A(\phi)$ in a minimal realization [334]. In fact, it can be demonstrated that ESGB theories are a particular subclass of Horndeski gravity [335], which is by definition the most general ghost-free scalar-tensor theory with second-order field equations [310]. Finally, a bridge between standard scalar-tensor theories and quadratic gravity is represented by $f(R)$ theories, which can both accept a description in terms of a specific sub-class of FJBD scalar-tensor theories and be viewed as an example of higher-curvature gravity [336, 337].

2.1.5 Other theories

Other natural generalizations consist in the addition of multiple scalar [338], vector and/or tensor fields; or even combinations of the three at once. However, all the models that introduce new dynamical fields that couple to matter typically violate the strong equivalence principle and can be constrained by experimental searches of such violations. In addition, many of the vector-tensor [339, 340] and scalar-vector-tensor [341, 342] theories considered in the literature also introduce a fundamental violation of the Lorentz symmetry, although this is a small price that can buy such theories a better behaved high-energy limit [250]. Recently a new surge of interest in diffeomorphism-breaking theories has been stimulated by the *minimal modified gravity* program, that aims at building theories propagating only two tensor degrees of freedom at the cost of preserving only space-diffeomorphisms [343–345]. A non-extensive list of possible extensions of general relativity that have been extensively studied in the past literature includes massive gravity [346–348], bimetric gravity [349–352] and theories with torsion and non-metricity [353, 354]. The work collected in this thesis, however, focuses mainly on the scalar-tensor models described in the subsections above.

2.2 Scalar effects beyond General Relativity

2.2.1 Superradiance

The mechanism known as *superradiance* is a classical process of wave-amplification that appears in many contexts [355]. One of the incarnations of superradiance, in the context of black hole physics, is *superradiant scattering* [355–361], which constitutes a sort of "wave" generalization of the Penrose process [356]: bosonic waves (and also nonlinear Dirac waves [362]) as they scatter off the ergoregion of a black hole can extract energy and angular momentum (and possibly charge [363]) from

it. In gravitational physics, the existence of an ergoregion in a certain spacetime is a sufficient condition for superradiance [362]. The ergoregion is a portion of spacetime delimited by an infinitely-redshifted surface, which allows for negative-energy states in its interior: in general relativity it can be shown that if a stationary and axisymmetric spacetime possesses an event horizon (e.g. is a rotating black hole), then it must also feature an ergoregion [364]. Note however that neither the presence of an horizon nor of an ergoregion are necessary conditions for superradiance, which can manifest also with horizonless objects (though in association with an instability [362]) and in the context of stars [357, 365–368]. Arguably more interesting is the case in which the bosonic field is interacts repeatedly with the black hole ergoregion, for instance by placing a reflecting mirror around the black hole. In this scenario, the boson will get continuous superradiant amplification over time that will trigger an exponentially growing instability dramatically called a *black hole bomb* [369]. A more natural realization of *superradiant instabilities* occurs, for instance, when black holes of sufficiently high spins interact with massive bosons of sufficiently small mass [361, 369, 370]. In fact, superradiant instabilities are known to be relevant (i.e. the typical timescale does not exceed the age of our universe) only when the boson Compton wavelength, $\lambda_c = \hbar/mc$, is comparable to the gravitational radius of the black hole, $r_g = GM/c^2$, such that $r_g/\lambda_c \lesssim 1$. For a solar-mass black hole, the order-of-magnitude mass for a superradiant boson field will correspond to $m \sim 10^{-10}$ eV. The Standard Model does not contain such ultralight massive bosons, which are very common in extended particle and gravitational physics models: axion-like particles [371–377], dark photons [378–380] massive gravitons [346–348] and massive scalar-tensor theories [381, 382]. If the conditions for the instability to set in are met, a stationary superradiant cloud forms powered by the energy extracted from the black hole, which on its turn spins down until the instability is quenched (which happens typically for dimensionless spin parameters $\chi = cJ/(GM^2) \sim 0.1$–$0.4$, c.f. e.g. Fig. 1 of Ref. [383]). In fact, the typical size of these scalar clouds is large and the energy density stored inside them low enough as to make the backreaction on the geometry negligible [384]. The cloud, generally non-spherical, will emit gravitational waves and dissipate over time [375, 383–387]. Fully nonlinear numerical simulations that follow through the evolution of the superradiant instability, from onset to saturation and final dissipation, are very challenging because of the long characteristic timescales (around 10^5–10^6), but recent numerical effort has confirmed the picture described above [388–393]. As a matter of fact, when the instability develops in an axisymmetric Kerr spacetime no-hair theorems guarantee that the endstate will be again a Kerr black hole with reduced spin and mass [268, 270, 394–396]. There are some notable exceptions to this picture, one of them consisting in black holes with "sinchronized hair" [397] in which a time-dependent complex scalar field can evade no-hair theorems and yield non-Kerr vacuum configurations [397–401]. And finally, ultralight bosons with either an axion-like coupling to the electromagnetic sector or a nonlinear self-interaction can predict catastrophic endstates, in which the energy stored in the superradiant cloud is released in violent bursts of electromagnetic [402–404] or scalar radiation (i.e. *bosenovae*) [375, 405, 406]. In Chapter 3 I will elaborate thoroughly on a study of photon superradiant instabilities triggered by plasma effects in the accretion disks of black holes.

2.2.2 Scalarization

The phenomenon scalarization was first discovered in the context of neutron stars in scalar-tensor theories *à la* Damour-Esposito-Farese [338, 407], which can predict observable scalar effects in the strong-field regime while still abiding the weak-field bounds [1, 2, 29, 408, 409]. In particular, scalar fields that are suitably coupled to the trace of its stress-energy tensor of matter become unstable inside sufficiently compact neutron stars [407]. At the perturbative level, the onset of the instability can be observed as the appearance of a negative mass (squared) term that makes scalar perturbations grow unbounded. At the full nonlinear level, the compact star is undergoing a phase-transition (analogous, for instance, to spontaneous magnetization in ferromagnetism [58]) to an energetically-favoured configuration with non-trivial scalar charge [58, 407, 410]. Related "dynamical" scalarization effects [411–414] are present in the same theories for neutron star binaries, whenever their separation is sufficiently small (or the binary's "compactness" sufficiently large). In fact, binary pulsar experiments are the main source of constraints on theories that predict spontaneous scalarization [52, 58, 59, 76, 409, 410]. However, in the class of theories considered in [407, 411–414], scalarization is not present without matter, and vacuum solutions are standard general-relativistic black holes. Note that black holes can scalarize if they have matter in their vicinity [381, 415], but the densities necessary to obtain a measurable effect are probably astrophysically unrealistic.

In general, scalar-tensor theories do not typically leave any characteristic imprint in the physics of vacuum solutions: no-hair theorems (see [416–418] for reviews) exist for stationary BHs in scalar-tensor theories [394, 395], and static, spherically symmetric and slowly rotating BHs in shift-symmetric Horndeski theories [419, 420]. In fact, no-hair theorems also exist for stars in shift-symmetric scalar-tensor theories [421–424]. Nonetheless, it turns out that there is a single coupling term in the Horndeski class that gives rise to hair: a linear coupling between the scalar and the Gauss-Bonnet invariant [420, 425], given by

$$\mathcal{G} = R^{\mu\nu\rho\sigma}R_{\mu\nu\rho\sigma} - 4\,R^{\mu\nu}R_{\mu\nu} + R^2. \tag{2.8}$$

Considering that the Horndeski class contains all actions for a massless scalar non-minimally coupled to gravity that yield second order equations upon variation, absence of hair actually seems to be the norm rather than the exception for scalar fields. Indeed, known hairy black hole solutions circumvent theorems by evading one or more of their assumptions, see *e.g.* [381, 397, 415, 418, 420, 426, 427]. An interesting alternative isgiven by theories in which both vacuum solutions with and without hair can coexist. These have been considered only recently, as the first models of *black hole spontaneous scalarization* appeared in the literature [428, 429]. For concreteness, consider the action

$$S = \frac{1}{2}\int d^4x\sqrt{-g}\left(R - \frac{1}{2}\nabla_\mu\phi\nabla^\mu\phi + f(\phi)\mathcal{G}\right), \tag{2.9}$$

where f is some function of ϕ, and where we have also set $8\pi G = c = 1$. Varying the action with respect to ϕ yields

$$\Box\phi = -f'(\phi)\mathcal{G}, \tag{2.10}$$

where $f'(\phi) \equiv df/d\phi$. Assume that $f'(\phi_0) = 0$, for some constant ϕ_0. Then solutions with $\phi = \phi_0$ are admissible and they are also solutions of general relativity. A no-hair theorem [428] ensures that they are unique if they are stationary, provided that $f''(\phi)\mathcal{G} < 0$. The fact that black holes in general relativity are stationary solutions

is not sufficient to conclude that there are no observable deviations, as the perturbations over these solutions do not generally obey the Einstein field equations [430]. These perturbations may even grow unstable, thus rendering the general-relativistic solutions irrelevant. Indeed, one can think of $-f''\mathcal{G}$ as the (square of the) mass of the scalar perturbation on a fixed background. Hence, the condition above ensures that this effective (squared) mass is positive. If the condition is violated and the effective (squared) mass becomes sufficiently negative, the general relativity solutions suffer a tachyonic instability and the scalar develops a nontrivial profile, in strict analogy to the neutron star scalarization phenomenon described above.

Black hole scalarization is fairly well understood [149, 420, 425, 427–429, 431, 432]. It starts as a linear tachyonic instability and, as such, its onset is controlled only by terms that contribute to linear perturbations around general relativity solutions. In this sense, action (2.9) with $f(\phi) = \eta\phi^2/2$ is sufficient to study the onset of scalarization [428, 433]. As the instability develops and the scalar grows, nonlinear terms become increasingly important and eventually quench the instability. Hence, the endpoint and properties of the scalarized solutions are actually controlled by the nonlinear interactions of the scalar [434, 435]. A characteristic example is that in models with different nonlinear interactions, scalarized solutions have different stability properties [434, 436].

Theories that include couplings to the Gauss-Bonnet invariant have been introduced in section 2.1.4, and the onset of scalarization in high-spin black hole backgrounds will be discussed extensively in Chapter 4.

2.2.3 Screening mechanisms

Scalar extensions to the gravitational standard model have been traditionally considered for their cosmological applications, although agreement with both local and cosmological scales is not always easy to ensure. In fact, these models naturally introduce deviations from general relativity in the weak-field regime and are severely affected by Solar-System bounds [1, 2, 29, 408, 409]. S Particularly interesting is the existence of classes of scalar-tensor theories that are endowed with *screening mechanisms* devised to hide non-general-relativistic effects on astrophysical (local) scales, while leaving room for modifications on cosmological ones. To introduce the different varieties of screening mechanisms, we shall consider a general scalar-tensor theory described, schematically, by the following action for the scalar sector [437]

$$\mathcal{S} = \int d^4x\sqrt{-g}\left[-\frac{1}{2}Z^{\mu\nu}(\phi,\partial\phi,...)\partial_\mu\phi\partial_\nu\phi - V(\phi) + \alpha(\phi)T_m\right] \tag{2.11}$$

where ϕ is the dimensionful scalar field, V is a generic potential, $Z^{\mu\nu}$ and $\alpha(\phi)T_m$ are a schematical representation of,respectively, the derivative self-interactions of the field and its universal coupling to the trace of the stress-energy tensor of matter, T. Specializing to a single source object of mass M and radius R in the static Newtonian limit (where T_m typically reduces to $\simeq -\rho$) the scalar perturbation equation reduces to a generalized Poisson equations [438]

$$Z^{ij}(\bar{\phi})\partial_i\phi\partial_j\phi + m^2(\bar{\phi})\phi = 8\pi G\alpha(\bar{\phi})\rho\,, \tag{2.12}$$

where $\bar{\phi}$ is a background solution for the scalar field, m^2 is an effective mass term derived from V, and ρ is the rest-mass density of the object. The schematic solution

to this equation can be written as

$$\phi \sim \alpha(\bar{\phi}) \frac{GM}{|Z(\bar{\phi})|r} e^{-m(\bar{\phi})r}, \tag{2.13}$$

and based on the detailed mechanism that suppresses (2.13) and its gradient, which is proportional to the fifth-force mediated by the scalar field [438], one can distinguish the three cathegories of screening:

- $Z^{ij} \gg 1$, *kinetic* screening based on the kinetic factor becoming large in the nonlinear regime. Examples are *k-mouflage* [439–442] and *Vainshtein* screening [443–446];
- $\alpha \ll 1$, screening based on an *environmentally-dependent coupling* of the scalar field to matter becoming weak in dense matter distributions. Such mechanisms are realized in symmetron [447–449] and dilaton models [450, 451]);
- $mR \gg 1$, *environmentally-dependent mass* screening mechanisms, in which large densities correspond to the scalar dynamics being suppressed by the large mass. Screening in chameleon models of gravity follows this principle [452, 453].

Proof of the effectiveness of screening mechanisms in suppressing deviations from general relativity is typically provided in the weak-field regime, but there are counterexamples that indicate they might break down when considering higher-order operators [454–460] or strong-gravity regimes such as those of isolated neutron stars [461] or binary systems [462].

Chameleon screening is realized by endowing the scalar degree of freedom with an effective mass that depends on the ambient matter density: in high-density environments (e.g. compact objects, our solar system or even galaxies and clusters) small perturbations are suppressed by the large inertia of the field, while on larger cosmological scales lower densities allow for *quintessence*-like effects, arising from to the non-trivial self-interaction potential [453]. Moreover, the scalar charge of compact objects receives contributions only from a small volume located close to the surface: this *thin-shell effect* effectively suppresses the scalar force [452]. The chameleon screening mechanism in highly-relativistic compact stars will be discussed in details in Chapter 5.

Chapter 3

Black holes and plasma-driven superradiance

3.1 Black holes, superradiance and superradiant photons

The detection of gravitational waves [463] by Advanced LIGO [159] and Advanced VIRGO [464] was a major milestone in the history of astronomy. Not only have these observations confirmed directly the existence of gravitational waves (already indirectly proven by binary pulsars [49, 50]), but they also provide a way to test astrophysical models for the formation of binaries of compact objects [465] and to verify the validity of general relativity in the hitherto unexplored highly relativistic strong field regime [226, 227]. Crucial in both respects are the spins of the binary components, which could in principle be large, especially for black holes.

Black hole spins provide useful diagnostics to discriminate between astrophysical formation scenarios for binaries [466, 467], e.g. the field binary formation channel [468] vs the dynamical one [469]. Moreover, thanks to superradiance (see section 2.2.1), moderate to large black hole spins would allow for testing the presence of ultralight bosons [374, 375, 383, 384, 387]. Unfortunately, LIGO and VIRGO have so far gathered (mild) evidence for non-zero spins in only two of the ten black hole binaries detected during the first and second run of observations [470, 471]. This is quite surprising, since black holes in X-ray binaries have spins (measured by fitting the continuum spectrum [85] or iron Kα lines [472]) that seem distributed uniformly between zero and the maximal Kerr limit [473], and because field binary formation models tend to predict non-vanishing values for the effective spin parameter $\chi_{\rm eff}$ measured by LIGO–VIRGO [474]. Since $\chi_{\rm eff}$ is only sensitive to the projections of the spins on the orbital angular momentum direction, it is of course possible that LIGO binaries may simply have moderate/large *and* randomly oriented spins. However, in the field binary scenario, random spin orientations are generally produced only by large supernova kicks [475, 476], which are disfavored by the merger rate measured by LIGO–VIRGO [477]. The dynamical formation channel, where random orientations are natural [478], typically predicts fewer coalescences than observed.

An interesting proposal to explain the low values of the LIGO–VIRGO black hole spins was put forward by Conlon and Herdeiro [479] (see also Ref. [480]), who noted that spinning black holes surrounded by a tenuous plasma may be susceptible to superradiant instabilities. Indeed, the plasma induces a change in the dispersion relation of photons propagating through it [481]: $\omega^2 = k^2 + \omega_p^2$, where n_e is the electron number density and $\alpha = e^2/(4\pi)$ is the fine structure constant in natural units ($G = \hbar = c = 1$, which we will adopt throughout this chapter). As a result, photons acquire an effective mass equal to the plasma frequency, $\mu = \omega_{\rm p}$, defined

by

$$\omega_{\rm p} = \sqrt{\frac{4\pi\alpha n_e}{m_e}} = 1.2 \cdot 10^{-12} \sqrt{\frac{n_e}{10^{-3}{\rm cm}^{-3}}} {\rm eV}. \tag{3.1}$$

For $n_e \sim 10^{-3}$–10^{-2} cm^{-3}, corresponding to typical conditions in the interstellar medium (ISM) [482–484], the photon develops an effective mass $\mu \sim 10^{-12}$–10^{-10} eV, whose wavelength is comparable to the gravitational radius of LIGO–VIRGO black holes. Indeed, for these densities the "mass coupling" – i.e. the ratio between the black hole's gravitational radius M and the Compton wavelength $1/\mu$ – is

$$\mu M = \left(\frac{M}{M_\odot}\right)\left(\frac{\mu}{10^{-10}{\rm eV}}\right) \sim O(0.01)\text{–}O(1)\left(\frac{M}{M_\odot}\right). \tag{3.2}$$

Since the fastest growing superradiant modes are found numerically for nearly extremal black holes ($\chi = 0.99$) and $\mu M \sim 0.42$ [485], Ref. [479] argues that LIGO–VIRGO black holes immersed in a plasma with $n_e \sim 10^{-3}$–10^{-2} cm^{-3} are potentially unstable to superradiance, i.e. rotational energy can be extracted from them and transferred to a "photon cloud" surrounding the black hole, and as a result the black hole spin decreases.

As already pointed out in Ref. [479], however, one obvious problem with this scenario is its applicability to accreting black holes in the real Universe. The standard picture of accretion onto black holes assumes that the accreting gas will generally have sizeable angular momentum per unit mass and will form an (energetically favored) disk configuration as it spirals in [105]. Because of effective viscous processes (probably due to magneto-hydrodynamic turbulence [486, 487]), angular momentum is trasferred outwards and as a result a net mass inflow arises toward the black hole. The gravitational energy of the gas will be dissipated into heat, which will be either radiated away or advected directly into the black hole.

Accretion disk models can be classified according the accretion rate $\dot{M}$ (see e.g. Ref. [488] for a review). A natural scale for accretion is given by the Eddigton accretion rate $\dot{M}_{\rm Edd} = L_{\rm Edd}/\eta$, where $L_{\rm Edd}$ is the Eddington luminosity and η the disk's radiative efficiency. For $\dot{M} \lesssim \dot{M}_{\rm Edd}$, the radiative efficiency is sufficient to remove the heat, and the result is a cold geometrically thin disk [107, 489, 490]. The case $\dot{M} \gtrsim \dot{M}_{\rm Edd}$ corresponds to a thick disk, where high accretion rates produce high densities that make the gas optically thick and the radiative transport inefficient. This results in a hot and "inflated" disk [491, 492]. If instead $\dot{M} \ll \dot{M}_{\rm Edd}$, the radiative transport is not sufficiently effective to cool down the (low density) gas, which therefore expands into quasi-spherical configurations, often referred to as Advection Dominated Accretion Flows (ADAFs) [113–115]. Note that ADAFs, even though dynamically very different, are geometrically somewhat similar to spherically symmetric Bondi accretion flows [493]. The latter correspond to purely radial accretion of matter, and are a good approximation for compact objects accreting gas with negligible angular momentum from the surrounding interstellar medium.

A common element to all these accretion models is the increase of the matter density as the black hole is approached, even though the density may be as low as $n_e \sim 10^{-3}$ cm^{-3} far away from it. Notice, for example, that the Bondi accretion model predicts that the plasma number density should be enhanced by a factor $v_s(\infty)^{-3}$, where $v_s(\infty)$ is the speed of sound at infinity [493, 494]. Therefore, number densities close to black hole horizons are expected to be potentially several orders of magnitude higher than in the surrounding insterstellar medium. Similarly, ADAF models in the literature also feature very high electron number densities

$n_e \sim 10^{19}\,(M_\odot/M)\ \mathrm{cm}^{-3}$ [115] near the black hole horizon.

Ref. [479] thus concluded that only relatively "bare" black holes could be prone to plasma-driven instabilities, e.g. black holes surrounded by a tenuous plasma because they may have been kicked out of their dense accretion disk after a merger, or because they formed from a violent supernova explosion that blew away most of the stellar material. Nevertheless, it is not at all clear whether superradiance will occur even under these favorable conditions, because the increase of the plasma density near the black hole (and particularly inside the ergoregion) was not studied by Refs. [479, 480], and may suppress the instability. In fact, it seems likely that the plasma density near the horizon may increase not only because of accretion, but also because of pair production [274] due to the large electromagnetic field produced by the instability.

Note that on physical grounds one would expect the plasma density in the ergoregion, and not at spatial infinity, to play a role, since the existence of an ergoregion is crucial for superradiance and the Penrose process (as it allows for the presence of the negative energy modes responsible for the extraction of rotational energy from the black hole). Indeed, a well-known semi-analytic result by Eardley and Zouros [495], valid for scalar perturbations with constant mass $\mu \gg 1/M$ and based on a WKB approximation scheme near the peak of the effective potential, seems to suggest that high densities close to the black hole would produce instabilities with very long and practically unobservable timescales, i.e. $\tau_I \simeq 10^7 e^{1.84 M\mu} M$ for the fastest growing mode [495].

However, another important analytic result by Detweiler [360], valid in the opposite limit $M\mu \ll 1$ and based on matching two asymptotic wave solutions (one valid near the black hole and one near spatial infinity), seems to suggest instead that only the density at large distances from the black hole should matter. Indeed, in the matching procedure of Ref. [360] the scalar's mass (corresponding to the plasma frequency and thus to the density) only appears in the solution valid near spatial infinity, and not in the near-black hole solution. The resulting instability timescale is [360] $\tau_I \sim 48(\mu M)^{-9} M/\chi$.

In the light of the conflicting intuition from these analytic results, we will undertake in this work a detailed numerical analysis of superradiance for fast spinning Kerr black holes surrounded by tenous but accreting plasmas. To this end, we adopt a simplified toy model where we represent the electromagnetic field propagating in a plasma by a scalar field with a position-dependent mass. The dependence on position is required to identify the mass with the plasma frequency, whose local value changes with the density. We evolve the Klein-Gordon equation for this toy scalar field in the time domain, by using a spectral technique that was introduced in Ref. [496], and which allows for efficiently integrating over long timescales. We consider several choices for the density profile of the plasma, in order to explore the impact of the different astrophysical accretion models outlined above.

This chapter is organized as follows. In Sec. 3.2, we outline the physical setup and present several models for the plasma density profile that we employ. In Sec. 3.3 we present our numerical method, while in Sec. 3.4 we describe our results. Our main conclusions are discussed in Sec. 3.5. Throughout this work, we will adopt a signature $(-,+,+,+)$ for the metric. Partial time derivatives will be denoted by an overdot, and radial derivatives by a prime.

3.2 Physical Model

3.2.1 Background and perturbation equations

In general relativity, the spacetime of a rotating black hole is described by the Kerr vacuum solution of the Einstein field equations. In Boyer-Lindquist coordinates $\{t, r, \theta, \phi\}$, the corresponding line element is

$$\begin{aligned} ds^2 =& g_{\mu\nu} dx^\mu dx^\nu \\ =& -\left(1 - \frac{2Mr}{\rho^2}\right) dt^2 - \frac{4aMr\sin^2\theta}{\rho^2} dt d\phi + \frac{\rho^2}{\Delta} dr^2 + \rho^2 d\theta^2 + \\ &+ \left(r^2 + a^2 + \frac{2a^2 Mr\sin^2\theta}{\rho^2}\right) \sin^2\theta d\phi^2 \,, \end{aligned} \tag{3.3}$$

where M is the mass of the black hole, $a = \chi M$, $\Delta = r^2 - 2Mr + a^2$ and $\rho^2 = r^2 + a^2\cos^2\theta$. On this background, we study the evolution of scalar perturbations with a mass term depending on r and θ (to be specified in detail in the following), as a toy model for photons propagating in a plasma surrounding the black hole.

The evolution of the perturbations is governed by the Klein-Gordon equation on a curved background:

$$\left(\Box - \mu^2(r,\theta)\right) \Psi = 0 \,. \tag{3.4}$$

The explicit form of the d'Alembertian differential operator is given by

$$\Box\Psi = \frac{1}{\sqrt{-g}} \partial_\mu \left(\sqrt{-g} g^{\mu\nu} \partial_\nu \Psi\right) \,, \tag{3.5}$$

where g is the determinant of the metric.

Since the Boyer-Linquist azimuthal coordinate ϕ is known to be singular on the Kerr event horizon, we change it to Kerr-Schild angle, φ, defined by

$$d\varphi = d\phi + \frac{a}{\Delta} dr. \tag{3.6}$$

We also change the radial coordinate r to the tortoise radial coordinate, x, defined by

$$dx = \frac{r^2 + a^2}{\Delta} dr \,. \tag{3.7}$$

Using then Eqs. (3.6) and (3.7) in Eq. (3.4), we obtain the following explicit expression for the Klein-Gordon equation in our coordinates:

$$\begin{aligned} &\Big[\Sigma^2 \partial_{tt} + 4aMr\partial_{t\varphi} - (r^2+a^2)^2 \partial_{xx} - 2a(r^2+a^2)\partial_{x\varphi} + 2a^2\Delta\partial_x + \frac{2a\Delta}{r}\partial_\varphi \\ &+ \Delta\Big(-\partial_{\theta\theta} + \cot\theta\partial_\theta + \frac{1}{\sin^2\theta}\partial_{\varphi\varphi}\Big) + \Delta\Big(\frac{2M}{r} - \frac{2a}{r^2} + (r^2 + a^2\cos^2\theta)\mu^2(r,\theta)\Big)\Big]\Psi = 0 \,, \end{aligned} \tag{3.8}$$

where $\Sigma^2 = (r^2+a^2)^2 - \Delta a^2\cos^2\theta$.

From Eq. (3.8), one can observe that the separability of the perturbation equations in a radial and an angular part depends crucially on the effective mass term. Indeed, only the special choice $\mu^2(r,\theta) = (\mathcal{F}(\theta) + \mathcal{G}(r))/(r^2 + a^2\cos^2\theta)$ renders the equations separable [381]. Except for this special case, the equations are non-separable, and the properties of the perturbations (with particular regards to their spectrum

Model	Mass profile
(I)	$\mu_0^2(r) = \mu_H^2 \left(\frac{r_+}{r}\right)^\lambda$
(II)	$\mu_0^2(r) \sin^2\theta$
(III)	$\mu_0^2(r) + \mu_c^2$
(IV)	$\mu_0^2(r) \sin^2\theta + \mu_c^2$
(V)	$\mu_1^2(r) = \mu_H^2 \Theta(r - r_0) \left(1 - \frac{r_0}{r}\right) \left(\frac{r_0}{r}\right)^\lambda$
(VI)	$\mu_1^2(r) \sin^2\theta$
(VII)	$\mu_1^2(r) + \mu_c^2$
(VIII)	$\mu_1^2(r) \sin^2\theta + \mu_c^2$

TABLE 3.1: Mass terms models considered in this work. The effective mass at the horizon is chosen in the range $\mu_H = (1\text{–}5)M^{-1}$, corresponding to $n_H \sim O(10) - O(10^2)(M_\odot/M)^2\,\mathrm{cm}^{-3}$ .The constant mass term can take the values $\mu_c = \{0.1, 0.2, 0.3, 0.42, 0.5\}M^{-1}$, with corresponding densities in the range $n_c \sim O(0.1) - O(1)(M_\odot/M)^2\,\mathrm{cm}^{-3}$. The slope λ is chosen among $\lambda = \{1/2, 1, 3/2, 2\}$. For models featuring an inner edge, the latter is placed at $r_0 = \{r_{ISCO}, 3, 6, 8\}M$.

and their possible superradiant instabilities) are more conveniently computed in the time domain (i.e. via an initial value evolution) than in the frequency domain.

3.2.2 Mass terms

The various mass terms that we consider (corresponding to different density profiles for the plasma) are summarized in Table 3.1. Model **(I)** aims to qualitatively describe Bondi spherically symmetric accretion. The latter predicts a power-law density profile [493], which in turn gives, through Eq. (3.1), a mass term

$$\mu_0^2 = \mu_H^2 \left(\frac{r_+}{r}\right)^\lambda . \tag{3.9}$$

The normalization is provided by the mass μ_H at the horizon r_+, while the radial profile is set by the slope λ. In this work, we explore values $\mu_H = (1\text{–}5)M^{-1}$, which can be converted [via Eqs. (3.1) and (3.2)] into plasma densities near the horizon $n_H \sim O(10) - O(10^2)(M_\odot/M)^2\,\mathrm{cm}^{-3}$.

We adopt such low values of the density to focus on the case of black holes radially accreting from the insterstellar medium, like in Ref. [479]. As we will discuss in Section 3.4, larger values of μ_H will not produce superradiant instabilities. Bondi accretion in the transonic flow regime would predict a slope $\lambda = 3/2$, but we also explore the impact of different values $\lambda = \{1/2, 1, 3/2, 2\}$.

In model **(II)**, we multiply the mass term of model **(I)** by $\sin^2\theta$:

$$\mu^2(r, \theta) = \mu_0^2(r) \sin^2\theta\,. \tag{3.10}$$

Model **(II)** therefore attempts to capture the effect of an axisymmetric "thick" disk that qualitatively realizes the ADAF models mentioned in the introduction. The case of a much thinner disk than model **(II)** is difficult to study with our code, for reasons that we will discuss in the following. Nevertheless, we will make the case that model **(II)** captures the main qualitative effect of axisymmetric accretion.

In order to understand the interplay between the values of the density (and effective mass) far away from and close to the black hole, in models **(III)** and **(IV)** we consider respectively the mass terms

$$\mu^2(r) = \mu_H^2 \left(\frac{r_+}{r}\right)^\lambda + \mu_c^2 \tag{3.11}$$

and

$$\mu^2(r,\theta) = \mu_H^2 \left(\frac{r_+}{r}\right)^\lambda \sin^2\theta + \mu_c^2\,, \tag{3.12}$$

where the additional constant term serves as a non-trivial asymptotic value $\mu(r \to \infty) = \mu_c$, and we choose $\mu_c = \{0.1, 0.2, 0.3, 0.42, 0.5\}M^{-1}$ [corresponding to plasma densities $n \simeq \{0.1, 0.5, 1.2, 2.3, 3.2\}(M_\odot/M)^2\mathrm{cm}^{-3}$]. We recall that $\mu = 0.42M^{-1}$, in the *constant mass* case, gives the fastest growing superradiant mode for $a = 0.99M$ [496], which will be also our choice for the spin parameter.

In order to account for the possibility that the accretion disk may be truncated at some finite distance from the black hole, we also consider the effective mass radial profile

$$\mu_1^2(r) = \Theta(r - r_0)\mu_H^2 \left(1 - \frac{r_0}{r}\right)\left(\frac{r_0}{r}\right)^\lambda\,, \tag{3.13}$$

where r_0 is the radius of the disk's inner edge. In our numerical experiments, we choose $r_0 = \{r_{ISCO}, 3, 6, 8\}M$, where r_{ISCO} is the radius of the innermost stable circular orbit around a Kerr black hole. This radial profile is employed, respectively with and without a $\sin^2\theta$ factor, in models **(V)** and **(VI)**.

Finally, models **(VII)** and **(VIII)** only differ from models **(V)** and **(VI)** because of the addition of a constant mass term $\mu_c = \{0.1, 0.2, 0.3, 0.42, 0.5\}M^{-1}$. The latter allows for mimicking the presence of a spherical "corona" inside the disk's inner radius, whose density is non-vanishing but suppressed relative to that of the disk.

3.3 Numerical method

3.3.1 Spectral decomposition

Our time-domain evolution code for scalar perturbations with a space-dependent mass term utilizes the setup described in Ref. [496] for the constant mass case. We refer the reader to that work for more details, and we focus here solely on the changes that we had to introduce to deal with a non-constant mass term.

The method is based on a decomposition of the scalar field in a series of spherical harmonics (see e.g. appendix A in Ref. [497]):

$$\Psi(t,r,\theta,\phi) = \sum_m \sum_{l=|m|}^{\infty} \frac{\psi_{lm}(t,r)}{r} \mathbf{Y}_{lm}(\theta) e^{im\phi}\,. \tag{3.14}$$

By inserting this decomposition into Eq. (3.8), we obtain a set of coupled partial differential equations in the t and x variables. Because of axisymmetry, different m-modes decouple from one another, but the decomposition in spherical harmonics generates couplings for each l-mode to the $l \pm 2$ modes.

A first set of couplings arises from the $\cos^2\theta$ terms present both in the coefficients of the time derivatives of the field and in the coefficient in front of the mass term [c.f. Eq. (3.8)]. The projection of these terms on the basis of spherical harmonics can be

computed by using

$$c^m_{jl} = \langle lm|\cos^2\theta|jm\rangle = \frac{\delta_{lj}}{3} + \frac{2}{3}\sqrt{\frac{2j+1}{2l+1}}\langle j,2,m,0|l,m\rangle\cdot\langle j,2,0,0|l,0\rangle, \tag{3.15}$$

where we have defined

$$\langle lm|f(\theta)|jm\rangle = 2\pi\int_{-1}^{1}\mathbf{Y}^*_{lm}(\theta)f(\theta)\mathbf{Y}_{jm}(\theta)d(\cos\theta)\,, \tag{3.16}$$

and the notation $\langle j_1,j_2,m_1,m_2|j_3,m_3\rangle$ is used for the Clebsch-Gordan coefficients [498].

The $\cos^2\theta$ terms generate couplings to $\pi_{l\pm2}$, which are present also in the massless case, and to $\psi_{l\pm2}$, which appear in the constant mass case. Both of these "classes" of couplings are "geometric" in nature, as they arise from the g^{tt} element of the inverse metric. Let us stress that both classes of couplings can in principle be eliminated by projecting onto a basis of spheroidal (rather than spherical) harmonics [499, 500], at least in the constant mass case. Note however that spheroidal harmonics are not easy to manipulate in practice, since there are no general analytic expressions for them. The latter is presumably the reason why Ref. [496] used spherical harmonics even in the constant mass case.

Another different set of l-couplings arises from the angular dependence of the effective mass term. For this reason, these couplings do not appear in the evolution of scalar perturbations with a constant mass term studied in Ref. [496]. In our problem, couplings of this kind are encountered only in the case of the θ-dependent mass profile used in models **(II)**, **(IV)**, **(VI)**, **(VIII)**, and can be computed by projecting $\sin^2\theta$ and $\sin^2\theta\cos^2\theta$ as follows:

$$s^m_{jl} = \langle lm|\sin^2\theta|jm\rangle = \frac{2\delta_{lj}}{3} - \frac{2}{3}\sqrt{\frac{2j+1}{2l+1}}\langle j,2,m,0|l,m\rangle\cdot\langle j,2,0,0|l,0\rangle, \tag{3.17}$$

$$cs^m_{jl} = \langle lm|\sin^2\theta\cos^2\theta|jm\rangle = \frac{c^m_{jl}}{7} + \frac{3\delta_{jl}}{35} - \frac{8}{35}\sqrt{\frac{2j+1}{2l+1}}\langle j,4,m,0|l,m\rangle\cdot\langle j,4,0,0|l,0\rangle. \tag{3.18}$$

The angular dependence of our mass models therefore generates additional couplings to $\psi_{l\pm2}$ and $\psi_{l\pm4}$, as a result of the intrinsic non-separability of the scalar perturbation equations. Therefore, these couplings cannot be eliminated, even if we were to perform a decomposition into spheroidal harmonics.

Finally, we stress that in practice we cut off the decomposition (4.3) at a maximum angular momentum number, l_{max}, which we vary to check the robustness of our results.

3.3.2 Perturbation equations

By inserting the decomposition (4.3) into the scalar perturbation equation and introducing the auxiliary variable $\pi = \dot{\psi}$, we can reformulate the problem in first order form. The result is a system of coupled partial differential equations:

$$\begin{aligned}&\left(\Sigma^2_{(0)} + a^2\Delta c^m_{ll}\right)\dot{\pi}_l + a^2\Delta\left(c^m_{l,l+2}\dot{\pi}_{l+2} + c^m_{l,l-2}\dot{\pi}_{l-2}\right) = \\ &\left(r^2+a^2\right)^2\psi_l'' + \left[2iam\left(r^2+a^2\right) - 2a^2\frac{\Delta}{r}\right]\psi_l' - 4iamMr\pi_l - V_0 - V_l - V_{l\pm2} - V_{l\pm4}\,,\end{aligned} \tag{3.19}$$

where we defined

$$\Sigma^2_{(0)} = \left(r^2 + a^2\right)^2 - a^2\Delta\,, \tag{3.20}$$

$$V_0 = \Delta\left[l\,(l+1) + \frac{2M}{r}\left(1 - \frac{a^2}{Mr}\right) + \frac{2iam}{r}\right]\psi_l\,, \tag{3.21}$$

$$V_l = \Delta\Big[\mu_i^2(r)\left(r^2 + a^2c^m_{ll} + r^2s^m_{ll} + a^2cs^m_{ll}\right) + \mu_c^2\left(r^2 + a^2c^m_{ll}\right)\Big]\psi_l\,, \tag{3.22}$$

$$V_{l\pm2} = \Delta\Big[\mu_i^2(r)\left(a^2c^m_{l,l+2} + r^2s^m_{l,l+2} + a^2cs^m_{l,l+2}\right) + \mu_c^2a^2c^m_{l,l+2}\Big]\psi_{l+2} + [(l+2)\to(l-2)]\,, \tag{3.23}$$

$$V_{l\pm4} = \Delta\mu_i^2(r)\left(a^2cs^m_{l,l+4}\right)\psi_{l+4} + [(l+4)\to(l-4)]\,. \tag{3.24}$$

Eq. (3.21) gives the effective potential for a scalar in the Kerr spacetime. That potential is obviously common to all the mass models that we consider (and to the massless and constant-mass problems as well). In Eqs. (3.22) and (3.23), the terms proportional to μ_c^2 are also present in the constant-mass case, while the terms proportional to μ_i^2 are typical of the inhomogenoeus-mass problem. The index i selects between the two radial profiles given by Eqs. (3.9) and (3.13). As already discussed, terms in (3.22), (3.23) and (3.24) that are proportional to s^m_{jl} and cs^m_{jl} are only encountered in models **(II)**, **(IV)** , **(VI)** and **(VIII)**, which feature an axisymmetric mass term.

3.3.3 Evolution scheme

We evolve numerically Eq. (4.4) by the method of lines. We obtain a set of ordinary differential equations by approximating the spatial derivatives with a fourth-order finite-difference scheme in the interior of a finite uniform grid in the tortoise coordinate x. The grid extends typically from $x_H = -300M$ to $x_\infty = 600 - 1000M$, with typical values of the spacing $\Delta x = 0.125M$. In more detail, we employ a symmetric fourth order approximation scheme for the first and second derivatives of the variables at the inner points of the grid:

$$\psi_i' \approx \frac{-\psi_{i+2} + 8\psi_{i+1} - 8\psi_{i-1} + \psi_{i-2}}{12\Delta x} \tag{3.25}$$

$$\psi_i'' \approx \frac{-\psi_{i+2} + 16\psi_{i+1} - 30\psi_i + 16\psi_{i-1} - \psi_{i-2}}{12\Delta x^2} \tag{3.26}$$

where we have defined $\psi_i' = \psi'(x_i = x_H + i\Delta x)$. In the neighborhood of the endpoints of the spatial grid we resort to a symmetric but lower order, $O(\Delta x^2)$, derivative scheme

$$\psi_i' \approx \frac{\psi_{i+1} - \psi_{i-1}}{2\Delta x} \tag{3.27}$$

$$\psi_i'' \approx \frac{\psi_{i+1} - 2\psi_i + \psi_{i-1}}{\Delta x^2} \tag{3.28}$$

At the innermost and outermost points of the grid we impose appropriate boundary conditions, discussed in details in the following subsection. The time evolution of the equations is performed by a fourth-order Runge-Kutta algorithm with a time-step properly chosen to satisfy Courant-Friederich-Lewy bound for numerical instabilities, $\Delta t = \kappa\Delta x$, with $\kappa < 1$. Here, we choose $\kappa = 0.8$.

3.3.4 Boundary conditions

Boundary conditions play a key role in the study of the spectrum of characteristic modes of a system. Physical wave solutions in the near-horizon region of a Kerr spacetime must propagate into the event horizon (which corresponds to $r_* \to -\infty$), i.e. they must behave as $\psi \propto e^{-i\omega(t+r_*)}$ when $r_* \to -\infty$. This reflects the known fact that the event horizon effectively behaves as a one-way membrane for classical fields [501]. These boundary conditions , which one can equivalently recast as $\dot{\psi} \approx \psi'$ when $r_* \to -\infty$, are usually referred to as "ingoing" (into the horizon) boundary conditions , and are the ones typically adopted to determine e.g. the spectrum of *quasi-normal modes* of massless scalar perturbations [273]. At spatial infinity, $r_* \to +\infty$, the general solutions to a wave equation are comprised of both ingoing (i.e. moving into the grid) and outgoing (i.e. moving away from the systems) modes, i.e. a generic solution will be $\psi \sim Ae^{-i\omega(t+r_*)} + Be^{-i\omega(t-r_*)}$ (with A and B constants). If the system is isolated, as assumed in the calculation of quasi-normal modes [273], it is appropriate to impose outgoing boundary conditions ($\dot{\psi} \approx -\psi'$) to eliminate fluxes entering the system from infinity. However, when considering fields that have a mass $\mu \neq 0$, physical modes with frequency $|\omega| \lesssim \mu^{1/2}$ are exponentially (Yukawa) suppressed at spatial infinity. For this reason, when solving for the *quasi-bound states* of massive perturbations, one typically adopts "simple zero" (i.e. reflective) boundary conditions at spatial infinity, $\psi(r \to \infty) = 0$, as considered in [496].

Implementing proper physical boundary conditions in a numerical method is a non-trivial task. In our numerical setup, for example, the left and right grid boundaries are placed at finite values of the tortoise coordinate, and imposing any boundary condition on them generates spurious reflections of the scalar perturbations. Ingoing/outgoing boundary conditions involve spatial derivatives of the field, which we approximate with an asymmetric fourth order scheme, e.g. at the innermost point of the spatial grid ($i = 0$) we impose

$$\dot{\psi}_{i=0} = \psi'_{i=0} \approx -\frac{11\psi_{i=0} - 18\psi_{i=1} + 9\psi_{i=2} - 2\psi_{i=3}}{6\Delta x} \,. \tag{3.29}$$

Thus, imposing such boundary conditions generates a spurious reflected flux of the same order of the numerical error, $\sim O(\Delta x^4)$. For outgoing boundary conditions at the right boundary, we adopt the same scheme. The si ro boundary conditions behave instead as a perfect mirror: they reflect back the entire incident flux (including the non-superradiant modes) and give rise to unphysical instabilities known as "black hole bombs" [369], which could potentially pollute the spectrum of the superradiant modes.

To deal with these artificial reflected scalar fluxes at the left boundary of the grid (i.e. at the horizon), we utilize the same solution suggested in Ref. [496]. We adopt the finite-difference implementation of an ingoing boundary condition [Eq. (3.29)], and we also define a near-horizon region where the equations are modified by the introduction of an artificial damping, in the spirit of the *perfectly-matched layers* (PML) technique. This way, the propagation of any spurious reflected signal is effectively suppressed. For further details about the PML technique, we refer the interested reader to Ref. [496] and references therein.

At the right boundary, instead, we observed that for our problem the choice of an outgoing boundary condition is preferable over the simple zero boundary condition used in Ref. [496]. In fact, we found that an outgoing boundary condition yields smaller reflected scalar fluxes than the simple-zero condition. The reason of

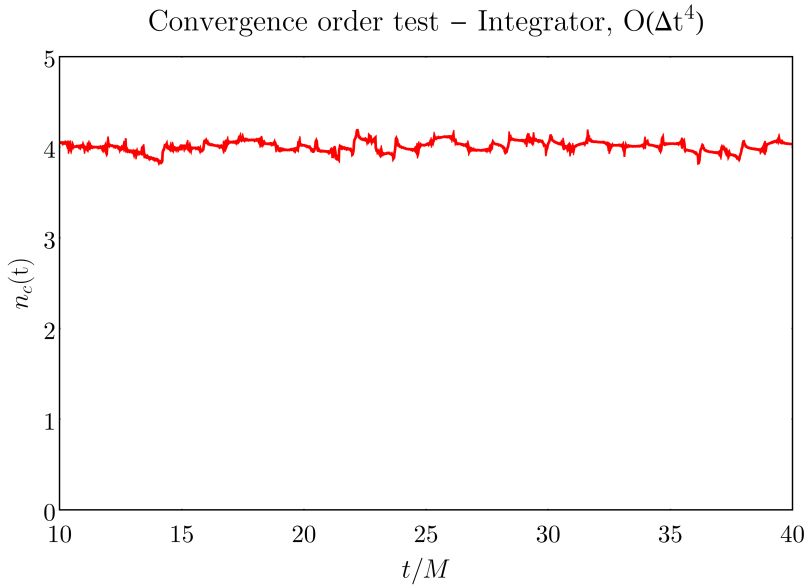

FIGURE 3.1: *Convergence order test - time discretization.* Convergence order in Δt vs time. The convergence order is estimated as $n_c(t) = \log_2(|\Phi_1 - \Phi_2|/|\Phi_2 - \Phi_3|)$, where $\Phi_r^2 \equiv \sum_{l=1}^{lmax} |\psi_{lm;r}(x = 0; t)|^2$, with r labelling the resolutions $\Delta t/M = \{0.08, 0.04, 0.02\}$. The figure shows the moving average of $n_c(t)$ with period $\simeq 1.5M$.

the poorer performance of the simple-zero boundary condition relative to what was observed in Ref. [496] is probably to be ascribed to the non-constant mass term that appears in our problem. Since the plasma density, and thus the mass term, increase when approaching the black hole, the potential barrier is higher near the ergoregion in our scenario. A higher potential barrier is more effective at reflecting back incident modes generated by the spurious reflection at spatial infinity. As a result, these modes remain trapped between the outer grid boundary and the potential's peak, polluting the numerical evolution. This behavior is instead suppressed if we use outgoing boundary conditions at spatial infinity.

3.3.5 Validation

We have performed several tests to validate our results. First, we have tested that the difference of the results obtained with various time and space resolutions scales as expected from our finite difference scheme, as shown in Figs. 3.1 and 3.2.

Second, we have extracted from our evolutions the quasi-normal modes of the scalar perturbations of the Kerr spacetime, and obtained results in good agreement with the frequencies tabulated in the literature [273]. We have also computed the superradiant spectrum for a scalar field with a mirror (black hole-bomb) and for a scalar field with a constant mass term, and found good agreement respectively with the approximated formulae of Ref. [369] and with the numerical results of Ref. [496]. Moreover, we have reproduced the frequency domain results obtained by Ref. [381] for a scalar field with a specific mass term yielding separable perturbation equations. Finally, we have verified that the total energy and angular momentum of the scalar field (supplemented by the scalar fluxes at infinity and through the horizon) are conserved to within a good approximation along our numerical evolutions, and we have checked the robustness of our results against changes of the "internal" parameters of our code (e.g. grid size, step, angular momentum cutoff and PML parameters).

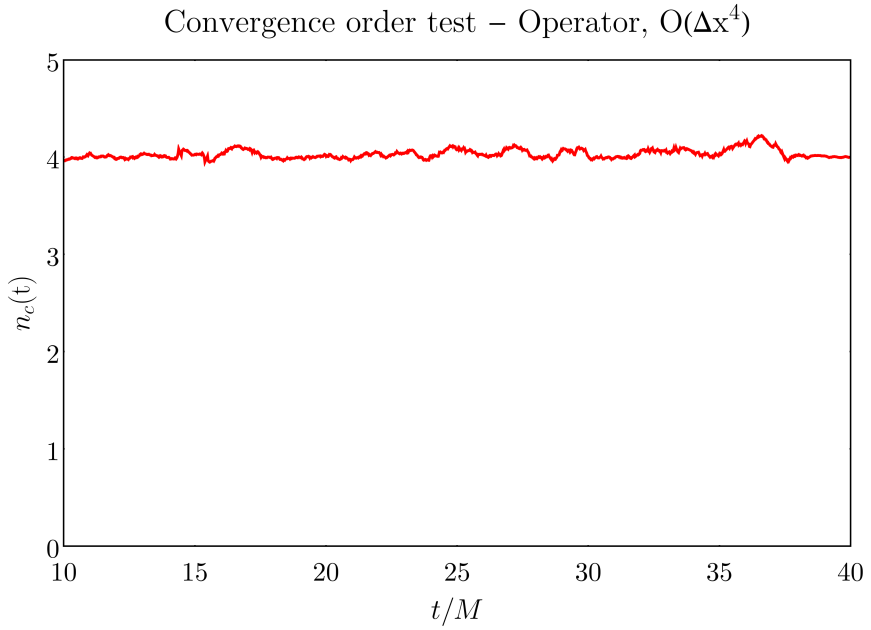

FIGURE 3.2: *Convergence order test - space discretization.* The same as Fig. 3.1, but for the convergence order in Δx vs time. The resolutions used are $\Delta x/M = \{0.25, 0.125, 0.0625\}$.

3.4 Results

In the following, we present examples of numerical results for the time-domain evolution of the scalar field around a Kerr black hole with spin $a = 0.99M$, with the various mass terms reviewed in Sec. 3.2 and Table 3.1.

3.4.1 Models (I) and (II)

We find no evidence for quasi-bound states and for superradiant instabilities in models **(I)** and **(II)**, in which the asymptotic mass value at infinity is zero. In fact, in these numerical experiments the scalar field decays exponentially in time, and the extracted spectrum resembles the usual Kerr quasi-normal mode ringdown, though with modified frequencies. A representative example of the spectra that we obtain is given in Fig. 3.3, where we show the time evolution of the amplitude of the scalar mode $l = m = 1$ in a realization of model **(I)**.

From these results, we conclude that a non-vanishing asymptotic mass value at infinity is a necessary condition for the existence of quasi-bound states and superradiant instabilities. This can be understood by looking at the effective potential in the limit $a \to 0$: if $V_{eff}(r \to \infty) \to$ const and $V'_{eff}(r \to \infty) \to 0^+$, then the potential features a trapping well that can host quasi-bound states [502]. As one can immediately notice, this is not the case for models where $V_{eff} \sim O(1/r^\lambda)$ at infinity.

As we have already mentioned, however, the quasi-normal mode frequencies are modified by the presence of a plasma-induced effective mass, with respect to those of a massless scalar on a Kerr background [273]. We find that the presence of the plasma can sustain the quasi-normal oscillations for slightly shorter times than in pure vacuum. As expected, in the limit $\mu_H \to 0$, one recovers the usual Kerr spacetime quasi-normal modes.

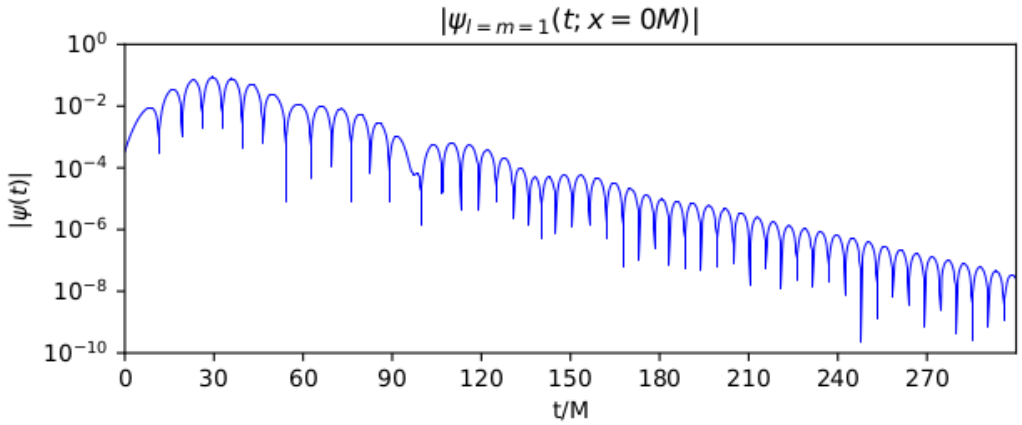

FIGURE 3.3: *Quasi-normal mode ringdown.* Example of ringdown in model **(I)**, with $M\mu_H = 1$ and $\lambda = 3/2$: the plot shows the amplitude of ψ_{lm} (with $l = m = 1$), extracted at $x = 0$. This mode decays quickly over time, which signals stability. As discussed in the main text, this is to be expected since mass profile goes to zero at infinity ($\mu(r \to \infty) = 0$). The extracted quasi-normal mode frequency $M\omega = 0.566 - i\,4.99 \cdot 10^{-2}$ is to be compared with the frequency for a massless scalar field in Kerr, $M\omega = 0.493 - i\,3.67 \cdot 10^{-2}$ [273]. Qualitatively similar results are obtained for the other modes, and for model (**II**).

3.4.2 Models (III) and (IV)

For these models, superradiant modes exist with instability timescales typically longer than in the corresponding constant mass problem. In more detail, we find instability timescales of the order of $\tau_I = \mathrm{Im}(\omega M)^{-1} \sim 10^{11} M$, which is still shorter than the typical accretion timescale, and thus potentially relevant in astrophysics.

Nevertheless, these instabilities appear to be very "fragile", as they are present only in a small region of the parameter space of models (**III**) and (**IV**). In fact, we find no superradiant modes for $\mu_H \gtrsim 2M^{-1}$, i.e. a small increase (from $n_H \simeq 0.1$ cm^{-3} to $n_H \simeq 0.5$ cm^{-3}) in the density at the horizon is sufficient to quench completely the superradiant instability. When that is the case, the time evolutions of the scalar field show a damped quasi-normal mode ringdown, like for models **(I)** and **(II)**, but with typically longer decay times $\sim 10^5 - 10^{10} M$. Similarly, as discussed in the previous section about models **(I)** and **(II)**, a non-zero value for the mass μ_c at spatial infinity is needed to get superradiant instabilities, but as soon as $\mu_c M$ is above a critical value $\mu_{crit} M \simeq 0.5$ the instability disappears.

The details of the time evolutions depend also on the exponent λ that controls the slope of the density (and thus mass) profiles: the smaller λ, the slower the decrease of the mass profile toward its asymptotic value, and the shorter the lifetime of the stable modes. Moreover, we also find that there is a critical exponent, $\lambda_{crit} \simeq 2$, below which no superradiant modes exist at all.

Fig. 3.4 shows examples of two scalar field evolutions. The two upper panels show a realization of model **(III)** that is subject to superradiant instabilities, while the two lower panels correspond to a realization with higher effective mass at the horizon, and thus no instabilities. In both cases, we show the power spectrum (i.e. the absolute value of the Fourier transform of ψ_{lm}, with $l = m = 1$), where one can clearly see the dominant mode and its overtones, as well as a plot of the time evolution, which is dominated by the main mode and which shows a clear exponential growth/decay in the unstable/stable case respectively .

Overall, we find that the differences between the spherically symmetric model **(III)** and the axisymmetric model **(IV)** are minor, although "thick" disks [model **(IV)**] seem to produce slightly faster instabilities.

3.4.3 Models (V) and (VI)

In these models, in which the mass (and plasma density) profiles feature an inner edge but go to zero at spatial infinity, we find both stable quasi-normal modes and superradiantly unstable modes. Fig. 3.5 shows examples of both.

Mass profiles with the inner edge placed close to the horizon – $r_0 = r_{ISCO}, 3M$ – only show signs of stable modes. We have compared the quasi-normal mode frequencies and decay times extracted from our simulations with the corresponding quantities for massless scalar perturbations on a Kerr background [273]. We find that, for fixed r_0, in the limit $\mu_H \to 0$ one correctly recovers the massless Kerr quasi-normal modes: $\mathrm{Re}(M\omega) \to 0.493$, $\mathrm{Im}(M\omega) \to 3.67 \cdot 10^{-2}$, for $a = 0.99M$. In the opposite limit of increasing μ_H, $\mathrm{Re}(M\omega)$ grows rapidly, while the decay time shows indications of a maximum around $\mu_H \simeq 1M^{-1}$ and then relaxes to an almost constant value. The latter depends on the choice of the slope and inner edge parameters and is, in general, different from the decay time of the quasi-normal modes for a massless scalar in Kerr.

Superradiant unstable modes appear instead only when the inner edge is placed sufficiently far away from the horizon. To make sense of this result, one can again rely on intuition from the shape of effective potential in the limit $a \to 0$. When $r_0 \lesssim 3M$, the peak of the mass profile and that of the effective potential for massless fields are roughly in the same region, which results in a "flattening" of the total effective potential, which in turn prevents the formation of quasi-bound states. For $r_0 = 6M, 8M$, instead, a potential well clearly appears, which can lead to the formation of quasi-bound states. In fact, for $r_0 = 6M, 8M$ one obtains fast growing instabilities with $\tau_I \sim 10^5 M$ for spherically symmetric models, while instabilities triggered by "thick" disks seem to grow even slightly faster (by a few percent). For these reasons, we expect that similar (or even stronger) superradiant instabilities should be present even in the limit of razon-thin disks (which we cannot simulate numerically) with inner edge sufficiently far from the black hole. Furthermore, the superradiant spectrum resembles closely the results obtained in Ref. [381] for mass terms similar to ours but yielding separable perturbation equations for the scalar.

In spite of these results, we will argue in the following, when dealing with models **(VII)** and **(VIII)**, that in more realistic accretion scenarios the presence of a non-zero (albeit very low) plasma density in a quasi-spherical "corona" inside the disk's inner edge will likely quench these superradiant instabilities.

3.4.4 Models (VII) and (VIII)

These models show results qualitatively similar to models **(V)** and **(VI)**. When the peak of the mass profile (which is in turn set by the disk's inner edge) is well separated from the centrifugal potential barrier, perturbations can get trapped in a potential well and grow superradiantly with a typical timescale of $\tau_I \sim 10^5 M$. Instead, when the peak of the mass profile overlaps with the centrifugal barrier, no quasi-bound states can form and perturbations undergo a damped ringdown. Fig. 3.7 shows an example of superradiant mode growing over time. In the upper panel, we present snapshots of the quasi-stationary oscillations of a superradiant mode with

support in the ergoregion, a t different times. The lower panel, instead, shows the fractional amplitude increment of the perturbation over the spatial grid.

Note however that models **(VII)** and **(VIII)** present a constant mass term μ_c mimicking the presence of a "corona", i.e. a (roughly spherical) region within the disk's inner edge where the accretion flow (and thus the density) are suppressed but non-zero. Note that astrophysical black holes, and particularly those in intermediate states between ADAF and "thin" disk accretion are expected to present this kind of additional structure [503]. This corona suppresses the superradiant modes that were found in models **(V)** and **(VI)**. Indeed, as can be seen from the examples shown in Fig. 3.6, the superradiant modes are completely quenched (for both spherically symmetric and axisymmetric models, irrespective of the slope λ) for $M\mu_c \gtrsim 0.42$. For a black hole of $M = 10M_\odot$ this corresponds to a very tenuous corona of density $n_e \sim 0.02\,\mathrm{cm}^{-3}$. Even higher densities in the corona are expected for realistic accretion scenarios, where the densities in the accretion disk may also be significantly higher. This will have the effect of quenching the instabilities even further, as larger densities correspond to large scalar field masses, which stabilize the dynamics. We therefore conclude that realistic accreting black holes are likely safe from superradiant instabilities even when triggered by mass profiles, such as the ones of models **(VII)** and **(VIII)**, that exhibit a sharp cut-off at some inner edge.

3.5 Discussion

3.5.1 Conclusions

We have investigated the superradiant instabilities that Refs. [479, 480] suggested might be triggered by tenuous plasmas (with densities $n_e \sim 10^{-3}$–10^{-2} cm^{-3} close to those of the insterstellar medium) around spinning astrophysical black holes. We have used a *1+1* spectral decomposition inspired by Ref. [496] to numerically evolve scalar perturbations with a position-dependent mass on a Kerr spacetime. This scalar is a toy model for the photon field, while the position-dependent mass term captures the effective photon mass induced by the plasma frequency. The profile of this mass term is a non-separable function of the radial and polar angle coordinates, and is chosen to mimic astrophysically relevant accretion disk profiles.

From the results of our numerical experiments, we conclude that a small ($\sim 10^{-3}$–10^{-2} cm^{-3}) but non-zero asymptotic plasma density at spatial infinity is crucial for the development of superradiant modes. Indeed, mass (and thus density) profiles that decrease monotonically exactly to zero at spatial infinity do not develop an instability in our simulations. However, even if the asymptotic plasma density at infinity is small and non-zero, superradiant instabilities can be easily quenched if the plasma density increases (even slightly) near the black hole, as expected in realistic accretion flows. This non-trivial interplay between the two asymptotic mass (i.e. density) values, near the horizon and near spatial infinity, can be qualitatively understood by looking at the effective potential for the scalar in the limit of vanishing or low spin. Indeed, one can easily see that while a constant mass term generates a "trapping well" where quasi-bound states can form and grow exponentially, a mass term that increases near the black hole does not allow for the formation of mimina (and thus quasi-bound states) in the effective potential. We find indeed that plasma densities as low as $n_e \sim O(1)(M_\odot/M)^2\,\mathrm{cm}^{-3}$ near the black hole are enough to prevent the the formation of superradiant states.

A notable exception is provided by a plasma density profile exhibiting a sharp cut-off at distances from the horizon larger than a few gravitational radii. If the

plasma density is zero within such an inner edge, superradiant modes can form. However, if the accretion flow (as expected in astrophysically relevant scenarios) forms a corona with densities as low as ~ 0.02 cm^{-3} (for a 10 $M_\odot$ black hole), even these instabilities will be easily quenched.

Overall, our results suggest that astrophysical black holes are likely unaffected by plasma-driven superradiant instabilities.

3.5.2 Limitations

Our work presents several limitations, which we expect should not affect our main conclusions. First, our numerical integration scheme cannot handle plasma densities that rise too fast as the black hole horizon is approached. Indeed, large plasma densities correspond to large scalar field masses, which make our equations stiff. As a result, here we only consider mass terms as large as $\mu M \sim 5$, which correspond to $n_e \sim 3$ cm^{-3} for a black hole with mass of $\sim 10 M_\odot$. While implicit-explicit methods [504, 505] would probably allow for dealing with even larger mass terms, the values that we consider are already enough to quench superradiant instabilities, and on general physical grounds larger masses are anyway expected to stabilize the dynamics even further.

Second, our numerical method cannot handle a razor-thin accretion disk, but only "thick" disks. The reason is that to resolve a thin disk one would need to push our spectral decomposition to multipole numbers $l \to \infty$. Nevertheless, the scenario envisioned by Ref. [479], where black holes are immersed in a tenous insterstellar medium plasma, is expected to produce radiatively inefficient geometrically "thick" accretion flows, which we can study with our code. Moreover, densities and accretion rates in geometrically thin accretion disks are expected to be much larger than in thick disks, which would make the effective mass term larger, thus suppressing superradiant instabilities even further.

Obviously, another approximation that may impact our work is the choice of studying simple toy scalar perturbations instead of a massive photon (i.e. a Proca field). While superradiant instabilities, when present, are generally stronger for vector modes than for scalar ones [391, 506, 507], the effective potential is very similar for scalars and vectors. Therefore, we expect that our qualitative arguments, which relate the suppression of superradiant modes to the shape of the effective potential, should hold even in the vector case.

We also stress that the dispersion relation given by Eq. (3.1) and which provides the effective mass term for the photon is only valid for an unmagnetized cold plasma. This approximation is likely to break down as the temperature of the accretion disk rises close to the black hole, where magnetic fields are also expected to be present. However, if the dispersion relation given by Eq. (3.1) is modified, it is not even clear if superradiant instabilities would arise in the first place, even under favorable conditions.

Note that a further increase of the plasma density near the black hole may occur due to pair production by the large electromagnetic fields produced by the superradiant instability [274]. While computing this effect is beyond the scope of this work, as it would require deriving the structure of the black hole magnetosphere produced by the instability (which we cannot do in our scalar toy-problem), it would actually strengthen our results, since it would lead to an even stronger suppression of superradiant instabilities.

More recent work has investigated further the matter focusing on cases in which accretion is negligible, e.g. the rotating black hole originated from a mergers capable of projecting the remnant out of its hosting galaxy (i.e. "super-kicks" [508–511]). Their findings indicate that even in this ideal condition there are several other mechanisms that can alter either the dispersion relation or the plasma frequency itself (3.1), effectively quenching the photon superradiant instability of short timescales [380, 512–515].

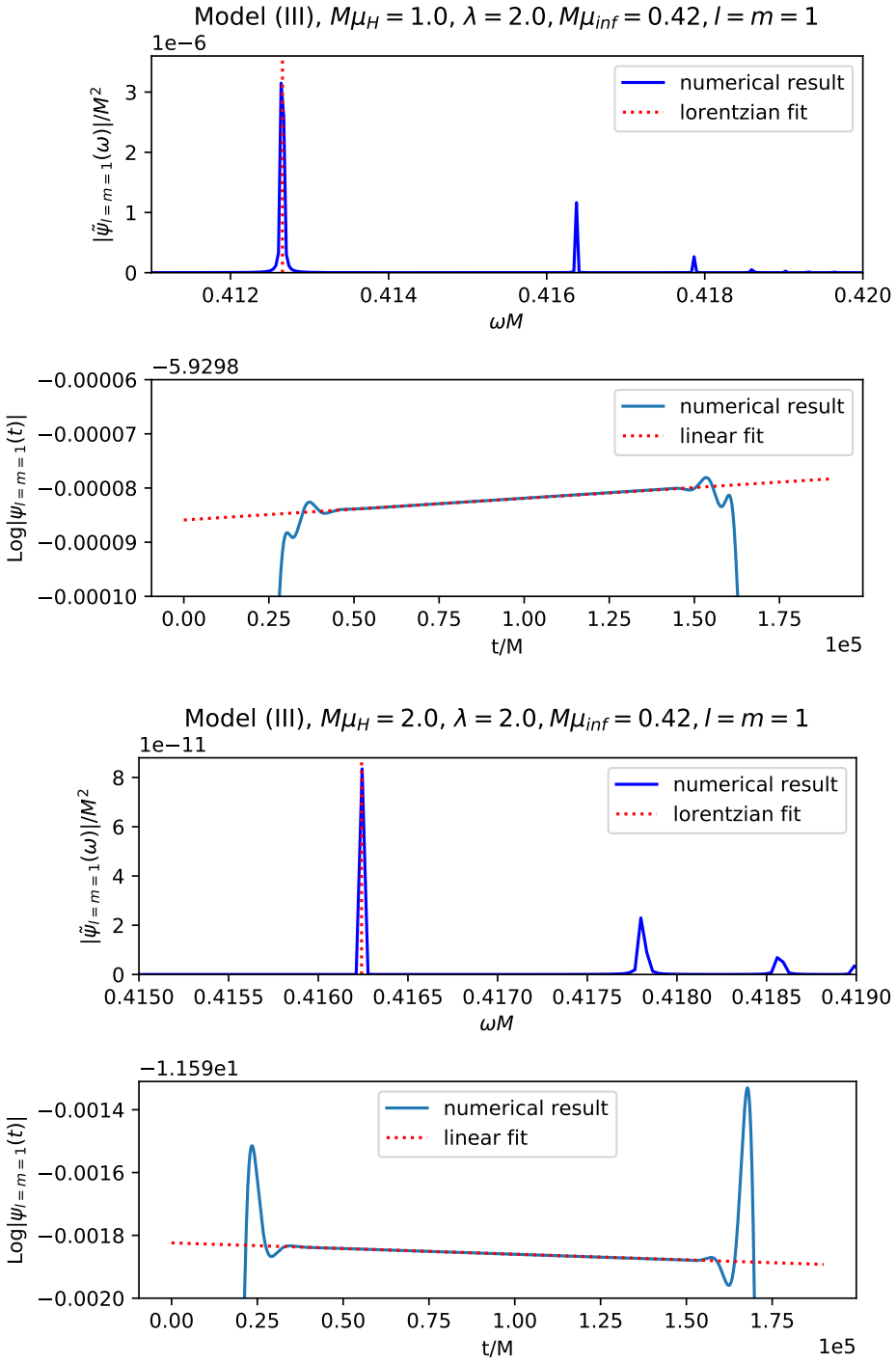

FIGURE 3.4: *Spectral analysis - model III.* Power spectrum and time evolution for two realizations of model (**III**), one giving a superradiant instability (top panel) and one giving a stable evolution (bottom panel), for the $l = m = 1$ mode. The two model realizations are respectively one with $M\mu_H = 1$ (density at the horizon $n_e \simeq 0.13$ cm^{-3} for a black hole with $M = 10M_\odot$), and one with $M\mu_H = 2$ ($n_e \simeq 0.52$ cm^{-3} for the same black hole mass). Time evolutions are band-pass filtered to avoid showing the transient due to the initial conditions. This band-pass filter is responsible for the artifacts at the start and end of the evolution. Dotted lines show Lorentzian fits to the power spectra and log-linear fits to the time evolutions. The extracted frequencies of the dominant modes are $M\omega = 0.413 + i\,3.99 \cdot 10^{-11}$ and $M\omega = 0.416 - i\,3.61 \cdot 10^{-10}$, respectively.

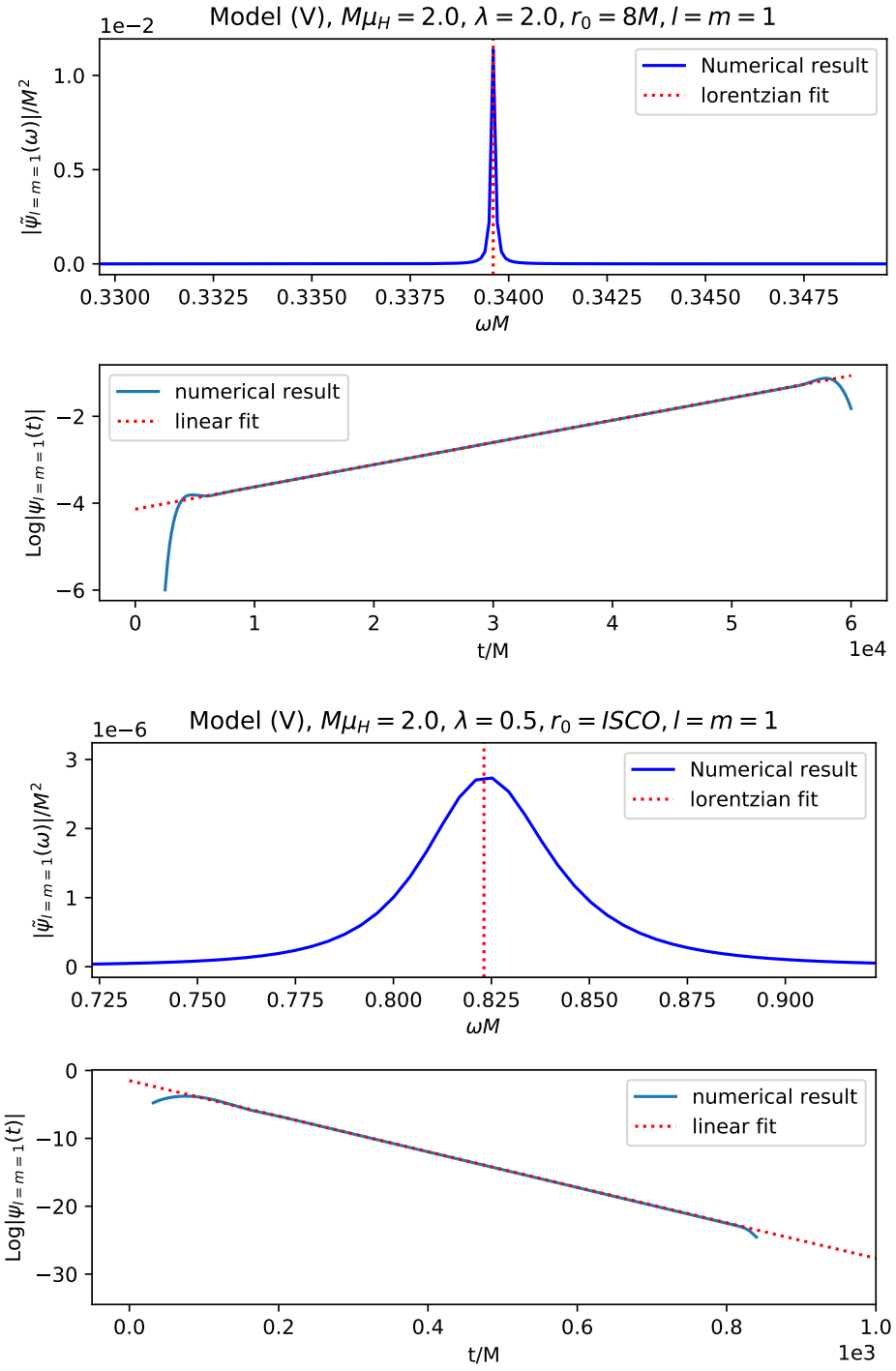

FIGURE 3.5: *Spectral analysis - model V.* Same as in Fig. 3.4, but for unstable and stable modes ($l = m = 1$) obtained with two realizations of model (**V**), namely one with an inner edge at $r_0 = 8M$ (top panel) and one where density profile is cut off at the ISCO. The top panel shows a strong instability ($\omega M = 0.340 + i\ 5.13 \cdot 10^{-5}$), while the bottom one shows a stable evolution with dominant mode $\omega M = 0.823 - i\ 2.62 \cdot 10^{-2}$.

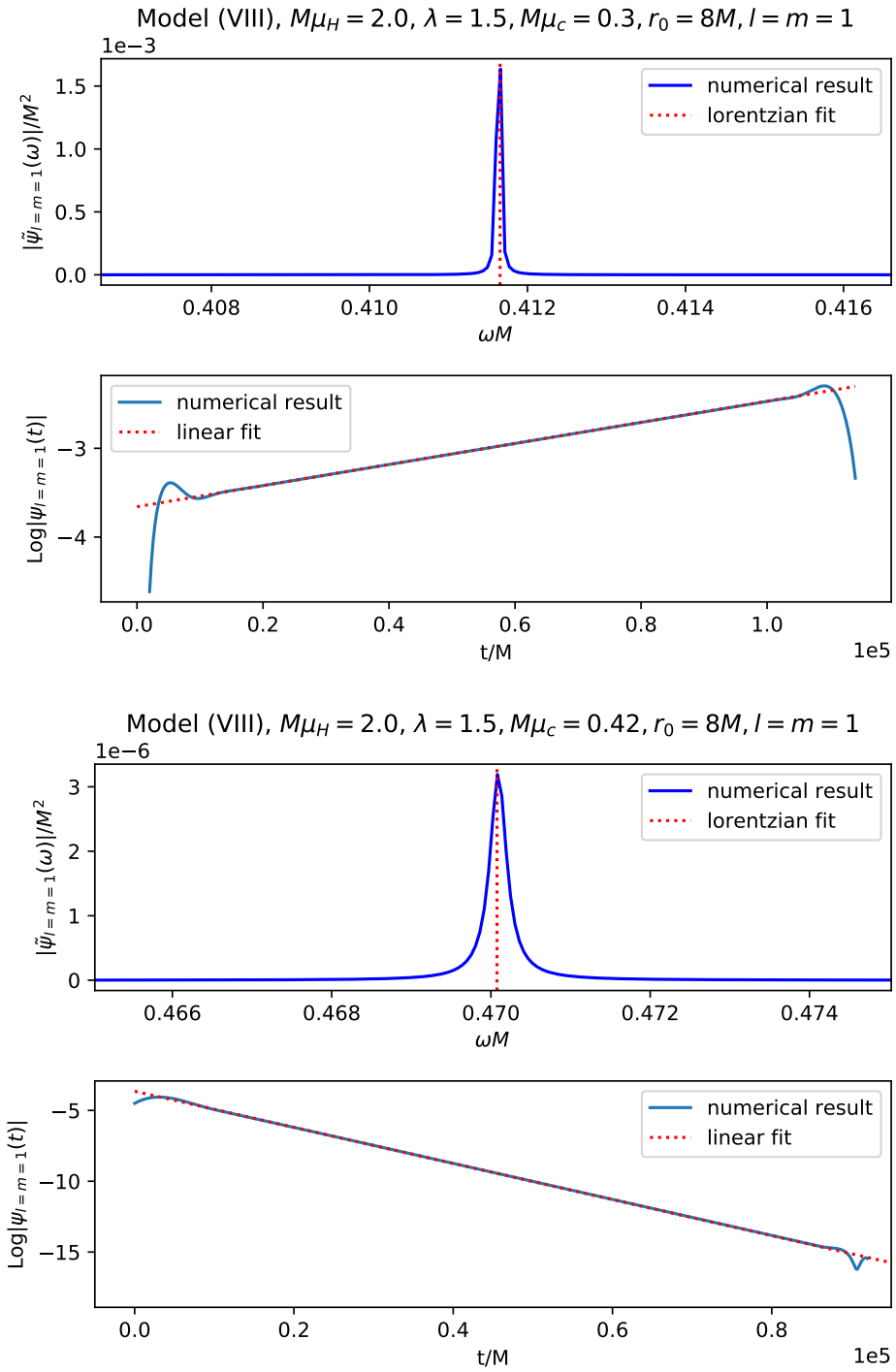

FIGURE 3.6: *Spectral analysis - model VIII.* Same as in Fig. 3.4, but for two realizations of model (**VIII**), one with $M\mu_c = 0.3$ (top panels; corresponding to $n_e \simeq 0.01\ \mathrm{cm}^{-3}$ for a black hole of $10M_\odot$) and one with $M\mu_c = 0.42$ (i.e. $n_e \simeq 0.02\ \mathrm{cm}^{-3}$ for a $10M_\odot$ black hole). Note that the minor increase of the corona density from the top to the lower panels is enough to quench the instability ($\omega M = 0.412 + i\,1.19 \cdot 10^{-5}$ vs $\omega M = 0.468 - i\,1.39 \cdot 10^{-4}$ for the top vs bottom case). Results are for the $l = m = 1$ mode.

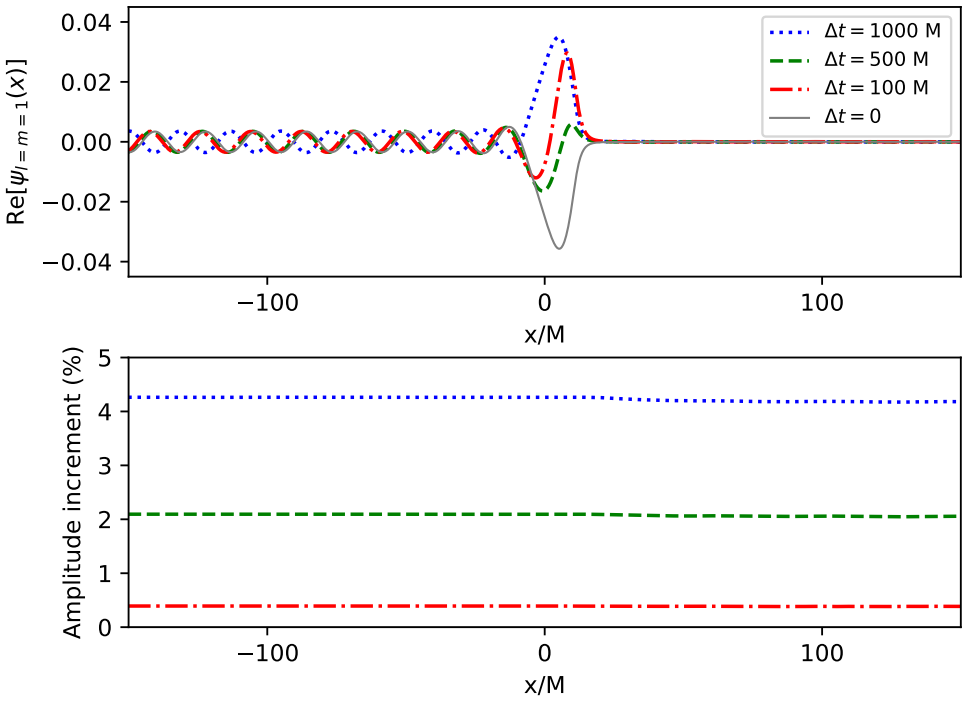

FIGURE 3.7: *Growth of superradiant instability.* Example of growing superradiant instability (with $\omega M = 0.345 + i\ 4.20 \cdot 10^{-5}$) in model (**VIII**), with $\mu_H M = 2.0$, $\mu_c M = 0.1$, $\lambda = 1.5$, $r_0 = 8M$. The upper panel shows snapshots, taken at different times, of the real part of the $l = m = 1$ mode over the spatial grid. The lower panel shows the relative fractional amplitude increment relative to some reference time $t = t_0$ (with $\Delta t = t - t_0$).

Chapter 4

Black hole scalarization

4.1 Black holes in "curvature-squared" gravity

In this chapter we will focus exclusively on the onset of scalarization (see section 2.2.2), so we will restrict our attention to quadratic scalar Gauss-Bonnet (qsGB) gravity, i.e. $f(\phi) = \eta\phi^2/2$ (without loss of generality [433]). The effective (squared) mass of the scalar on a fixed background is then

$$\mu_{\rm eff}^2 = -\eta\mathcal{G}. \tag{4.1}$$

For the Schwarzschild solution, one has $\mathcal{G} = 48M^2/r^6$, which is always positive and decreasing with r, and which yields the horizon value $\mathcal{G}(r = 2M) = 3/(4M^4)$. Hence, a tachyonic instability only occurs for $\eta > 0$, and the instability is expected to be more violent for smaller masses. Note that in curved spacetimes $\mu_{\rm eff}^2$ can be somewhat negative without necessarily developing a tachyonic instability (see Fig. 4.1). This is why the focus in the literature so far has been on $\eta > 0$ (or the equivalent condition in more complicated models). However, for a Kerr black hole of mass M and spin parameter a in Boyer-Lindquist (t, r, θ, φ) one has

$$\mathcal{G}_{\rm Kerr} = \frac{48M^2}{(r^2+\chi^2)^6}\left(r^6 - 15r^4\chi^2 + 15r^2\chi^4 - \chi^6\right) \tag{4.2}$$

where, for brevity, $\chi \equiv a\cos\theta$. Clearly, $\mathcal{G}_{\rm Kerr}$ is not monotonic, and can even become negative close to the horizon. This explains the results of [148, 516], where it was shown that rotation suppresses scalarization for $\eta > 0$.

We specialize to $\eta < 0$, which yields a real effective mass $\mu_{\rm eff}$ for low black hole spins, but which can yield an imaginary $\mu_{\rm eff}$ for high spins. We investigate the behavior of linear scalar perturbations to the general relativity solution by evolving Eq. (2.10) on a Kerr background, with the goal of assessing for what black hole spins and couplings η the perturbations become unstable. Indeed, at least two possible instability mechanisms may be at play in Eq. (2.10). The first is the tachyonic instability associated to spontaneous scalarization, mentioned above. The second could be a superradiant instability, which is known to exist at high spins for constant real masses [360, 370, 485, 495], and potentially also for non-constant effective masses [517] such as the one of Eq. (4.1). Superradiance occurs when bosonic waves with non-vanishing angular momentum are amplified when scattered by a spinning black hole, at the expense of the rotational energy of the black hole, which as a result spins down. For massive bosons, superradiant scattering can develop into an instability because the field is confined near the black hole by its own mass.

It should be stressed that, in principle, both instabilites could be present. However, they have distinct features (timescales, the angular momenta involved, dependence on the black hole spin). We show below that the tachyonic instability is by far

the dominant effect for $\eta < 0$. More broadly, our results strongly suggest that there exist theories in which scalarization occurs only for rapidly rotating black holes.

4.2 Onset of spin-induced scalarization

For $f(\phi) = 0$ and over a Kerr background, Eq. (2.10) separates into ordinary differential equations when ϕ is decomposed onto a basis of spheroidal harmonics. However, the choice $f(\phi) = \eta\phi^2/2$ yields an intrinsically non-separable equation. We therefore resort to a time-domain numerical integration of this equation, by using techniques akin to those presented in [496, 517], to which we refer for more details.

In brief, the idea is to project Eq. (2.10) onto a basis of *spherical*[1] harmonics $\mathbf{Y}_{lm}$, which yields 1+1 evolutions equations (in t and r) for the components of the scalar field,

$$\psi_{lm}(t,r) \equiv \int \mathbf{Y}^*_{lm}(r\phi)d\Omega \tag{4.3}$$

These equations are coupled and given explicitly by

$$\begin{aligned}
&\left[(r^2+a^2)^2 - a^2\Delta(1-c^m_{ll})\right]\ddot{\psi}_l + a^2\Delta(c^m_{l,l+2}\ddot{\psi}_{l+2} + c^m_{l,l-2}\ddot{\psi}_{l-2}) + 4iamMr\dot{\psi}_l \\
&- (r^2+a^2)^2\psi_l'' - \left(2iam(r^2+a^2) - 2a^2\frac{\Delta}{r}\right)\psi_l' \\
&+ \Delta\left[l(l+1) + \frac{2M}{r} - \frac{2a^2}{r^2} + \frac{2iam}{r}\right]\psi_l + \Delta\sum_j \langle lm|\mu^2_{\rm eff}(r^2+\chi^2)|jm\rangle\psi_j = 0\,,
\end{aligned} \tag{4.4}$$

$$\Delta \equiv r^2 - 2Mr + a^2\,, \tag{4.5}$$

$$c^m_{jl} \equiv \langle lm|\cos^2\theta|jm\rangle = \frac{\delta_{lj}}{3} + \frac{2}{3}\sqrt{\frac{2j+1}{2l+1}}\langle j,2,m,0|l,m\rangle\cdot\langle j,2,0,0|l,0\rangle\,, \tag{4.6}$$

where $\langle j_1, j_2, m_1, m_2|j_3, m_3\rangle$ are the Clebsch-Gordan coefficients [498]. Note that the evolution of modes of different m decouples because of the axisymmetry of the problem. Moreover, because of reflection symmetry with respect to the origin, even-l and odd-l modes also decouple: the evolution of a mode (l,m) is coupled to that of all the modes $(l+2k,m)$, with $k = 1,2,3,\ldots$.

To numerically evolve the system (4.4), we discretize the spatial grid and use a method of lines. By integrating in time using a fourth order explicit Runge-Kutta time-step inside the computational grid (as done e.g in [517]), it becomes apparent that the equations are stiff for large η, and that the numerical integration becomes unstable. To overcome this problem, we have used an Implicit-Explicit (IMEX) Runge-Kutta solver with adaptive time step, namely the IMEX-SSP3(3,3,2) and IMEX-SSP(4,3,3) schemes of [518]. Note that implicit methods [519], while effective at dealing with stiff problems, are typically less accurate and more computationally expensive. However, implicit-explicit algorithms, by employing explicit steps for the non-stiff terms and implicit steps only for the stiff ones, can tackle stiff problems with limited computational overhead. We successfully compared our code to results from both frequency-domain techniques [273] and similar time-domain codes [496]. Our implementation was also tested by analysing the convergence of the results (and their overall robustness) vs time-step and spatial-grid resolution.

[1] There is no advantage in using spheroidal harmonics, for which analytic expressions are unavailable, as they do not lead to a separable equation anyway.

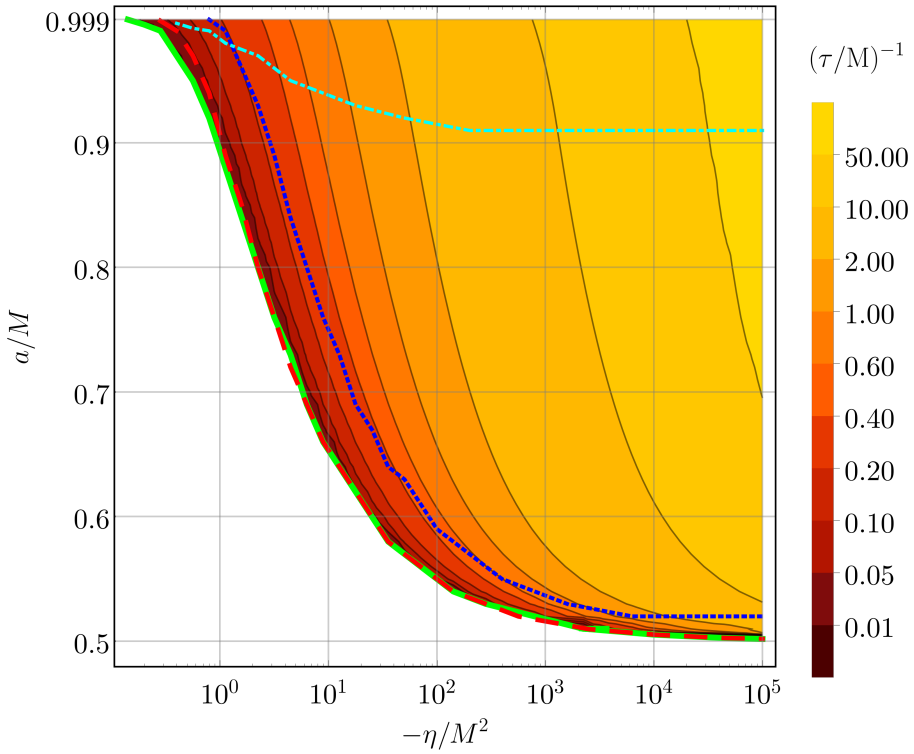

FIGURE 4.1: *Instability timescale τ (color code) for the reconstructed field as a function of spin and Gauss-Bonnet coupling.* The instability threshold for the total reconstructed field is shown by the solid green line, while the threshold when the $m = 0$ modes are excluded is shown by a blue dotted line. The red dashed line corresponds the instability threshold for the $m = 0$ odd modes, while the dot-dashed cyan line marks the instability threshold for the spherical mode $l = m = 0$ (see text for details). Note that all shown values of η are unconstrained by different observables (c.f. discussion in the conclusions).

4.3 Results

To investigate the possible presence of an instability, we evolve the scalar field by integrating the system given by Eq. (4.4), with l ranging from 0 to $l_{\rm max} = 30$ and $|m| \leq l$, and with Gaussian initial conditions for each mode ψ_{lm}. The results are robust against the choice of the cutoff $l_{\rm max}$ – as long as that is sufficiently large – and initial conditions, which only affect the early transient evolution of the scalar and not the unstable growth phase, if present. We consider black hole spins $a/M \sim 0.5$ – 0.999 and qsGB coupling $|\eta|/M^2 \sim 0.1 - 10^5$.

From the simulations showing an exponential scalar growth, we extract the instability timescale τ of the reconstructed field $|\phi| = \left(\sum_{lm} |\psi_{lm}|^2\right)^{1/2} \propto \exp(t/\tau)$ by fitting the time evolution of the scalar's amplitude after the initial transient. The contours in Fig. 4.1 show τ^{-1} as a function of a/M and $|\eta|/M^2$. The instability becomes stronger as either the spin or the coupling increases. Moreover, there is a minimum spin $a_{\rm min}$ below which the instability disappears. For $|\eta| \to \infty$, it appears that $a_{\rm min}/M \to 0.5$ (up to percent level numerical errors). The solid green line denotes the combinations of parameters for which the instability disappears (i.e. $\tau \to \infty$). With the blue dotted line we show the same marginal instability curve for the reconstructed field, but excluding the $m = 0$ modes. As can be seen, when the latter are

excluded the parameter space region yielding an instability shrinks, i.e. the main contribution to the instability comes from the $m = 0$ modes. As a further test of this conclusion, we also computed the marginal instability curve for the $m = 0$ modes alone, and that does indeed match the solid green line in Fig. 4.1.

Even and odd parity modes (i.e. modes with even and odd l) automatically decouple in Eq. (4.4). In the $m = 0$ sector, which dominates the instability shown in Fig. 4.1, the odd and even modes give roughly comparable contributions. We have verified this by considering the marginal instability curves for the odd and even $m = 0$ modes separately, which are both very close to the solid green line of Fig. 4.1. As an example, the red dashed line in Fig. 4.1 represents the marginal instability curve for the $m = 0$ odd modes.

Indeed, odd modes seem to have only marginally shorter instability times (by $\sim 1 - 2\%$) than even ones for high spins and large couplings. Conversely, in the region $|\eta| < 1, a/M > 0.9$ the even modes are slightly more unstable, as can be seen from the somewhat increased distance between the red dashed and solid green line curves.

Next we consider if some individual angular mode l, m gives the dominant contribution to the instability. To answer this question, we have to override the non-separability of the problem. To this end, we have forcefully decoupled each l-mode in Eq. (4.4) , suppressing "by hand" all the couplings between angular modes (i.e. $\langle lm|\mu^2_{\rm eff}(r^2+\chi^2)|jm\rangle$ with $l \neq j$) generated by the Gauss-Bonnet invariant; we have only kept active the contributions to the effective mass of the single l-mode. We have then let the system evolve, selecting Gaussian initial data for the chosen mode only. By this technique, we have isolated, for instance, the instability parameter space for the spherical mode $l = m = 0$, whose marginal instability curve is shown in Fig. 4.1 by a cyan dot-dashed line. However, we could not find any single l, m mode for which the marginal instability curve obtained in this way matched, even roughly, the solid green line for the whole reconstructed field. We therefore conclude that the gravitational coupling between angular modes plays a fundamental role in the onset of the observed instability.

We now proceed to examine whether the instability is dominantly tachyonic or powered by superradiance. The growth times, as shown in Fig. 4.1, can be as small as $\sim 0.01M$. This seems to favor a tachyonic origin, as superradiance acts on longer timescales (see e.g. [485, 517]). Moreover, the fact that the instability is mostly due to the $m = 0$ modes, and that even the spherical mode $l = m = 0$ can be unstable (see cyan long-dashed critical line in Fig. 4.1) bodes ill for superradiance, as these modes can never satisfy the superradiance condition $\omega < m\Omega$ (with ω and Ω respectively the wave and horizon angular frequencies).

One may naively expect the spherical mode $l = m = 0$ not to suffer from a tachyonic instability either, since $\mu^2_{\rm eff} = -\eta\mathcal{G}$ is positive everywhere in a Schwarzschild spacetime when $\eta < 0$ (as considered here). However, the (squared) effective mass for the $l = m = 0$ mode is actually $-\eta\langle 00|\mathcal{G}_{\rm Kerr}|00\rangle$, which only matches the naive estimate $-\eta\mathcal{G}_{\rm Schwarzschild}$ at leading order in spin, correcting it by terms $\mathcal{O}(a^2)$. This explains, in particular, why the spherical mode is stable at low spins.

To further confirm the tachyonic nature of the instabilities, we have conducted the following test. We re-ran our simulations with the (squared) effective mass replaced by its absolute value, $\mu^2_{\rm eff} \to |\mu^2_{\rm eff}|$. This is enough to suppress the instabilities, and further shows that the latter were due to the change of sign of the Gauss-Bonnet invariant close to the horizon. One can also look at the scalar fluxes through the event horizon after the initial transient. In Fig. 4.2, we compare the scalar field's energy flux through the horizon for $\eta = -10M^2$ (blue) vs the same fluxes for minimally

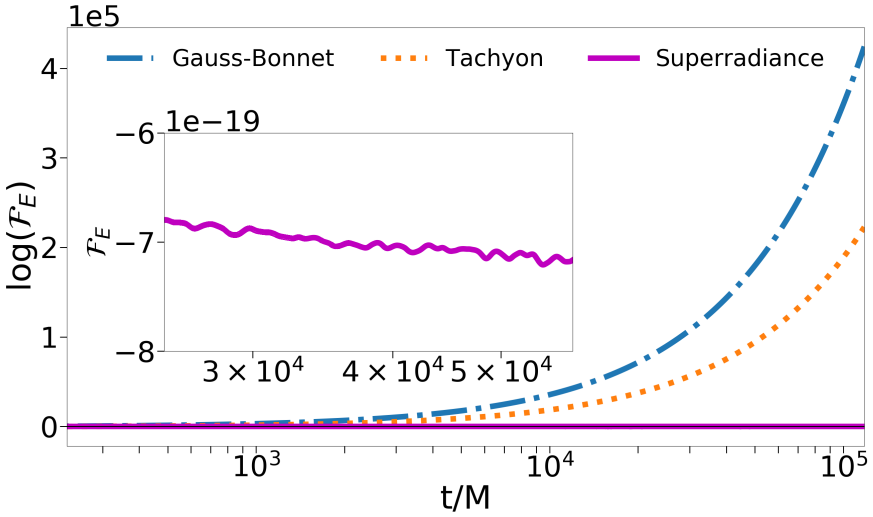

FIGURE 4.2: *Energy flux $\mathcal{F}_E$ through the black hole horizon vs time, for $a = 0.99M$.* The blue, orange and magenta lines correspond respectively to $\eta = -10M^2$, to a tachyonic mass $\mu M = i$, and to a constant, real mass $\mu M = 0.42$. The inset zooms on the constant, real mass flux (of which we show a moving average to decrease the oscillations caused by the dynamics). That flux is negative, signaling energy extraction from the black hole, as expected for superradiant instabilities.

coupled scalar fields with imaginary (orange) and real (magenta) constant masses. Clearly, the flux for a scalar coupled to the Gauss-Bonnet invariant resembles more closely the tachyonic (i.e. imaginary mass) scalar field evolution, both in timescale and sign. Note that the constant, real mass case, whose evolution is unstable due to superradiance, shows a slower growth and negative energy fluxes. The latter are indeed the hallmark of a superradiant instability, which *removes* rotational energy and angular momentum from the black hole.

The most plausible explanation for why Kerr black holes in qsGB do not suffer from superradiant instabilities seems to be the rapid falloff of the Gauss-Bonnet invariant (thus of the effective mass) at large distances, $\mathcal{G}(r \to \infty) \sim 1/r^6$. Scalar perturbations with a position-dependent mass were studied in [517], which showed that a steep decay of the mass with distance quenches the superradiant instability. This happens because the effective potential for scalar perturbations does not develop wells, and thus quasi-bound states, unless the mass remains relatively constant till at least $r \sim 2 - 3M$ [517].

4.4 Conclusions

We have shown that a coupling, with a suitable sign, between a scalar and the Gauss-Bonnet invariant can lead to an instability triggered by rapid rotation. We have also demonstrated that this instability is not related to superradiance, but is instead tachyonic in nature. Nonlinear effects, which our approach does not capture, are expected to quench that instability and lead to a black hole with scalar hair. The process is analogous to the more conventional spontaneous scalarization, but the threshold is controlled by the black hole rotation instead of its curvature.

The action that we use is sufficient for studying the onset of the instability that we have found for black holes. However, the endpoint of this instability, and hence the amount of hair a black hole would carry, will strongly depend on nonlinear (self)interactions. There is no obvious reason to believe that this instability is restricted to black holes, and it could well affect rapidly rotating stars as well. Hence, our results demonstrate that there is a broad class of theories where rotation might control deviations from GR. Our findings also have clear implications for searches of new physics in the strong-field regime. Black hole scalar hair induces vacuum dipole gravitational emission, which is potentially observable in the low frequency inspiral of binary system by gravitational wave interferometers [520, 521], deviations from general relativityin the spectrum of the gravitational wave ringdown [522] or in the electromagnetic spectrum of accretion disks [96], and it may also impact the black hole shadow observed by the Event Horizon Telescope [102].

We stress that we are not aware of any observational upper bounds on η, which we therefore allow here to reach very high values, for illustrative purposes and in order to excite higher modes. Note that slowly rotating black holes in qsGB would be identical to their general relativitycounterpart. Compact stars can scalarize for $\eta < 0$ [428] and hence yield constraints. However, this effect could easily be quenched by adding a coupling between the scalar field and the Ricci scalar [433, 523]. The latter might be necessary to get a sensible cosmology [524], and would have no effect for black holes, thus leaving our analysis unaffected.

Chapter 5

Screened scalar fields around compact stars

5.1 Compact objects in screened modified gravity

Screening mechanisms generally make modifications of gravity elusive and hard to constrain with astrophysical observations. Nonetheless, their efficacy at screening compact stars is typically tested in the static non-relativistic limit, and little work has been done outside these simplifying approximations (e.g. see [525, 526] for the dynamics of k-mouflage). This is also the case for chameleon screening, the robustness of which has only been tested so far in the dynamical Newtonian limit [527], or in the relativistic but static regime [461, 528, 529] (see also [530, 531] for other relevant work on chameleon screening). In this regard, one potential loophole in chameleon screening could be opened by a tachyonic instability developing inside relativistic compact stars. This instability arises in scalar-tensor theories without screening [532], where it leads either to scalarization or alternatively to gravitational collapse [533]. Past work [528, 529] reported instabilities of the chameleon field inside neutron stars that feature a pressure-dominated core. These instabilities were interpreted as due to the chameleon effective potential not having a well defined minimum for the scalar field to relax to, as a consequence of the trace of the matter stress-energy tensor changing sign in the highly-relativistic interior of the stars. Recently, however, Ref. [461] has studied static neutron star solutions coupled to chameleon scalar fields and, in contrast to previous work, found no sign of such instabilities. Instead, they observed that neutron stars with pressure-dominated cores typically present a partial *descreening* in their interior and are linearly stable. Many realistic candidates for the equation of state (EoS) of nuclear matter predict pressure-dominated cores at sufficiently high densities, while agreeing with current experimental constraints [534]. One may therefore place bounds on theories with chameleon screening from observations of the most massive neutron stars.

As our first main contribution, in this work we will confirm and generalize the conclusions obtained in Ref. [461], which are in principle valid only at the level of linear perturbations around static solutions. We will do that by demonstrating numerically the long-term nonlinear stability of neutron star solutions coupled to a chameleon scalar field, which we will henceforth refer to as chameleon neutron stars (CNSs). To our knowledge, these are the first dynamical simulations of the chameleon screening mechanism, thanks to which we confirm that the partial descreening inside pressure-dominated cores leads to stable CNSs that deviate strongly from GR.

As is well know, in GR, radial oscillations of relativistic stars do not source gravitational wave (gravitational wave) emissions (although in principle they can couple to non-radial modes [535–537] and potentially be observable during the post-merger

phase [538–540]). For this reason, they are typically studied only for assessing the stability of neutron star solutions [541–545]. However, in scalar-tensor theories a new family of modes typically appears in association with the additional degree of freedom [546, 547]. These radial modes can source the emission of (scalar) gravitational waves [548] (for instance, during collapse [526, 549–551]). In this work, we study the spectrum of radially perturbed CNSs, characterizing the deviations from general relativity induced by the chameleon field. In addition, we compute the scalar flux radiated by CNSs when oscillating or collapsing to a BH, focusing on the comparison between screened and descreened stars and on the observability with current and future gravitational wave detectors.

This Chapter is organized as follows. In Sec. 5.2 we briefly review chameleon gravity and its screening mechanism. We also discuss the current constraints and the relevance of these theories for cosmological applications. In Sec. 5.3, we discuss the initial data that are used in our simulations and the numerical method employed to produce them. The evolution formalism is presented in Sec. 5.4, where we also discuss the stability of CNSs. In Sec. 5.5 we discuss characteristic radial oscillations of CNSs and in Sec. 5.6 we characterize the monopole emission of oscillating and collapsing CNSs. Finally, in Sec. 5.7 we discuss our conclusions and the future prospects to test chameleon screening with neutron stars. Throughout this Chapter, we use natural units where $\hbar = c = 1$.

5.2 Theoretical framework

5.2.1 Screened modified gravity action

ST theories with environmentally dependent screening, such as symmetron, dilaton or chameleon screening (including certain $f(R)$ models), are described by the following action [552]:

$$S = \int d^4x\sqrt{-g}\left[\frac{M_{\rm pl}^2}{2}R - \frac{1}{2}g^{\mu\nu}\nabla_\mu\phi\nabla_\nu\phi - V(\phi)\right] + S_m[A(\phi)^2 g_{\mu\nu}; \psi_m]\,, \tag{5.1}$$

where g and R are the determinant and Ricci scalar of the *Einstein frame* metric $g_{\mu\nu}$, and $M_{\rm pl} = 1/\sqrt{(8\pi G)}$ is the (reduced) Planck mass. The scalar field ϕ has a self-interaction potential $V(\phi)$, and is coupled to matter (collectively represented by the field ψ_m) through the conformal coupling $A(\phi)$. Because of this coupling, test particles do not follow geodesics of $g_{\mu\nu}$, but ones of the *Jordan frame* metric [309]

$$\tilde{g}_{\mu\nu} \equiv A(\phi)^2 g_{\mu\nu}\,. \tag{5.2}$$

Matter fields in the Jordan frame are minimally coupled to the metric (5.2) and follow its geodesics. Therefore, in this frame one can define a stress-energy tensor,

$$\tilde{T}^m_{\mu\nu} \equiv -\frac{2}{\sqrt{-\tilde{g}}}\left(\frac{\delta S_m}{\delta \tilde{g}^{\mu\nu}}\right)\,, \tag{5.3}$$

and a baryon mass current, $\tilde{J}^\mu$, that are covariantly conserved

$$\tilde{\nabla}_\mu \tilde{J}^\mu = 0\,, \tag{5.4}$$
$$\tilde{\nabla}_\mu \tilde{T}^{\mu\nu}_m = 0\,, \tag{5.5}$$

where $\tilde{\nabla}$ indicates the covariant derivative compatible with the Jordan frame metric (5.2). In this work, the matter content of the spacetime is modeled as a perfect fluid in the Jordan frame, with stress-energy tensor

$$\tilde{T}^{\mu\nu}_m \equiv (\tilde{\epsilon} + \tilde{p})\tilde{u}^\mu \tilde{u}^\nu + \tilde{p} g^{\mu\nu}\,. \tag{5.6}$$

The Jordan-frame fluid variables in this equation (total energy density, $\tilde{\epsilon}$, and isotropic pressure, $\tilde{p}$) are defined as measured by an observer comoving with the fluid elements with four-velocity $\tilde{u}^\mu$.

By defining the Einstein-frame stress-energy tensor as $T^{\mu\nu}_m \equiv -2/\sqrt{-g}\,(\delta S_m/\delta g^{\mu\nu})$ and comparing the latter with (5.3), one obtains the relation $T^m_{\mu\nu} = A(\phi)^2 \tilde{T}^m_{\mu\nu}$. From this conformal transformation, and from $u^\mu = A(\phi)\tilde{u}^\mu$ (obtained from the normalization $g_{\mu\nu}u^\mu u^\nu = -1$) one can read the dictionary between fluid variables in the two frames, $\epsilon = A(\phi)^4\tilde{\epsilon}$ and $p = A(\phi)^4\tilde{p}$. The conserved Jordan-frame baryon mass current, $\tilde{J}^\mu \equiv \tilde{\rho}\tilde{u}^\mu$, where $\tilde{\rho}$ is the rest-mass density, is related to the corresponding Einstein-frame quantity by $J^\mu = A(\phi)^5\tilde{J}^\mu$ [412]. Note that in the Einstein frame covariant conservation of the stress-energy tensor and baryon mass current is lost, and Eqs. (5.4), (5.5) are replaced by:

$$\nabla_\mu J^\mu = \frac{d\ln A(\phi)}{d\phi} J^\mu \nabla_\mu \phi\,, \tag{5.7}$$
$$\nabla_\mu T^{\mu\nu}_m = \frac{d\ln A(\phi)}{d\phi} T_m \nabla^\nu \phi\,, \tag{5.8}$$

where $T^m = g^{\mu\nu}T^m_{\mu\nu}$ is the trace of the stress-energy tensor.

Variation of the action (5.1) with respect to the Einstein metric gives the modified Einstein field equations:

$$G_{\mu\nu} = 8\pi G\left(T^\phi_{\mu\nu} + T^m_{\mu\nu}\right)\,, \tag{5.9}$$

which are sourced by the stress-energy tensor of the scalar field

$$T^\phi_{\mu\nu} \equiv \nabla_\mu\phi\nabla_\nu\phi - g_{\mu\nu}\left(\frac{1}{2}\nabla_\sigma\phi\nabla^\sigma\phi + V(\phi)\right)\,. \tag{5.10}$$

The scalar field equation is obtained by variation of (5.1) with respect to ϕ:

$$\Box\phi = \frac{dV(\phi)}{d\phi} - \frac{d\ln A(\phi)}{d\phi}T^m\,, \tag{5.11}$$

which is a generalized wave equation on curved spacetime with $\Box \equiv g^{\mu\nu}\nabla_\mu\nabla_\nu$, sourced by the scalar self-interaction and by the coupling to the Einstein-frame trace of the stress-energy tensor.

Specifying $V(\phi)$ and $A(\phi)$ one specializes to a particular model of chameleon gravity. In this work, we will focus on the classic chameleon models that feature an inverse power-law self-interaction potential in combination with an exponential

conformal coupling to matter, i.e.:

$$V(\phi) = \frac{\Lambda^{n+4}}{\phi^n}\,, \qquad A(\phi) = \exp\left(\alpha_0 \phi\right)\,, \tag{5.12}$$

where Λ is the chameleon energy scale and α_0 is the dimensionful conformal coupling. Plugging (5.12) into (5.11), one can see that the chameleon scalar field obeys an effective potential

$$V_{\rm eff}(\phi) \equiv \frac{\Lambda^{n+4}}{\phi^n} - \frac{1}{4} e^{4\alpha_0\phi}\tilde{T}_m\,. \tag{5.13}$$

In this project, we consider only the simplest chameleon model $n = 1$. The scalar configuration that minimizes the potential (5.13), $\bar{\phi}$, can be found by requiring $dV_{\rm eff}/d\phi|_{\bar{\phi}} = 0$ or, equivalently, by solving the trascendental equation $\phi^2 e^{4\alpha_0\phi} + \Lambda^5/(\alpha_0\tilde{T}_m) = 0$, which in the limit $\phi \ll M_{\rm pl}$ yields

$$\bar{\phi} \simeq \frac{\Lambda^{5/2}}{\sqrt{-\alpha_0\tilde{T}_m}}\,. \tag{5.14}$$

From the effective potential (5.13) one can determine the chameleon effective mass,

$$m^2_{\rm eff} \equiv \frac{d^2V_{\rm eff}}{d\phi^2} = \frac{2\Lambda^5}{\phi^3} - 4\alpha_0^2 e^{4\alpha_0\phi}\tilde{T}_m\,. \tag{5.15}$$

5.2.2 Chameleon screening

The field configuration that minimizes the effective potential (5.13) strongly depends on the ambient matter distribution: in denser regions the chameleon will settle to lower field values and scalar perturbations around the minimum will feature a larger effective mass (5.15). As a result, the chameleon fifth force will be short-range in high-density environments (i.e. stars, clusters or galaxies), while being effectively long-range on cosmological scales. In addition, a *thin-shell effect* will further suppress the fifth force around compact objects (e.g. neutron stars [453]).

As an illustrative example, let us consider a non-relativistic, static and spherical star of mass M and radius R, surrounded by a medium (e.g. the interstellar medium, or even the cosmological background) with lower density, $\tilde{\epsilon}_\infty$. Inside the star and far from it, the chameleon will settle to different field values. The large effective mass, corresponding to the high density in the interior, will suppress exponentially the scalar perturbations and keep the chameleon field small up to a *screening radius*, r_s. The latter can be defined as the distance from the center at which the field starts rolling towards the "exterior" minimum. Inside the screening radius, the gradient of the scalar field is negligible and the fifth force (proportional to the gradient) reactivates only outside of it, $r \gtrsim r_s$. One can show that sufficiently far away from the star, at $r \gg R_{star}$, the scalar field solution is

$$\phi \simeq \phi_\infty - \left(\frac{Q}{4\pi M_{\rm pl}}\right)\frac{Me^{-m_\infty(r-R_{star})}}{r}\,, \tag{5.16}$$

with Q being the (dimensionless) effective scalar charge of the object and m_∞ the chameleon effective mass (5.15) at large distances. From (5.16) one can notice that the chameleon mass term introduces an exponential suppression of the "Yukawa" type.

In the non-relativistic Newtonian limit the charge reads $QM \simeq \alpha_0 M_{\rm pl}(M - M(r_s))$, where $M(r_s)$ is the gravitational mass contained inside the screening radius [452, 553]. When the star is efficiently screened, i.e. $r_s \sim R$, the scalar charge is only sourced by a "thin shell" of matter between r_s and R, and the fifth force is additionally suppressed by the factor $Q \ll 1$ [452, 453, 554, 555]. As long as $T < 0$ (which in the non-relativistic limit is automatically satisfied), the chameleon effective potential (5.13) has a minimum in the stellar interior, and this thin-shell effect is present. However, in the pressure-dominated core of very dense neutron stars, T can change sign, leading to a partial breakdown of chameleon screening [461]. In this project, we will explore the dynamics of this breakdown, or *descreeeing*.

5.2.3 Constraints

Although it has been demonstrated that chameleon scalar fields cannot give rise to self-acceleration [556], they could still be relevant for cosmological applications in combination with a cosmological constant, as both could have a common origin at high-energies [557]. Indeed, the low-energy effective theories derived from string theory are generically populated with light scalar fields and the chameleon screening might be a viable mechanism to hide their presence in experiments. In this perspective, relatively recent work has found that chameleon models are compatible with the swampland program, provided that a lower bound on the conformal coupling is satisfied [558].

However, while not completely ruled out yet, classic chameleon models are constrained by a variety of observations (see [438, 555, 559] for reviews). The viable region of the parameter space of the most studied chameleon model (i.e. (5.13) with $n = 1$) is $\alpha_0 M_{\rm pl} \lesssim O(10^2)$ for energy scales $\Lambda \lesssim \Lambda_{\rm DE}$ [555], where $\Lambda_{\rm DE} = 2.4$ meV is the Dark Energy scale. Further constraints may come from the scales of galaxies/galaxy clusters, although they have not been worked out in detail [560], and from short-range experiments [561].

5.3 Initial Data

In this section, we derive static and spherically symmetric solutions for CNSs, by generalizing the Tolman-Oppenheimer-Volkoff (TOV) equations to the chameleon case and solving them numerically. We also discuss the EoS of nuclear matter and the boundary conditions used, and present results for the mass-radius relation of CNSs.

5.3.1 Chameleon-TOV equations

To obtain the modified TOV equations, we adopt the following spherically symmetric ansatz (in polar coordinates):

$$ds^2 = -e^{2\nu(r)}dt^2 + e^{2\lambda(r)}dr^2 + r^2(d\theta^2 + \sin^2\theta d\varphi^2)\,. \tag{5.17}$$

By inserting the ansatz (5.17) in the chameleon field equations (5.9) and (5.11), one obtains

$$\frac{d\nu}{dr} = \left(\frac{e^{2\lambda}-1}{2r}\right) + 4\pi G r e^{2\lambda}\left(e^{4\alpha_0\phi}\tilde{p} + \frac{\Lambda^5}{\phi} - \frac{e^{-2\lambda}}{2}\sigma^2\right), \tag{5.18}$$

$$\frac{d\lambda}{dr} = \left(\frac{1-e^{2\lambda}}{2r}\right) + 4\pi G r e^{2\lambda}\left(e^{4\alpha_0\phi}\tilde{\epsilon} - \frac{\Lambda^5}{\phi} - \frac{e^{-2\lambda}}{2}\sigma^2\right), \tag{5.19}$$

$$\frac{d\sigma}{dr} = \left(\frac{d\lambda}{dr} - \frac{d\nu}{dr} - \frac{2}{r}\right)\sigma - e^{2\lambda}\left(\alpha_0 e^{4\alpha_0\phi}(3\tilde{p}-\tilde{\epsilon}) + \frac{\Lambda^5}{\phi^2}\right), \tag{5.20}$$

$$\frac{d\phi}{dr} = \sigma, \tag{5.21}$$

$$\frac{d\tilde{p}}{dr} = -(\tilde{p}+\tilde{\epsilon})\left(\frac{d\nu}{dr} + \alpha_0\sigma\right). \tag{5.22}$$

The differences from the TOV equations ingeneral relativity depend on the conformal coupling α_0 and the chameleon energy scale Λ, both introduced in Eq. (5.12). This system of equations can be solved numerically by using suitable boundary conditions and choosing an adequate EoS for nuclear matter, as we explain in detail in the next subsection.

5.3.2 Equation of state and boundary conditions

To close the system of equations (5.18), (5.19), (5.20), (5.21) and (5.22), a relation between the fluid variables must be provided. We choose to describe the stellar interior with a polytropic EoS

$$\tilde{p}(\tilde{\rho}) \equiv K\tilde{\rho}^{\Gamma}, \qquad \tilde{\epsilon}(\tilde{p}) = \frac{\tilde{p}}{\Gamma-1} + \left(\frac{\tilde{p}}{K}\right)^{1/\Gamma}, \tag{5.23}$$

where K is the polytropic constant and Γ is the (constant) adiabatic index. This EoS, while approximate, allows for reproducing the relativistic effects found in pressure-dominated neutron star cores (e.g., see [533] for an application to scalarized neutron stars) for appropriately stiff polytropic coefficients [534]. In this work, we generally set $\Gamma = 3$, which approximates the polytropic exponent of more realistic EoSs [562], and $K \simeq 6.9\times10^4 G^6 M_\odot^4 c^{-10}$. In GR, this EoS yields a maximum mass $M_{\rm max} \simeq 2.03 M_\odot$, consistent with current bounds [563]. As we will see, this stiff EoS yields static stars with a partially descreened interior. We will also use a different polytropic EoS with $\Gamma = 2$ and $K = 123\ G^3 M_\odot^2 c^{-4}$ to obtain CNSs with similar baryon mass but with a completely screened interior, for comparison (see section 5.5).

Outside the star, $r \geq R_{star}$, we assume a homogeneous atmosphere, $\tilde{\epsilon} = \tilde{\epsilon}_\infty =$ const., with "cosmological" EoS, $\tilde{p} = -\tilde{\epsilon}_\infty$, corresponding to a cosmological constant. Chameleon models with a runaway potential such as that of Eq. (5.12) do not admit a constant scalar field solution in pure vacuum, and for this reason a homogeneous atmosphere is required to have a well-behaved exterior solution. In fact, it is easy to see that with this cosmological atmosphere the field equations allow for the asymptotic solution $\tilde{\epsilon} = \tilde{\epsilon}_\infty$, $\tilde{p} = -\tilde{\epsilon}_\infty$, $\phi = \phi_\infty$ at $r \gg R_{star}$, with R_{star} being the radius of the star. Once fixed the atmosphere density, $\tilde{\epsilon}_\infty$, the asymptotic chameleon configuration, ϕ_∞, is determined by (5.14), where $\tilde{T}_m = -4\tilde{\epsilon}_\infty$. Consistently, the

metric is then given (asymptotically) by the Schwarzschild-de Sitter solution

$$ds^2 = -f(r)dt^2 + f(r)^{-1}dr^2 + r^2(d\theta^2 + \sin^2\theta d\varphi^2)\,, \tag{5.24}$$

where $f(r) \equiv 1 - 2GM/r - b\,r^2/3$, with M the gravitational mass and $b = 8\pi G V_{\rm eff}(\tilde{\epsilon}_\infty)|_{\phi_\infty}$. Instead, the (Jordan-frame) baryon mass of the star is defined as

$$M_{bar} \equiv \int d^3x \sqrt{-\tilde{g}}\tilde{J}^0\,. \tag{5.25}$$

Other prescriptions for the atmosphere are possible, for instance in terms of a non-relativistic homogeneous dust distribution modeling the interstellar medium, but the advantage of choosing a cosmological EoS is that it yields a simple exterior solution [461].

5.3.3 Static Chameleon Neutron Stars

Static and spherically symmetric CNS solutions are obtained numerically by integrating outwards the modified TOV equations starting from the center of the star, where we impose regular boundary conditions. To implement the Schwarzschild-de Sitter boundary conditions [Eq. (5.24)] far away from the star, we use a direct shooting method.

We consider atmosphere densities of order $\tilde{\epsilon}_\infty \sim 10^{-6}$–$10^{-4}\rho_{\rm nuc}c^2$, where $\rho_{\rm nuc} = 1.7\times10^{14}$ g/cm^3 is a typical nuclear density. These are the lowest atmosphere density values that our direct shooting method can deal with, and our results and conclusions are robust to changes of up to one order of magnitude in this parameter. Notice that this value is many orders of magnitude higher than the background cosmological density, $\rho_c \simeq 1.0\times10^{-23}$ g/cm^3 [1]. An alternative realistic atmosphere value that could be considered is given by the density of the interstellar medium (in a giant molecular cloud [565]), $\rho_{GMC} \simeq 1.7\times10^{-20}$ g/cm^3.

For the chameleon action parameters, we set $\alpha_0 M_{\rm pl} = 1$ and $\Lambda \simeq 73$–175 GeV. Note that these chameleon energy scales are inconsistent with current bounds [555], but lower (and viable) values of Λ are impossible to explore with our shooting method. This is because to solve for CNSs we have to utilize code units adapted to the problem, where $G = c = M_\odot = 1$. Reinstating all $\hbar$, c and G factors one obtains $\Lambda^5 = (8\pi)^{-3/2}(M_{\rm pl}/\hbar c)^2(GM_\odot/c^2)^2(\bar{\Lambda}/M_{\rm pl})^5 \approx 2.6\times10^{72}\,(\bar{\Lambda}/M_{\rm pl})^5$, and realistic values of Λ therefore become tiny and hard to handle numerically. This is a problem commonly encountered when simulating compact stars in theories with screening (see e.g. [441, 461, 526]), and it stems from the separation between the cosmological scale Λ and that of neutron stars.

Mass-radius curves for different values of Λ are shown in Fig. 5.1, where we also show thegeneral relativity case ($\Lambda = 0$). These curves are comprised of stable and unstable stars, which lie, respectively, on the right of the maximum mass configuration (red star tokens) and on its left. Additionally, solutions between the red star token and the cyan round token have $T > 0$ (pressure dominated core).

As mentioned previously, in chameleon gravity, a pressure-dominated core can produce a partial *descreening*. As can be observed from Fig. 5.2, that consists of a re-activation of the scalar gradient (and thus of the fifth force) in the stellar interior, where it would normally be suppressed by screening. For fixed mass, screened CNSs are typically smaller in size and more compact than neutron stars in GR. However,

[1] The critical cosmological density is $\rho_c = 1.8788\times10^{-23}h^2$ g/cm^3: for $H_0 = 0.732 \pm 1.3$ km s^{-1} Mpc^{-1} [564], one obtains the estimate above.

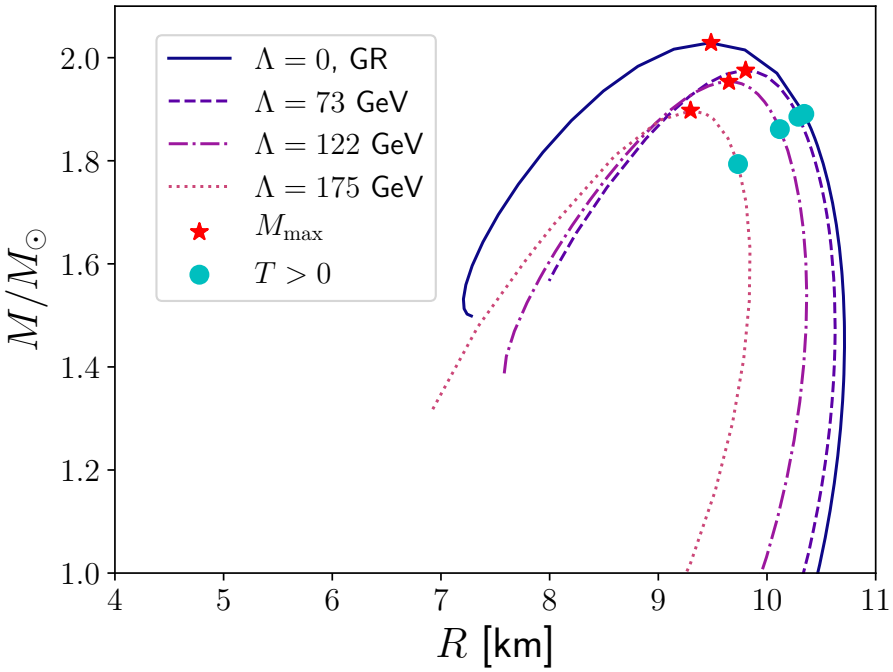

FIGURE 5.1: *Mass-radius plots for varying chameleon energy scales.* Dotted, dashed-dotted and dashed lines correspond to CNSs with $\alpha_0 M_{\rm pl} = 1$: darker lines correspond to lower chameleon energy scales. The darkest solid line corresponds to neutron star solutions in GR ($\alpha_0 = 0$ and $\Lambda = 0$). Red star tokens indicate the solutions with maximum mass. Cyan round tokens, instead, indicate the lightest star featuring a pressure-dominated ($T > 0$) core: stable CNSs with a partially descreened core are those between the star and round tokens.

in the limit $\Lambda \to 0$ screened solutions tend smoothly togeneral relativity configurations. Descreened solutions, instead, feature strong deviations, as can be observed from the fact that the maximum mass is typically lower than in general relativity and in the limit $\Lambda \to 0$ the most massive general relativity configuration is not recovered smoothly. Moreover, the branch of unstable solutions shows the strongest structural deviations from GR, even for smaller chameleon energy scales Λ.

5.4 Time evolution in spherical symmetry

In this section, we explain in detail how we perform fully non-linear evolutions of CNSs and summarize our numerical methods. We present results for the dynamics of CNS stars by analyzing their stability. We have considered screened and descreened CNSs, under perturbations that trigger either oscillations or collapse to a BH.

5.4.1 Evolution equations

The fully non-linear evolution of CNS stars is followed in the Einstein frame, where the equations of motion for CNSs are given by the Einstein equations (5.9); the

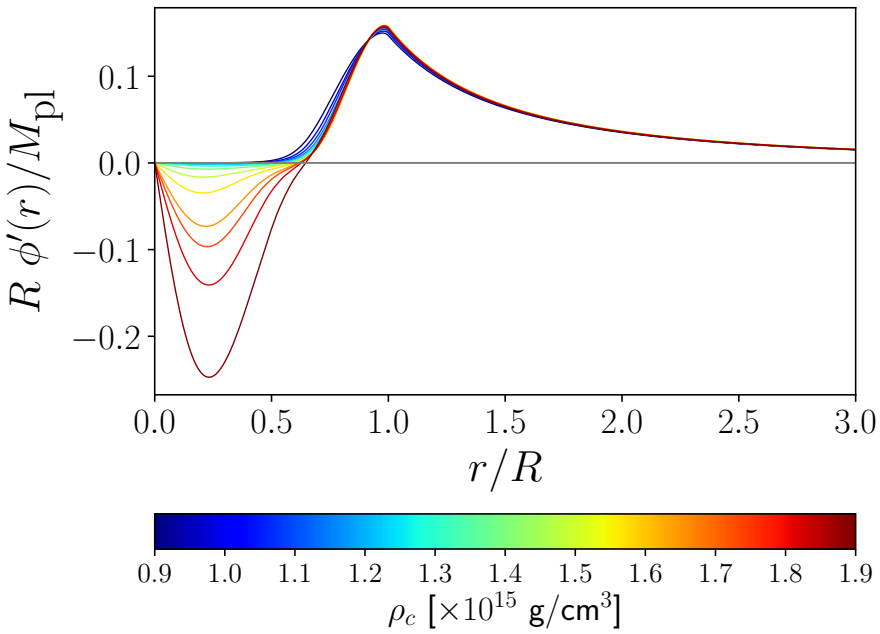

FIGURE 5.2: *Partial descreening of CNSs.* Gradient of the chameleon field around CNS solutions with varying central densities: less dense stars (blue end of the color scale) are screened in their interior, as can be seen from the suppression of the scalar field gradient; stellar solutions with higher central densities (red end of the color scale) feature a scalar field gradient (proportional to the chameleon-propagated fifth force) reactivated in their interior as a result of relativistic effects, i.e. the pressure-dominated cores.

conservation laws for the Einstein-frame baryon mass current [Eq. (5.7)] and stress-energy tensor [Eq. (5.8)]; and the scalar field equation (5.11). We restrict our study to spherical symmetry and decompose the spacetime tensors into their space (radial) and time components.

We consider the following line element:

$$ds^2 = -\alpha^2(t,r)dt^2 + g_{rr}(t,r)dr^2 + r^2 g_{\theta\theta}(t,r)d\Omega^2 \ , \tag{5.26}$$

where $\alpha(t,r)$ is the lapse function, $g_{rr}(t,r)$ and $g_{\theta\theta}(t,r)$ are positive metric functions, and $d\Omega^2 = d\theta^2 + \sin^2\theta d\varphi^2$ is the solid angle element. These quantities are defined on each leaf Σ_t of the spatial foliation, which has normal vector $n_\mu = (-\alpha, 0)$ and extrinsic curvature $K_{ij} \equiv -\frac{1}{2}\mathcal{L}_n\gamma_{ij}$. Here, $\mathcal{L}_n$ is the Lie derivative along n^μ and γ_{ij} is the metric induced on each leaf.

The Einstein equations (5.9) are written as an evolution system by using the Z3 formulation in spherical symmetry [566, 567]. We can express Eq. (5.9) as a first order system by introducing first derivatives of the fields as independent variables, namely

$$A_r = \frac{1}{\alpha}\partial_r\alpha \,, \quad D_{rr}{}^r = \frac{g^{rr}}{2}\partial_r g_{rr} \,, \quad D_{r\theta}{}^\theta = \frac{g^{\theta\theta}}{2}\partial_r g_{\theta\theta} \,,$$

and write the system of equations in the conservative form

$$\partial_t \mathbf{U} + \partial_r F(\mathbf{U}) = \mathcal{S}(\mathbf{U}) \,, \tag{5.27}$$

where $\mathbf{U} = \{\alpha \,, g_{rr} \,, g_{\theta\theta} \,, K_r{}^r \,, K_\theta{}^\theta \,, A_r \,, D_{rr}{}^r \,, D_{r\theta}{}^\theta \,, Z_r \}$ is a vector containing the full set of evolution fields. In the Z3 formulation, the momentum constraint has been included in the evolution system by considering an additional vector Z_i as an evolution field [568]. In fact, the Z_r component is the time integral of the momentum constraint. In addition, $F(\mathbf{U})$ is the radial flux and $\mathcal{S}(\mathbf{U})$ is a source term. The evolution equations for the Z3 formulation can be found explicitly in Ref. [569]. A gauge condition for the lapse is required to close the system. We use the singularity-avoidance $1+\log$ slicing condition $\partial_t \alpha = -2\alpha \, \mathrm{tr}K$, where $\mathrm{tr}K = K^r_r + 2K^\theta{}_\theta$, see [570].

In addition, the equations of motion for the fluid [Eq. (5.7)-(5.8)] and for the scalar field [Eq. (5.11)] are written in conservative form:

$$\partial_t(\zeta D) = -\partial_r[\zeta D \alpha v^r] - \alpha\zeta D \left(\frac{2}{r} v^r - \alpha_0 (v^r \Phi + \sqrt{g^{rr}}\Pi)\right) \,, \tag{5.28}$$

$$\partial_t(\zeta U) = -\partial_r[\zeta \alpha S^r] + \alpha\zeta \left[S^r{}_r K^r{}_r + 2S^\theta{}_\theta K^\theta{}_\theta - S^r \left(A_r + \frac{2}{r}\right) - \alpha_0 T \sqrt{g^{rr}}\Pi\right] \,, \tag{5.29}$$

$$\partial_t(\zeta S_r) = -\partial_r[\zeta \alpha S^r{}_r] + \alpha\zeta \left[S^r{}_r \left(D_{rr}{}^r - \frac{2}{r}\right) + 2S^\theta{}_\theta \left(D_{r\theta}{}^\theta + \frac{1}{r}\right) - U A_r + \alpha_0 T \Phi\right] \,, \tag{5.30}$$

$$\partial_t \phi = \frac{\alpha}{\sqrt{g_{rr}}} \Pi \,, \tag{5.31}$$

$$\partial_t \Phi = \partial_r \left[\frac{\alpha}{\sqrt{g_{rr}}} \Pi\right] \,, \tag{5.32}$$

$$\partial_t \Pi = \partial_r \left[\frac{\alpha}{\sqrt{g_{rr}}} \Phi\right] + \frac{\alpha}{\sqrt{g_{rr}}} \left(2\left(D_{r\theta}{}^\theta + \frac{1}{r}\right)\Phi + 2\sqrt{g_{rr}} K_\theta{}^\theta \Pi - g_{rr} \frac{dV_{\rm eff}}{d\phi}\right) \,, \tag{5.33}$$

where $\zeta = \sqrt{g_{rr}} g_{\theta\theta}$ and

$$\Phi \;=\; \partial_r \phi \,, \qquad \Pi = \frac{\sqrt{g_{rr}}}{\alpha} \partial_t \phi \,. \tag{5.34}$$

Note that Eqs. (5.28)-(5.30) are given in terms of the *conserved* quantities $\{D, U, S_r\}$, which are defined in terms of the physical (or *primitive*) variables, i.e.: fluid pressure p, rest-mass density ρ, specific internal energy ξ [2], radial velocity of the fluid v^r, and the enthalpy of the fluid, $h \equiv \rho(1+\xi) + p$. The conserved quantities are explicitly defined as follows:

$$D \;=\; \rho W \,, \;\; U = hW^2 - p \,, \;\; S_r = hW^2 v_r \,, \tag{5.35}$$

$$S_r{}^r \;=\; hW^2 v_r v^r + p \,, \;\; S_\theta{}^\theta = p \,, \;\; T = -h + 4p \,, \tag{5.36}$$

with $W^2 = 1/(1 - v_r v^r)$ the Lorentz factor, and $S_r{}^r$ and $S_\theta{}^\theta$ the spatial projections of the stress energy tensor of the fluid in the Einstein frame. Finally, to recover the physical fields $\{\rho, \xi, p, v^r\}$ during the evolution, the algebraic relation (5.35) has to be inverted, which involves solving a nonlinear equation at each time-step. During this

[2] Note that this quantity must not be confused with the (total) energy density, ϵ. The connection between the too is given by the relation $\xi = \epsilon/\rho - 1$, from which it becomes clear that ξ is adimensional.

process, we employ an ideal-gas EoS $P = (\Gamma - 1)\rho\xi$ (see Appendix B in Ref. [571]), with the appropriate Γ depending on the CNS simulation, as explained in Sec. 5.3.

5.4.2 Implementation

The one-dimensional (1D) numerical code used in this work is an extension of the one presented in Ref. [571] for fully non-linear simulations of fermion-boson stars, and used in Refs. [525, 566, 572, 573] to study the dynamics of BHs, boson stars, anisotropic stars and neutron stars with kinetic screening mechanism. As initial data, we use the static CNS solutions discussed in Sec. 5.3, transformed from the areal coordinates of Eq. (5.17) to the maximal isotropic coordinates, in which the line element is given by

$$ds^2 = -\alpha^2(r)dt^2 + \psi^4(r)(dr^2 + r^2 d\Omega^2) \,, \tag{5.37}$$

being ψ the conformal factor.

We have used a high-resolution shock-capturing finite-difference (HRSC) scheme, described in Ref. [566], to discretise the spacetime, the scalar field and the fluid matter fields. In particular, this method can be viewed as a fourth-order finite difference scheme plus third-order adaptive dissipation. The dissipation coefficient is given by the maximum propagation speed at each grid point. The method of lines is used to perform the time evolution through a third-order accurate strong stability preserving Runge-Kutta integration scheme, with a Courant factor of $\Delta t/\Delta r = 0.25$, so that the Courant-Friedrichs-Levy condition imposed by the principal part of the system of equations is satisfied. Most of the simulations presented in this work have been performed with spatial resolutions of $\Delta r = \{0.005, 0.0025, 0.00125\}\ M_\odot$, in a domain with outer boundary located between $r = 500M_\odot$ and $r = 1000M_\odot$. We have verified convergence of results with increasing resolution as well as their robustness against changes in the position of the outer boundary. We use maximally dissipative boundary conditions for the spacetime variables, and outgoing boundary conditions for the scalar field and for the fluid matter fields.

5.4.3 Screened and descreened CNSs

To test the stability of CNSs, we have first evolved the initial data described in Sec. 5.3, subjected only to the small perturbations given by truncation errors. In addition, we have tested the migration of CNSs from the unstable to the stable branch of solutions. In the subsections below we report and discuss examples of such tests. Finally, we discuss the results from simulations of gravitational collapse to a BH. All results shown in this section have been produced for the parameter choice $(\Lambda, \tilde{\epsilon}_\infty) = (175\ \text{GeV}, 6.5 \times 10^{10}\ \text{g/cm}^3)$.

Stability

In Fig. 5.3 we show the time evolution of the central density (upper panel) and central scalar field (bottom panel) for two CNSs, one with complete screening (solid magenta line) and one with partial descreening in the core (dash-dotted cyan line). The first star has a lighter gravitational mass $M = 1.72M_\odot$ and initial (Jordan-frame) central density $\rho_c \simeq 1.38 \times 10^{15}\ \text{g/cm}^3$. The descreened star is heavier, with a mass of $M = 1.84M_\odot$ and initial central density $\rho_c \simeq 1.57 \times 10^{15}\ \text{g/cm}^3$. The simulations were conducted on a grid that extends up to $r = 1000M_\odot$ with a spacing as fine as

$\Delta r = 0.0025 M_\odot$ for the screened star. For simulations of the descreened star, however, we have doubled the number of points of our spatial grid, which correspond to $\Delta r = 0.00125 M_\odot$. We have observed that simulations of descreened stars are more challenging, as higher resolutions are typically needed to keep the numerical dissipation under control during the evolution. We interpret this technical issue as stemming again from the separation between stellar and cosmological scales.

Both stars were evolved in time with no other perturbation but the one introduced by truncation errors: their stability is manifest in Fig. 5.3, which shows that the central density and central scalar field remain constant over time.

Migration

The migration test is a standard diagnostics tool utilized in general relativity to characterize the (in)stability of neutron star solutions (e.g., see [574–576]): depending on the initial perturbation [577], solutions that lie on the unstable branch (i.e. to the left of the maximum mass configuration in mass-radius plots such as Fig. 5.1) can either collapse to a BH or undergo a series of wide oscillations and migrate towards a solution on the stable branch (with approximately the same mass). In our simulations, migration of highly compact and unstable CNSs is induced via small perturbations given by the truncation error. An example of migration is given in Fig. 5.4, where a star with initial central density $\rho_c \simeq 1.87 \times 10^{15}$ g/cm^3 can be seen undergoing large dampened oscillations, which eventually relax it to a stable descreened star with approximately the same gravitational mass $M = 1.88 M_\odot$ (modulo a small loss due to numerical dissipation) and central density $\rho_c \simeq 1.66 \times 10^{15}$ g/cm^3.

Spherical collapse

We have conducted simulations of spherical collapse to BHs, which are another standard benchmark for numerical relativity simulations of neutron stars. The collapse has been induced by an initial pressure gradient up to ten percent. We illustrate the results of this test by discussing the case of a collapsing descreened CNS with gravitational mass $M = 1.89 M_\odot$ and initial central density $\rho_c = 1.70 \times 10^{15}$ g/cm^3. In Fig. 5.5, we show the time evolution of the density, chameleon field and lapse at the center of the collapsing star. As matter collapses to the center of the star, the density and pressure in the core grow, pushing the chameleon field down its effective potential (i.e. to higher values). This is counterintuitive, as the minimum of the effective potential (5.13) moves to larger ϕ when the density increases, as long as the star remains non-relativistic. However, this behavior breaks down when the configuration becomes relativistic, as a result of the change of sign of T_m. Indeed, for $T_m > 0$ the effective potential has no minimum, and the scalar field rolls down to larger and large values.

The lapse decreases to zero and, as a consequence of the $1 + \log$ slicing coordinate choice that we employ, the time evolution of matter in the collapsing core is effectively frozen. In Fig. 5.6, we show time snapshots of the radial profile of the lapse and chameleon scalar field. Inside the star, as the lapse goes to zero an apparent horizon (black dots) forms and slowly expands, until it eventually engulfs the whole matter content. While the chameleon field inside the apparent horizon grows as a result of the (runaway) effective potential, outside the horizon it slowly relaxes to the exterior configuration minimizing the effective potential in the presence of an atmosphere. No instabilities develop during collapse outside the apparent horizon, and the end state is therefore a BH with a trivial scalar field solution.

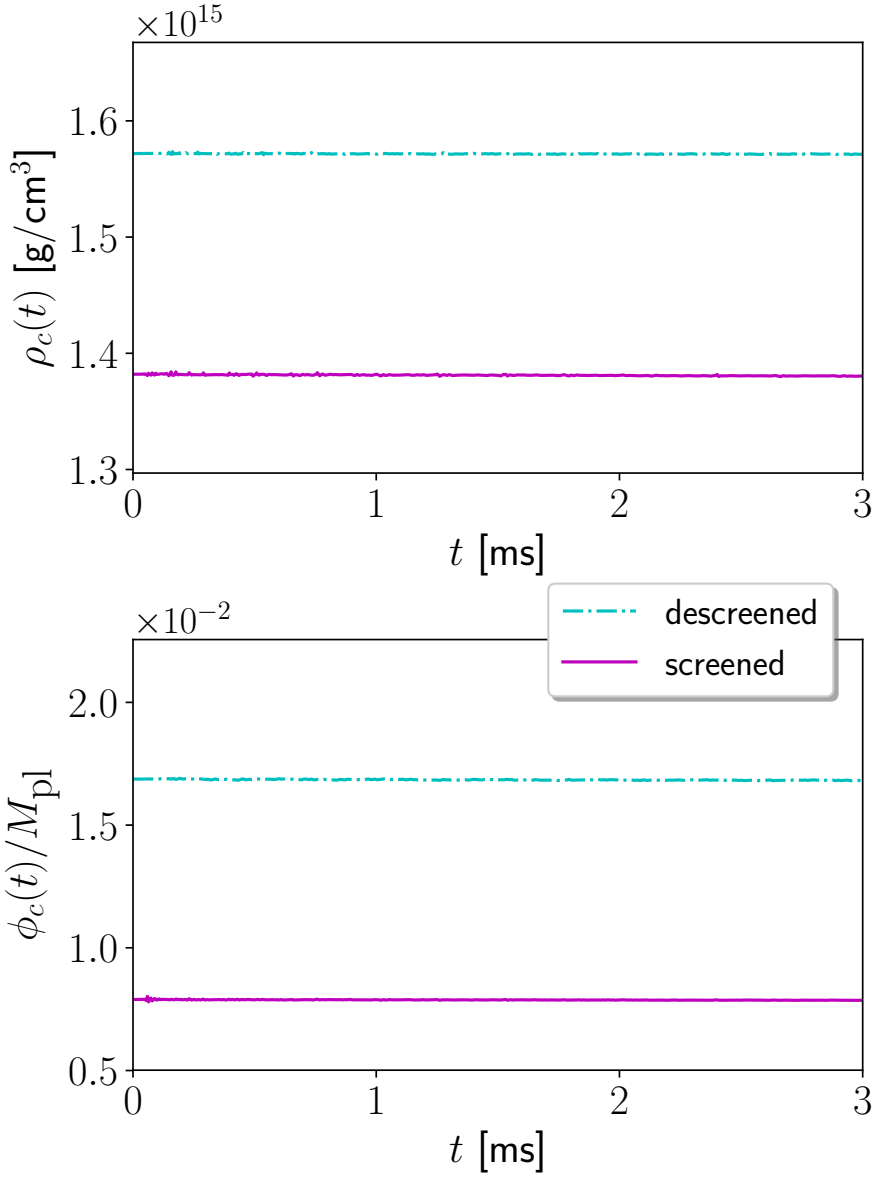

FIGURE 5.3: *Stability of CNS.* Top panel: $\rho_c(t) \equiv \tilde{\rho}(t, r = 0)$ (Jordan frame) vs time. Bottom panel: $\phi_c(t) \equiv \phi(t, r = 0)$ vs time. The (magenta) solid line corresponds to a screened CNS with initial central density $\rho_c \simeq 1.38 \times 10^{15}$ g/cm^3. The (cyan) dash-dotted line corresponds to a descreened CNS with initial central density $\rho_c \simeq 1.57 \times 10^{15}$ g/cm^3. The matter and chameleon field configurations are stable against small perturbations given by truncation errors.

5.5 Radial oscillations

In this section, we analyze the spectrum of the radial oscillations of spherically symmetric CNSs, and compare to the oscillation spectrum of neutron stars with similar gravitational masses in GR. The CNSs have been produced with the parameter choice $(\Lambda, \tilde{\epsilon}_\infty) = (175 \text{ GeV}, 6.5 \times 10^{10} \text{ g/cm}^3)$. As a first step, we test the accuracy of our code by producing a neutron star in GR, with gravitational mass $M = 1.4 M_\odot$

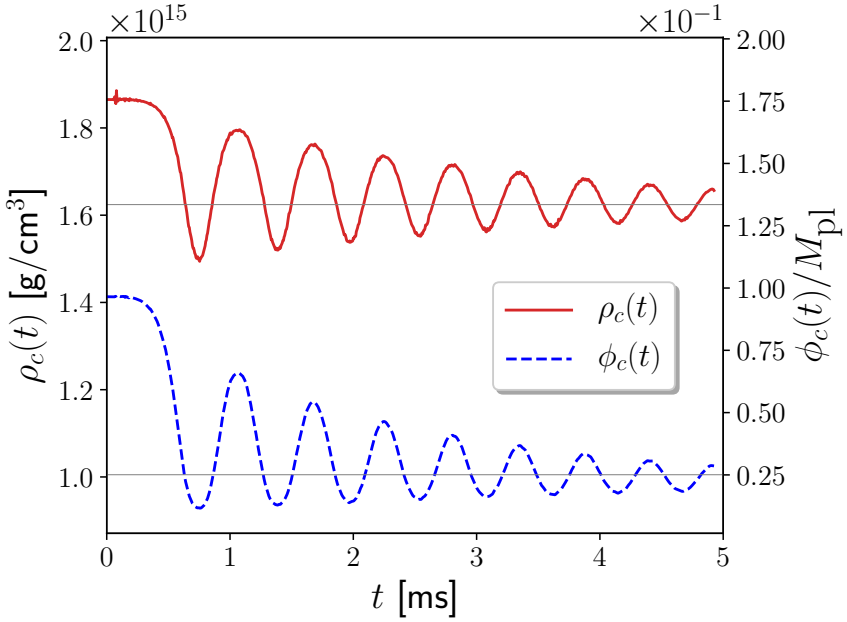

FIGURE 5.4: *Migration test*. The time evolution of the (Jordan-frame) central density $\rho_c(t) \equiv \tilde{\rho}(t, r = 0)$ (red solid line) and central scalar field $\phi_c(t) \equiv \phi(t, r = 0)$ (blue dashed line), for an unstable and partially descreened CNS with gravitational mass $M \simeq 1.88 M_\odot$ and $\rho_c \simeq 1.87 \times 10^{15}$ g/cm^3. The star is expanding in volume and relaxes through large dampened oscillations to a stable descreened CNS with the same mass, but lower central density $\rho_c \simeq 1.66 \times 10^{15}$ g/cm^3.

and EoS defined by $\Gamma = 2$ and $K = 100\ G^3 M_\odot^2 c^{-4}$. From sufficiently long simulations, the frequencies of the characteristic radial oscillations (induced by truncation errors) have been extracted and compared with the ones estimated in [577] from an independent three-dimensional (3D) code. The results, summarized in Table 5.1, are an indicator of the accuracy of our frequency estimates.

mode	1D code (kHz)	3D code (kHz)	Rel. diff. (%)
F	1.443	1.450	0.6
H1	3.952	3.958	0.2
H2	5.902	5.935	0.6
H3	7.763	7.812	0.6

TABLE 5.1: *Radial oscillations frequencies of a neutron star in GR*. Comparison between estimates with our 1D code vs an independent 3D code [577].

From long-term simulations of several CNSs with central densities in the range $\rho_c = (0.96 - 1.67) \times 10^{15}$ g/cm^3, we have then computed the power spectral density (PSD) of the density perturbations and extracted the peak frequency of the fundamental radial mode (F) and its higher overtones (H_N, with $N = 1, 2, ...$). As a reference, we have also evolved spherical neutron stars produced in general relativity with comparable gravitational masses, using the same EoS ($\Gamma = 3$).

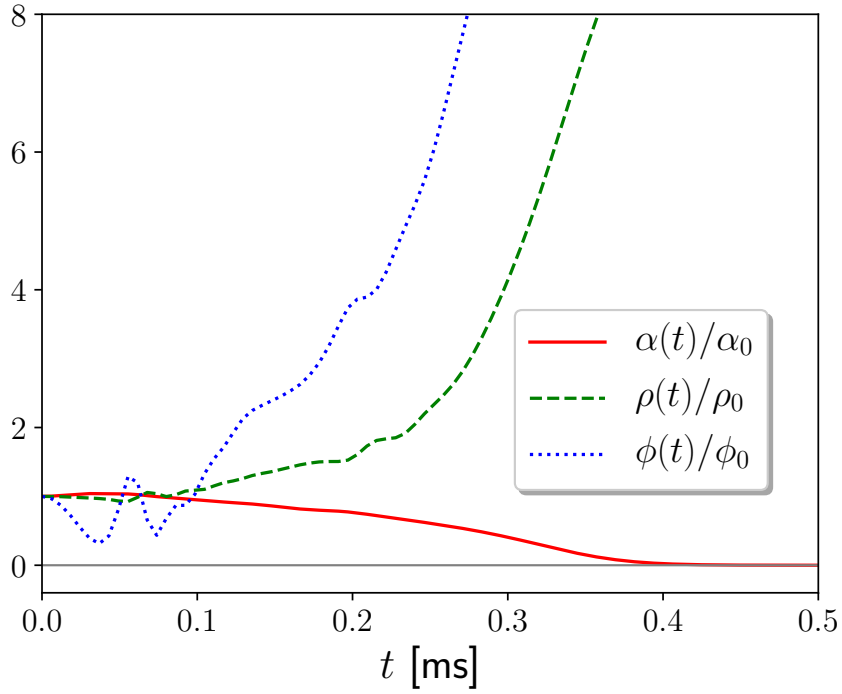

FIGURE 5.5: *Collapse of a descreened CNS*. Time evolution of the lapse (solid red line), density (dashed green line) and chameleon field (dotted blue line) at the center of a collapsing descreened star with gravitational mass $M = 1.88 M_\odot$, normalized by their initial value. As matter collapses towards the center, the density chameleon field increase. The lapse function decreases to small values close to zero.

The presence of the chameleon field coupled to matter inside the star has multiple effects on the spectrum. The first, which can be observed in Fig. 5.7, consists in a modification of the relation between the peak frequencies and the properties of the stars.

Radial oscillations of neutron stars in general relativity have been studied extensively in the past. For instance, it is known that non-relativistic homogeneous stars feature a fundamental mode frequency, F, that is proportional to the (constant) rest-mass density [494]. This relation is more complicated in the relativistic regime, and the result for non-relativistic homogeneous stars only holds approximately at low densities [545, 578]. In order to quantify the difference between spectra in general relativity and chameleon gravity, we have fitted the relation between the F-mode frequency and the average density, $\bar{\rho} \equiv (4\pi/3)^{-1} M/R_{star}^3$, in either theory. We present the result of the comparison in Fig. 5.8.

The additional scalar degree of freedom of scalar-tensor theories can also produce a new family of characteristic oscillations inside neutron stars. These scalar radial modes correspond to monopole gravitational wave emission. Indeed, in the spectra of CNSs, we observe several high-frequency peaks that do not have any correspondence in the general relativity power spectra (see Fig. 5.7, bottom panel). We interpret these peaks as due to the chameleon field oscillations. The fundamental (massive) scalar mode of oscillation has a frequency, $F_s \equiv m_{\rm eff}/2\pi$, that is of order of the inverse of the Compton wavelength: the larger the mass, the larger the corresponding frequency (see e.g., Fig. 2 in [547]). For $\Lambda = 175$ GeV, the chameleon

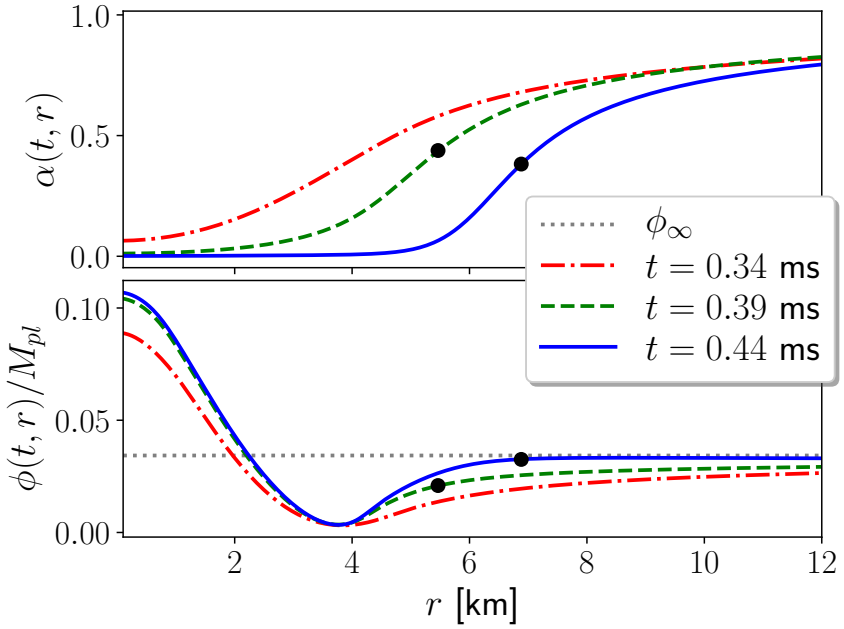

FIGURE 5.6: *Collapse of a descreened CNS.* Snapshots of the radial profile of the lapse function (top panel) and scalar field (bottom panel) for the same collapsing star as in Fig. 5.5. Black dots indicate the position of the apparent horizon.

field inside objects as dense as neutron stars acquires a very large mass (5.15), which yields frequencies $F_s \sim O(10)$ kHz. This is indeed the correct order of magnitude for the frequencies of the new family of modes that we observe. For $\Lambda \simeq 2.4$ meV, one can check that $F_s \gg$ kHz, because the chameleon acquires even larger masses inside relativistic stars. These modes are hardly excited and are unobservable with gravitational wave detectors.

Regarding the shift in the peak frequencies, note that such effect is present even in CNSs with a screened interior (see e.g. the $\rho_c \simeq 1.38 \times 10^{15}$ g/cm^3 configuration in Fig. 5.7). Like in the case of the mass-radius relation (c.f. Fig. 5.1 and related discussion), we expect deviations from general relativity in the spectrum of oscillations to disappear in the limit $\Lambda \to 0$ for screened stars, while they could survive for descreened CNSs. As we will see in the following, however, these effects are likely outside the reach of ground-based gravitational interferometers.

5.6 Scalar radiation

In this section, we investigate the characteristic gravitational wave output of CNSs, focusing on detectability with current and future detectors. To this end, for each signal produced with our simulations we estimate the signal-to-noise ratio (SNR) as [264]

$$\rho^2 \equiv \int_0^\infty \frac{4|\tilde{h}(f)|^2}{S_n(f)} df \,, \tag{5.38}$$

where $\tilde{h}(f)$ is the strain signal in the frequency domain and $S_n(f)$ is the one-sided noise power spectral density of the detector. As a reference, we compare the simulated signals with the design sensitivity curves of the Advanced Laser Interferometer

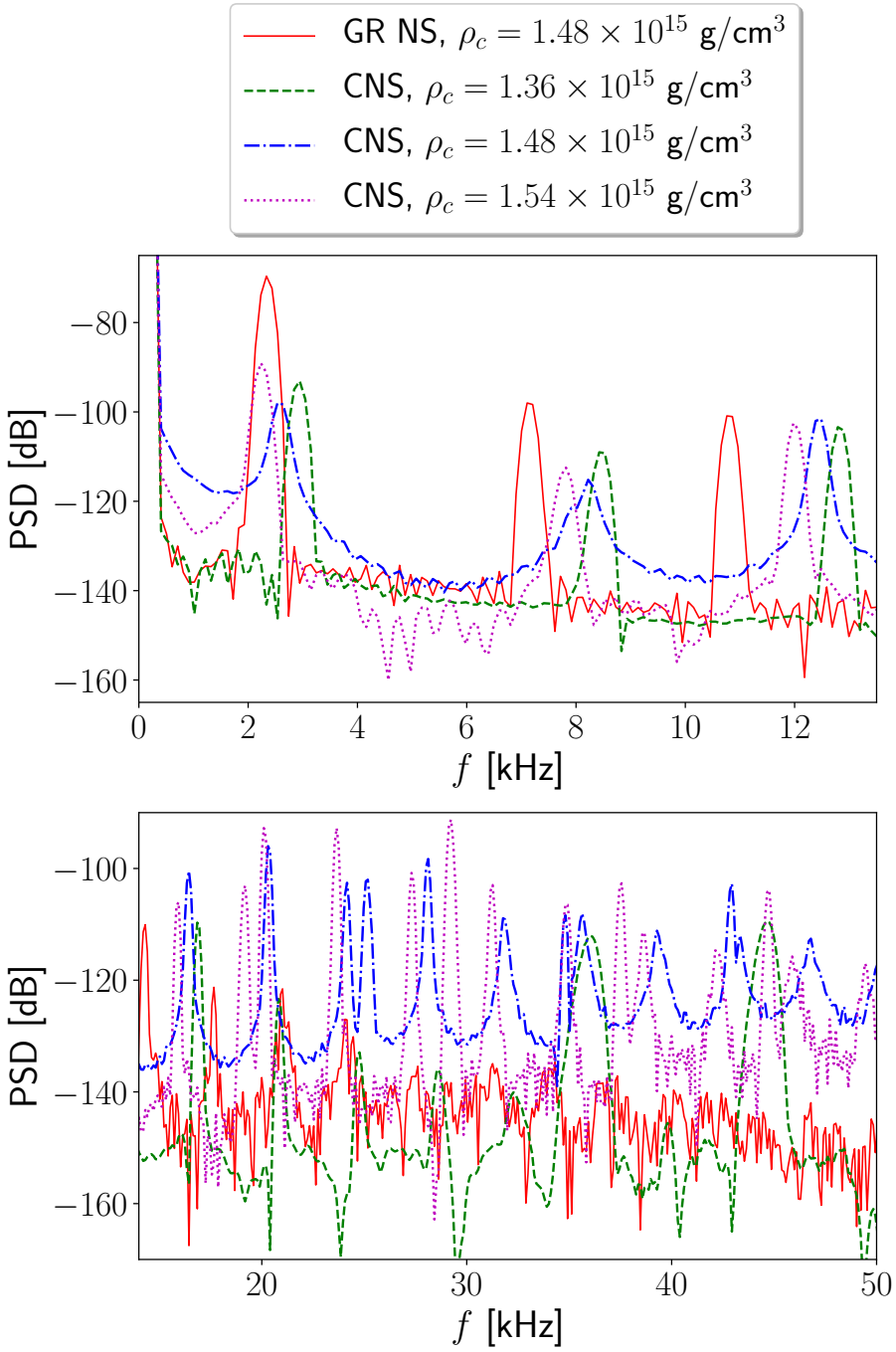

FIGURE 5.7: *Spectra of radial oscillations*. The two plots show the PSDs of the radial modes extracted from the time evolution of the central rest-mass density for three CNSs and one general relativity neutron star. Top panel: F, H1 and H2 modes. Bottom panel: higher overtones, H_N with $N > 2$, and the new family of scalar modes (F_s and higher overtones). The results shown in this plot are valid for the parameter choice $(\Lambda, \tilde{\epsilon}_\infty) = (175\ \text{GeV}, 6.5 \times 10^{10}\ \text{g/cm}^3)$.

Gravitational-Wave Observatory (Advanced LIGO) [159, 579][3], Einstein Telescope

[3]For the sensitivity we refer to the zero detuning, high power configuration.

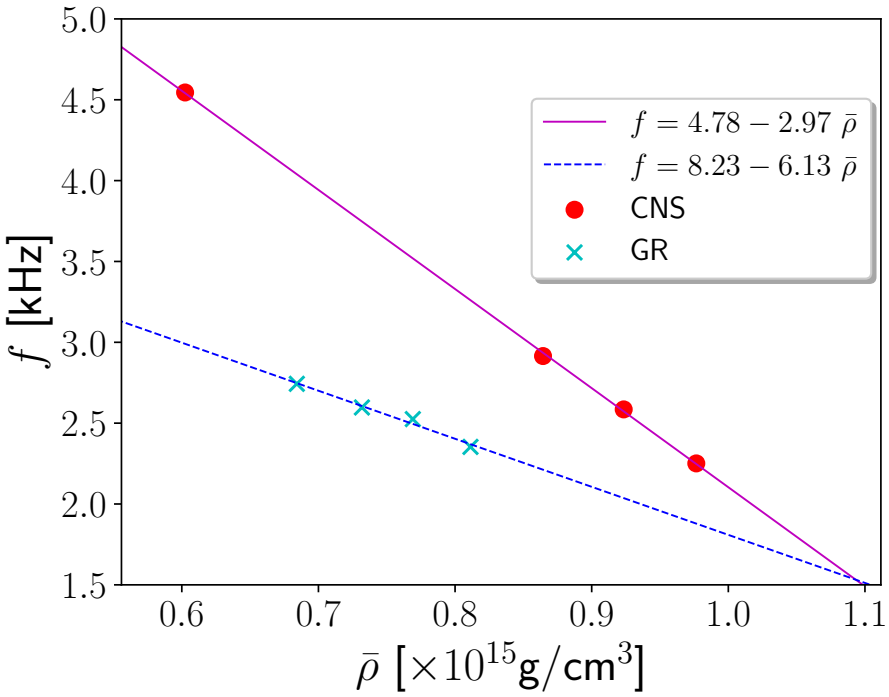

FIGURE 5.8: *F-mode frequency vs average density*. Linear fits of the fundamental mode (F) frequency as a function of the average density ($\bar{\rho}$) for neutron stars respectively in general relativity (blue dotted line, cyan cross tokens) and in chameleon gravity (magenta dash-dotted line, red round tokens). The results shown in this plot are valid for the parameter choice $(\Lambda, \tilde{\epsilon}_\infty) = (175\ \text{GeV}, 6.5 \times 10^{10}\ \text{g/cm}^3)$.

(ET) [580] and Laser Interferometer Space Antenna (LISA) [164, 581]. The geometry of the detector is encoded in the pattern functions, $F_+, F_\times, F_0$, which are different in the case of a tensor wave ($\tilde{h}(f) = F_+\tilde{h}_+(f) + F_\times\tilde{h}_\times(f)$) and for a scalar wave (breathing mode, $\tilde{h}(f) = F_0\tilde{h}_0(f)$). For simplicity, we will assume optimal detector orientation [549, 582, 583] in our calculations, i.e. $F_0 = 1/2$.

The effect of gravitational waves on the detector is encoded in the Newmann-Penrose curvature scalars [584]. The latter can be obtained by projecting the Riemann tensor onto a null tetrad basis $(k, l, m, \bar{m})$ adapted to the wavefronts. In particular, the scalar mode is encoded in $\Phi_{22} = -R_{lml\bar{m}}$ (computed in the Jordan frame) [263]. This quantity can be computed from our simulations (which are performed in the Einstein frame) via

$$\Phi_{22} = A(\phi)^{-2}\left(\Phi_{22}^E + l^a l^b \nabla_a \nabla_b \log A(\phi) - (l^a \nabla_a \log A(\phi))^2\right) , \tag{5.39}$$

where Φ_{22}^E is the same Newman-Penrose scalar in the Einstein frame. Since in that frame the scalar-tensor theories that we consider simply reduce (in vacuum) to GR with a minimally coupled scalar field, we can conclude that $\Phi_{22}^E \simeq 0$, and the only significant contribution comes from the oscillating chameleon field, i.e. [411]

$$\Phi_{22} \simeq 2\alpha_0 \partial_t^2 \phi + O\left(\frac{1}{r^2}\right) , \tag{5.40}$$

in deriving which we have used $\partial_t^2 \varphi \sim O(1/r)$ and neglected terms decaying as $1/r^2$

or faster. In practice, Φ_{22} is computed from our simulations by evaluating (5.40) at an extraction radius placed sufficiently far away from the star, $r_{ext} \gg R_{star}$. At the same time, the extraction radius must be far from the cosmological horizon, $r_{ext} \ll r_{cosmo}$, in an intermediate region where geometrical effects from the de Sitter asymptotics are negligible and the geometry is approximately flat. In addition to the spacetime flatness requirement, the extraction radius must also be chosen to satisfy $r_{ext} \gg \lambda_c = 1/m_\infty$, so that the extracted signal is decoupled from the dynamics of the matter and chameleon field inside the star. The extraction region where all the requirements listed above are satisfied, sometimes referred to as the "wave zone", is thus defined by $\lambda_c \ll r_{ext} \ll r_{cosmo}$. (Note that one typically has $\lambda_c \gg R_{star}$.) Because of the rather large effective cosmological constant, in our simulations the wave zone requirements are met only in a rather tight range of the isotropic radius coordinate (e.g. $r_{ext} = 50 - 100 M_\odot$ for $\Lambda = 175$ GeV). We have checked that our results are robust with respect to variations of the extraction radius in this range and to the position of the outer boundary of our simulations, which we place sufficiently far from the extraction point, at distances typically larger than $500 M_\odot$.

The signal is produced as a function of the retarded time, $t_{ret} \approx t - r_*$, defined in terms of the Schwarzschild-de Sitter tortoise coordinate, $r_* \equiv \int dr/f(r)$. This approximate prescription works well for our purposes, even though more involved expressions can be employed [585, 586]. We finally reconstruct the scalar strain in two independent ways. In the first method, with a Fast Fourier Transform algorithm we compute the frequency-domain Newmann-Penrose scalar $\tilde{\Phi}_{22}(f)$, from which we reconstruct the scalar strain h_s (with $\Phi_{22} \equiv \partial_t^2 h_s$) with the following filter in the frequency domain:

$$\tilde{h}_s(f) = \begin{cases} -\frac{1}{(2\pi f)^2}\tilde{\Phi}_{22}(f) & f > f_0 \\ -\frac{(2\pi f)^2}{(2\pi f_0)^4}\tilde{\Phi}_{22}(f) & f \leq f_0 \end{cases} , \tag{5.41}$$

inspired by [586, 587] with the addition of a factor $\sim (f/f_0)^2$ suppressing unphysical low-frequency noise. The frequency cutoff, f_0, is chosen according to the lowest physical frequency of the system. In practice, for simulations of oscillating stars we fix this to be of the order of the fundamental mode of radial oscillations, F, since under this threshold there is no stellar mode that can source the scalar radiation. Instead, the gravitational collapse produces what is sometimes referred to as an "inverse chirp" [549–551]: the gravitational wave burst excites lower and lower frequencies as the matter collapses. In this case, the mass of the chameleon field in the exterior introduces a natural cutoff frequency, $f_\infty \equiv m_\infty/2\pi$, as the propagation of modes with lower frequencies, $f \lesssim f_\infty$, is exponentially suppressed. As a test we checked the robustness of our results by varying the cutoff frequency down to the lowest resolvable frequency in our simulations, $f_0 \simeq 1/T$, where T is the total simulation time. The second method consists in computing the strain of the scalar monopole radiation directly from the formula [549–551]

$$h_s = 2\alpha_0(\phi - \phi_\infty) , \tag{5.42}$$

which comes from combining $\Phi_{22} = \partial_t^2 h_s$ and Eq. (5.40), which is approximately valid in the "wave zone" defined earlier. The agreement of the results obtained with the two methods confirms the robustness of our conclusions.

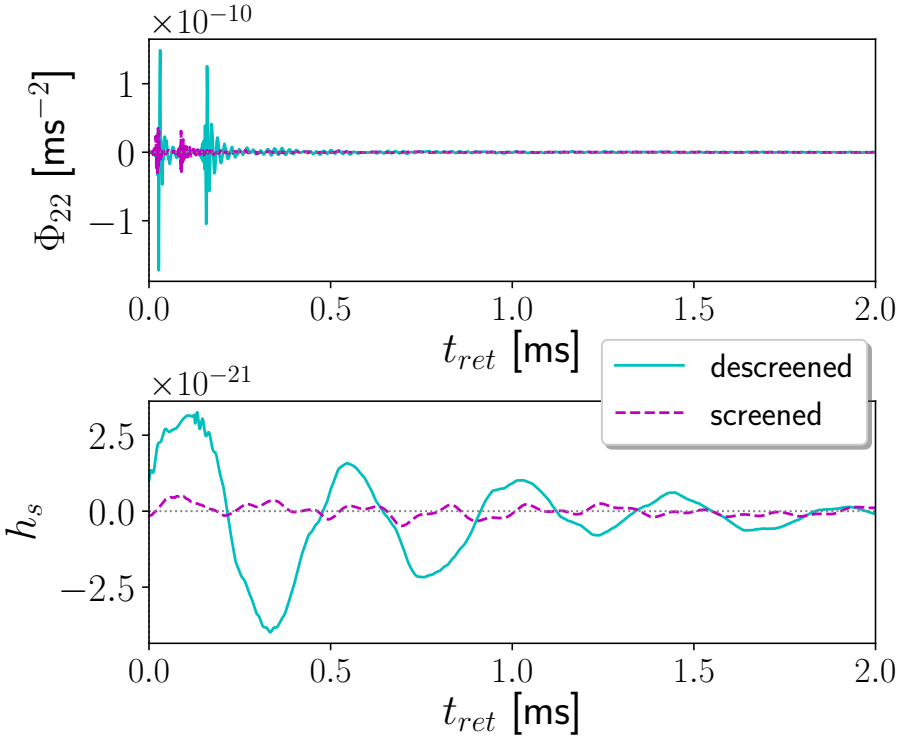

FIGURE 5.9: *Scalar radiation from oscillating stars.* Top panel: Φ_{22} vs retarded time. Bottom panel: strain amplitude vs retarded time. The results shown in these plots have been obtained for $(\Lambda, \tilde{\epsilon}_\infty) = (175\,\text{GeV}, 6.5 \times 10^{10}\,\text{g/cm}^3)$. The scalar radiation is extracted from simulations of oscillating CNSs respectively with (dashed magenta lines) and without (continuous cyan lines) screening in the interior. The gravitational masses of the stars are, respectively, $M = 1.02 M_\odot$ (screened CNS) and $M = 1.84 M_\odot$ (descreened CNS). The distance of the detector from the source is set to $D_L = 10$ kpc. To trigger the oscillations, an initial perturbation with amplitude $\delta\xi_0 = 10^{-6}$ is employed.

5.6.1 Oscillating CNSs

Oscillations in the CNSs were induced by an initial perturbation in the specific internal energy (see sec. 5.4.A), $\delta\xi(r) = \delta\xi_0 \cos(\sigma r) \exp(-r^2/\sigma^2)$, with $\sigma = 5 M_\odot$ and $\delta\xi_0 = \{10^{-6}, 10^{-5}, 10^{-4}, 10^{-3}, 4 \times 10^{-3}\}$. We have compared CNSs with different masses, the lighter one having $M = 1.02 M_\odot$ and belonging to the screened branch of solutions, while the heavier, $M = 1.84 M_\odot$, belongs to the branch with partial descreening. Here we take $(\Lambda, \tilde{\epsilon}_\infty) = (175\,\text{GeV}, 6.5 \times 10^{10}\,\text{g/cm}^3)$.

Let us first assess the effectiveness of the screening mechanism at suppressing the scalar radiation emitted by CNSs. In Fig. 5.9 we plot the monopole gravitational wave signal sourced by an oscillating star at a luminosity distance of $D_L = 10$ kpc. One can observe that both the Φ_{22} curvature scalar and the strain amplitude h_s, respectively in the top and bottom panel, are suppressed (by a factor $\sim O(10)$) when the screening mechanism is active inside the star.

To investigate the observability of the gravitational waves sourced by the characteristic modes of matter inside oscillating CNSs (see Fig. 5.7), we compare the strain amplitude (in the frequency domain) of the signals produced by the screened and

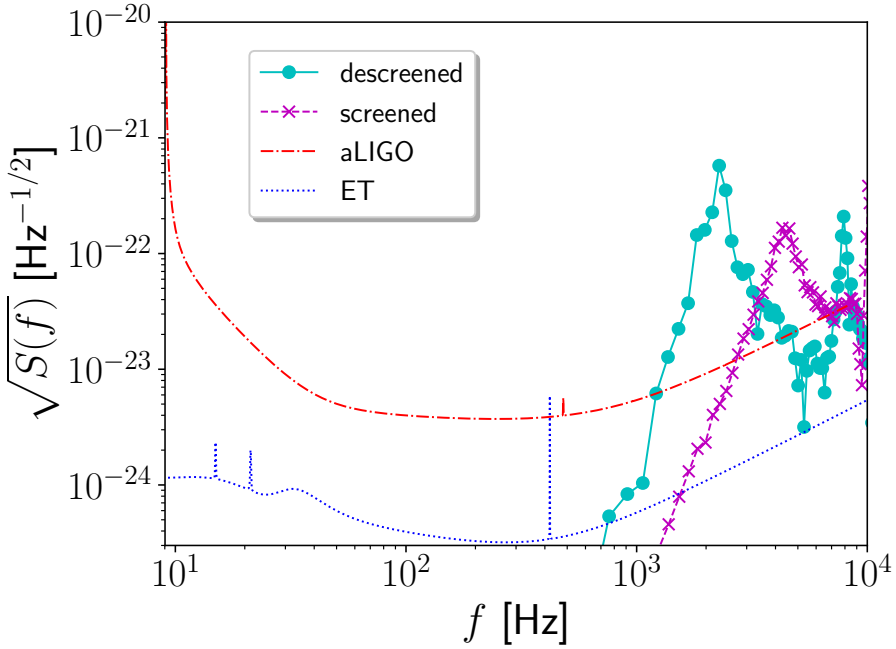

FIGURE 5.10: *Signal vs detector sensitivity curves - oscillating stars.* The strain amplitude in the frequency domain is compared to the design sensitivity curves of Advanced LIGO (red dot-dashed line) and ET (blue dotted line). The source-detector distance is set to $D_L = 10$ kpc. The signals correspond to the monopole gravitational waves produced by screened (continuous magenta line) and descreened (dashed cyan line) stars. The gravitational masses of the stars are, respectively, $M = 1.02 M_\odot$ (screened CNS) and $M = 1.84 M_\odot$ (descreened CNS). The initial perturbations (in the specific internal energy) employed to triggered the oscillations and scalar gravitational waves emission have an amplitude of $\delta\xi_0 = 4 \times 10^{-3}$. The visible peaks in the signals correspond to the fundamental mode, F, of the characteristic radial oscillations of the CNSs. The results have been obtained for $(\Lambda, \tilde{\epsilon}_\infty) = (175\ \text{GeV}, 6.5 \times 10^{10}\ \text{g/cm}^3)$.

descreened stars (both perturbed with the largest initial perturbation that we consider, $\delta\xi_0 = 4 \times 10^{-3}$) with the sensitivity curves of Advanced LIGO and ET, as is shown in Fig. 5.10. We observe that only the fundamental mode F (and, depending on the mass of the star, the first overtone H_1) have frequency falling in the (high end of) the sensitivity range of ground-based detectors. We conclude that oscillating CNSs located within our Galaxy would produce signals that are well above the sensitivity threshold of Advanced LIGO, even in the case of the screened star, for the theory considered in these simulations. Conversely, oscillating stars located outside our Galaxy ($D_L \gtrsim$ Mpc) might be undetectable by Advanced LIGO (even in case of descreened CNSs) but within reach of third generation detectors such as the ET, for which we predict higher SNR values (see Table 5.2).

The scaling of our results with the the initial perturbation amplitude is shown (together with a power-law fit) in Fig. 5.11. As can be seen, the logarithmic dependence on the initial amplitude suggests that our results are robust against changes in that quantity. We stress again, however, that all the results presented in this section have been obtained for $\Lambda \simeq 175$ GeV. When the chameleon energy scale is comparable to the dark-energy scale ($\sim$ meV), we expect the frequency of the F-mode

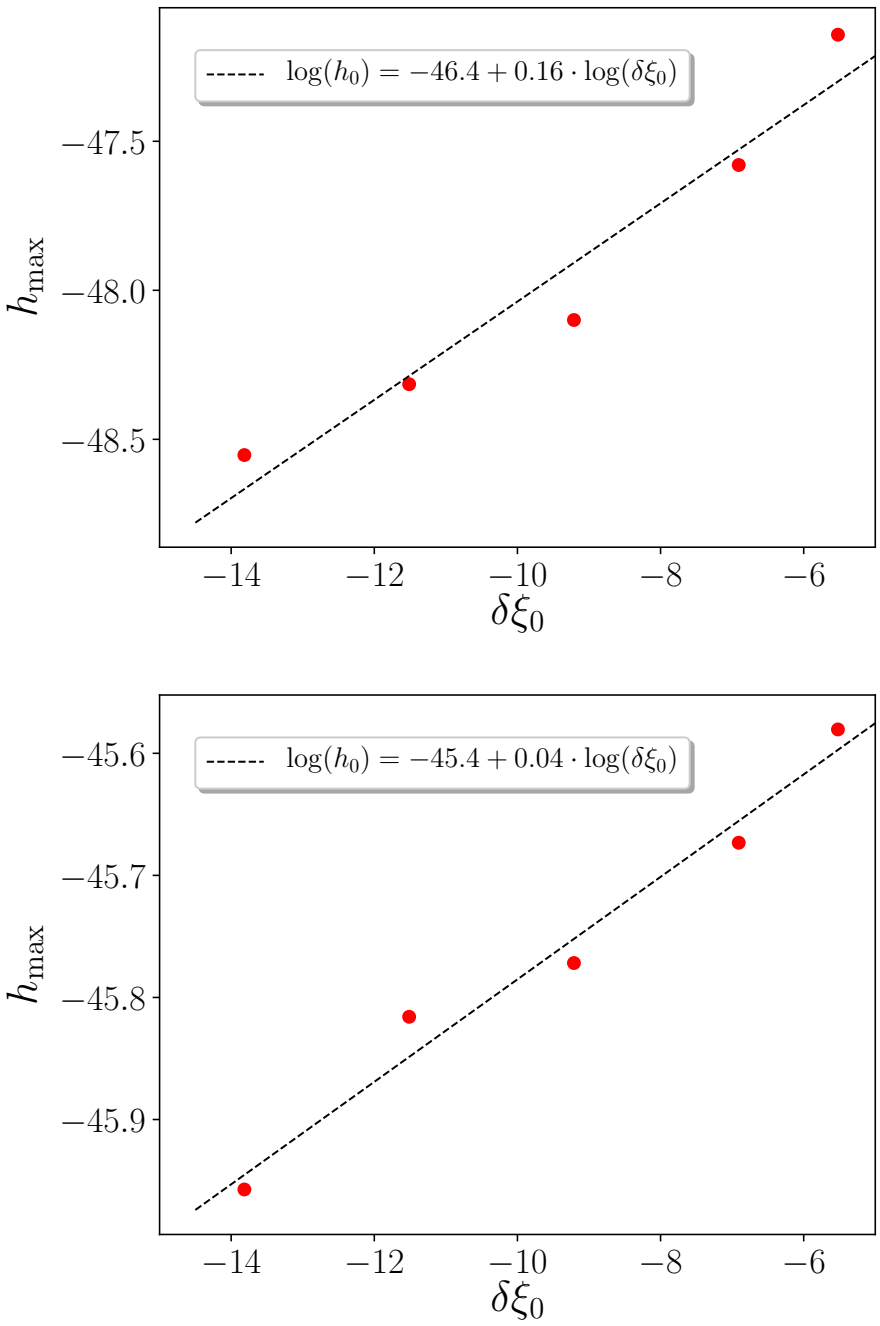

FIGURE 5.11: *Scalar strain vs initial perturbation amplitude.* The plots show the maximum amplitude of the monopole scalar radiation against the maximum amplitude of the initial perturbation of the specific internal energy, $\delta\xi$. Top and bottom panel correspond to a screened star with $M = 1.02M_\odot$ and a descreened star with $M = 1.84M_\odot$, respectively, located at a $D_L = 10$ kpc distance from the detector. The initial perturbation (in the specific internal energy) amplitudes considered are $\delta\xi_0 = \{10^{-6}, 10^{-5}, 10^{-4}, 10^{-3}, 4 \times 10^{-3}\}$. The parameters of the model are set to $(\Lambda, \tilde{\epsilon}_\infty) = (175$ GeV, 6.5×10^{10} g/cm^3). The black dashed lines show a power-law fit.

to approach the general relativity predictions and thus to remain in the kHz range. However, the fundamental scalar mode, F_s, will have even higher frequencies because of the huge mass (5.15) acquired by the chameleon field at nuclear densities, which may render detection of scalar effects challenging. As for the amplitude of the scalar signal, we expect it to be suppressed for $\Lambda \sim$ meV and more realistic atmosphere densities. We will show this in detail for the (much stronger) scalar emission produced in gravitational collapse, in the next section.

Scenario	Screening	LIGO	ET
Oscillations	Yes	4	3.3×10^1
	No	2.0×10^1	1.6×10^2
Collapse	Yes	7.6×10^3	7.8×10^4
	No	5.6×10^3	5.6×10^4

TABLE 5.2: *SNR.* Estimates of the SNR of scalar gravitational waves produced by oscillating and collapsing CNSs. Results are labelled by the presence or absence of screening in the core of the stars, and by the detector taken as a reference (Advanced LIGO or ET). The source-detector distance is set to $D_L = 10$ kpc. The gravitational masses of the oscillating stars are, respectively, $M = 1.02 M_\odot$ (screened CNS) and $M = 1.84 M_\odot$ (descreened CNS). The collapsing CNSs have been chosen to have a fixed baryon mass $M_{bar} = 1.75 M_\odot$. The results are obtained for $(\Lambda, \tilde{\epsilon}_\infty) = (175 \text{ GeV}, 6.5 \times 10^{10} \text{ g/cm}^3)$.

5.6.2 Collapsing CNSs

In this subsection, we extract the scalar (monopole) gravitational wave emission from simulations of collapsing unstable CNSs, respectively with and without descreened cores. In particular, we fixed the parameters of the theory to $(\Lambda, \tilde{\epsilon}_\infty) = (175 \text{ GeV}, 6.5 \times 10^{10} \text{ g/cm}^3)$ and chose two CNSs with the same baryon mass (5.25) $M_{bar} = 1.75 M_\odot$; but with different EoS polytropic index, respectively $\Gamma = 3$ and $\Gamma = 2$. For the latter value (and unlike for the former), the CNS does not feature a pressure-dominated core and the chameleon screening is fully effective. The collapse is induced with a small initial perturbation, introduced by decreasing the polytropic index by a tiny amount ($\sim 0.1\%$), which corresponds to a small increase of the initial pressure (by less than two percent) and of the specific internal energy (by half a percent).

The plots in Fig. 5.12 show the monopole scalar gravitational wave produced by the two CNSs described above, at a distance of $D_L = 10$ kpc. The infalling matter produces a typical burst signal, visible in both the Newman-Penrose scalar Φ_{22} (top panel) and in the scalar strain amplitude h_s (bottom panel). In these simulations we see no evidence of a suppression of the scalar emission due to screening (complete or partial). In Fig. 5.13 we compare the two scalar strain amplitudes, in the frequency domain, to the design sensitivity curves of current and next-generation terrestrial interferometers. As can be seen in the plot, a collapsing (screened or descreened) CNS would produce a very loud burst that would correspond to large SNR already in Advanced LIGO (see Table 5.2).

One may wonder, however, whether this large monopole radiation persists for smaller values of $(\Lambda, \tilde{\epsilon}_\infty)$. To answer this question, let us try to gain some insight on

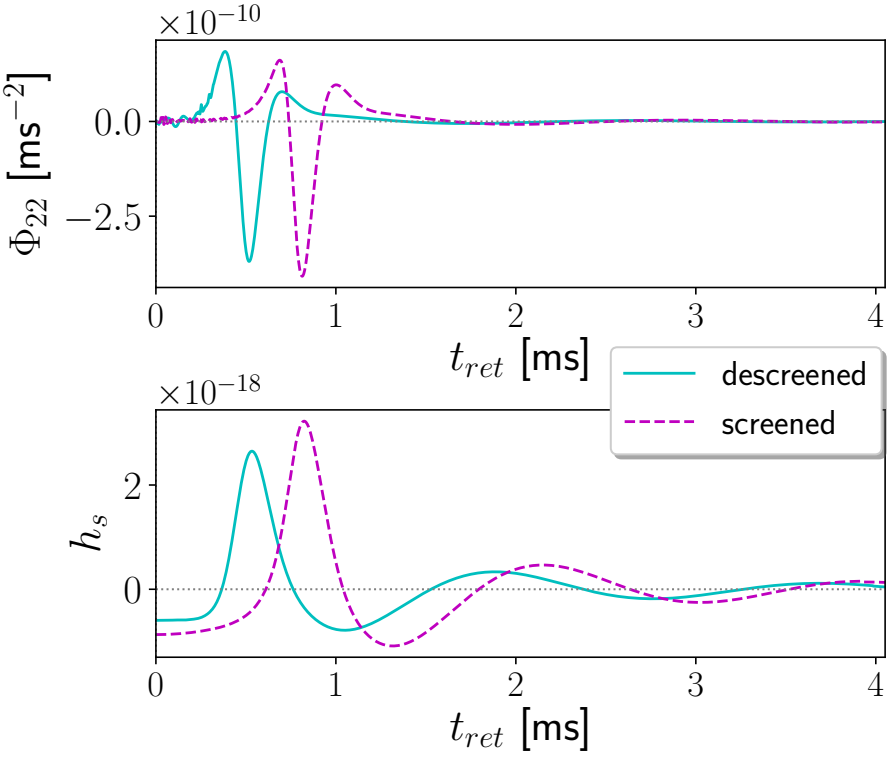

FIGURE 5.12: *Scalar radiation from collapsing stars.* Top panel: Φ_{22} vs retarded time. Bottom panel: strain amplitude vs retarded time. Bursts signals are extracted from simulations of collapsing CNSs, respectively with (dashed magenta lines) and without (continuous cyan lines) screening in the interior. The source-detector distance is set to $D_L = 10$ kpc.

why large scalar signals are produced in our simulations. As mentioned in Sec. 5.3, the end state of the collapse of a CNS is a "hairless" BH with the chameleon field lying in the constant "exterior" vacuum, $\phi = \phi_\infty$. Note indeed that vacuum solutions with "hair" (i.e. non-constant scalar field) are forbidden by a trivial generalization of the Hawking-Bekenstein "no-scalar-hair" theorem [394, 588, 589]. As a result, the scalar charge of the star must be shed away via gravitational wave emission during collapse. Therefore, larger initial charges will correspond to larger burst amplitudes. Note that a similar mechanism, whereby gravitational collapse has to shed away (because of no-hair theorems) any scalar hair that a star may initially have, thus producing a strong scalar monopole emission, was recently discovered for theories that yield kinetic screening [526].

In our case, we observe that at large values of $(\Lambda, \tilde{\epsilon}_\infty)$ the scalar charges of CNSs are not efficiently suppressed by the "thin-shell" effect. In fact, one can notice that the screening radius (see sec. 5.2.2 for the definition) of the TOV solutions obtained by choosing $(\Lambda, \tilde{\epsilon}_\infty) = (175\ \text{GeV}, 6.5 \times 10^{10}\ \text{g/cm}^3)$ is typically $\lesssim 70\%$ of the size of the stars (see Fig. 5.2 and also Fig. 2 in [461]). The relativistic stars are thus in a "thick-shell" regime, i.e. a non-negligible fraction of the stellar mass sources the scalar charge. In our simulations, in particular, the screened and descreened CNSs shown in Fig. 5.12 emit loud scalar gravitational waves because they have relatively large and comparable charges, respectively $Q \simeq 0.15$ and $Q \simeq 0.11$. The descreened star actually features a charge slightly smaller than the screened CNS. We interpret

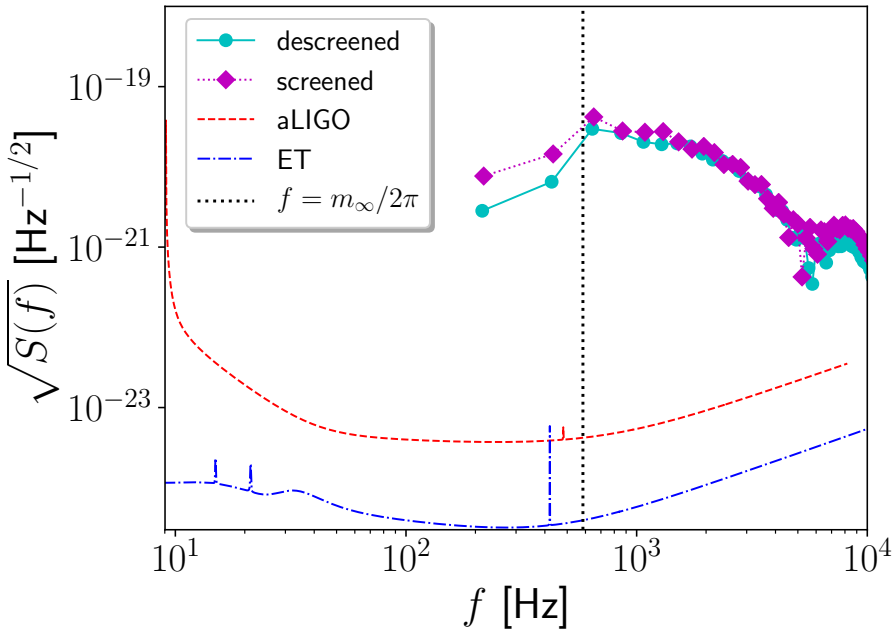

FIGURE 5.13: *Signal vs detector sensitivity curves - collapsing stars.* The strain amplitude in the frequency domain is compared to the design sensitivity curves of Advanced LIGO (red dot-dashed line) and ET (blue dotted line). The source-detector distance is set to $D_L = 10$ kpc. The signals correspond to the monopole gravitational waves produced by screened and descreened stars undergoing gravitational collapse. The vertical dash-dotted black line corresponds to $f_\infty = m_\infty/2\pi$, i.e. the peak frequency of the burst, below which all frequencies are Yukawa-suppressed.

this as due to the descreened core, which gives a negative contribution to charge and thus decreases the its total value.

To extrapolate the charges of CNSs to realistic values of $(\Lambda, \tilde{\epsilon}_\infty)$, we use the scaling

$$Q(\Lambda, \tilde{\epsilon}_\infty) = (\Lambda/\Lambda_0)^a (\tilde{\epsilon}_\infty/\tilde{\epsilon}_0)^b Q(\Lambda_0, \tilde{\epsilon}_0)\,, \tag{5.43}$$

where the coefficients $a \simeq 2$ and $b \simeq -3/5$ were obtained by power-law fits of simulations with baryon mass $M_{bar} = 1.75 M_\odot$ (c.f. Figs 5.14–5.15).

Based on Eq. (5.43), we predict that the CNSs of mass $M_{bar} = 1.75 M_\odot$ considered above will have a scalar charge of, respectively, $Q \simeq 6 \times 10^{-11}$ and $Q \simeq 5 \times 10^{-11}$ for the realistic values $(\Lambda, \tilde{\epsilon}_\infty) \simeq (2.4\ \text{meV}, 1.67 \times 10^{-20}\ \text{g/cm}^3)$. We interpret this suppression of the scalar charge as a vindication of the "thin-shell" effect, which appears to be restored, even for relativistic stars, at realistic values of the parameters of the theory.

Motivated by this result, we turn now to estimate the SNR of burst signals for realistic/viable values of $(\Lambda, \tilde{\epsilon}_\infty)$. To overcome the technical challenges of directly simulating stars at very small Λ and $\tilde{\epsilon}_\infty$ (see discussion in Sec. 5.4), we resort again to determining the scaling of the scalar monopole signal with these quantities. From simulations of the collapse with $\Lambda \simeq \{175, 122, 73\}$ GeV and $\tilde{\epsilon}_\infty = $ const., we fit the maximum strain amplitude of the burst as a function of Λ using a power law, as is displayed in Fig. 5.16. We then fit (again with a power law) the same quantity against the exterior density, $\tilde{\epsilon}_\infty = \{6.5, 2.6, 1.1\} \times 10^{10}\ \text{g/cm}^3$, using simulations with fixed

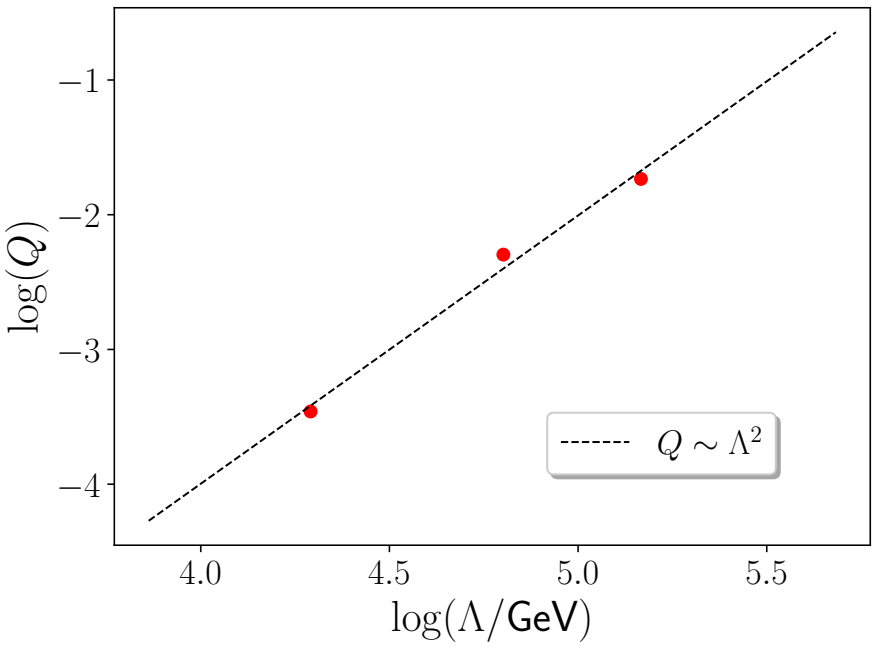

FIGURE 5.14: *Scalar charge vs chameleon energy scale.* The plot shows the scalar charge, Q, of CNSs with $M_{bar} = 1.75 M_\odot$ against chameleon energy scale, Λ; the atmosphere density is kept constant, $\tilde{\epsilon}_\infty = 6.5 \times 10^{10}$ g/cm^3. Red dots represent data corresponding to $\Lambda = \{175, 122, 73\}$ GeV. The black dashed line represents the power law $Q \sim \Lambda^a$ (with $a \simeq 2$) fitting the data.

ϕ_∞. The result is shown in Fig. 5.17.

Combining the results from these power-law fits, one obtains a scaling relation for the maximum scalar amplitude

$$h_s(\Lambda, \tilde{\epsilon}_\infty, D_L; t_{ret}) = (\Lambda/\Lambda_0)^c (\tilde{\epsilon}_\infty/\tilde{\epsilon}_0)^d (D_0/D_L) \cdot \\ \cdot \; h_s(\Lambda_0, \tilde{\epsilon}_0, D_0; (m_0/m_\infty)\, t_{ret}) \,, \tag{5.44}$$

with $c \simeq 5/2$ and $d \simeq -7/10$. Note that the scaling with Λ coincides with that of the quantity $(\phi_\infty - \phi_s)$, where ϕ_s is the minimum of the scalar field inside the CNS. Indeed, from (5.14) one obtains ϕ_∞, $\phi_s \sim \Lambda^{5/2}$. Let us also note, as can be seen from Fig. 5.13, that the burst signal peaks at $f = f_\infty \equiv m_\infty(\Lambda, \tilde{\epsilon}_\infty)/2\pi$, while lower frequencies are suppressed. Making use of expression (5.15), one can check that lower values of Λ and $\tilde{\epsilon}_\infty$ correspond to smaller chameleon masses, and thus lower peak frequencies. Hence, to extrapolate to lower $(\Lambda, \tilde{\epsilon}_\infty)$ one also needs to rescale the time by the factor (m_0/m_∞) that appears in (5.44).

Finally, by applying Eq. (5.44) to extrapolate to $(\Lambda, \tilde{\epsilon}_\infty) \simeq (2.4\ \text{meV}, 1.67 \times 10^{-20}$ g/cm$^3)$ (the latter corresponding to the order of magnitude of the density inside large molecular clouds), we find that the monopole signal would peak in the mHz band, outside the band of terrestrial detectors but within that of LISA. Although we have computed the SNR for LISA, that is completely unobservable ($\rho \simeq 10^{-10}$), even for distances of a few kpc.

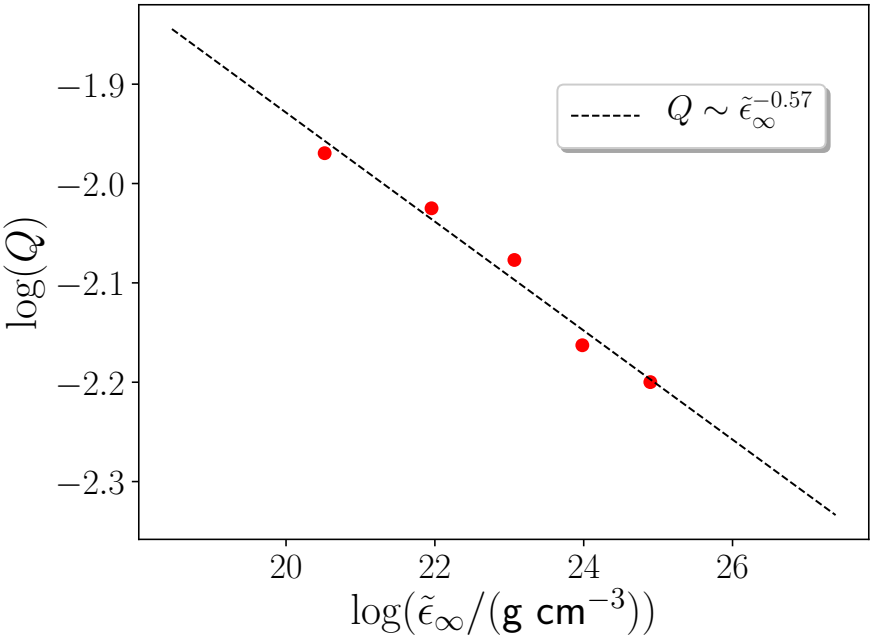

FIGURE 5.15: *Scalar charge vs atmosphere density.* The plot shows the scalar charge, Q, of CNSs with $M_{bar} = 1.75 M_\odot$ against atmosphere density, $\tilde{\epsilon}_\infty$; the asymptotic value of the chameleon field is fixed to $\phi_\infty \simeq 0.17 M_{\rm pl}$. Red dots represent data corresponding to $\tilde{\epsilon}_\infty = \{6.5, 2.6, 1.1, 0.34, 0.081\} \times 10^{10}$ g/cm^3. The black dashed line represents the power-law $Q \sim \tilde{\epsilon}_\infty^b$ (with $b \simeq -3/5$) fitting the data.

5.6.3 Binary systems

From the extrapolation presented in the previous section, we have concluded that the monopole emission from collapsing CNSs is pratically unobservable with current (and future) detectors, at least for realistic values of the chameleon model. When it comes to (quasi-circular) binary systems involving at least oneneutron star, the strongest effect is expected to be dipole scalar emission, which potentially dominates the binary's evolution at low frequencies [52, 58, 76, 338, 411, 412, 520, 530] The deviations from general relativity induced by dipole emission can be parametrized via [520]

$$\dot{E} = \dot{E}_{GR} \left(1 + \frac{B}{v^2} \right) , \tag{5.45}$$

where v is the relative velocity of the binary, $\dot{E}$ and $\dot{E}_{GR}$ are the total energy fluxes in chameleon gravity and in GR, respectively, and $B \sim (Q_1 - Q_2)^2$ (with Q_1 ad Q_2 the component charges).

Note that Eq. (5.45) is valid for scalar-tensor theories with a massless scalar, while the chameleon field possesses a non-vanishing mass. We therefore expect the energy loss due to dipole radiation to be given by Eq. (5.45) only at binary separations smaller than the Compton wavelength. For $(\Lambda, \tilde{\epsilon}_\infty) \simeq (2.4\ \text{meV}, 1.67 \times 10^{-20}\ \text{g/cm}^3)$, the Compton wavelength is $\lambda_c = 1/m_\infty \simeq O(10^8)$ km, which is larger than the typical separation of binary pulsars (which is $\lesssim 10^6$ km). However, from the scaling (5.43), the scalar charge of relativistic stars extrapolated at $(\Lambda, \tilde{\epsilon}_\infty) \simeq (2.4\ \text{meV}, 1.67 \times 10^{-20}\ \text{g/cm}^3)$ would be $Q \lesssim O(10^{-10})$, corresponding to $B \sim 10^{-20}$.

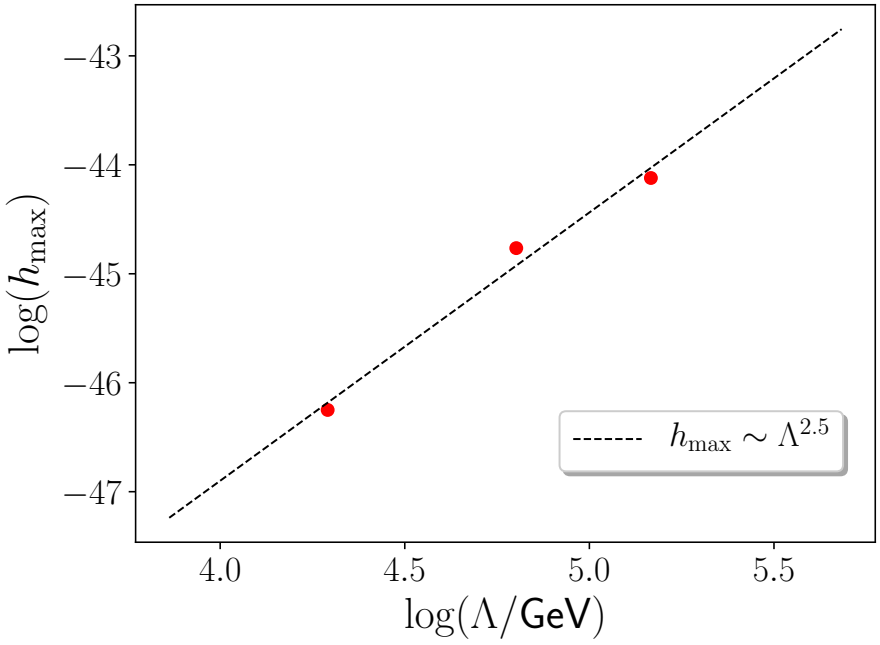

FIGURE 5.16: *Maximum burst amplitude vs chameleon energy scale*. The plot shows the maximum amplitude, $h_{\rm max}$, of the burst produced by collapsing CNSs with $M_{bar} = 1.75 M_\odot$ against the chameleon energy scale, Λ; the atmosphere density is kept constant, $\tilde{\epsilon}_\infty = 6.5 \times 10^{10}$ g/cm^3. Red dots represent data corresponding to $\Lambda = \{175, 122, 73\}$ GeV. The black dashed line represents the power law $h_{\rm max} \sim \Lambda^c$ (with $c \simeq 5/2$) fitting the data.

This is at least 10 orders of magnitude lower than what is currently measurable [520]

5.7 Conclusion

In this work, we have investigated the chameleon screening mechanism in the fully dynamical and nonlinear regime of oscillating and collapsing neutron stars, in spherical symmetry. Our simulations confirm the static results of Ref. [461], and in particular the partial breakdown of the chameleon screening inside stars with pressure-dominated cores, but also provide evidence of the nonlinear stability of both screened and partially descreened stars in chameleon gravity.

We have focused first on the characteristic spectrum of (radial) oscillations of neutron stars. We observed a shift in the frequencies of the fundamental mode and higher overtones with respect to the general relativity predictions. While this effect could be degenerate with the EoS, the appearance of a new family of modes may potentially constitute the "smoking gun" of a gravitational scalar field. However, these modes have frequencies of the order of the large mass that the chameleon field acquires inside relativistic stars (i.e. $\gtrsim$ kHz). Moreover, we find that chameleon screening is also very efficient at suppressing the scalar mode amplitude in oscillating screened CNSs, already at large $\Lambda \sim 100$ GeV. For this reason, scalar effects in oscillating stars are probably unobservable for realistic chameleon energy scales $\Lambda \simeq$ meV.

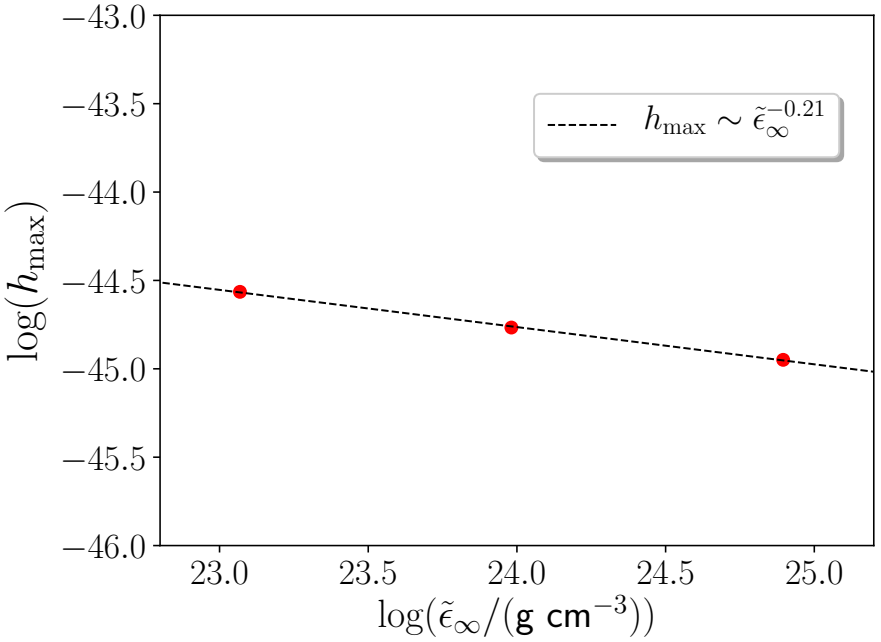

FIGURE 5.17: *Maximum burst amplitude vs atmosphere density.* The plot shows the maximum amplitude, $h_{\rm max}$, of the scalar gravitational wave burst against the atmosphere density, $\tilde{\epsilon}_\infty$. The collapsing CNSs have a fixed baryon mass $M_{bar} = 1.75 M_\odot$ and the asymptotic value of the chameleon field is fixed to $\phi_\infty \simeq 0.17 M_{\rm pl}$. Red dots represent data corresponding to $\tilde{\epsilon}_\infty = \{6.5, 2.6, 1.1\} \times 10^{10}$ g/cm^3. The black dashed line represents the power law $h_{\rm max} \sim \tilde{\epsilon}_\infty^d$ (with $d \simeq -7/10$) fitting the data.

We have also simulated gravitational collapse of neutron stars, which can lead to larger monopole scalar signals than stellar oscillations. We have assessed detectability by existing and future gravitational wave interferometers, concluding that the scalar radiation would be observable in the Galaxy for large chameleon energy scales $\Lambda \sim 100$ GeV. However, if one extrapolates our results down to viable chameleon energy scales $\Lambda \simeq$ meV, the screening suppresses the signal's amplitude, and the signal also gets shifted to lower ($\sim$ mHz) frequencies. We have checked that, as a result, this scalar emission would be undetectable even with LISA. Similarly, our results for the scalar charge of isolated neutron stars suggest that scalar effects would be suppressed by screening also in pulsar binary systems for $\Lambda \simeq$ meV.

Chapter 6

Concluding remarks

During the research work collected in this thesis I have explored the signatures that a scalar field could leave in the strong-gravity environment of black holes and neutron stars, focusing in particular on the observability through gravitational-wave astronomy.

The hypothesis of superradiant instabilities triggered by a plasma-induced mass of the photon was considered in Chapter 3. As it turned out, while the conditions for observable superradiant effects might be achieved in a homogeneous plasma distribution with an appropriately low density (i.e. of order of the interstellar medium one), a more realistic plasma distribution around astrophysical black holes would need to include the effects of an accretion-induced density increment that spoils the conditions for the onset of the superradiant instability (see Chapter 3). In addition, more recent work has demonstrated that even when accretion is negligible (e.g. black holes kicked out of their accretion nest) other mechanisms will intervene and quench superradiance very rapidly before any observable effect is produced [380, 512–515].

In Chapter 4 we discussed a similar problem involving scalar effects in vacuum spacetimes triggered by a position-dependent effective mass term. We considered an alternative model of gravity in which the gravitational interaction is mediated by both the metric and an additional fundamental scalar field. The key element of the model is the coupling of the scalar field to the spacetime curvature, which is negligible where gravity is weak (i.e. the Solar System) and typically relevant only in the strong-field regime of compact objects. While because of no-hair theorems many scalar-tensor models predict no deviation from General Relativity in the physics of black holes, there are known examples of models with a coupling to higher-order curvature invariants that allow vacuum solutions with scalar hair. In particular, the specific model to which we specialized in Chapter 4 is protected by a no-hair theorem in the case of static spherically symmetric vacuum spacetimes. By generalizing to an axisymmetric scenario, we were able to discover the onset of an interesting variant of the curvature-induced scalarization process that triggers the growth of scalar hair only in rapidly rotating black holes. Other groups subsequently confirmed our findings [590, 591] and further explored the evolution and endstate of spin-induced scalarization [149, 432, 592, 593].

In general, extending the theory of gravity with an additional scalar sector requires the introduction of a free scale that controls the scalar effects. In typical scalar-tensor theories this scale can be tightly constrained with the standard set of weak-field tests of gravity that we briefly reviewed in section 1.2.1. With the advent of the era of gravitational-wave observations and with the increasing number of other strong-gravity probes, even tighter bounds can now be placed and large portions of the space of viable scalar-tensor theories of gravity have already been ruled out (see section 1.2.3 and 2.1.3). Instead, screened scalar-tensor theories are

inherently more difficult to constrain because of the built-in mechanisms that hide the scalar signatures. However, proof of the effectiveness of screening mechanisms is typically produced with semi-analytic arguments in the static, non-relativistic Newtonian limit. Given the complexity of the problem the results obtained outside these simplifying assumptions are scarce in number. The fully dynamical, highly-relativistic and strong-field regimes of screened modified gravity remain still largely unknown. Chapter 5 was dedicated to work that attempts to improve on this issue: the investigation of isolated neutron stars coupled to a scalar field with chameleon screening. The nonlinear potential of the chameleon field in combination with the conformal coupling to matter result in a dynamical effective mass that grows with the local value of the ambient density. The large inertia acquired by the scalar in correspondence of dense matter distributions (e.g. the Earth, a star or the Solar System) effectively screens the scalar field dynamics. Our work presented in Chapter 5 is among the first contributions to the numerical modeling of neutron stars in screened modified gravity with full-fledged numerical relativity techniques.

The general approach employed in all the work collected in this thesis followed closely the model-builder logic of exploring alternative theories of gravity starting from minimal modifications. In particular, my research was focused on strong-field effects produced by scalar fields with dynamical mass terms when interacting with strong-gravitating compact objects like black holes and neutron stars. The mass dynamics was given either by a photon-plasma coupling, a universal conformal coupling to matter or a coupling to spacetime curvature (see Chapters 3, 4 and 5, respectively). The restricted scope of this approach can be both a point of strength and a limitation at the same time. On the one hand, considering only a (generalized) mass-term potential in the action of the gravitational model can simplify significantly the process of producing quantitative predictions. On the other hand, scalar fields with more general potentials or higher-order derivative operators (like those that appear in the most general scalar-tensor Lagrangian in section 2.1.3) could keep in store interesting new physics to explore. To list only a few examples concerning vacuum spacetimes: "higher-order" black-hole scalarization [594], novel families of solitonic scalar solutions [595–597], "stealth" hairy black holes [598–600]. Regarding extreme matter spacetimes, higher-derivative scalar-tensor theories allow for an entirely different class of kinetic screening mechanisms (see section 2.2.3) whose behavior in the strong-field regime remains yet mostly unknown.

However, numerical modeling of the strong-gravity regime in more general scalar-tensor theories presents many unsolved challenges, an example of which is given by the multiscale problem introduced by screening mechanisms. Resolving numerically the typically large separation of scales between the screened solution (in the nonlinear regime of compact objects) and the cosmological solution (recovered sufficiently far outside compact stars) can be in practice very challenging both for standard methods for initial data production and for the subsequent time evolution. This issue was discussed in Chapter 5 in relation to chameleon screening. Note, however, how this issue seems not unique to chameleon gravity but apparently plagues also theories with different screening mechanisms (see [462, 526]). Future prospects for addressing this particular issue could consist of resorting to adaptative stepsize and/or implicit-explicit algorithms for handling arbitrarily small values of the fundamental scale of the problem (see Chapter 4 for an example); or to more refined numerical methods for multiscale problems [601].

Moreover numerical simulations are destined to fail if the theory does not admit a well-posed initial value problem or, in other words, if it is not granted that

the field equations admit a unique, continuously dependent and bounded solution [602]. Well-posedness of the initial value problem has been a longtime major obstacle in the way of numerical modeling of the strong-field regime of gravity. In fact, since the seminal work by Yvonne Choquet-Bruhat [603, 604] it took several decades before a well-posed formulation of the nonlinear Einstein field equations could be found [605]. In recent years modified gravity is facing a tougher incarnation of the same problem, since finding a well-posed formulation of the modified/extended field equations beyond-General Relativity can be highly non-trivial [606–611]. In fact, well-posedness has been fully established only for scalar-tensor theories in the Bergman-Wagoner formulation [612, 613], for Lovelock gravity and Horndeski theories at weak coupling [614–618], and Einstein-aether theories [619]. However, due to the enhanced nonlinearities in the field equations the initial value problem can see a dynamical breakdown of the well-posedness during the simulations [620–622]. One solution that has been proposed consists in adapting the Israel-Stewart techniques used in hydrodynamics problems to numerical relativity [623, 624]. Another interesting alternative to the quest for well-posed schemes tailored for modified gravity is given by *order-reduction schemes*. In brief, these consist in a small-coupling expansion of the system of field equations followed by numerical simulations conducted order-by-order, the leading-order typically coinciding with the limit of decoupled evolution of the extra degrees of freedom on a general relativistic background (or *decoupling limit*). With this approach numerical results have been obtained earlier on in cubic galileon theories [625], on binary black hole simulations in Chern-Simons gravity [626–629] and Einstein-scalar-Gauss-Bonnet models [610, 630, 631]. Although the order-reduction approach allows one to study such involved theories with only minimal modifications to the numerical schemes used in general-relativistic problems, typically concerns are risen regarding the applicability of the method to theories where the fundamental couplings are not necessarily small, e.g. in screened modified gravity, and such perturbative approaches necessarily fail to capture important nonlinear effects. Moreover, a well-known problem in perturbative methods for near-periodic problems (like the inspiral of two compact objects [629, 632, 633]) consists in the pertubed numerical solution growing secularly apart from the true non-perturbative solution. Recently progress has been achieved on remeding with *dynamical renormalization group* methods to the secular growth of perturbative solutions see [634].

In conclusion, the research work behind this doctoral thesis allowed me to face the scientific questions and technical challenges involved when testing our current understanding of the theory of gravitation. Although I had the opportunity to give a little personal contribution to some of these questions and challenges, many more still lie ahead: in the era of gravitational-wave astronomy, renewed efforts are required in modeling systematically the strong-gravity phenomenology of compact objects beyond general relativity.

Bibliography

[1] C. M. Will. "The Confrontation between General Relativity and Experiment". In: *Living Rev. Rel.* 17 (2014), p. 4. DOI: 10.12942/lrr-2014-4. arXiv: 1403.7377 [gr-qc].

[2] C. M. Will. *Theory and Experiment in Gravitational Physics*. 2nd ed. Cambridge University Press, 2018. DOI: 10.1017/9781316338612.

[3] E. Di Casola, S. Liberati, and S. Sonego. "Nonequivalence of equivalence principles". In: *Am. J. Phys.* 83 (2015), p. 39. DOI: 10.1119/1.4895342. arXiv: 1310.7426 [gr-qc].

[4] I. Newton. *Philosophiæ Naturalis Principia Mathematica*. England, 1687.

[5] G. Nordström. "Zur Theorie der Gravitation vom Standpunkt des Relativitätsprinzips". In: *Annalen der Physik* 347.13 (1913), pp. 533–554. DOI: https://doi.org/10.1002/andp.19133471303. eprint: https://onlinelibrary.wiley.com/doi/pdf/10.1002/andp.19133471303. URL: https://onlinelibrary.wiley.com/doi/abs/10.1002/andp.19133471303.

[6] N. Deruelle. "Nordstrom's scalar theory of gravity and the equivalence principle". In: *Gen. Rel. Grav.* 43 (2011), pp. 3337–3354. DOI: 10.1007/s10714-011-1247-x. arXiv: 1104.4608 [gr-qc].

[7] C. Lanczos. "A Remarkable property of the Riemann-Christoffel tensor in four dimensions". In: *Annals Math.* 39 (1938), pp. 842–850. DOI: 10.2307/1968467.

[8] D. Lovelock. "The Einstein tensor and its generalizations". In: *J. Math. Phys.* 12 (1971), pp. 498–501. DOI: 10.1063/1.1665613.

[9] T. Padmanabhan and D. Kothawala. "Lanczos-Lovelock models of gravity". In: *Phys. Rept.* 531 (2013), pp. 115–171. DOI: 10.1016/j.physrep.2013.05.007. arXiv: 1302.2151 [gr-qc].

[10] D. Lovelock. "The Four-Dimensionality of Space and the Einstein Tensor". In: *Journal of Mathematical Physics* 13.6 (1972), pp. 874–876. DOI: 10.1063/1.1666069. eprint: https://doi.org/10.1063/1.1666069. URL: https://doi.org/10.1063/1.1666069.

[11] D. Hilbert. "Die Grundlagen der Physik. 1." In: *Gott. Nachr.* 27 (1915). Ed. by J.-P. Hsu and D. Fine, pp. 395–407.

[12] A. S. Eddington. *The mathematical theory of relativity / by A.S. Eddington.* Chelsea Pub.Co., 1975. ISBN: 0-8284-0278-7. URL: http://search.ebscohost.com/login.aspx?direct=true&db=cat00961a&AN=sissa.8903&site=eds-live.

[13] H. P. Robertson. "Relativity and Cosmology". In: *Space Age Astronomy*. Ed. by A. J. Deutsch and W. B. Klemperer. Jan. 1962, p. 228.

[14] L. I. Schiff. In: *Proceedings of the 1965 Summer Seminar on Relativity and Astrophysics*. 1965.

[15] K. Nordtvedt. "Equivalence Principle for Massive Bodies. 2. Theory". In: *Phys. Rev.* 169 (1968), pp. 1017–1025. DOI: 10.1103/PhysRev.169.1017.

[16] C. M. Will. "Theoretical Frameworks for Testing Relativistic Gravity. 2. Parametrized Post-Newtonian Hydrodynamics, and the Nordtvedt Effect". In: *Astrophys. J.* 163 (1971), pp. 611–627. DOI: 10.1086/150804.

[17] C. M. Will and K. Nordtvedt Jr. "Conservation Laws and Preferred Frames in Relativistic Gravity. I. Preferred-Frame Theories and an Extended PPN Formalism". In: *Astrophys. J.* 177 (1972), p. 757. DOI: 10.1086/151754.

[18] L. Blanchet et al. "Gravitational radiation from inspiralling compact binaries completed at the third post-Newtonian order". In: *Phys. Rev. Lett.* 93 (2004), p. 091101. DOI: 10.1103/PhysRevLett.93.091101. arXiv: gr-qc/0406012.

[19] H. Y. Ip, J. Sakstein, and F. Schmidt. "Solar System Constraints on Disformal Gravity Theories". In: *JCAP* 10 (2015), p. 051. DOI: 10.1088/1475-7516/2015/10/051. arXiv: 1507.00568 [gr-qc].

[20] F. W. Dyson, A. S. Eddington, and C. Davidson. "A Determination of the Deflection of Light by the Sun's Gravitational Field, from Observations Made at the Total Eclipse of May 29, 1919". In: *Philosophical Transactions of the Royal Society of London Series A* 220 (Jan. 1920), pp. 291–333. DOI: 10.1098/rsta.1920.0009.

[21] S. B. Lambert and C. Le Poncin-Lafitte. "Determination of the relativistic parameter gamma using very long baseline interferometry". In: *Astron. Astrophys.* 499 (2009), p. 331. DOI: 10.1051/0004-6361/200911714. arXiv: 0903.1615 [gr-qc].

[22] A. S. Bolton, S. Rappaport, and S. Burles. "Constraint on the Post-Newtonian Parameter gamma on Galactic Size Scales". In: *Phys. Rev. D* 74 (2006), p. 061501. DOI: 10.1103/PhysRevD.74.061501. arXiv: astro-ph/0607657.

[23] T. Prusti et al. "The Gaia Mission". In: *Astron. Astrophys.* 595.Gaia Data Release 1 (2016), A1. DOI: 10.1051/0004-6361/201629272. arXiv: 1609.04153 [astro-ph.IM].

[24] F. Mignard and S. A. Klioner. "Gaia: Relativistic modelling and testing". In: *Proceedings of the International Astronomical Union* 5.S261 (2009), 306–314. DOI: 10.1017/S174392130999055X.

[25] I. I. Shapiro. "Fourth Test of General Relativity". In: *Phys. Rev. Lett.* 13 (1964), pp. 789–791. DOI: 10.1103/PhysRevLett.13.789.

[26] M. Pössel. "The Shapiro time delay and the equivalence principle". In: (Dec. 2019). arXiv: 2001.00229 [gr-qc].

[27] I. I. Shapiro et al. "Fourth Test of General Relativity: Preliminary Results". In: *Phys. Rev. Lett.* 20 (1968), pp. 1265–1269. DOI: 10.1103/PhysRevLett.20.1265.

[28] I. I. Shapiro et al. "Fourth test of general relativity - new radar result". In: *Phys. Rev. Lett.* 26 (1971), pp. 1132–1135. DOI: 10.1103/PhysRevLett.26.1132.

[29] B. Bertotti, L. Iess, and P. Tortora. "A test of general relativity using radio links with the Cassini spacecraft". In: *Nature* 425.6956 (Sept. 2003), pp. 374–376. DOI: 10.1038/nature01997.

[30] A. Einstein. "Erklärung der Perihelbewegung des Merkur aus der allgemeinen Relativitätstheorie". In: *Sitzungsberichte der Königlich Preußischen Akademie der Wissenschaften (Berlin* (Jan. 1915), pp. 831–839.

[31] A. Fienga et al. "INPOP new release: INPOP13b". In: *arXiv e-prints*, arXiv:1405.0484 (May 2014), arXiv:1405.0484. arXiv: 1405.0484 [astro-ph.EP].

[32] A. Genova et al. "Geodesy, Geophysics and Fundamental Physics Investigations of the BepiColombo Mission". In: *Space Sci. Rev.* 217.2 (2021), p. 31. DOI: 10.1007/s11214-021-00808-9.

[33] K. Nordtvedt. "Equivalence Principle for Massive Bodies. 1. Phenomenology". In: *Phys. Rev.* 169 (1968), pp. 1014–1016. DOI: 10.1103/PhysRev.169.1014.

[34] P. G. Roll, R. Krotkov, and R. H. Dicke. "The Equivalence of inertial and passive gravitational mass". In: *Annals Phys.* 26 (1964), pp. 442–517. DOI: 10.1016/0003-4916(64)90259-3.

[35] F. Hofmann and J. Müller. "Relativistic tests with lunar laser ranging". In: *Class. Quant. Grav.* 35.3 (2018), p. 035015. DOI: 10.1088/1361-6382/aa8f7a.

[36] S. M. Merkowitz. "Tests of Gravity Using Lunar Laser Ranging". In: *Living Rev. Rel.* 13 (2010), p. 7. DOI: 10.12942/lrr-2010-7.

[37] T. W. Murphy Jr. et al. "APOLLO: millimeter lunar laser ranging". In: *Class. Quant. Grav.* 29 (2012), p. 184005. DOI: 10.1088/0264-9381/29/18/184005.

[38] A. M. Archibald et al. "Universality of free fall from the orbital motion of a pulsar in a stellar triple system". In: *Nature* 559.7712 (2018), pp. 73–76. DOI: 10.1038/s41586-018-0265-1. arXiv: 1807.02059 [astro-ph.HE].

[39] G. Voisin et al. "An improved test of the strong equivalence principle with the pulsar in a triple star system". In: *Astron. Astrophys.* 638 (2020), A24. DOI: 10.1051/0004-6361/202038104. arXiv: 2005.01388 [gr-qc].

[40] A. Hewish et al. "Observation of a Rapidly Pulsating Radio Source". In: *Nature* 217.5130 (Feb. 1968), pp. 709–713. DOI: 10.1038/217709a0.

[41] T. Gold. "Rotating neutron stars as the origin of the pulsating radio sources". In: *Nature* 218 (1968), pp. 731–732. DOI: 10.1038/218731a0.

[42] F Pacini. "Rotating Neutron Stars, Pulsars and Supernova Remnants". In: *Nature* 219 (1968), pp. 145–146. DOI: 10.1038/219145a0.

[43] T. Gold. "Rotating Neutron Stars and the Nature of Pulsars". In: *Nature* 221.5175 (Jan. 1969), pp. 25–27. DOI: 10.1038/221025a0.

[44] D. H. Staelin and E. C. Reifenstein. "Pulsating Radio Sources near the Crab Nebula". In: *Science* 162.3861 (1968), pp. 1481–1483. ISSN: 0036-8075. DOI: 10.1126/science.162.3861.1481. eprint: https://science.sciencemag.org/content/162/3861/1481.full.pdf. URL: https://science.sciencemag.org/content/162/3861/1481.

[45] D. C. Backer et al. "A millisecond pulsar". In: *Nature* 300.5893 (Dec. 1982), pp. 615–618. DOI: 10.1038/300615a0.

[46] D. Bhattacharya and E. P. J. van den Heuvel. "Formation and evolution of binary and millisecond radio pulsars". In: *physrep* 203.1-2 (Jan. 1991), pp. 1–124. DOI: 10.1016/0370-1573(91)90064-S.

[47] D. R. Lorimer. "Binary and Millisecond Pulsars". In: *Living Rev. Rel.* 11 (2008), p. 8. DOI: 10.12942/lrr-2008-8. arXiv: 0811.0762 [astro-ph].

[48] F. D'Antona and M. Tailo. "Origin and binary evolution of millisecond pulsars". In: (Nov. 2020). arXiv: 2011.11385 [astro-ph.HE].

[49] R. A. Hulse and J. H. Taylor. "Discovery of a pulsar in a binary system". In: *Astrophys. J.* 195 (1975), pp. L51–L53. DOI: 10.1086/181708.

[50] J. H. Taylor and J. M. Weisberg. "A new test of general relativity: Gravitational radiation and the binary pulsar PS R 1913+16". In: *Astrophys. J.* 253 (1982), pp. 908–920. DOI: 10.1086/159690.

[51] I. H. Stairs. "Testing general relativity with pulsar timing". In: *Living Rev. Rel.* 6 (2003), p. 5. DOI: 10.12942/lrr-2003-5. arXiv: astro-ph/0307536.

[52] N. Wex. "Testing Relativistic Gravity with Radio Pulsars". In: (Feb. 2014). arXiv: 1402.5594 [gr-qc].

[53] M. E. Pati and C. M. Will. "PostNewtonian gravitational radiation and equations of motion via direct integration of the relaxed Einstein equations. 1. Foundations". In: *Phys. Rev. D* 62 (2000), p. 124015. DOI: 10.1103/PhysRevD.62.124015. arXiv: gr-qc/0007087.

[54] M. E. Pati and C. M. Will. "PostNewtonian gravitational radiation and equations of motion via direct integration of the relaxed Einstein equations. 2. Two-body equations of motion to second postNewtonian order, and radiation reaction to 3.5 postNewtonia order". In: *Phys. Rev. D* 65 (2002), p. 104008. DOI: 10.1103/PhysRevD.65.104008. arXiv: gr-qc/0201001.

[55] T. Futamase and Y. Itoh. "The post-Newtonian approximation for relativistic compact binaries". In: *Living Rev. Rel.* 10 (2007), p. 2. DOI: 10.12942/lrr-2007-2.

[56] L. Blanchet. "Gravitational Radiation from Post-Newtonian Sources and Inspiralling Compact Binaries". In: *Living Rev. Rel.* 17 (2014), p. 2. DOI: 10.12942/lrr-2014-2. arXiv: 1310.1528 [gr-qc].

[57] D. M. Eardley. "Observable effects of a scalar gravitational field in a binary pulsar". In: *The Astrophysical Journal* 196 (Feb. 1975), pp. L59–L62. DOI: 10.1086/181744.

[58] T. Damour and G. Esposito-Farese. "Tensor - scalar gravity and binary pulsar experiments". In: *Phys. Rev. D* 54 (1996), pp. 1474–1491. DOI: 10.1103/PhysRevD.54.1474. arXiv: gr-qc/9602056.

[59] J. Alsing et al. "Gravitational radiation from compact binary systems in the massive Brans-Dicke theory of gravity". In: *Phys. Rev. D* 85 (2012), p. 064041. DOI: 10.1103/PhysRevD.85.064041. arXiv: 1112.4903 [gr-qc].

[60] S. Mirshekari and C. M. Will. "Compact binary systems in scalar-tensor gravity: Equations of motion to 2.5 post-Newtonian order". In: *Phys. Rev. D* 87.8 (2013), p. 084070. DOI: 10.1103/PhysRevD.87.084070. arXiv: 1301.4680 [gr-qc].

[61] R. N. Lang. "Gravitational radiation from compact binaries in scalar-tensor gravity". In: *J. Phys. Conf. Ser.* 610.1 (2015). Ed. by G. Ciani, J. W. Conklin, and G. Mueller, p. 012045. DOI: 10.1088/1742-6596/610/1/012045. arXiv: 1408.0860 [gr-qc].

[62] R. N. Lang. "Compact binary systems in scalar-tensor gravity. II. Tensor gravitational waves to second post-Newtonian order". In: *Phys. Rev. D* 89.8 (2014), p. 084014. DOI: 10.1103/PhysRevD.89.084014. arXiv: 1310.3320 [gr-qc].

[63] R. N. Lang. "Compact binary systems in scalar-tensor gravity. III. Scalar waves and energy flux". In: *Phys. Rev. D* 91.8 (2015), p. 084027. DOI: 10.1103/PhysRevD.91.084027. arXiv: 1411.3073 [gr-qc].

[64] L. Bernard. "Dynamics of compact binary systems in scalar-tensor theories: II. Center-of-mass and conserved quantities to 3PN order". In: *Phys. Rev. D* 99.4 (2019), p. 044047. DOI: 10.1103/PhysRevD.99.044047. arXiv: 1812.04169 [gr-qc].

[65] L. Bernard. "Dynamics of compact binary systems in scalar-tensor theories: Equations of motion to the third post-Newtonian order". In: *Phys. Rev. D* 98.4 (2018), p. 044004. DOI: 10.1103/PhysRevD.98.044004. arXiv: 1802.10201 [gr-qc].

[66] J. M. Weisberg, D. J. Nice, and J. H. Taylor. "Timing Measurements of the Relativistic Binary Pulsar PSR B1913+16". In: *Astrophys. J.* 722 (2010), pp. 1030–1034. DOI: 10.1088/0004-637X/722/2/1030. arXiv: 1011.0718 [astro-ph.GA].

[67] T. Damour and J. H. Taylor. "Strong field tests of relativistic gravity and binary pulsars". In: *Phys. Rev. D* 45 (1992), pp. 1840–1868. DOI: 10.1103/PhysRevD.45.1840.

[68] R. Blandford and S. A. Teukolsky. "Arrival-time analysis for a pulsar in a binary system." In: *APJ* 205 (Apr. 1976), pp. 580–591. DOI: 10.1086/154315.

[69] T. Damour and N. Deruelle. "General relativistic celestial mechanics of binary systems. I. The post-newtonian motion". en. In: *Annales de l'I.H.P. Physique théorique* 43.1 (1985), pp. 107–132. URL: http://www.numdam.org/item/AIHPA_1985__43_1_107_0/.

[70] T. Damour and N. Deruelle. "General relativistic celestial mechanics of binary systems. II. The post-newtonian timing formula". en. In: *Annales de l'I.H.P. Physique théorique* 44.3 (1986), pp. 263–292. URL: http://www.numdam.org/item/AIHPA_1986__44_3_263_0/.

[71] J. H. Taylor, L. A. Fowler, and P. M. McCulloch. "Measurements of general relativistic effects in the binary pulsar PSR 1913+16". In: *Nature* 277 (1979), pp. 437–440. DOI: 10.1038/277437a0.

[72] M. Kramer and I. Stairs. "The Double Pulsar". In: *Annual Review of Astronomy and Astrophysics* 46.1 (2008), pp. 541–572. DOI: 10.1146/annurev.astro.46.060407.145247. eprint: https://doi.org/10.1146/annurev.astro.46.060407.145247. URL: https://doi.org/10.1146/annurev.astro.46.060407.145247.

[73] M Kramer and N Wex. "The double pulsar system: a unique laboratory for gravity". In: *Classical and Quantum Gravity* 26.7 (2009), p. 073001. DOI: 10.1088/0264-9381/26/7/073001. URL: https://doi.org/10.1088/0264-9381/26/7/073001.

[74] J. Antoniadis et al. "The relativistic pulsar-white dwarf binary PSR J1738+0333 I. Mass determination and evolutionary history". In: *Mon. Not. Roy. Astron. Soc.* 423 (2012), p. 3316. DOI: 10.1111/j.1365-2966.2012.21124.x. arXiv: 1204.3948 [astro-ph.HE].

[75] J. M. Gerard and Y. Wiaux. "Gravitational dipole radiations from binary systems". In: *Phys. Rev. D* 66 (2002), p. 024040. DOI: 10.1103/PhysRevD.66.024040. arXiv: gr-qc/0109062.

[76] P. C. C. Freire et al. "The relativistic pulsar-white dwarf binary PSR J1738+0333 II. The most stringent test of scalar-tensor gravity". In: *Mon. Not. Roy. Astron. Soc.* 423 (2012), p. 3328. DOI: 10.1111/j.1365-2966.2012.21253.x. arXiv: 1205.1450 [astro-ph.GA].

[77] C. Bambi. "Astrophysical Black Holes: A Compact Pedagogical Review". In: *Annalen Phys.* 530 (2018), p. 1700430. DOI: 10.1002/andp.201700430. arXiv: 1711.10256 [gr-qc].

[78] R. A. Remillard and J. E. McClintock. "X-ray Properties of Black-Hole Binaries". In: *Ann. Rev. Astron. Astrophys.* 44 (2006), pp. 49–92. DOI: 10.1146/annurev.astro.44.051905.092532. arXiv: astro-ph/0606352.

[79] C. Bambi. "Testing General Relativity with Black Hole X-ray Data". In: *4th Zeldovich Meeting: An international conference in honor of Ya. B. Zeldovich*. Oct. 2020. arXiv: 2010.03793 [gr-qc].

[80] L. W. Brenneman and C. S. Reynolds. "Constraining Black Hole Spin Via X-ray Spectroscopy". In: *Astrophys. J.* 652 (2006), pp. 1028–1043. DOI: 10.1086/508146. arXiv: astro-ph/0608502.

[81] C. S. Reynolds. "Observing black holes spin". In: *Nature Astron.* 3.1 (2019), pp. 41–47. DOI: 10.1038/s41550-018-0665-z. arXiv: 1903.11704 [astro-ph.HE].

[82] M. Zhou et al. "Modeling uncertainties in X-ray reflection spectroscopy measurements I: Impact of higher order disk images". In: *Phys. Rev. D* 101.4 (2020), p. 043010. DOI: 10.1103/PhysRevD.101.043010. arXiv: 1910.12494 [gr-qc].

[83] A. Cardenas-Avendano, M. Zhou, and C. Bambi. "Modeling uncertainties in X-ray reflection spectroscopy measurements II: Impact of the radiation from the plunging region". In: *Phys. Rev. D* 101.12 (2020), p. 123014. DOI: 10.1103/PhysRevD.101.123014. arXiv: 2005.06719 [astro-ph.HE].

[84] S. N. Zhang, W. Cui, and W. Chen. "Black hole spin in X-ray binaries: Observational consequences". In: *Astrophys. J. Lett.* 482 (1997), p. L155. DOI: 10.1086/310705. arXiv: astro-ph/9704072.

[85] J. E. McClintock, R. Narayan, and J. F. Steiner. "Black Hole Spin via Continuum Fitting and the Role of Spin in Powering Transient Jets". In: *Space Sci. Rev.* 183 (2014), pp. 295–322. DOI: 10.1007/s11214-013-0003-9. arXiv: 1303.1583 [astro-ph.HE].

[86] T. Johannsen. "Regular Black Hole Metric with Three Constants of Motion". In: *Phys. Rev. D* 88.4 (2013), p. 044002. DOI: 10.1103/PhysRevD.88.044002. arXiv: 1501.02809 [gr-qc].

[87] L. Rezzolla and A. Zhidenko. "New parametrization for spherically symmetric black holes in metric theories of gravity". In: *Phys. Rev. D* 90.8 (2014), p. 084009. DOI: 10.1103/PhysRevD.90.084009. arXiv: 1407.3086 [gr-qc].

[88] A. Cardenas-Avendano et al. "Experimental Relativity with Accretion Disk Observations". In: *Phys. Rev. D* 100.2 (2019), p. 024039. DOI: 10.1103/PhysRevD.100.024039. arXiv: 1903.04356 [gr-qc].

[89] A. Cardenas-Avendano, S. Nampalliwar, and N. Yunes. "Gravitational-wave versus X-ray tests of strong-field gravity". In: *Class. Quant. Grav.* 37.13 (2020), p. 135008. DOI: 10.1088/1361-6382/ab8f64. arXiv: 1912.08062 [gr-qc].

[90] A. Tripathi et al. "Testing general relativity with the stellar-mass black hole in LMC X-1 using the continuum-fitting method". In: *Astrophys. J.* 897.1 (2020), p. 84. DOI: 10.3847/1538-4357/ab9600. arXiv: 2001.08391 [gr-qc].

[91] Z. Cao et al. "Iron Kα line of boson stars". In: *JCAP* 10 (2016), p. 003. DOI: 10.1088/1475-7516/2016/10/003. arXiv: 1609.00901 [gr-qc].

[92] Y. Ni et al. "Iron Kα line of Kerr black holes with scalar hair". In: *JCAP* 07 (2016), p. 049. DOI: 10.1088/1475-7516/2016/07/049. arXiv: 1606.04654 [gr-qc].

[93] M. Zhou et al. "Singularity-free black holes in conformal gravity: New observational constraints". In: *EPL* 125.3 (2019), p. 30002. DOI: 10.1209/0295-5075/125/30002. arXiv: 2003.03738 [gr-qc].

[94] J. Zhu et al. "X-ray reflection spectroscopy with Kaluza-Klein black holes". In: *Eur. Phys. J. C* 80 (2020), p. 622. DOI: 10.1140/epjc/s10052-020-8198-x. arXiv: 2005.00184 [gr-qc].

[95] A. Tripathi et al. "Testing General Relativity with NuSTAR data of Galactic Black Holes". In: *Astrophys. J.* 913.2 (2021), p. 79. DOI: 10.3847/1538-4357/abf6cd. arXiv: 2012.10669 [astro-ph.HE].

[96] C. Bambi and E. Barausse. "Constraining the quadrupole moment of stellar-mass black-hole candidates with the continuum fitting method". In: *Astrophys. J.* 731 (2011), p. 121. DOI: 10.1088/0004-637X/731/2/121. arXiv: 1012.2007 [gr-qc].

[97] C. Bambi. "A code to compute the emission of thin accretion disks in non-Kerr space-times and test the nature of black hole candidates". In: *Astrophys. J.* 761 (2012), p. 174. DOI: 10.1088/0004-637X/761/2/174. arXiv: 1210.5679 [gr-qc].

[98] M. Zhou et al. "XSPEC model for testing the Kerr black hole hypothesis using the continuum-fitting method". In: *Phys. Rev. D* 99.10 (2019), p. 104031. DOI: 10.1103/PhysRevD.99.104031. arXiv: 1903.09782 [gr-qc].

[99] M. van der Klis. "A Review of rapid x-ray variability in x-ray binaries". In: (Oct. 2004). arXiv: astro-ph/0410551.

[100] K. Rink, I. Caiazzo, and J. Heyl. "Testing General Relativity using Quasi-Periodic Oscillations from X-ray Black Holes: XTE J1550-564 and GRO J1655-40". In: (July 2021). arXiv: 2107.06828 [astro-ph.HE].

[101] *The Event Horizon Telescope and Global mm-VLBI Array on the Earth*. https://www.eso.org/public/images/ann17015a/.

[102] K. Akiyama et al. "First M87 Event Horizon Telescope Results. I. The Shadow of the Supermassive Black Hole". In: *Astrophys. J.* 875.1 (2019), p. L1. DOI: 10.3847/2041-8213/ab0ec7. arXiv: 1906.11238 [astro-ph.GA].

[103] K. Akiyama et al. "First M87 Event Horizon Telescope Results. VI. The Shadow and Mass of the Central Black Hole". In: *Astrophys. J. Lett.* 875.1 (2019), p. L6. DOI: 10.3847/2041-8213/ab1141. arXiv: 1906.11243 [astro-ph.GA].

[104] M. Schmidt. "3C 273 : A Star-Like Object with Large Red-Shift". In: *NAT* 197.4872 (Mar. 1963), p. 1040. DOI: 10.1038/1971040a0.

[105] D. Lynden-Bell. "Galactic nuclei as collapsed old quasars". In: *Nature* 223 (1969), p. 690. DOI: 10.1038/223690a0.

[106] D. B. Sanders et al. "Continuum Energy Distributions of Quasars: Shapes and Origins". In: *APJ* 347 (Dec. 1989), p. 29. DOI: 10.1086/168094.

[107] N. I. Shakura and R. A. Sunyaev. "Black holes in binary systems. Observational appearance". In: *Astron. Astrophys.* 24 (1973), pp. 337–355.

[108] A. Eckart and R. Genzel. "Stellar proper motions in the central 0.1 PC of the Galaxy". In: *MNRAS* 284.3 (Jan. 1997), pp. 576–598. DOI: 10.1093/mnras/284.3.576.

[109] A. M. Ghez et al. "High Proper-Motion Stars in the Vicinity of Sagittarius A*: Evidence for a Supermassive Black Hole at the Center of Our Galaxy". In: *APJ* 509.2 (Dec. 1998), pp. 678–686. DOI: 10.1086/306528. arXiv: astro-ph/9807210 [astro-ph].

[110] R. Abuter et al. "Detection of orbital motions near the last stable circular orbit of the massive black hole SgrA*". In: *Astron. & Astrophys.* 618 (Oct. 2018), p. L10. DOI: 10.1051/0004-6361/201834294. arXiv: 1810.12641 [astro-ph.GA].

[111] K. Gebhardt et al. "The Black Hole Mass in M87 from Gemini/NIFS Adaptive Optics Observations". In: *APJ* 729.2, 119 (Mar. 2011), p. 119. DOI: 10.1088/0004-637X/729/2/119. arXiv: 1101.1954 [astro-ph.CO].

[112] J. L. Walsh et al. "The M87 Black Hole Mass from Gas-dynamical Models of Space Telescope Imaging Spectrograph Observations". In: *APJ* 770.2, 86 (June 2013), p. 86. DOI: 10.1088/0004-637X/770/2/86. arXiv: 1304.7273 [astro-ph.CO].

[113] R. Narayan and I.-s. Yi. "Advection dominated accretion: A Selfsimilar solution". In: *Astrophys. J.* 428 (1994), p. L13. DOI: 10.1086/187381. arXiv: astro-ph/9403052 [astro-ph].

[114] R. Narayan and I. Yi. "Advection-dominated Accretion: Self-Similarity and Bipolar Outflows". In: *Astrophys. J.* 444 (1995), p. 231. DOI: 10.1086/175599. arXiv: astro-ph/9411058 [astro-ph].

[115] R. Narayan and I. Yi. "Advection-dominated Accretion: Underfed Black Holes and Neutron Stars". In: *Astrophys. J.* 452 (1995), p. 710. DOI: 10.1086/176343. arXiv: astro-ph/9411059 [astro-ph].

[116] H. Falcke, K. Mannheim, and P. L. Biermann. "The Galactic Center radio jet." In: *aap* 278 (Oct. 1993), pp. L1–L4. arXiv: astro-ph/9308031 [astro-ph].

[117] L. C. Ho. "The Spectral Energy Distributions of Low-Luminosity Active Galactic Nuclei". In: *APJ* 516.2 (May 1999), pp. 672–682. DOI: 10.1086/307137. arXiv: astro-ph/9905012 [astro-ph].

[118] F. Yuan, S. Markoff, and H. Falcke. "A Jet-ADAF model for Sgr A*". In: *aap* 383 (Mar. 2002), pp. 854–863. DOI: 10.1051/0004-6361:20011709. arXiv: astro-ph/0112464 [astro-ph].

[119] H. Falcke, F. Melia, and E. Agol. "The shadow of the black hole at the galactic center". In: *Cosmic Explosions: Tenth AstroPhysics Conference*. Ed. by S. S. Holt and W. W. Zhang. Vol. 522. American Institute of Physics Conference Series. June 2000, pp. 317–320. DOI: 10.1063/1.1291730.

[120] K. Schwarzschild. "Über das Gravitationsfeld eines Massenpunktes nach der Einsteinschen Theorie". In: *Sitzungsberichte der Königlich Preußischen Akademie der Wissenschaften (Berlin), 1916, Seite 189-196* (1916).

[121] R. P. Kerr. "Gravitational Field of a Spinning Mass as an Example of Algebraically Special Metrics". In: *PRL* 11.5 (Sept. 1963), pp. 237–238. DOI: 10.1103/PhysRevLett.11.237.

[122] J. M. Bardeen. "Timelike and null geodesics in the Kerr metric." In: *Black Holes (Les Astres Occlus)*. Jan. 1973, pp. 215–239.

[123] R. Takahashi. "Shapes and Positions of Black Hole Shadows in Accretion Disks and Spin Parameters of Black Holes". In: *APJ* 611.2 (Aug. 2004), pp. 996–1004. DOI: 10.1086/422403. arXiv: astro-ph/0405099 [astro-ph].

[124] T. Johannsen and D. Psaltis. "Testing the No-hair Theorem with Observations in the Electromagnetic Spectrum. II. Black Hole Images". In: *APJ* 718.1 (July 2010), pp. 446–454. DOI: 10.1088/0004-637X/718/1/446. arXiv: 1005.1931 [astro-ph.HE].

[125] J. P. Luminet. "Image of a spherical black hole with thin accretion disk." In: *AAP* 75 (May 1979), pp. 228–235.

[126] S. C. Noble et al. "Simulating the emission and outflows from accretion discs". In: *Classical and Quantum Gravity* 24.12 (June 2007), S259–S274. DOI: 10.1088/0264-9381/24/12/S17. arXiv: astro-ph/0701778 [astro-ph].

[127] A. E. Broderick and A. Loeb. "Imaging the Black Hole Silhouette of M87: Implications for Jet Formation and Black Hole Spin". In: *APJ* 697.2 (June 2009), pp. 1164–1179. DOI: 10.1088/0004-637X/697/2/1164. arXiv: 0812.0366 [astro-ph].

[128] A. B. Kamruddin and J. Dexter. "A geometric crescent model for black hole images". In: *MNRAS* 434.1 (Sept. 2013), pp. 765–771. DOI: 10.1093/mnras/stt1068. arXiv: 1306.3226 [astro-ph.HE].

[129] R.-S. Lu et al. "Imaging the Supermassive Black Hole Shadow and Jet Base of M87 with the Event Horizon Telescope". In: *APJ* 788.2, 120 (June 2014), p. 120. DOI: 10.1088/0004-637X/788/2/120. arXiv: 1404.7095 [astro-ph.IM].

[130] K. Akiyama et al. "First M87 Event Horizon Telescope Results. V. Physical Origin of the Asymmetric Ring". In: *Astrophys. J. Lett.* 875.1 (2019), p. L5. DOI: 10.3847/2041-8213/ab0f43. arXiv: 1906.11242 [astro-ph.GA].

[131] K. Akiyama et al. "First M87 Event Horizon Telescope Results. II. Array and Instrumentation". In: *Astrophys. J. Lett.* 875.1 (2019), p. L2. DOI: 10.3847/2041-8213/ab0c96. arXiv: 1906.11239 [astro-ph.IM].

[132] G. S. Bisnovatyi-Kogan and O. Y. Tsupko. "Gravitational Lensing in Presence of Plasma: Strong Lens Systems, Black Hole Lensing and Shadow". In: *Universe* 3.3 (2017), p. 57. DOI: 10.3390/universe3030057. arXiv: 1905.06615 [gr-qc].

[133] Y. Mizuno et al. "The Current Ability to Test Theories of Gravity with Black Hole Shadows". In: *Nature Astron.* 2.7 (2018), pp. 585–590. DOI: 10.1038/s41550-018-0449-5. arXiv: 1804.05812 [astro-ph.GA].

[134] D. Psaltis. "Testing General Relativity with the Event Horizon Telescope". In: *Gen. Rel. Grav.* 51.10 (2019), p. 137. DOI: 10.1007/s10714-019-2611-5. arXiv: 1806.09740 [astro-ph.HE].

[135] P. V. P. Cunha and C. A. R. Herdeiro. "Shadows and strong gravitational lensing: a brief review". In: *Gen. Rel. Grav.* 50.4 (2018), p. 42. DOI: 10.1007/s10714-018-2361-9. arXiv: 1801.00860 [gr-qc].

[136] P. G. Nedkova, V. K. Tinchev, and S. S. Yazadjiev. "Shadow of a rotating traversable wormhole". In: *Phys. Rev. D* 88.12 (2013), p. 124019. DOI: 10.1103/PhysRevD.88.124019. arXiv: 1307.7647 [gr-qc].

[137] H. Olivares et al. "How to tell an accreting boson star from a black hole". In: *Mon. Not. Roy. Astron. Soc.* 497.1 (2020), pp. 521–535. DOI: 10.1093/mnras/staa1878. arXiv: 1809.08682 [gr-qc].

[138] R. Shaikh et al. "Shadows of spherically symmetric black holes and naked singularities". In: *Mon. Not. Roy. Astron. Soc.* 482.1 (2019), pp. 52–64. DOI: 10.1093/mnras/sty2624. arXiv: 1802.08060 [astro-ph.HE].

[139] D. Dey, R. Shaikh, and P. S. Joshi. "Shadow of nulllike and timelike naked singularities without photon spheres". In: *Phys. Rev. D* 103.2 (2021), p. 024015. DOI: 10.1103/PhysRevD.103.024015. arXiv: 2009.07487 [gr-qc].

[140] C. A. R. Herdeiro et al. "The imitation game: Proca stars that can mimic the Schwarzschild shadow". In: *JCAP* 04 (2021), p. 051. DOI: 10.1088/1475-7516/2021/04/051. arXiv: 2102.01703 [gr-qc].

[141] C. Bambi and K. Freese. "Apparent shape of super-spinning black holes". In: *Phys. Rev. D* 79 (2009), p. 043002. DOI: 10.1103/PhysRevD.79.043002. arXiv: 0812.1328 [astro-ph].

[142] C. Bambi and N. Yoshida. "Shape and position of the shadow in the $\delta = 2$ Tomimatsu-Sato space-time". In: *Class. Quant. Grav.* 27 (2010), p. 205006. DOI: 10.1088/0264-9381/27/20/205006. arXiv: 1004.3149 [gr-qc].

[143] L. Amarilla, E. F. Eiroa, and G. Giribet. "Null geodesics and shadow of a rotating black hole in extended Chern-Simons modified gravity". In: *Phys. Rev. D* 81 (2010), p. 124045. DOI: 10.1103/PhysRevD.81.124045. arXiv: 1005.0607 [gr-qc].

[144] L. Amarilla and E. F. Eiroa. "Shadow of a Kaluza-Klein rotating dilaton black hole". In: *Phys. Rev. D* 87.4 (2013), p. 044057. DOI: 10.1103/PhysRevD.87.044057. arXiv: 1301.0532 [gr-qc].

[145] S.-W. Wei and Y.-X. Liu. "Observing the shadow of Einstein-Maxwell-Dilaton-Axion black hole". In: *JCAP* 11 (2013), p. 063. DOI: 10.1088/1475-7516/2013/11/063. arXiv: 1311.4251 [gr-qc].

[146] F. Atamurotov, S. G. Ghosh, and B. Ahmedov. "Horizon structure of rotating Einstein–Born–Infeld black holes and shadow". In: *Eur. Phys. J. C* 76.5 (2016), p. 273. DOI: 10.1140/epjc/s10052-016-4122-9. arXiv: 1506.03690 [gr-qc].

[147] A. Abdujabbarov et al. "Shadow of rotating regular black holes". In: *Phys. Rev. D* 93.10 (2016), p. 104004. DOI: 10.1103/PhysRevD.93.104004. arXiv: 1604.03809 [gr-qc].

[148] P. V. P. Cunha, C. A. R. Herdeiro, and E. Radu. "Spontaneously Scalarized Kerr Black Holes in Extended Scalar-Tensor–Gauss-Bonnet Gravity". In: *Phys. Rev. Lett.* 123.1 (2019), p. 011101. DOI: 10.1103/PhysRevLett.123.011101. arXiv: 1904.09997 [gr-qc].

[149] C. A. R. Herdeiro et al. "Spin-induced scalarized black holes". In: *Phys. Rev. Lett.* 126.1 (2021), p. 011103. DOI: 10.1103/PhysRevLett.126.011103. arXiv: 2009.03904 [gr-qc].

[150] P. Kocherlakota et al. "Constraints on black-hole charges with the 2017 EHT observations of M87*". In: *Phys. Rev. D* 103.10 (2021), p. 104047. DOI: 10.1103/PhysRevD.103.104047. arXiv: 2105.09343 [gr-qc].

[151] S. H. Völkel et al. "EHT tests of the strong-field regime of General Relativity". In: (Nov. 2020). arXiv: 2011.06812 [gr-qc].

[152] J. M. Antelis and C. Moreno. "Obtaining gravitational waves from inspiral binary systems using LIGO data". In: *Eur. Phys. J. Plus* 132.1 (2017). [Erratum: Eur.Phys.J.Plus 132, 103 (2017)], p. 10. DOI: 10.1140/epjp/i2017-11283-5. arXiv: 1610.03567 [astro-ph.IM].

[153] A. Einstein and N. Rosen. "On Gravitational Waves". In: *Journal of The Franklin Institute* 223 (Jan. 1937), pp. 43–54. DOI: 10.1016/S0016-0032(37)90583-0.

[154] D. Kennefick. "Einstein Versus the Physical Review". In: *Physics Today* 58.9 (Jan. 2005), p. 43. DOI: 10.1063/1.2117822.

[155] B. P. Abbott et al. "Observation of Gravitational Waves from a Binary Black Hole Merger". In: *Phys. Rev. Lett.* 116.6 (2016), p. 061102. DOI: 10.1103/PhysRevLett.116.061102. arXiv: 1602.03837 [gr-qc].

[156] B. P. Abbott et al. "GW170817: Observation of Gravitational Waves from a Binary Neutron Star Inspiral". In: *Phys. Rev. Lett.* 119.16 (2017), p. 161101. DOI: 10.1103/PhysRevLett.119.161101. arXiv: 1710.05832 [gr-qc].

[157] B. P. Abbott et al. "GW190425: Observation of a Compact Binary Coalescence with Total Mass $\sim 3.4 M_{\odot}$". In: *Astrophys. J. Lett.* 892.1 (2020), p. L3. DOI: 10.3847/2041-8213/ab75f5. arXiv: 2001.01761 [astro-ph.HE].

[158] R. Abbott et al. "Observation of Gravitational Waves from Two Neutron Star–Black Hole Coalescences". In: *Astrophys. J. Lett.* 915.1 (2021), p. L5. DOI: 10.3847/2041-8213/ac082e. arXiv: 2106.15163 [astro-ph.HE].

[159] J. Aasi et al. "Advanced LIGO". In: *Class. Quant. Grav.* 32 (2015), p. 074001. DOI: 10.1088/0264-9381/32/7/074001. arXiv: 1411.4547 [gr-qc].

[160] F. Acernese et al. "Advanced Virgo: a second-generation interferometric gravitational wave detector". In: *Class. Quant. Grav.* 32.2 (2015), p. 024001. DOI: 10.1088/0264-9381/32/2/024001. arXiv: 1408.3978 [gr-qc].

[161] T. Tomaru. "KAGRA-Large-scale Cryogenic Gravitational wave Telescope". In: *12th International Conference on Gravitation, Astrophysics and Cosmology*. 2016. DOI: 10.1142/9789814759816_0022.

[162] M. Punturo et al. "The third generation of gravitational wave observatories and their science reach". In: *Class. Quant. Grav.* 27 (2010). Ed. by Z. Marka and S. Marka, p. 084007. DOI: 10.1088/0264-9381/27/8/084007.

[163] D. Reitze et al. "Cosmic Explorer: The U.S. Contribution to Gravitational-Wave Astronomy beyond LIGO". In: *Bull. Am. Astron. Soc.* 51.7 (2019), p. 035. arXiv: 1907.04833 [astro-ph.IM].

[164] *ESA, LISA science requirements document (SciRD)*. https://www.cosmos.esa.int/documents/678316/1700384/SciRD.pdf.

[165] S. Babak, M. Hewitson, and A. Petiteau. "LISA Sensitivity and SNR Calculations". In: (Aug. 2021). arXiv: 2108.01167 [astro-ph.IM].

[166] J. Luo et al. "TianQin: a space-borne gravitational wave detector". In: *Class. Quant. Grav.* 33.3 (2016), p. 035010. DOI: 10.1088/0264-9381/33/3/035010. arXiv: 1512.02076 [astro-ph.IM].

[167] K. Yagi and N. Seto. "Detector configuration of DECIGO/BBO and identification of cosmological neutron-star binaries". In: *Phys. Rev. D* 83 (2011). [Erratum: Phys.Rev.D 95, 109901 (2017)], p. 044011. DOI: 10.1103/PhysRevD.83.044011. arXiv: 1101.3940 [astro-ph.CO].

[168] S. Isoyama, H. Nakano, and T. Nakamura. "Multiband Gravitational-Wave Astronomy: Observing binary inspirals with a decihertz detector, B-DECIGO". In: *PTEP* 2018.7 (2018), 073E01. DOI: 10.1093/ptep/pty078. arXiv: 1802.06977 [gr-qc].

[169] M. V. Sazhin. "Opportunities for detecting ultralong gravitational waves". In: *SOVAST* 22 (Feb. 1978), pp. 36–38.

[170] S. L. Detweiler. "Pulsar timing measurements and the search for gravitational waves". In: *Astrophys. J.* 234 (1979), pp. 1100–1104. DOI: 10.1086/157593.

[171] R. Foster and D. Backer. "Constructing a Pulsar Timing Array". In: *The Astrophysical Journal* 361 (1990), pp. 300–308.

[172] R. N. Manchester et al. "The Parkes Pulsar Timing Array Project". In: *Publ. Astron. Soc. Austral.* 30 (2013), p. 17. DOI: 10.1017/pasa.2012.017. arXiv: 1210.6130 [astro-ph.IM].

[173] M. A. McLaughlin. "The North American Nanohertz Observatory for Gravitational Waves". In: *Class. Quant. Grav.* 30 (2013), p. 224008. DOI: 10.1088/0264-9381/30/22/224008. arXiv: 1310.0758 [astro-ph.IM].

[174] M. Kramer and D. J. Champion. "The European Pulsar Timing Array and the Large European Array for Pulsars". In: *Class. Quant. Grav.* 30 (2013), p. 224009. DOI: 10.1088/0264-9381/30/22/224009.

[175] G. Hobbs et al. "The international pulsar timing array project: using pulsars as a gravitational wave detector". In: *Class. Quant. Grav.* 27 (2010). Ed. by Z. Marka and S. Marka, p. 084013. DOI: 10.1088/0264-9381/27/8/084013. arXiv: 0911.5206 [astro-ph.SR].

[176] C. J. Moore, R. H. Cole, and C. P. L. Berry. "Gravitational-wave sensitivity curves". In: *Class. Quant. Grav.* 32.1 (2015), p. 015014. DOI: 10.1088/0264-9381/32/1/015014. arXiv: 1408.0740 [gr-qc].

[177] E. Abdikamalov, G. Pagliaroli, and D. Radice. "Gravitational Waves from Core-Collapse Supernovae". In: (Oct. 2020). arXiv: 2010.04356 [astro-ph.SR].

[178] A. Mezzacappa et al. "Physical, numerical, and computational challenges of modeling neutrino transport in core-collapse supernovae". In: *Living Reviews in Computational Astrophysics* 6.1, 4 (Dec. 2020), p. 4. DOI: 10.1007/s41115-020-00010-8. arXiv: 2010.09013 [astro-ph.HE].

[179] A. Burrows and D. Vartanyan. "Core-Collapse Supernova Explosion Theory". In: *Nature* 589.7840 (2021), pp. 29–39. DOI: 10.1038/s41586-020-03059-w. arXiv: 2009.14157 [astro-ph.SR].

[180] B. P. Abbott et al. "Optically targeted search for gravitational waves emitted by core-collapse supernovae during the first and second observing runs of advanced LIGO and advanced Virgo". In: *Phys. Rev. D* 101.8 (2020), p. 084002. DOI: 10.1103/PhysRevD.101.084002. arXiv: 1908.03584 [astro-ph.HE].

[181] J. Abadie et al. "A search for gravitational waves associated with the August 2006 timing glitch of the Vela pulsar". In: *Phys. Rev. D* 83 (2011), p. 042001. DOI: 10.1103/PhysRevD.83.042001. arXiv: 1011.1357 [gr-qc].

[182] B. P. Abbott et al. "Search for Transient Gravitational-wave Signals Associated with Magnetar Bursts during Advanced LIGO's Second Observing Run". In: *Astrophys. J.* 874.2 (2019), p. 163. DOI: 10.3847/1538-4357/ab0e15. arXiv: 1902.01557 [astro-ph.HE].

[183] M. Ebersold and S. Tiwari. "Search for nonlinear memory from subsolar mass compact binary mergers". In: *Phys. Rev. D* 101.10 (2020), p. 104041. DOI: 10.1103/PhysRevD.101.104041. arXiv: 2005.03306 [gr-qc].

[184] R. Abbott et al. "Constraints on Cosmic Strings Using Data from the Third Advanced LIGO–Virgo Observing Run". In: *Phys. Rev. Lett.* 126.24 (2021), p. 241102. DOI: 10.1103/PhysRevLett.126.241102. arXiv: 2101.12248 [gr-qc].

[185] R. Abbott et al. "All-sky search for short gravitational-wave bursts in the third Advanced LIGO and Advanced Virgo run". In: (July 2021). arXiv: 2107.03701 [gr-qc].

[186] F. Gittins, N. Andersson, and D. I. Jones. "Modelling neutron star mountains". In: *Mon. Not. Roy. Astron. Soc.* 500.4 (2020), pp. 5570–5582. DOI: 10.1093/mnras/staa3635. arXiv: 2009.12794 [astro-ph.HE].

[187] M. Sieniawska and M. Bejger. "Continuous gravitational waves from neutron stars: current status and prospects". In: *Universe* 5.11 (2019), p. 217. DOI: 10.3390/universe5110217. arXiv: 1909.12600 [astro-ph.HE].

[188] B. Haskell and K. Schwenzer. "Gravitational waves from isolated neutron stars". In: (Apr. 2021). arXiv: 2104.03137 [gr-qc].

[189] B. P. Abbott et al. "Results of the deepest all-sky survey for continuous gravitational waves on LIGO S6 data running on the Einstein@Home volunteer distributed computing project". In: *Phys. Rev. D* 94.10 (2016), p. 102002. DOI: 10.1103/PhysRevD.94.102002. arXiv: 1606.09619 [gr-qc].

[190] C. Dreissigacker, R. Prix, and K. Wette. "Fast and Accurate Sensitivity Estimation for Continuous-Gravitational-Wave Searches". In: *Phys. Rev. D* 98.8 (2018), p. 084058. DOI: 10.1103/PhysRevD.98.084058. arXiv: 1808.02459 [gr-qc].

[191] R. Abbott et al. "All-sky search in early O3 LIGO data for continuous gravitational-wave signals from unknown neutron stars in binary systems". In: *Phys. Rev. D* 103.6 (2021), p. 064017. DOI: 10.1103/PhysRevD.103.064017. arXiv: 2012.12128 [gr-qc].

[192] N. Christensen. "Stochastic Gravitational Wave Backgrounds". In: *Rept. Prog. Phys.* 82.1 (2019), p. 016903. DOI: 10.1088/1361-6633/aae6b5. arXiv: 1811.08797 [gr-qc].

[193] L. P. Grishchuk. "Relic gravitational waves and limits on inflation". In: *Phys. Rev. D* 48 (1993), pp. 3513–3516. DOI: 10.1103/PhysRevD.48.3513. arXiv: gr-qc/9304018.

[194] B. P. Abbott et al. "GW150914: Implications for the stochastic gravitational wave background from binary black holes". In: *Phys. Rev. Lett.* 116.13 (2016), p. 131102. DOI: 10.1103/PhysRevLett.116.131102. arXiv: 1602.03847 [gr-qc].

[195] B. P. Abbott et al. "GW170817: Implications for the Stochastic Gravitational-Wave Background from Compact Binary Coalescences". In: *Phys. Rev. Lett.* 120.9 (2018), p. 091101. DOI: 10.1103/PhysRevLett.120.091101. arXiv: 1710.05837 [gr-qc].

[196] Z. Arzoumanian et al. "The NANOGrav 11-year Data Set: Pulsar-timing Constraints On The Stochastic Gravitational-wave Background". In: *Astrophys. J.* 859.1 (2018), p. 47. DOI: 10.3847/1538-4357/aabd3b. arXiv: 1801.02617 [astro-ph.HE].

[197] Z. Arzoumanian et al. "The NANOGrav 12.5 yr Data Set: Search for an Isotropic Stochastic Gravitational-wave Background". In: *Astrophys. J. Lett.* 905.2 (2020), p. L34. DOI: 10.3847/2041-8213/abd401. arXiv: 2009.04496 [astro-ph.HE].

[198] Z. Arzoumanian et al. "Searching For Gravitational Waves From Cosmological Phase Transitions With The NANOGrav 12.5-year dataset". In: (Apr. 2021). arXiv: 2104.13930 [astro-ph.CO].

[199] J. R. Gair et al. "Testing General Relativity with Low-Frequency, Space-Based Gravitational-Wave Detectors". In: *Living Rev. Rel.* 16 (2013), p. 7. DOI: 10.12942/lrr-2013-7. arXiv: 1212.5575 [gr-qc].

[200] A. Einstein. "Näherungsweise Integration der Feldgleichungen der Gravitation". In: *Sitzungsberichte der Königlich Preußischen Akademie der Wissenschaften (Berlin* (Jan. 1916), pp. 688–696.

[201] W. de Sitter. "Einstein's theory of gravitation and its astronomical consequences, Second Paper". In: *Mon. Not. Roy. Astron. Soc.* 77 (1916), pp. 155–184.

[202] A. Einstein. "Über Gravitationswellen". In: *Sitzungsber. Preuss. Akad. Wiss.* 1 (1918). cited By 265, pp. 154–167.

[203] A. S. Eddington. "The Propagation of Gravitational Waves". In: *Proceedings of the Royal Society of London Series A* 102.716 (Dec. 1922), pp. 268–282. DOI: 10.1098/rspa.1922.0085.

[204] H. A. Lorentz and J. Droste. "The Motion of a System of Bodies under the Influence of their Mutual Attraction, According to Einstein's Theory". In: *Collected Papers: Volume V*. Dordrecht: Springer Netherlands, 1937, pp. 330–355. ISBN: 978-94-015-3445-1. DOI: 10.1007/978-94-015-3445-1_11. URL: https://doi.org/10.1007/978-94-015-3445-1_11.

[205] A. Einstein, L. Infeld, and B. Hoffmann. "The Gravitational Equations and the Problem of Motion". In: *Annals of Mathematics* 39.1 (Jan. 1938), pp. 65–100.

[206] V. A. Fock. *The theory of space, time and gravitation / Translated from the Russian by N. Kemmer.* Pergamon Press, 1959. URL: http://search.ebscohost.com/login.aspx?direct=true&db=cat00961a&AN=sissa.15031&site=eds-live.

[207] S. Chandrasekhar. "The Post-Newtonian Equations of Hydrodynamics in General Relativity." In: *APJ* 142 (Nov. 1965), p. 1488. DOI: 10.1086/148432.

[208] J. Ehlers et al. "Comments on Gravitational Radiation Damping and Energy Loss in Binary Systems". In: *Astrophys. J. Lett.* 208 (1976), pp. L77–L81. DOI: 10.1086/182236.

[209] M. Alcubierre. *Introduction to 3+1 numerical relativity / Miguel Alcubierre.* International series of monographs on physics: v.140. Oxford University Press, 2008. ISBN: 9780199205677. URL: http://search.ebscohost.com/login.aspx?direct=true&db=cat00961a&AN=sissa.24833&site=eds-live.

[210] C. Bona, C. Palenzuela-Luque, and C. Bona-Casas. *Elements of Numerical Relativity and Relativistic Hydrodynamics : From Einstein' s Equations to Astrophysical Simulations.* Springer Berlin Heidelberg, 2009. URL: http://search.ebscohost.com/login.aspx?direct=true&db=edsbbd&AN=edsbbd.32999e57.bee6.11ea.87a9.0a28bb48d135&site=eds-live.

[211] E. Gourgoulhon. *3+1 Formalism in General Relativity*. Vol. 846. 2012. DOI: 10.1007/978-3-642-24525-1.

[212] C. Palenzuela. "Introduction to Numerical Relativity". In: *Front. Astron. Space Sci.* 7 (2020), p. 58. DOI: 10.3389/fspas.2020.00058. arXiv: 2008.12931 [gr-qc].

[213] S. G. Hahn and R. W. Lindquist. "The two-body problem in geometrodynamics". In: *Annals of Physics* 29.2 (Sept. 1964), pp. 304–331. DOI: 10.1016/0003-4916(64)90223-4.

[214] L. Smarr. "SPACE-TIMES GENERATED BY COMPUTERS: BLACK HOLES WITH GRAVITATIONAL RADIATION*". In: *Annals of the New York Academy of Sciences* 302.1 (1977), pp. 569–604. DOI: https://doi.org/10.1111/j.1749-6632.1977.tb37076.x. eprint: https://nyaspubs.onlinelibrary.wiley.com/doi/pdf/10.1111/j.1749-6632.1977.tb37076.x. URL: https://nyaspubs.onlinelibrary.wiley.com/doi/abs/10.1111/j.1749-6632.1977.tb37076.x.

[215] K. R. Eppley. "Numerical evolution of the collision of two black holes". In: (1975), p. 263. URL: http://inis.iaea.org/search/search.aspx?orig_q=RN:08314225.

[216] M. W. Choptuik. "Universality and scaling in gravitational collapse of a massless scalar field". In: *Phys. Rev. Lett.* 70 (1993), pp. 9–12. DOI: 10.1103/PhysRevLett.70.9.

[217] M. Alcubierre et al. "Gauge conditions for long term numerical black hole evolutions without excision". In: *Phys. Rev. D* 67 (2003), p. 084023. DOI: 10.1103/PhysRevD.67.084023. arXiv: gr-qc/0206072.

[218] F. Pretorius. "Numerical relativity using a generalized harmonic decomposition". In: *Class. Quant. Grav.* 22 (2005), pp. 425–452. DOI: 10.1088/0264-9381/22/2/014. arXiv: gr-qc/0407110.

[219] F. Pretorius. "Evolution of binary black hole spacetimes". In: *Phys. Rev. Lett.* 95 (2005), p. 121101. DOI: 10.1103/PhysRevLett.95.121101. arXiv: gr-qc/0507014.

[220] J. G. Baker et al. "Gravitational wave extraction from an inspiraling configuration of merging black holes". In: *Phys. Rev. Lett.* 96 (2006), p. 111102. DOI: 10.1103/PhysRevLett.96.111102. arXiv: gr-qc/0511103.

[221] M. Campanelli et al. "Accurate evolutions of orbiting black-hole binaries without excision". In: *Phys. Rev. Lett.* 96 (2006), p. 111101. DOI: 10.1103/PhysRevLett.96.111101. arXiv: gr-qc/0511048.

[222] P. Pani. "Advanced Methods in Black-Hole Perturbation Theory". In: *Int. J. Mod. Phys. A* 28 (2013). Ed. by V. Cardoso et al., p. 1340018. DOI: 10.1142/S0217751X13400186. arXiv: 1305.6759 [gr-qc].

[223] A. Pound and B. Wardell. "Black hole perturbation theory and gravitational self-force". In: (Jan. 2021). arXiv: 2101.04592 [gr-qc].

[224] A. Buonanno and T. Damour. "Effective one-body approach to general relativistic two-body dynamics". In: *Phys. Rev. D* 59 (1999), p. 084006. DOI: 10.1103/PhysRevD.59.084006. arXiv: gr-qc/9811091.

[225] B. P. Abbott et al. "Tests of general relativity with GW150914". In: *Phys. Rev. Lett.* 116.22 (2016), p. 221101. DOI: 10.1103/PhysRevLett.116.221101. arXiv: 1602.03841 [gr-qc].

[226] B. P. Abbott et al. "Tests of General Relativity with GW170817". In: *Phys. Rev. Lett.* 123.1 (2019), p. 011102. DOI: 10.1103/PhysRevLett.123.011102. arXiv: 1811.00364 [gr-qc].

[227] B. P. Abbott et al. "Tests of General Relativity with the Binary Black Hole Signals from the LIGO-Virgo Catalog GWTC-1". In: *Phys. Rev.* D100.10 (2019), p. 104036. DOI: 10.1103/PhysRevD.100.104036. arXiv: 1903.04467 [gr-qc].

[228] R. Abbott et al. "Tests of general relativity with binary black holes from the second LIGO-Virgo gravitational-wave transient catalog". In: *Phys. Rev. D* 103.12 (2021), p. 122002. DOI: 10.1103/PhysRevD.103.122002. arXiv: 2010.14529 [gr-qc].

[229] P. Jaranowski and A. Krolak. "Gravitational-Wave Data Analysis. Formalism and Sample Applications: The Gaussian Case". In: *Living Rev. Rel.* 8 (2005), p. 3. arXiv: 0711.1115 [gr-qc].

[230] L. Blanchet and B. S. Sathyaprakash. "Detecting the tail effect in gravitational wave experiments". In: *Phys. Rev. Lett.* 74 (1995), pp. 1067–1070. DOI: 10.1103/PhysRevLett.74.1067.

[231] A. Ghosh et al. "Testing general relativity using golden black-hole binaries". In: *Phys. Rev. D* 94.2 (2016), p. 021101. DOI: 10.1103/PhysRevD.94.021101. arXiv: 1602.02453 [gr-qc].

[232] A. Ghosh et al. "Testing general relativity using gravitational wave signals from the inspiral, merger and ringdown of binary black holes". In: *Class. Quant. Grav.* 35.1 (2018), p. 014002. DOI: 10.1088/1361-6382/aa972e. arXiv: 1704.06784 [gr-qc].

[233] Z. Carson and K. Yagi. "Parameterized and Consistency Tests of Gravity with GravitationalWaves: Current and Future". In: *MDPI Proc.* 17.1 (2019). Ed. by C. Bambi and S. Nampalliwar, p. 5. DOI: 10.3390/proceedings2019017005. arXiv: 1908.07103 [gr-qc].

[234] Z. Carson and K. Yagi. "Probing beyond-Kerr spacetimes with inspiral-ringdown corrections to gravitational waves". In: *Phys. Rev. D* 101 (2020), p. 084050. DOI: 10.1103/PhysRevD.101.084050. arXiv: 2003.02374 [gr-qc].

[235] Z. Carson and K. Yagi. "Probing string-inspired gravity with the inspiral–merger–ringdown consistency tests of gravitational waves". In: *Class. Quant. Grav.* 37.21 (2020), p. 215007. DOI: 10.1088/1361-6382/aba221. arXiv: 2002.08559 [gr-qc].

[236] S. W. Hawking. "Gravitational Radiation from Colliding Black Holes". In: *Phys. Rev. Lett.* 26 (21 1971), pp. 1344–1346. DOI: 10.1103/PhysRevLett.26.1344. URL: https://link.aps.org/doi/10.1103/PhysRevLett.26.1344.

[237] M. Isi et al. "Testing the Black-Hole Area Law with GW150914". In: *Phys. Rev. Lett.* 127.1 (2021), p. 011103. DOI: 10.1103/PhysRevLett.127.011103. arXiv: 2012.04486 [gr-qc].

[238] L. Blanchet et al. "Gravitational radiation damping of compact binary systems to second postNewtonian order". In: *Phys. Rev. Lett.* 74 (1995), pp. 3515–3518. DOI: 10.1103/PhysRevLett.74.3515. arXiv: gr-qc/9501027.

[239] L. Blanchet et al. "Gravitational wave inspiral of compact binary systems to 7/2 postNewtonian order". In: *Phys. Rev. D* 65 (2002). [Erratum: Phys.Rev.D 71, 129902 (2005)], p. 061501. DOI: 10.1103/PhysRevD.71.129902. arXiv: gr-qc/0105099.

[240] K. G. Arun et al. "Testing post-Newtonian theory with gravitational wave observations". In: *Class. Quant. Grav.* 23 (2006), pp. L37–L43. DOI: 10.1088/0264-9381/23/9/L01. arXiv: gr-qc/0604018.

[241] C. K. Mishra et al. "Parametrized tests of post-Newtonian theory using Advanced LIGO and Einstein Telescope". In: *Phys. Rev. D* 82 (2010), p. 064010. DOI: 10.1103/PhysRevD.82.064010. arXiv: 1005.0304 [gr-qc].

[242] N. Yunes and F. Pretorius. "Fundamental Theoretical Bias in Gravitational Wave Astrophysics and the Parameterized Post-Einsteinian Framework". In: *Phys. Rev. D* 80 (2009), p. 122003. DOI: 10.1103/PhysRevD.80.122003. arXiv: 0909.3328 [gr-qc].

[243] L. Sampson, N. Yunes, and N. Cornish. "Rosetta stone for parametrized tests of gravity". In: *Phys. Rev. D* 88.6 (2013). [Erratum: Phys.Rev.D 88, 089902 (2013)], p. 064056. DOI: 10.1103/PhysRevD.88.064056. arXiv: 1307.8144 [gr-qc].

[244] S. Tahura and K. Yagi. "Parameterized Post-Einsteinian Gravitational Waveforms in Various Modified Theories of Gravity". In: *Phys. Rev. D* 98.8 (2018). [Erratum: Phys.Rev.D 101, 109902 (2020)], p. 084042. DOI: 10.1103/PhysRevD.98.084042. arXiv: 1809.00259 [gr-qc].

[245] K. G. Arun. "Generic bounds on dipolar gravitational radiation from inspiralling compact binaries". In: *Class. Quant. Grav.* 29 (2012), p. 075011. DOI: 10.1088/0264-9381/29/7/075011. arXiv: 1202.5911 [gr-qc].

[246] K. Chatziioannou, N. Yunes, and N. Cornish. "Model-Independent Test of General Relativity: An Extended post-Einsteinian Framework with Complete Polarization Content". In: *Phys. Rev. D* 86 (2012). [Erratum: Phys.Rev.D 95, 129901 (2017)], p. 022004. DOI: 10.1103/PhysRevD.86.022004. arXiv: 1204.2585 [gr-qc].

[247] N. Yunes, K. Yagi, and F. Pretorius. "Theoretical Physics Implications of the Binary Black-Hole Mergers GW150914 and GW151226". In: *Phys. Rev.* D94.8 (2016), p. 084002. DOI: 10.1103/PhysRevD.94.084002. arXiv: 1603.08955 [gr-qc].

[248] E. Berti, K. Yagi, and N. Yunes. "Extreme Gravity Tests with Gravitational Waves from Compact Binary Coalescences: (I) Inspiral-Merger". In: *Gen. Rel. Grav.* 50.4 (2018), p. 46. DOI: 10.1007/s10714-018-2362-8. arXiv: 1801.03208 [gr-qc].

[249] S. Mirshekari, N. Yunes, and C. M. Will. "Constraining Generic Lorentz Violation and the Speed of the Graviton with Gravitational Waves". In: *Phys. Rev. D* 85 (2012), p. 024041. DOI: 10.1103/PhysRevD.85.024041. arXiv: 1110.2720 [gr-qc].

[250] P. Horava. "Quantum Gravity at a Lifshitz Point". In: *Phys. Rev. D* 79 (2009), p. 084008. DOI: 10.1103/PhysRevD.79.084008. arXiv: 0901.3775 [hep-th].

[251] A. S. Sefiedgar, K. Nozari, and H. R. Sepangi. "Modified dispersion relations in extra dimensions". In: *Phys. Lett. B* 696 (2011), pp. 119–123. DOI: 10.1016/j.physletb.2010.11.067. arXiv: 1012.1406 [gr-qc].

[252] G. Amelino-Camelia. "Doubly special relativity". In: *Nature* 418 (2002), pp. 34–35. DOI: 10.1038/418034a. arXiv: gr-qc/0207049.

[253] G. Calcagni. "Fractal universe and quantum gravity". In: *Phys. Rev. Lett.* 104 (2010), p. 251301. DOI: 10.1103/PhysRevLett.104.251301. arXiv: 0912.3142 [hep-th].

[254] C. M. Will. "Bounding the mass of the graviton using gravitational wave observations of inspiralling compact binaries". In: *Phys. Rev. D* 57 (1998), pp. 2061–2068. DOI: 10.1103/PhysRevD.57.2061. arXiv: gr-qc/9709011.

[255] T. Jacobson and D. Mattingly. "Einstein-Aether waves". In: *Phys. Rev. D* 70 (2004), p. 024003. DOI: 10.1103/PhysRevD.70.024003. arXiv: gr-qc/0402005.

[256] E. Babichev, V. Mukhanov, and A. Vikman. "k-Essence, superluminal propagation, causality and emergent geometry". In: *JHEP* 02 (2008), p. 101. DOI: 10.1088/1126-6708/2008/02/101. arXiv: 0708.0561 [hep-th].

[257] C. de Rham and A. J. Tolley. "Causality in curved spacetimes: The speed of light and gravity". In: *Phys. Rev. D* 102.8 (2020), p. 084048. DOI: 10.1103/PhysRevD.102.084048. arXiv: 2007.01847 [hep-th].

[258] D. Blas et al. "On constraining the speed of gravitational waves following GW150914". In: *JETP Lett.* 103.10 (2016), pp. 624–626. DOI: 10.7868/S0370274X16100039. arXiv: 1602.04188 [gr-qc].

[259] N. Cornish, D. Blas, and G. Nardini. "Bounding the speed of gravity with gravitational wave observations". In: *Phys. Rev. Lett.* 119.16 (2017), p. 161102. DOI: 10.1103/PhysRevLett.119.161102. arXiv: 1707.06101 [gr-qc].

[260] B. P. Abbott et al. "Gravitational Waves and Gamma-rays from a Binary Neutron Star Merger: GW170817 and GRB 170817A". In: *Astrophys. J. Lett.* 848.2 (2017), p. L13. DOI: 10.3847/2041-8213/aa920c. arXiv: 1710.05834 [astro-ph.HE].

[261] B. P. Abbott et al. "Multi-messenger Observations of a Binary Neutron Star Merger". In: *Astrophys. J. Lett.* 848.2 (2017), p. L12. DOI: 10.3847/2041-8213/aa91c9. arXiv: 1710.05833 [astro-ph.HE].

[262] D. M. Eardley et al. "Gravitational-wave observations as a tool for testing relativistic gravity". In: *Phys. Rev. Lett.* 30 (1973), pp. 884–886. DOI: 10.1103/PhysRevLett.30.884.

[263] D. M. Eardley, D. L. Lee, and A. P. Lightman. "Gravitational-Wave Observations as a Tool for Testing Relativistic Gravity". In: *Phys. Rev. D* 8 (10 1973), pp. 3308–3321. DOI: 10.1103/PhysRevD.8.3308. URL: https://link.aps.org/doi/10.1103/PhysRevD.8.3308.

[264] M. Maggiore. *Gravitational Waves. Vol. 1: Theory and Experiments*. Oxford Master Series in Physics. Oxford University Press, 2007. ISBN: 978-0-19-857074-5, 978-0-19-852074-0.

[265] M. Isi, M. Pitkin, and A. J. Weinstein. "Probing Dynamical Gravity with the Polarization of Continuous Gravitational Waves". In: *Phys. Rev. D* 96.4 (2017), p. 042001. DOI: 10.1103/PhysRevD.96.042001. arXiv: 1703.07530 [gr-qc].

[266] M. Isi and A. J. Weinstein. "Probing gravitational wave polarizations with signals from compact binary coalescences". In: (Oct. 2017). arXiv: 1710.03794 [gr-qc].

[267] T. Callister et al. "Polarization-based Tests of Gravity with the Stochastic Gravitational-Wave Background". In: *Phys. Rev. X* 7.4 (2017), p. 041058. DOI: 10.1103/PhysRevX.7.041058. arXiv: 1704.08373 [gr-qc].

[268] B. Carter. "Axisymmetric Black Hole Has Only Two Degrees of Freedom". In: *Phys. Rev. Lett.* 26 (1971), pp. 331–333. DOI: 10.1103/PhysRevLett.26.331.

[269] W. Israel. "Event horizons in static vacuum space-times". In: *Phys. Rev.* 164 (1967), pp. 1776–1779. DOI: 10.1103/PhysRev.164.1776.

[270] D. C. Robinson. "Uniqueness of the Kerr black hole". In: *Phys. Rev. Lett.* 34 (1975), pp. 905–906. DOI: 10.1103/PhysRevLett.34.905.

[271] K. D. Kokkotas and B. G. Schmidt. "Quasi-Normal Modes of Stars and Black Holes". In: *Living Reviews in Relativity* 2, 2 (Sept. 1999), p. 2. DOI: 10.12942/lrr-1999-2. eprint: gr-qc/9909058.

[272] M. Sasaki and H. Tagoshi. "Analytic black hole perturbation approach to gravitational radiation". In: *Living Rev. Rel.* 6 (2003), p. 6. DOI: 10.12942/lrr-2003-6. arXiv: gr-qc/0306120.

[273] E. Berti, V. Cardoso, and A. O. Starinets. "Quasinormal modes of black holes and black branes". In: *Class. Quant. Grav.* 26 (2009), p. 163001. DOI: 10.1088/0264-9381/26/16/163001. arXiv: 0905.2975 [gr-qc].

[274] P. Goldreich and W. H. Julian. "Pulsar Electrodynamics". In: *Astrophys. J.* 157 (Aug. 1969), p. 869. DOI: 10.1086/150119.

[275] G. W. Gibbons. "Vacuum Polarization and the Spontaneous Loss of Charge by Black Holes". In: *Commun. Math. Phys.* 44 (1975), pp. 245–264. DOI: 10.1007/BF01609829.

[276] R. D. Blandford and R. L. Znajek. "Electromagnetic extraction of energy from Kerr black holes". In: *Monthly Notices of the Royal Astronomical Society* 179.3 (July 1977), pp. 433–456. ISSN: 0035-8711. DOI: 10.1093/mnras/179.3.433. eprint: https://academic.oup.com/mnras/article-pdf/179/3/433/9333653/mnras179-0433.pdf. URL: https://doi.org/10.1093/mnras/179.3.433.

[277] R. S. Hanni. "Limits on the charge of a collapsed object". In: *PRD* 25.10 (May 1982), pp. 2509–2514. DOI: 10.1103/PhysRevD.25.2509.

[278] E. Barausse, V. Cardoso, and P. Pani. "Can environmental effects spoil precision gravitational-wave astrophysics?" In: *Phys. Rev.* D89.10 (2014), p. 104059. DOI: 10.1103/PhysRevD.89.104059. arXiv: 1404.7149 [gr-qc].

[279] O. Dreyer et al. "Black hole spectroscopy: Testing general relativity through gravitational wave observations". In: *Class. Quant. Grav.* 21 (2004), pp. 787–804. DOI: 10.1088/0264-9381/21/4/003. arXiv: gr-qc/0309007.

[280] E. Berti, V. Cardoso, and C. M. Will. "On gravitational-wave spectroscopy of massive black holes with the space interferometer LISA". In: *Phys. Rev. D* 73 (2006), p. 064030. DOI: 10.1103/PhysRevD.73.064030. arXiv: gr-qc/0512160.

[281] G. Carullo, W. Del Pozzo, and J. Veitch. "Observational Black Hole Spectroscopy: A time-domain multimode analysis of GW150914". In: *Phys. Rev. D* 99.12 (2019). [Erratum: Phys.Rev.D 100, 089903 (2019)], p. 123029. DOI: 10.1103/PhysRevD.99.123029. arXiv: 1902.07527 [gr-qc].

[282] M. Isi et al. "Testing the no-hair theorem with GW150914". In: *Phys. Rev. Lett.* 123.11 (2019), p. 111102. DOI: 10.1103/PhysRevLett.123.111102. arXiv: 1905.00869 [gr-qc].

[283] M. Cabero et al. "Black hole spectroscopy in the next decade". In: *Phys. Rev. D* 101.6 (2020), p. 064044. DOI: 10.1103/PhysRevD.101.064044. arXiv: 1911.01361 [gr-qc].

[284] C. D. Capano et al. "Observation of a multimode quasi-normal spectrum from a perturbed black hole". In: (May 2021). arXiv: 2105.05238 [gr-qc].

[285] M. Isi and W. M. Farr. "Analyzing black-hole ringdowns". In: (July 2021). arXiv: 2107.05609 [gr-qc].

[286] I. Kamaretsos et al. "Black-hole hair loss: learning about binary progenitors from ringdown signals". In: *Phys. Rev. D* 85 (2012), p. 024018. DOI: 10.1103/PhysRevD.85.024018. arXiv: 1107.0854 [gr-qc].

[287] S. Borhanian et al. "Signature of horizon dynamics in binary black hole gravitational waveforms". In: *APS April Meeting Abstracts*. Vol. 2019. APS Meeting Abstracts. Jan. 2019, p. L16.006.

[288] S. A. Hughes et al. "Learning about black hole binaries from their ringdown spectra". In: *Phys. Rev. Lett.* 123.16 (2019), p. 161101. DOI: 10.1103/PhysRevLett.123.161101. arXiv: 1901.05900 [gr-qc].

[289] A. Apte and S. A. Hughes. "Exciting black hole modes via misaligned coalescences: I. Inspiral, transition, and plunge trajectories using a generalized Ori-Thorne procedure". In: *Phys. Rev. D* 100.8 (2019), p. 084031. DOI: 10.1103/PhysRevD.100.084031. arXiv: 1901.05901 [gr-qc].

[290] H. Lim et al. "Exciting black hole modes via misaligned coalescences: II. The mode content of late-time coalescence waveforms". In: *Phys. Rev. D* 100.8 (2019), p. 084032. DOI: 10.1103/PhysRevD.100.084032. arXiv: 1901.05902 [gr-qc].

[291] E. E. Flanagan and S. A. Hughes. "Measuring gravitational waves from binary black hole coalescences: 1. Signal-to-noise for inspiral, merger, and ringdown". In: *Phys. Rev. D* 57 (1998), pp. 4535–4565. DOI: 10.1103/PhysRevD.57.4535. arXiv: gr-qc/9701039.

[292] E. Berti et al. "Matched-filtering and parameter estimation of ringdown waveforms". In: *Phys. Rev. D* 76 (2007), p. 104044. DOI: 10.1103/PhysRevD.76.104044. arXiv: 0707.1202 [gr-qc].

[293] A. H. Nitz and C. D. Capano. "GW190521 may be an intermediate mass ratio inspiral". In: *Astrophys. J. Lett.* 907.1 (2021), p. L9. DOI: 10.3847/2041-8213/abccc5. arXiv: 2010.12558 [astro-ph.HE].

[294] J. C. Bustillo et al. "GW190521 as a Merger of Proca Stars: A Potential New Vector Boson of 8.7×10^{-13} eV". In: *Phys. Rev. Lett.* 126.8 (2021), p. 081101. DOI: 10.1103/PhysRevLett.126.081101. arXiv: 2009.05376 [gr-qc].

[295] V. Cardoso et al. "Parametrized black hole quasinormal ringdown: Decoupled equations for nonrotating black holes". In: *Phys. Rev. D* 99.10 (2019), p. 104077. DOI: 10.1103/PhysRevD.99.104077. arXiv: 1901.01265 [gr-qc].

[296] R. McManus et al. "Parametrized black hole quasinormal ringdown. II. Coupled equations and quadratic corrections for nonrotating black holes". In: *Phys. Rev. D* 100.4 (2019), p. 044061. DOI: 10.1103/PhysRevD.100.044061. arXiv: 1906.05155 [gr-qc].

[297] A. Maselli et al. "Parametrized ringdown spin expansion coefficients: a data-analysis framework for black-hole spectroscopy with multiple events". In: *Phys. Rev. D* 101.2 (2020), p. 024043. DOI: 10.1103/PhysRevD.101.024043. arXiv: 1910.12893 [gr-qc].

[298] B. Ratra and P. J. E. Peebles. "Cosmological Consequences of a Rolling Homogeneous Scalar Field". In: *Phys. Rev. D* 37 (1988), p. 3406. DOI: 10.1103/PhysRevD.37.3406.

[299] R. R. Caldwell, R. Dave, and P. J. Steinhardt. "Cosmological imprint of an energy component with general equation of state". In: *Phys. Rev. Lett.* 80 (1998), pp. 1582–1585. DOI: 10.1103/PhysRevLett.80.1582. arXiv: astro-ph/9708069.

[300] V. Sahni and L.-M. Wang. "A New cosmological model of quintessence and dark matter". In: *Phys. Rev. D* 62 (2000), p. 103517. DOI: 10.1103/PhysRevD.62.103517. arXiv: astro-ph/9910097.

[301] T. Matos, F. S. Guzman, and L. A. Urena-Lopez. "Scalar field as dark matter in the universe". In: *Class. Quant. Grav.* 17 (2000), pp. 1707–1712. DOI: 10.1088/0264-9381/17/7/309. arXiv: astro-ph/9908152.

[302] W. Hu, R. Barkana, and A. Gruzinov. "Cold and fuzzy dark matter". In: *Phys. Rev. Lett.* 85 (2000), pp. 1158–1161. DOI: 10.1103/PhysRevLett.85.1158. arXiv: astro-ph/0003365.

[303] T. Matos and L. A. Urena-Lopez. "Quintessence and scalar dark matter in the universe". In: *Class. Quant. Grav.* 17 (2000), pp. L75–L81. DOI: 10.1088/0264-9381/17/13/101. arXiv: astro-ph/0004332.

[304] L. A. Ureña-López. "Brief Review on Scalar Field Dark Matter Models". In: *Frontiers in Astronomy and Space Sciences* 6 (2019), p. 47. ISSN: 2296-987X. DOI: 10.3389/fspas.2019.00047. URL: https://www.frontiersin.org/article/10.3389/fspas.2019.00047.

[305] M. Fierz. "On the physical interpretation of P.Jordan's extended theory of gravitation". In: *Helv. Phys. Acta* 29 (1956), pp. 128–134.

[306] P. Jordan. "The present state of Dirac's cosmological hypothesis". In: *Z. Phys.* 157 (1959), pp. 112–121. DOI: 10.1007/BF01375155.

[307] C. Brans and R. H. Dicke. "Mach's principle and a relativistic theory of gravitation". In: *Phys. Rev.* 124 (1961). Ed. by J.-P. Hsu and D. Fine, pp. 925–935. DOI: 10.1103/PhysRev.124.925.

[308] P. G. Bergmann. "Comments on the scalar tensor theory". In: *Int. J. Theor. Phys.* 1 (1968), pp. 25–36. DOI: 10.1007/BF00668828.

[309] R. V. Wagoner. "Scalar tensor theory and gravitational waves". In: *Phys. Rev. D* 1 (1970), pp. 3209–3216. DOI: 10.1103/PhysRevD.1.3209.

[310] G. W. Horndeski. "Second-order scalar-tensor field equations in a four-dimensional space". In: *Int. J. Theor. Phys.* 10 (1974), pp. 363–384. DOI: 10.1007/BF01807638.

[311] J. Gleyzes et al. "Healthy theories beyond Horndeski". In: *Phys. Rev. Lett.* 114.21 (2015), p. 211101. DOI: 10.1103/PhysRevLett.114.211101. arXiv: 1404.6495 [hep-th].

[312] J. Gleyzes et al. "Exploring gravitational theories beyond Horndeski". In: *JCAP* 02 (2015), p. 018. DOI: 10.1088/1475-7516/2015/02/018. arXiv: 1408.1952 [astro-ph.CO].

[313] D. Langlois and K. Noui. "Degenerate higher derivative theories beyond Horndeski: evading the Ostrogradski instability". In: *JCAP* 02 (2016), p. 034. DOI: 10.1088/1475-7516/2016/02/034. arXiv: 1510.06930 [gr-qc].

[314] M. Crisostomi, K. Koyama, and G. Tasinato. "Extended Scalar-Tensor Theories of Gravity". In: *JCAP* 04 (2016), p. 044. DOI: 10.1088/1475-7516/2016/04/044. arXiv: 1602.03119 [hep-th].

[315] D. Langlois. "Dark energy and modified gravity in degenerate higher-order scalar–tensor (DHOST) theories: A review". In: *Int. J. Mod. Phys. D* 28.05 (2019), p. 1942006. DOI: 10.1142/S0218271819420069. arXiv: 1811.06271 [gr-qc].

[316] D. Langlois, K. Noui, and H. Roussille. "Quadratic degenerate higher-order scalar-tensor theories revisited". In: *Phys. Rev. D* 103.8 (2021), p. 084022. DOI: 10.1103/PhysRevD.103.084022. arXiv: 2012.10218 [gr-qc].

[317] G. 't Hooft and M. J. G. Veltman. "One loop divergencies in the theory of gravitation". In: *Ann. Inst. H. Poincare Phys. Theor. A* 20 (1974), pp. 69–94.

[318] M. H. Goroff and A. Sagnotti. "The ultraviolet behavior of Einstein gravity". In: *Nuclear Physics B* 266.3 (1986), pp. 709–736. ISSN: 0550-3213. DOI: https://doi.org/10.1016/0550-3213(86)90193-8. URL: https://www.sciencedirect.com/science/article/pii/0550321386901938.

[319] K. S. Stelle. "Renormalization of Higher Derivative Quantum Gravity". In: *Phys. Rev. D* 16 (1977), pp. 953–969. DOI: 10.1103/PhysRevD.16.953.

[320] M. Ostrogradsky. "Mémoires sur les équations différentielles, relatives au problème des isopérimètres". In: *Mem. Acad. St. Petersbourg* 6.4 (1850), pp. 385–517.

[321] J. Z. Simon. "The Stability of flat space, semiclassical gravity, and higher derivatives". In: *Phys. Rev. D* 43 (1991), pp. 3308–3316. DOI: 10.1103/PhysRevD.43.3308.

[322] J. F. Donoghue. "General relativity as an effective field theory: The leading quantum corrections". In: *Phys. Rev. D* 50 (1994), pp. 3874–3888. DOI: 10.1103/PhysRevD.50.3874. arXiv: gr-qc/9405057.

[323] T. Biswas, A. Mazumdar, and W. Siegel. "Bouncing universes in string-inspired gravity". In: *JCAP* 03 (2006), p. 009. DOI: 10.1088/1475-7516/2006/03/009. arXiv: hep-th/0508194.

[324] L. Modesto. "Super-renormalizable Quantum Gravity". In: *Phys. Rev. D* 86 (2012), p. 044005. DOI: 10.1103/PhysRevD.86.044005. arXiv: 1107.2403 [hep-th].

[325] D. Becker, C. Ripken, and F. Saueressig. "On avoiding Ostrogradski instabilities within Asymptotic Safety". In: *JHEP* 12 (2017), p. 121. DOI: 10.1007/JHEP12(2017)121. arXiv: 1709.09098 [hep-th].

[326] I. Kuntz. "Exorcising ghosts in quantum gravity". In: *Eur. Phys. J. Plus* 135.10 (2020), p. 859. DOI: 10.1140/epjp/s13360-020-00875-x. arXiv: 1909.11072 [hep-th].

[327] K. Aoki and S. Mukohyama. "Ghostfree quadratic curvature theories with massive spin-2 and spin-0 particles". In: *Phys. Rev. D* 100.6 (2019), p. 064061. DOI: 10.1103/PhysRevD.100.064061. arXiv: 1907.09690 [hep-th].

[328] A. ASHTEKAR, A. BALACHANDRAN, and S. JO. "THE CP PROBLEM IN QUANTUM GRAVITY". In: *International Journal of Modern Physics A* 04.06 (1989), pp. 1493–1514. DOI: 10.1142/S0217751X89000649. eprint: https://doi.org/10.1142/S0217751X89000649. URL: https://doi.org/10.1142/S0217751X89000649.

[329] J. Polchinski. *String Theory*. Vol. 1. Cambridge Monographs on Mathematical Physics. Cambridge University Press, 1998. DOI: 10.1017/CBO9780511816079.

[330] C. P. Burgess. "Quantum gravity in everyday life: General relativity as an effective field theory". In: *Living Rev. Rel.* 7 (2004), pp. 5–56. DOI: 10.12942/lrr-2004-5. arXiv: gr-qc/0311082.

[331] S. H. S. Alexander and S. J. Gates Jr. "Can the string scale be related to the cosmic baryon asymmetry?" In: *JCAP* 06 (2006), p. 018. DOI: 10.1088/1475-7516/2006/06/018. arXiv: hep-th/0409014.

[332] N. Yunes and L. C. Stein. "Non-Spinning Black Holes in Alternative Theories of Gravity". In: *Phys. Rev. D* 83 (2011), p. 104002. DOI: 10.1103/PhysRevD.83.104002. arXiv: 1101.2921 [gr-qc].

[333] P. Pani et al. "Slowly rotating black holes in alternative theories of gravity". In: *Phys. Rev. D* 84 (2011), p. 087501. DOI: 10.1103/PhysRevD.84.087501. arXiv: 1109.3996 [gr-qc].

[334] P. Kanti et al. "Dilatonic black holes in higher curvature string gravity". In: *Phys. Rev. D* 54 (1996), pp. 5049–5058. DOI: 10.1103/PhysRevD.54.5049. arXiv: hep-th/9511071.

[335] T. Kobayashi, M. Yamaguchi, and J. Yokoyama. "Generalized G-Inflation: —Inflation with the Most General Second-Order Field Equations—". In: *Progress of Theoretical Physics* 126.3 (Sept. 2011), pp. 511–529. ISSN: 0033-068X. DOI: 10.1143/PTP.126.511. eprint: https://academic.oup.com/ptp/article-pdf/126/3/511/6866310/126-3-511.pdf. URL: https://doi.org/10.1143/PTP.126.511.

[336] T. P. Sotiriou and V. Faraoni. "f(R) Theories Of Gravity". In: *Rev. Mod. Phys.* 82 (2010), pp. 451–497. DOI: 10.1103/RevModPhys.82.451. arXiv: 0805.1726 [gr-qc].

[337] A. De Felice and S. Tsujikawa. "f(R) theories". In: *Living Rev. Rel.* 13 (2010), p. 3. DOI: 10.12942/lrr-2010-3. arXiv: 1002.4928 [gr-qc].

[338] T. Damour and G. Esposito-Farese. "Tensor multiscalar theories of gravitation". In: *Class. Quant. Grav.* 9 (1992), pp. 2093–2176. DOI: 10.1088/0264-9381/9/9/015.

[339] T. Jacobson and D. Mattingly. "Gravity with a dynamical preferred frame". In: *Phys. Rev. D* 64 (2001), p. 024028. DOI: 10.1103/PhysRevD.64.024028. arXiv: gr-qc/0007031.

[340] D. Mattingly and T. Jacobson. "Relativistic gravity with a dynamical preferred frame". In: *2nd Meeting on CPT and Lorentz Symmetry*. Dec. 2001. DOI: 10.1142/9789812778123_0042. arXiv: gr-qc/0112012.

[341] C. Skordis. "TOPICAL REVIEW: The tensor-vector-scalar theory and its cosmology". In: *Classical and Quantum Gravity* 26.14, 143001 (July 2009), p. 143001. DOI: 10.1088/0264-9381/26/14/143001. arXiv: 0903.3602 [astro-ph.CO].

[342] B. Famaey and S. McGaugh. "Modified Newtonian Dynamics (MOND): Observational Phenomenology and Relativistic Extensions". In: *Living Rev. Rel.* 15 (2012), p. 10. DOI: 10.12942/lrr-2012-10. arXiv: 1112.3960 [astro-ph.CO].

[343] S. Mukohyama and K. Noui. "Minimally Modified Gravity: a Hamiltonian Construction". In: *JCAP* 07 (2019), p. 049. DOI: 10.1088/1475-7516/2019/07/049. arXiv: 1905.02000 [gr-qc].

[344] A. De Felice, A. Doll, and S. Mukohyama. "A theory of type-II minimally modified gravity". In: *JCAP* 09 (2020), p. 034. DOI: 10.1088/1475-7516/2020/09/034. arXiv: 2004.12549 [gr-qc].

[345] Z.-B. Yao et al. "Minimally modified gravity with an auxiliary constraint: A Hamiltonian construction". In: *Phys. Rev. D* 103.2 (2021), p. 024032. DOI: 10.1103/PhysRevD.103.024032. arXiv: 2011.00805 [gr-qc].

[346] K. Hinterbichler. "Theoretical Aspects of Massive Gravity". In: *Rev. Mod. Phys.* 84 (2012), pp. 671–710. DOI: 10.1103/RevModPhys.84.671. arXiv: 1105.3735 [hep-th].

[347] C. de Rham. "Massive Gravity". In: *Living Rev. Rel.* 17 (2014), p. 7. DOI: 10.12942/lrr-2014-7. arXiv: 1401.4173 [hep-th].

[348] C. Rham. "Introduction to Massive Gravity". In: *Lect. Notes Phys.* 892 (2015). Ed. by E. Papantonopoulos, pp. 139–159. DOI: 10.1007/978-3-319-10070-8_5.

[349] S. F. Hassan and R. A. Rosen. "Bimetric Gravity from Ghost-free Massive Gravity". In: *JHEP* 02 (2012), p. 126. DOI: 10.1007/JHEP02(2012)126. arXiv: 1109.3515 [hep-th].

[350] A. De Felice et al. "Minimal Theory of Bigravity: construction and cosmology". In: *JCAP* 04 (2021), p. 015. DOI: 10.1088/1475-7516/2021/04/015. arXiv: 2012.01073 [gr-qc].

[351] M. Högås and E. Mörtsell. "Constraints on bimetric gravity. Part I. Analytical constraints". In: *JCAP* 05 (2021), p. 001. DOI: 10.1088/1475-7516/2021/05/001. arXiv: 2101.08794 [gr-qc].

[352] M. Högås and E. Mörtsell. "Constraints on bimetric gravity. Part II. Observational constraints". In: *JCAP* 05 (2021), p. 002. DOI: 10.1088/1475-7516/2021/05/002. arXiv: 2101.08795 [gr-qc].

[353] V. C. De Andrade, L. C. T. Guillen, and J. G. Pereira. "Teleparallel gravity: An Overview". In: *9th Marcel Grossmann Meeting on Recent Developments in Theoretical and Experimental General Relativity, Gravitation and Relativistic Field Theories (MG 9)*. Nov. 2000. arXiv: gr-qc/0011087.

[354] S. Bahamonde et al. "Teleparallel Gravity: From Theory to Cosmology". In: (June 2021). arXiv: 2106.13793 [gr-qc].

[355] R. Brito, V. Cardoso, and P. Pani. "Superradiance". In: *Lect. Notes Phys.* 906 (2015), pp.1–237. DOI: 10.1007/978-3-319-19000-6. arXiv: 1501.06570 [gr-qc].

[356] R. Penrose. "Gravitational collapse: The role of general relativity". In: *Riv. Nuovo Cim.* 1 (1969). [Gen. Rel. Grav.34,1141(2002)], pp. 252–276. DOI: 10.1023/A:1016578408204.

[357] Y. B. Zel'Dovich. "Generation of Waves by a Rotating Body". In: *Soviet Journal of Experimental and Theoretical Physics Letters* 14 (1971), p. 180.

[358] A. A. Starobinskij. "Amplification of waves reflected from a rotating "black hole"." In: *Zhurnal Eksperimentalnoi i Teoreticheskoi Fiziki* 64 (1973), pp. 48–57.

[359] A. A. Starobinskij and S. M. Churilov. "Amplification of electromagnetic and gravitational waves scattered by a rotating black hole." In: *Zhurnal Eksperimentalnoi i Teoreticheskoi Fiziki* 65 (1973), pp. 3–11.

[360] S. L. Detweiler. "Klein-Gordon equation and rotating Black Holes". In: *Phys. Rev.* D22 (1980), pp. 2323–2326. DOI: 10.1103/PhysRevD.22.2323.

[361] W. H. Press and S. A. Teukolsky. "Floating Orbits, Superradiant Scattering and the Black-hole Bomb". In: *Nature* 238 (1972), pp. 211–212. DOI: 10.1038/238211a0.

[362] R. Vicente, V. Cardoso, and J. C. Lopes. "Penrose process, superradiance, and ergoregion instabilities". In: *Phys. Rev. D* 97.8 (2018), p. 084032. DOI: 10.1103/PhysRevD.97.084032. arXiv: 1803.08060 [gr-qc].

[363] O. Baake and O. Rinne. "Superradiance of a charged scalar field coupled to the Einstein-Maxwell equations". In: *Phys. Rev. D* 94.12 (2016), p. 124016. DOI: 10.1103/PhysRevD.94.124016. arXiv: 1610.08352 [gr-qc].

[364] V. Cardoso and P. Pani. "Tidal acceleration of black holes and superradiance". In: *Class. Quant. Grav.* 30 (2013), p. 045011. DOI: 10.1088/0264-9381/30/4/045011. arXiv: 1205.3184 [gr-qc].

[365] M. Richartz and A. Saa. "Superradiance without event horizons in General Relativity". In: *Phys. Rev. D* 88 (2013), p. 044008. DOI: 10.1103/PhysRevD.88.044008. arXiv: 1306.3137 [gr-qc].

[366] V. Cardoso, R. Brito, and J. L. Rosa. "Superradiance in stars". In: *Phys. Rev. D* 91.12 (2015), p. 124026. DOI: 10.1103/PhysRevD.91.124026. arXiv: 1505.05509 [gr-qc].

[367] D. E. Kaplan, S. Rajendran, and P. Riggins. "Particle Probes with Superradiant Pulsars". In: (Aug. 2019). arXiv: 1908.10440 [hep-ph].

[368] F. V. Day and J. I. McDonald. "Axion superradiance in rotating neutron stars". In: *JCAP* 10 (2019), p. 051. DOI: 10.1088/1475-7516/2019/10/051. arXiv: 1904.08341 [hep-ph].

[369] V. Cardoso et al. "The Black hole bomb and superradiant instabilities". In: *Phys. Rev.* D70 (2004). [Erratum: Phys. Rev.D70,049903(2004)], p. 044039. DOI: 10.1103/PhysRevD.70.049903,10.1103/PhysRevD.70.044039. arXiv: hep-th/0404096 [hep-th].

[370] T. Damour, N. Deruelle, and R. Ruffini. "On quantum resonances in stationary geometries". In: *Lettere al Nuovo Cimento* 15 (Feb. 1976), pp. 257–262. DOI: 10.1007/BF02725534.

[371] R. D. Peccei and H. R. Quinn. "CP Conservation in the Presence of Instantons". In: *Phys. Rev. Lett.* 38 (1977), pp. 1440–1443. DOI: 10.1103/PhysRevLett.38.1440.

[372] F. Wilczek. "Axions and Family Symmetry Breaking". In: *Phys. Rev. Lett.* 49 (1982), pp. 1549–1552. DOI: 10.1103/PhysRevLett.49.1549.

[373] Y. Chikashige, R. N. Mohapatra, and R. D. Peccei. "Are There Real Goldstone Bosons Associated with Broken Lepton Number?" In: *Phys. Lett. B* 98 (1981), pp. 265–268. DOI: 10.1016/0370-2693(81)90011-3.

[374] A. Arvanitaki et al. "String Axiverse". In: *Phys. Rev.* D81 (2010), p. 123530. DOI: 10.1103/PhysRevD.81.123530. arXiv: 0905.4720 [hep-th].

[375] A. Arvanitaki and S. Dubovsky. "Exploring the String Axiverse with Precision Black Hole Physics". In: *Phys. Rev. D* 83 (2011), p. 044026. DOI: 10.1103/PhysRevD.83.044026. arXiv: 1004.3558 [hep-th].

[376] J. E. Kim and D. J. E. Marsh. "An ultralight pseudoscalar boson". In: *Phys. Rev. D* 93.2 (2016), p. 025027. DOI: 10.1103/PhysRevD.93.025027. arXiv: 1510.01701 [hep-ph].

[377] A. Arvanitaki et al. "Search for light scalar dark matter with atomic gravitational wave detectors". In: *Phys. Rev. D* 97 (7 2018), p. 075020. DOI: 10.1103/PhysRevD.97.075020. URL: https://link.aps.org/doi/10.1103/PhysRevD.97.075020.

[378] L. Ackerman et al. "Dark Matter and Dark Radiation". In: *Phys. Rev. D* 79 (2009). Ed. by H. V. Klapdor-Kleingrothaus and I. V. Krivosheina, p. 023519. DOI: 10.1103/PhysRevD.79.023519. arXiv: 0810.5126 [hep-ph].

[379] K. Nakayama. "Vector Coherent Oscillation Dark Matter". In: *JCAP* 10 (2019), p. 019. DOI: 10.1088/1475-7516/2019/10/019. arXiv: 1907.06243 [hep-ph].

[380] A. Caputo et al. "Electromagnetic signatures of dark photon superradiance". In: *Phys. Rev. D* 104.4 (2021), p. 043006. DOI: 10.1103/PhysRevD.104.043006. arXiv: 2102.11280 [hep-ph].

[381] V. Cardoso et al. "Matter around Kerr black holes in scalar-tensor theories: scalarization and superradiant instability". In: *Phys. Rev.* D88 (2013), p. 044056. DOI: 10.1103/PhysRevD.88.044056. arXiv: 1305.6936 [gr-qc].

[382] T. Kolyvaris et al. "Superradiant instabilities in scalar-tensor Horndeski theory". In: *Phys. Rev. D* 98.2 (2018), p. 024045. DOI: 10.1103/PhysRevD.98.024045. arXiv: 1806.11110 [gr-qc].

[383] R. Brito et al. "Stochastic and resolvable gravitational waves from ultralight bosons". In: *Phys. Rev. Lett.* 119.13 (2017), p. 131101. DOI: 10.1103/PhysRevLett.119.131101. arXiv: 1706.05097 [gr-qc].

[384] R. Brito, V. Cardoso, and P. Pani. "Black holes as particle detectors: evolution of superradiant instabilities". In: *Class. Quant. Grav.* 32.13 (2015), p. 134001. DOI: 10.1088/0264-9381/32/13/134001. arXiv: 1411.0686 [gr-qc].

[385] H. Yoshino and H. Kodama. "Gravitational radiation from an axion cloud around a black hole: Superradiant phase". In: *PTEP* 2014 (2014), 043E02. DOI: 10.1093/ptep/ptu029. arXiv: 1312.2326 [gr-qc].

[386] H. Yoshino and H. Kodama. "The bosenova and axiverse". In: *Class. Quant. Grav.* 32.21 (2015), p. 214001. DOI: 10.1088/0264-9381/32/21/214001. arXiv: 1505.00714 [gr-qc].

[387] R. Brito et al. "Gravitational wave searches for ultralight bosons with LIGO and LISA". In: *Phys. Rev.* D96.6 (2017), p. 064050. DOI: 10.1103/PhysRevD.96.064050. arXiv: 1706.06311 [gr-qc].

[388] H. Witek et al. "Superradiant instabilities in astrophysical systems". In: *Phys. Rev. D* 87.4 (2013), p. 043513. DOI: 10.1103/PhysRevD.87.043513. arXiv: 1212.0551 [gr-qc].

[389] H. Okawa, H. Witek, and V. Cardoso. "Black holes and fundamental fields in Numerical Relativity: initial data construction and evolution of bound states". In: *Phys. Rev. D* 89.10 (2014), p. 104032. DOI: 10.1103/PhysRevD.89.104032. arXiv: 1401.1548 [gr-qc].

[390] M. Zilhão, H. Witek, and V. Cardoso. "Nonlinear interactions between black holes and Proca fields". In: *Class. Quant. Grav.* 32 (2015), p. 234003. DOI: 10.1088/0264-9381/32/23/234003. arXiv: 1505.00797 [gr-qc].

[391] W. E. East and F. Pretorius. "Superradiant Instability and Backreaction of Massive Vector Fields around Kerr Black Holes". In: *Phys. Rev. Lett.* 119.4 (2017), p. 041101. DOI: 10.1103/PhysRevLett.119.041101. arXiv: 1704.04791 [gr-qc].

[392] W. E. East. "Massive Boson Superradiant Instability of Black Holes: Nonlinear Growth, Saturation, and Gravitational Radiation". In: *Phys. Rev. Lett.* 121.13 (2018), p. 131104. DOI: 10.1103/PhysRevLett.121.131104. arXiv: 1807.00043 [gr-qc].

[393] G. Ficarra, P. Pani, and H. Witek. "Impact of multiple modes on the black-hole superradiant instability". In: *Phys. Rev. D* 99.10 (2019), p. 104019. DOI: 10.1103/PhysRevD.99.104019. arXiv: 1812.02758 [gr-qc].

[394] S. W. Hawking. "Black holes in the Brans-Dicke theory of gravitation". In: *Commun. Math. Phys.* 25 (1972), pp. 167–171. DOI: 10.1007/BF01877518.

[395] T. P. Sotiriou and V. Faraoni. "Black holes in scalar-tensor gravity". In: *Phys. Rev. Lett.* 108 (2012), p. 081103. DOI: 10.1103/PhysRevLett.108.081103. arXiv: 1109.6324 [gr-qc].

[396] A. A. H. Graham and R. Jha. "Stationary Black Holes with Time-Dependent Scalar Fields". In: *Phys. Rev. D* 90.4 (2014), p. 041501. DOI: 10.1103/PhysRevD.90.041501. arXiv: 1407.6573 [gr-qc].

[397] C. A. R. Herdeiro and E. Radu. "Kerr black holes with scalar hair". In: *Phys. Rev. Lett.* 112 (2014), p. 221101. DOI: 10.1103/PhysRevLett.112.221101. arXiv: 1403.2757 [gr-qc].

[398] O. Chodosh and Y. Shlapentokh-Rothman. "Time-Periodic Einstein–Klein–Gordon Bifurcations of Kerr". In: *Commun. Math. Phys.* 356.3 (2017), pp. 1155–1250. DOI: 10.1007/s00220-017-2998-3. arXiv: 1510.08025 [gr-qc].

[399] C. Herdeiro and E. Radu. "Construction and physical properties of Kerr black holes with scalar hair". In: *Class. Quant. Grav.* 32.14 (2015), p. 144001. DOI: 10.1088/0264-9381/32/14/144001. arXiv: 1501.04319 [gr-qc].

[400] R. Brito et al. "Proca stars: Gravitating Bose–Einstein condensates of massive spin 1 particles". In: *Phys. Lett. B* 752 (2016), pp. 291–295. DOI: 10.1016/j.physletb.2015.11.051. arXiv: 1508.05395 [gr-qc].

[401] C. Herdeiro, E. Radu, and H. Rúnarsson. "Kerr black holes with Proca hair". In: *Class. Quant. Grav.* 33.15 (2016), p. 154001. DOI: 10.1088/0264-9381/33/15/154001. arXiv: 1603.02687 [gr-qc].

[402] S. Sen. "Plasma effects on lasing of a uniform ultralight axion condensate". In: *Phys. Rev. D* 98.10 (2018), p. 103012. DOI: 10.1103/PhysRevD.98.103012. arXiv: 1805.06471 [hep-ph].

[403] M. Boskovic et al. "Axionic instabilities and new black hole solutions". In: *Phys. Rev. D* 99.3 (2019), p. 035006. DOI: 10.1103/PhysRevD.99.035006. arXiv: 1811.04945 [gr-qc].

[404] T. Ikeda, R. Brito, and V. Cardoso. "Blasts of Light from Axions". In: *Phys. Rev. Lett.* 122.8 (2019), p. 081101. DOI: 10.1103/PhysRevLett.122.081101. arXiv: 1811.04950 [gr-qc].

[405] H. Yoshino and H. Kodama. "Bosenova collapse of axion cloud around a rotating black hole". In: *Prog. Theor. Phys.* 128 (2012), pp. 153–190. DOI: 10.1143/PTP.128.153. arXiv: 1203.5070 [gr-qc].

[406] M. Baryakhtar et al. "Black hole superradiance of self-interacting scalar fields". In: *Phys. Rev. D* 103.9 (2021), p. 095019. DOI: 10.1103/PhysRevD.103.095019. arXiv: 2011.11646 [hep-ph].

[407] T. Damour and G. Esposito-Farese. "Nonperturbative strong field effects in tensor - scalar theories of gravitation". In: *Phys. Rev. Lett.* 70 (1993), pp. 2220–2223. DOI: 10.1103/PhysRevLett.70.2220.

[408] L. Perivolaropoulos. "PPN Parameter gamma and Solar System Constraints of Massive Brans-Dicke Theories". In: *Phys. Rev. D* 81 (2010), p. 047501. DOI: 10.1103/PhysRevD.81.047501. arXiv: 0911.3401 [gr-qc].

[409] E. Berti et al. "Testing General Relativity with Present and Future Astrophysical Observations". In: *Class. Quant. Grav.* 32 (2015), p. 243001. DOI: 10.1088/0264-9381/32/24/243001. arXiv: 1501.07274 [gr-qc].

[410] T. Damour and G. Esposito-Farese. "Gravitational wave versus binary - pulsar tests of strong field gravity". In: *Phys. Rev. D* 58 (1998), p. 042001. DOI: 10.1103/PhysRevD.58.042001. arXiv: gr-qc/9803031.

[411] E. Barausse et al. "Neutron-star mergers in scalar-tensor theories of gravity". In: *Phys. Rev. D* 87 (2013), p. 081506. DOI: 10.1103/PhysRevD.87.081506. arXiv: 1212.5053 [gr-qc].

[412] C. Palenzuela et al. "Dynamical scalarization of neutron stars in scalar-tensor gravity theories". In: *Phys. Rev. D* 89.4 (2014), p. 044024. DOI: 10.1103/PhysRevD.89.044024. arXiv: 1310.4481 [gr-qc].

[413] M. Shibata et al. "Coalescence of binary neutron stars in a scalar-tensor theory of gravity". In: *Phys. Rev. D* 89 (8 2014), p. 084005. DOI: 10.1103/PhysRevD.89.084005. URL: https://link.aps.org/doi/10.1103/PhysRevD.89.084005.

[414] N. Sennett and A. Buonanno. "Modeling dynamical scalarization with a resummed post-Newtonian expansion". In: *Phys. Rev.* D93.12 (2016), p. 124004. DOI: 10.1103/PhysRevD.93.124004. arXiv: 1603.03300 [gr-qc].

[415] V. Cardoso et al. "Black holes with surrounding matter in scalar-tensor theories". In: *Phys. Rev. Lett.* 111 (2013), p. 111101. DOI: 10.1103/PhysRevLett.111.111101. arXiv: 1308.6587 [gr-qc].

[416] J. D. Bekenstein. "Black hole hair: 25 - years after". In: *2nd International Sakharov Conference on Physics*. May 1996, pp. 216–219. arXiv: gr-qc/9605059.

[417] C. A. R. Herdeiro and E. Radu. "Asymptotically flat black holes with scalar hair: a review". In: *Int. J. Mod. Phys. D* 24.09 (2015). Ed. by C. A. R. Herdeiro et al., p. 1542014. DOI: 10.1142/S0218271815420146. arXiv: 1504.08209 [gr-qc].

[418] T. P. Sotiriou. "Black Holes and Scalar Fields". In: *Class. Quant. Grav.* 32.21 (2015), p. 214002. DOI: 10.1088/0264-9381/32/21/214002. arXiv: 1505.00248 [gr-qc].

[419] L. Hui and A. Nicolis. "No-Hair Theorem for the Galileon". In: *Phys. Rev. Lett.* 110 (2013), p. 241104. DOI: 10.1103/PhysRevLett.110.241104. arXiv: 1202.1296 [hep-th].

[420] T. P. Sotiriou and S.-Y. Zhou. "Black hole hair in generalized scalar-tensor gravity". In: *Phys. Rev. Lett.* 112 (2014), p. 251102. DOI: 10.1103/PhysRevLett.112.251102. arXiv: 1312.3622 [gr-qc].

[421] E. Barausse and K. Yagi. "Gravitation-Wave Emission in Shift-Symmetric Horndeski Theories". In: *Phys. Rev. Lett.* 115.21 (2015), p. 211105. DOI: 10.1103/PhysRevLett.115.211105. arXiv: 1509.04539 [gr-qc].

[422] E. Barausse. "Testing the strong equivalence principle with gravitational-wave observations of binary black holes". In: *PoS* KMI2017 (2017), p. 029. DOI: 10.22323/1.294.0029. arXiv: 1703.05699 [gr-qc].

[423] A. Lehebel, E. Babichev, and C. Charmousis. "A no-hair theorem for stars in Horndeski theories". In: *JCAP* 07 (2017), p. 037. DOI: 10.1088/1475-7516/2017/07/037. arXiv: 1706.04989 [gr-qc].

[424] K. Yagi, L. C. Stein, and N. Yunes. "Challenging the Presence of Scalar Charge and Dipolar Radiation in Binary Pulsars". In: *Phys. Rev. D* 93.2 (2016), p. 024010. DOI: 10.1103/PhysRevD.93.024010. arXiv: 1510.02152 [gr-qc].

[425] T. P. Sotiriou and S.-Y. Zhou. "Black hole hair in generalized scalar-tensor gravity: An explicit example". In: *Phys. Rev. D* 90 (2014), p. 124063. DOI: 10.1103/PhysRevD.90.124063. arXiv: 1408.1698 [gr-qc].

[426] E. Babichev and C. Charmousis. "Dressing a black hole with a time-dependent Galileon". In: *JHEP* 08 (2014), p. 106. DOI: 10.1007/JHEP08(2014)106. arXiv: 1312.3204 [gr-qc].

[427] G. Antoniou, A. Bakopoulos, and P. Kanti. "Evasion of No-Hair Theorems and Novel Black-Hole Solutions in Gauss-Bonnet Theories". In: *Phys. Rev. Lett.* 120.13 (2018), p. 131102. DOI: 10.1103/PhysRevLett.120.131102. arXiv: 1711.03390 [hep-th].

[428] H. O. Silva et al. "Spontaneous scalarization of black holes and compact stars from a Gauss-Bonnet coupling". In: *Phys. Rev. Lett.* 120.13 (2018), p. 131104. DOI: 10.1103/PhysRevLett.120.131104. arXiv: 1711.02080 [gr-qc].

[429] D. D. Doneva and S. S. Yazadjiev. "New Gauss-Bonnet Black Holes with Curvature-Induced Scalarization in Extended Scalar-Tensor Theories". In: *Phys. Rev. Lett.* 120.13 (2018), p. 131103. DOI: 10.1103/PhysRevLett.120.131103. arXiv: 1711.01187 [gr-qc].

[430] E. Barausse and T. P. Sotiriou. "Perturbed Kerr Black Holes can probe deviations from General Relativity". In: *Phys. Rev. Lett.* 101 (2008), p. 099001. DOI: 10.1103/PhysRevLett.101.099001. arXiv: 0803.3433 [gr-qc].

[431] A. Dima et al. "Spin-induced black hole spontaneous scalarization". In: *Phys. Rev. Lett.* 125.23 (2020), p. 231101. DOI: 10.1103/PhysRevLett.125.231101. arXiv: 2006.03095 [gr-qc].

[432] E. Berti et al. "Spin-induced black-hole scalarization in Einstein-scalar-Gauss-Bonnet theory". In: *Phys. Rev. Lett.* 126.1 (2021), p. 011104. DOI: 10.1103/PhysRevLett.126.011104. arXiv: 2009.03905 [gr-qc].

[433] N. Andreou et al. "Spontaneous scalarization in generalized scalar-tensor theory". In: *Phys. Rev.* D99.12 (2019), p. 124022. DOI: 10.1103/PhysRevD.99.124022. arXiv: 1904.06365 [gr-qc].

[434] H. O. Silva et al. "Stability of scalarized black hole solutions in scalar-Gauss-Bonnet gravity". In: *Phys. Rev.* D99.6 (2019), p. 064011. DOI: 10.1103/PhysRevD.99.064011. arXiv: 1812.05590 [gr-qc].

[435] C. F. B. Macedo et al. "Self-interactions and Spontaneous Black Hole Scalarization". In: *Phys. Rev.* D99.10 (2019), p. 104041. DOI: 10.1103/PhysRevD.99.104041. arXiv: 1903.06784 [gr-qc].

[436] J. L. Blázquez-Salcedo et al. "Radial perturbations of the scalarized Einstein-Gauss-Bonnet black holes". In: *Phys. Rev.* D98.8 (2018), p. 084011. DOI: 10.1103/PhysRevD.98.084011. arXiv: 1805.05755 [gr-qc].

[437] A. Joyce et al. "Beyond the Cosmological Standard Model". In: *Phys. Rept.* 568 (2015), pp. 1–98. DOI: 10.1016/j.physrep.2014.12.002. arXiv: 1407.0059 [astro-ph.CO].

[438] T. Baker et al. "The Novel Probes Project – Tests of Gravity on Astrophysical Scales". In: (Aug. 2019). arXiv: 1908.03430 [astro-ph.CO].

[439] E. Babichev, C. Deffayet, and R. Ziour. "k-Mouflage gravity". In: *Int. J. Mod. Phys. D* 18 (2009), pp. 2147–2154. DOI: 10.1142/S0218271809016107. arXiv: 0905.2943 [hep-th].

[440] E. Babichev, C. Deffayet, and G. Esposito-Farèse. "Improving relativistic modified Newtonian dynamics with Galileon k-mouflage". In: *PRD* 84.6, 061502 (Sept. 2011), p. 061502. DOI: 10.1103/PhysRevD.84.061502. arXiv: 1106.2538 [gr-qc].

[441] P. Brax, C. Burrage, and A.-C. Davis. "Screening fifth forces in k-essence and DBI models". In: *JCAP* 01 (2013), p. 020. DOI: 10.1088/1475-7516/2013/01/020. arXiv: 1209.1293 [hep-th].

[442] C. Burrage and J. Khoury. "Screening of scalar fields in Dirac-Born-Infeld theory". In: *Phys. Rev. D* 90.2 (2014), p. 024001. DOI: 10.1103/PhysRevD.90.024001. arXiv: 1403.6120 [hep-th].

[443] A. Vainshtein. "To the problem of nonvanishing gravitation mass". In: *Physics Letters B* 39.3 (1972), pp. 393–394. ISSN: 0370-2693. DOI: https://doi.org/10.1016/0370-2693(72)90147-5. URL: https://www.sciencedirect.com/science/article/pii/0370269372901475.

[444] C. Deffayet et al. "Nonperturbative continuity in graviton mass versus perturbative discontinuity". In: *Phys. Rev. D* 65 (2002), p. 044026. DOI: 10.1103/PhysRevD.65.044026. arXiv: hep-th/0106001.

[445] E. Babichev, C. Deffayet, and R. Ziour. "The Vainshtein mechanism in the Decoupling Limit of massive gravity". In: *JHEP* 05 (2009), p. 098. DOI: 10.1088/1126-6708/2009/05/098. arXiv: 0901.0393 [hep-th].

[446] E. Babichev, C. Deffayet, and R. Ziour. "The Recovery of General Relativity in massive gravity via the Vainshtein mechanism". In: *Phys. Rev. D* 82 (2010), p. 104008. DOI: 10.1103/PhysRevD.82.104008. arXiv: 1007.4506 [gr-qc].

[447] M. Pietroni. "Dark energy condensation". In: *Phys. Rev. D* 72 (2005), p. 043535. DOI: 10.1103/PhysRevD.72.043535. arXiv: astro-ph/0505615.

[448] K. A. Olive and M. Pospelov. "Environmental dependence of masses and coupling constants". In: *Phys. Rev. D* 77 (2008), p. 043524. DOI: 10.1103/PhysRevD.77.043524. arXiv: 0709.3825 [hep-ph].

[449] K. Hinterbichler and J. Khoury. "Symmetron Fields: Screening Long-Range Forces Through Local Symmetry Restoration". In: *Phys. Rev. Lett.* 104 (2010), p. 231301. DOI: 10.1103/PhysRevLett.104.231301. arXiv: 1001.4525 [hep-th].

[450] T. Damour and A. M. Polyakov. "The String dilaton and a least coupling principle". In: *Nucl. Phys. B* 423 (1994), pp. 532–558. DOI: 10.1016/0550-3213(94)90143-0. arXiv: hep-th/9401069.

[451] P. Brax et al. "Nonlinear structure formation with the environmentally dependent dilaton". In: *Phys. Rev. D* 83 (10 2011), p. 104026. DOI: 10.1103/PhysRevD.83.104026. URL: https://link.aps.org/doi/10.1103/PhysRevD.83.104026.

[452] J. Khoury and A. Weltman. "Chameleon cosmology". In: *Phys. Rev. D* 69 (2004), p. 044026. DOI: 10.1103/PhysRevD.69.044026. arXiv: astro-ph/0309411.

[453] J. Khoury and A. Weltman. "Chameleon Fields: Awaiting Surprises for Tests of Gravity in Space". In: *Phys. Rev. Lett.* 93 (17 2004), p. 171104. DOI: 10.1103/PhysRevLett.93.171104. URL: https://link.aps.org/doi/10.1103/PhysRevLett.93.171104.

[454] T. Kobayashi, Y. Watanabe, and D. Yamauchi. "Breaking of Vainshtein screening in scalar-tensor theories beyond Horndeski". In: *Phys. Rev. D* 91.6 (2015), p. 064013. DOI: 10.1103/PhysRevD.91.064013. arXiv: 1411.4130 [gr-qc].

[455] K. Koyama and J. Sakstein. "Astrophysical Probes of the Vainshtein Mechanism: Stars and Galaxies". In: *Phys. Rev. D* 91 (2015), p. 124066. DOI: 10.1103/PhysRevD.91.124066. arXiv: 1502.06872 [astro-ph.CO].

[456] M. Crisostomi and K. Koyama. "Vainshtein mechanism after GW170817". In: *Phys. Rev. D* 97.2 (2018), p. 021301. DOI: 10.1103/PhysRevD.97.021301. arXiv: 1711.06661 [astro-ph.CO].

[457] D. Langlois et al. "Scalar-tensor theories and modified gravity in the wake of GW170817". In: *Phys. Rev. D* 97.6 (2018), p. 061501. DOI: 10.1103/PhysRevD.97.061501. arXiv: 1711.07403 [gr-qc].

[458] A. Dima and F. Vernizzi. "Vainshtein Screening in Scalar-Tensor Theories before and after GW170817: Constraints on Theories beyond Horndeski". In: *Phys. Rev. D* 97.10 (2018), p. 101302. DOI: 10.1103/PhysRevD.97.101302. arXiv: 1712.04731 [gr-qc].

[459] S. Hirano, T. Kobayashi, and D. Yamauchi. "Screening mechanism in degenerate higher-order scalar-tensor theories evading gravitational wave constraints". In: *Phys. Rev. D* 99.10 (2019), p. 104073. DOI: 10.1103/PhysRevD.99.104073. arXiv: 1903.08399 [gr-qc].

[460] M. Crisostomi, M. Lewandowski, and F. Vernizzi. "Vainshtein regime in scalar-tensor gravity: Constraints on degenerate higher-order scalar-tensor theories". In: *Phys. Rev. D* 100.2 (2019), p. 024025. DOI: 10.1103/PhysRevD.100.024025. arXiv: 1903.11591 [gr-qc].

[461] B. F. de Aguiar and R. F. P. Mendes. "Highly compact neutron stars and screening mechanisms: Equilibrium and stability". In: *Phys. Rev. D* 102.2 (2020), p. 024064. DOI: 10.1103/PhysRevD.102.024064. arXiv: 2006.10080 [gr-qc].

[462] M. Bezares et al. "No evidence of kinetic screening in merging binary neutron stars". In: (July 2021). arXiv: 2107.05648 [gr-qc].

[463] T. D. Abbott et al. "Improved analysis of GW150914 using a fully spin-precessing waveform Model". In: *Phys. Rev.* X6.4 (2016), p. 041014. DOI: 10.1103/PhysRevX.6.041014. arXiv: 1606.01210 [gr-qc].

[464] F. Acernese et al. "Advanced Virgo: a second-generation interferometric gravitational wave detector". In: *Class. Quant. Grav.* 32.2 (2015), p. 024001. DOI: 10.1088/0264-9381/32/2/024001. arXiv: 1408.3978 [gr-qc].

[465] B. P. Abbott et al. "Binary Black Hole Population Properties Inferred from the First and Second Observing Runs of Advanced LIGO and Advanced Virgo". In: *Astrophys. J.* 882.2 (2019), p. L24. DOI: 10.3847/2041-8213/ab3800. arXiv: 1811.12940 [astro-ph.HE].

[466] B. P. Abbott et al. "Astrophysical Implications of the Binary Black-Hole Merger GW150914". In: *Astrophys. J.* 818.2 (2016), p. L22. DOI: 10.3847/2041-8205/818/2/L22. arXiv: 1602.03846 [astro-ph.HE].

[467] M. Zevin et al. "Constraining Formation Models of Binary Black Holes with Gravitational-Wave Observations". In: *Astrophys. J.* 846.1 (2017), p. 82. DOI: 10.3847/1538-4357/aa8408. arXiv: 1704.07379 [astro-ph.HE].

[468] B. Paczynski. "Common Envelope Binaries". In: IAU Symposium 73 (1976). Ed. by P. Eggleton, S. Mitton, and J. Whelan, p. 75.

[469] M. J. Benacquista and J. M. B. Downing. "Relativistic Binaries in Globular Clusters". In: *Living Reviews in Relativity* 16.1 (2013), p. 4. ISSN: 1433-8351. DOI: 10.12942/lrr-2013-4.

[470] B. P. Abbott et al. "GW151226: Observation of Gravitational Waves from a 22-Solar-Mass Binary Black Hole Coalescence". In: *Phys. Rev. Lett.* 116.24 (2016), p. 241103. DOI: 10.1103/PhysRevLett.116.241103. arXiv: 1606.04855 [gr-qc].

[471] B. P. Abbott et al. "GWTC-1: A Gravitational-Wave Transient Catalog of Compact Binary Mergers Observed by LIGO and Virgo during the First and Second Observing Runs". In: *Phys. Rev.* X9.3 (2019), p. 031040. DOI: 10.1103/PhysRevX.9.031040. arXiv: 1811.12907 [astro-ph.HE].

[472] J. F. e. a. Steiner. "A Broad Iron Line in LMC X-1". In: *Mon. Not. Roy. Astron. Soc.* 427 (2012), p. 2552. DOI: 10.1111/j.1365-2966.2012.22128.x. arXiv: 1209.3269 [astro-ph.HE].

[473] M. Middleton. "Black hole spin: theory and observation". In: (2016), pp. 99–151. DOI: 10.1007/978-3-662-52859-4_3. arXiv: 1507.06153 [astro-ph.HE].

[474] D. Gerosa et al. "Spin orientations of merging black holes formed from the evolution of stellar binaries". In: *Phys. Rev.* D98.8 (2018), p. 084036. DOI: 10.1103/PhysRevD.98.084036. arXiv: 1808.02491 [astro-ph.HE].

[475] W. M. Farr et al. "Spin tilts in the double pulsar reveal supernova spin angular-momentum production". In: *The Astrophysical Journal* 742.2 (2011), p. 81. DOI: 10.1088/0004-637x/742/2/81.

[476] T. M. Tauris et al. "Formation of Double Neutron Star Systems". In: *Astrophys. J.* 846.2 (2017), p. 170. DOI: 10.3847/1538-4357/aa7e89. arXiv: 1706.09438 [astro-ph.HE].

[477] B. P. Abbott et al. "GW170104: Observation of a 50-Solar-Mass Binary Black Hole Coalescence at Redshift 0.2". In: *Phys. Rev. Lett.* 118.22 (2017). [Erratum: Phys. Rev. Lett.121,no.12,129901(2018)], p. 221101. DOI: 10.1103/PhysRevLett.118.221101,10.1103/PhysRevLett.121.129901. arXiv: 1706.01812 [gr-qc].

[478] C. L. Rodriguez et al. "Illuminating Black Hole Binary Formation Channels with Spins in Advanced LIGO". In: *Astrophys. J.* 832.1 (2016), p. L2. DOI: 10.3847/2041-8205/832/1/L2. arXiv: 1609.05916 [astro-ph.HE].

[479] J. P. Conlon and C. A. R. Herdeiro. "Can black hole superradiance be induced by galactic plasmas?" In: *Phys. Lett.* B780 (2018), pp. 169–173. DOI: 10.1016/j.physletb.2018.02.073. arXiv: 1701.02034 [astro-ph.HE].

[480] P. Pani and A. Loeb. "Constraining Primordial Black-Hole Bombs through Spectral Distortions of the Cosmic Microwave Background". In: *Phys. Rev.* D88 (2013), p. 041301. DOI: 10.1103/PhysRevD.88.041301. arXiv: 1307.5176 [astro-ph.CO].

[481] L. Tonks and I. Langmuir. "Oscillations in Ionized Gases". In: *Phys. Rev.* 33 (2 1929), pp. 195–210. DOI: 10.1103/PhysRev.33.195.

[482] J. M. Cordes and T. J. W. Lazio. "NE2001. 1. A New model for the galactic distribution of free electrons and its fluctuations". In: (2002). arXiv: astro-ph/0207156 [astro-ph].

[483] D. H. F. M. Schnitzeler. "Modelling the Galactic distribution of free electrons". In: *MNRAS* 427.1 (2012), pp. 664–678. DOI: 10.1111/j.1365-2966.2012.21869.x. arXiv: 1208.3045 [astro-ph.GA].

[484] J. M. Yao, R. N. Manchester, and N. Wang. "A new electron-density model for estimation of pulsar and FRB distances". In: *The Astrophysical Journal* 835.1 (2017), p. 29. DOI: 10.3847/1538-4357/835/1/29.

[485] S. R. Dolan. "Instability of the massive Klein-Gordon field on the Kerr spacetime". In: *Phys. Rev.* D76 (2007), p. 084001. DOI: 10.1103/PhysRevD.76.084001. arXiv: 0705.2880 [gr-qc].

[486] S. Balbus and J. Hawley. "A powerful local shear instability in weakly magnetized disks. I - Linear analysis. II - Nonlinear evolution". In: *Astrophysical Journal; (United States)* 376 (July 1991). ISSN: 0004-637X. DOI: 10.1086/170270.

[487] S. A. Balbus and J. F. Hawley. "Instability, turbulence, and enhanced transport in accretion disks". In: *Rev. Mod. Phys.* 70 (1 1998), pp. 1–53. DOI: 10.1103/RevModPhys.70.1.

[488] S. Nampalliwar and C. Bambi. "Accreting Black Holes". In: (2018). arXiv: 1810.07041 [astro-ph.HE].

[489] I. D. Novikov and K. S. Thorne. "Astrophysics of black holes." In: (1973), pp. 343–450.

[490] D. N. Page and K. S. Thorne. "Disk-Accretion onto a Black Hole. Time-Averaged Structure of Accretion Disk". In: *Astrophys. J.* 191 (1974), pp. 499–506. DOI: 10.1086/152990.

[491] M. Jaroszynski, M. A. Abramowicz, and B. Paczynski. "Supercritical accretion disks around black holes". In: *Acta Astron.* 30.1 (1979), pp. 1–34.

[492] B. Paczyński and P. J. Wiita. "Thick accretion disks and supercritical luminosities." In: *aap* 500 (1980), pp. 203–211.

[493] H. Bondi. "On spherically symmetrical accretion". In: *Mon. Not. Roy. Astron. Soc.* 112 (1952), p. 195.

[494] S. L. Shapiro and S. A. Teukolsky. *Black holes, white dwarfs, and neutron stars : the physics of compact objects*. 1983.

[495] T. J. M. Zouros and D. M. Eardley. "Instabilities of massive scalar perturbations of a rotating Black Hole". In: *Annals Phys.* 118 (1979), pp. 139–155. DOI: 10.1016/0003-4916(79)90237-9.

[496] S. R. Dolan. "Superradiant instabilities of rotating black holes in the time domain". In: *Phys. Rev.* D87.12 (2013), p. 124026. DOI: 10.1103/PhysRevD.87.124026. arXiv: 1212.1477 [gr-qc].

[497] S. A. Hughes. "Evolution of circular, nonequatorial orbits of Kerr black holes due to gravitational wave emission. II. Inspiral trajectories and gravitational wave forms". In: *Phys. Rev.* D64 (2001). [Erratum: Phys. Rev.D88,no.10,109902(2013)], p. 064004. DOI: 10.1103/PhysRevD.64.064004, 10.1103/PhysRevD.88.109902. arXiv: gr-qc/0104041 [gr-qc].

[498] D. A. Varshalovich, A. N. Moskalev, and V. K. Khersonskii. *Quantum Theory of Angular Momentum*. WORLD SCIENTIFIC, 1988. DOI: 10.1142/0270.

[499] A. Fletcher. "Spheroidal Wave Functions. By C. Flammer. Pp. ix, 220. 68s. 1957. (Stanford University Press, Stanford, California)". In: *The Mathematical Gazette* 43.345 (1959). DOI: 10.2307/3610987.

[500] W. H. Press and S. A. Teukolsky. "Perturbations of a Rotating Black Hole. II. Dynamical Stability of the Kerr Metric". In: *Astrophys. J.* 185 (1973), pp. 649–674. DOI: 10.1086/152445.

[501] S. A. Teukolsky. "Perturbations of a rotating black hole. 1. Fundamental equations for gravitational electromagnetic and neutrino field perturbations". In: *Astrophys. J.* 185 (1973), pp. 635–647. DOI: 10.1086/152444.

[502] S. Hod. "On the instability regime of the rotating Kerr spacetime to massive scalar perturbations". In: *Phys. Lett.* B708 (2012), pp. 320–323. DOI: 10.1016/j.physletb.2012.01.054. arXiv: 1205.1872 [gr-qc].

[503] A. A. Esin, J. E. McClintock, and R. Narayan. "Advection - dominated accretion and the spectral states of black hole x-ray binaries: Application to Nova Muscae 1991". In: *Astrophys. J.* 489 (1997), p. 865. DOI: 10.1086/304829. arXiv: astro-ph/9705237 [astro-ph].

[504] U. M. Ascher, S. J. Ruuth, and B. T. R. Wetton. "Implicit-Explicit Methods for Time-Dependent Partial Differential Equations". In: *SIAM Journal on Numerical Analysis* 32.3 (1995), pp. 797–823.

[505] L. Pareschi and G. Russo. "Implicit-explicit Runge-Kutta schemes and applications to hyperbolic systems with relaxation". In: *arXiv e-prints*, arXiv:1009.2757 (2010), arXiv:1009.2757. arXiv: 1009.2757 [math.NA].

[506] M. Baryakhtar, R. Lasenby, and M. Teo. "Black Hole Superradiance Signatures of Ultralight Vectors". In: *Phys. Rev.* D96.3 (2017), p. 035019. DOI: 10.1103/PhysRevD.96.035019. arXiv: 1704.05081 [hep-ph].

[507] D. Baumann et al. "The Spectra of Gravitational Atoms". In: *JCAP* 1912.12 (2019), p. 006. DOI: 10.1088/1475-7516/2019/12/006. arXiv: 1908.10370 [gr-qc].

[508] M. Campanelli et al. "Maximum gravitational recoil". In: *Phys. Rev. Lett.* 98 (2007), p. 231102. DOI: 10.1103/PhysRevLett.98.231102. arXiv: gr-qc/0702133.

[509] B. Bruegmann et al. "Exploring black hole superkicks". In: *Phys. Rev. D* 77 (2008), p. 124047. DOI: 10.1103/PhysRevD.77.124047. arXiv: 0707.0135 [gr-qc].

[510] U. Sperhake et al. "Superkicks in ultrarelativistic encounters of spinning black holes". In: *Phys. Rev. D* 83 (2011), p. 024037. DOI: 10.1103/PhysRevD.83.024037. arXiv: 1011.3281 [gr-qc].

[511] U. Sperhake et al. "Amplification of superkicks in black-hole binaries through orbital eccentricity". In: *Phys. Rev. D* 101.2 (2020), p. 024044. DOI: 10.1103/PhysRevD.101.024044. arXiv: 1910.01598 [gr-qc].

[512] D. Blas and S. J. Witte. "Quenching Mechanisms of Photon Superradiance". In: *Phys. Rev. D* 102.12 (2020), p. 123018. DOI: 10.1103/PhysRevD.102.123018. arXiv: 2009.10075 [hep-ph].

[513] V. Cardoso et al. "The tune of the Universe: the role of plasma in tests of strong-field gravity". In: *Mon. Not. Roy. Astron. Soc.* 503.1 (2021), pp. 563–573. DOI: 10.1093/mnras/stab404. arXiv: 2009.07287 [gr-qc].

[514] E. Cannizzaro et al. "Plasma-photon interaction in curved spacetime I: formalism and quasibound states around nonspinning black holes". In: *Phys. Rev. D* 103 (2021), p. 124018. DOI: 10.1103/PhysRevD.103.124018. arXiv: 2012.05114 [gr-qc].

[515] E. Cannizzaro et al. "Plasma-photon interaction in curved spacetime II: collisions, thermal corrections, and superradiant instabilities". In: (July 2021). arXiv: 2107.01174 [gr-qc].

[516] L. G. Collodel et al. "Spinning and excited black holes in Einstein-scalar-Gauss–Bonnet theory". In: *Class. Quant. Grav.* 37.7 (2020), p. 075018. DOI: 10.1088/1361-6382/ab74f9. arXiv: 1912.05382 [gr-qc].

[517] A. Dima and E. Barausse. "Numerical investigation of plasma-driven superradiant instabilities". In: *Class. Quant. Grav.* 37.17 (2020), p. 175006. DOI: 10.1088/1361-6382/ab9ce0. arXiv: 2001.11484 [gr-qc].

[518] C. Palenzuela et al. "Beyond ideal MHD: towards a more realistic modeling of relativistic astrophysical plasmas". In: *Mon. Not. Roy. Astron. Soc.* 394 (2009), pp. 1727–1740. DOI: 10.1111/j.1365-2966.2009.14454.x. arXiv: 0810.1838 [astro-ph].

[519] L. Pareschi and G. Russo. "Implicit–Explicit Runge–Kutta Schemes and Applications to Hyperbolic Systems with Relaxation". In: *Journal of Scientific Computing* 25 (Jan. 2005), pp. 129–155. DOI: 10.1007/s10915-004-4636-4.

[520] E. Barausse, N. Yunes, and K. Chamberlain. "Theory-Agnostic Constraints on Black-Hole Dipole Radiation with Multiband Gravitational-Wave Astrophysics". In: *Phys. Rev. Lett.* 116.24 (2016), p. 241104. DOI: 10.1103/PhysRevLett.116.241104. arXiv: 1603.04075 [gr-qc].

[521] A. Toubiana et al. "Tests of general relativity with stellar-mass black hole binaries observed by LISA". In: *Phys. Rev. D* 101.10 (2020), p. 104038. DOI: 10.1103/PhysRevD.101.104038. arXiv: 2004.03626 [gr-qc].

[522] E. Berti et al. "Spectroscopy of Kerr black holes with Earth- and space-based interferometers". In: *Phys. Rev. Lett.* 117.10 (2016), p. 101102. DOI: 10.1103/PhysRevLett.117.101102. arXiv: 1605.09286 [gr-qc].

[523] G. Ventagli, A. Lehebel, and T. P. Sotiriou. "The onset of spontaneous scalarization in generalised scalar-tensor theories". In: (June 2020). arXiv: 2006.01153 [gr-qc].

[524] G. Antoniou, L. Bordin, and T. P. Sotiriou. "Compact object scalarization with general relativity as a cosmic attractor". In: (Apr. 2020). arXiv: 2004.14985 [gr-qc].

[525] L. ter Haar et al. "Dynamics of screening in modified gravity". In: (Sept. 2020). arXiv: 2009.03354 [gr-qc].

[526] M. Bezares et al. "Kinetic screening in non-linear stellar oscillations and gravitational collapse". In: (May 2021). arXiv: 2105.13992 [gr-qc].

[527] T. Nakamura et al. "Dynamical Analysis of Screening in Scalar-Tensor Theory". In: *Phys. Rev. D* 103.2 (2021), p. 024009. DOI: 10.1103/PhysRevD.103.024009. arXiv: 2010.14329 [gr-qc].

[528] E. Babichev and D. Langlois. "Relativistic stars in $f(R)$ and scalar-tensor theories". In: *Phys. Rev. D* 81 (12 2010), p. 124051. DOI: 10.1103/PhysRevD.81.124051. URL: https://link.aps.org/doi/10.1103/PhysRevD.81.124051.

[529] P. Brax, A.-C. Davis, and R. Jha. "Neutron stars in screened modified gravity: Chameleon versus dilaton". In: *Phys. Rev. D* 95 (8 2017), p. 083514. DOI: 10.1103/PhysRevD.95.083514. URL: https://link.aps.org/doi/10.1103/PhysRevD.95.083514.

[530] L. Sagunski et al. "Neutron star mergers as a probe of modifications of general relativity with finite-range scalar forces". In: *Phys. Rev. D* 97.6 (2018), p. 064016. DOI: 10.1103/PhysRevD.97.064016. arXiv: 1709.06634 [gr-qc].

[531] M. Lagos and H. Zhu. "Gravitational couplings in Chameleon models". In: *Journal of Cosmology and Astroparticle Physics* 2020.06 (2020), pp. 061–061. DOI: 10.1088/1475-7516/2020/06/061. URL: https://doi.org/10.1088/1475-7516/2020/06/061.

[532] R. F. P. Mendes. "Possibility of setting a new constraint to scalar-tensor theories". In: *Phys. Rev. D* 91 (6 2015), p. 064024. DOI: 10.1103/PhysRevD.91.064024. URL: https://link.aps.org/doi/10.1103/PhysRevD.91.064024.

[533] R. F. P. Mendes and N. Ortiz. "Highly compact neutron stars in scalar-tensor theories of gravity: Spontaneous scalarization versus gravitational collapse". In: *Phys. Rev. D* 93 (12 2016), p. 124035. DOI: 10.1103/PhysRevD.93.124035. URL: https://link.aps.org/doi/10.1103/PhysRevD.93.124035.

[534] D. M. Podkowka, R. F. P. Mendes, and E. Poisson. "Trace of the energy-momentum tensor and macroscopic properties of neutron stars". In: *Phys. Rev. D* 98.6 (2018), p. 064057. DOI: 10.1103/PhysRevD.98.064057. arXiv: 1807.01565 [gr-qc].

[535] A. Passamonti et al. "Coupling of radial and non-radial oscillations of relativistic stars: Gauge-invariant formalism". In: *Phys. Rev. D* 71 (2005), p. 024022. DOI: 10.1103/PhysRevD.71.024022. arXiv: gr-qc/0407108.

[536] A. Passamonti et al. "Coupling of radial and axial non-radial oscillations of compact stars: Gravitational waves from first-order differential rotation". In: *Phys. Rev. D* 73 (2006), p. 084010. DOI: 10.1103/PhysRevD.73.084010. arXiv: gr-qc/0601001.

[537] A. Passamonti, N. Stergioulas, and A. Nagar. "Gravitational waves from non-linear couplings of radial and polar nonradial modes in relativistic stars". In: *Phys. Rev. D* 75 (8 2007), p. 084038. DOI: 10.1103/PhysRevD.75.084038. URL: https://link.aps.org/doi/10.1103/PhysRevD.75.084038.

[538] N. Stergioulas et al. "Gravitational waves and non-axisymmetric oscillation modes in mergers of compact object binaries". In: *Monthly Notices of the Royal Astronomical Society* 418.1 (Nov. 2011), pp. 427–436. ISSN: 0035-8711. DOI: 10.1111/j.1365-2966.2011.19493.x. eprint: https://academic.oup.com/mnras/article-pdf/418/1/427/2849833/mnras0418-0427.pdf. URL: https://doi.org/10.1111/j.1365-2966.2011.19493.x.

[539] K. Takami, L. Rezzolla, and L. Baiotti. "Spectral properties of the post-merger gravitational-wave signal from binary neutron stars". In: *Phys. Rev. D* 91 (6 2015), p. 064001. DOI: 10.1103/PhysRevD.91.064001. URL: https://link.aps.org/doi/10.1103/PhysRevD.91.064001.

[540] S. Vretinaris, N. Stergioulas, and A. Bauswein. "Empirical relations for gravitational-wave asteroseismology of binary neutron star mergers". In: *Phys. Rev. D* 101.8 (2020), p. 084039. DOI: 10.1103/PhysRevD.101.084039. arXiv: 1910.10856 [gr-qc].

[541] S. Chandrasekhar. "Dynamical Instability of Gaseous Masses Approaching the Schwarzschild Limit in General Relativity". In: *Phys. Rev. Lett.* 12 (4 1964), pp. 114–116. DOI: 10.1103/PhysRevLett.12.114. URL: https://link.aps.org/doi/10.1103/PhysRevLett.12.114.

[542] S. Chandrasekhar. "The Dynamical Instability of Gaseous Masses Approaching the Schwarzschild Limit in General Relativity." In: *APJ* 140 (Aug. 1964), p. 417. DOI: 10.1086/147938.

[543] D. W. Meltzer and K. S. Thorne. "Normal Modes of Radial Pulsation of Stars at the End Point of Thermonuclear Evolution". In: *APJ* 145 (Aug. 1966), p. 514. DOI: 10.1086/148792.

[544] E. N. Glass and L. Lindblom. "The Radial Oscillations of Neutron Stars". In: *apjs* 53 (Sept. 1983), p. 93. DOI: 10.1086/190885.

[545] Kokkotas, K. D. and Ruoff, J. "Radial oscillations of relativistic stars*". In: *A&A* 366.2 (2001), pp. 565–572. DOI: 10.1051/0004-6361:20000216. URL: https://doi.org/10.1051/0004-6361:20000216.

[546] R. F. P. Mendes and N. Ortiz. "New class of quasinormal modes of neutron stars in scalar-tensor gravity". In: *Phys. Rev. Lett.* 120.20 (2018), p. 201104. DOI: 10.1103/PhysRevLett.120.201104. arXiv: 1802.07847 [gr-qc].

[547] J. L. Blázquez-Salcedo, F. Scen Khoo, and J. Kunz. "Ultra-long-lived quasinormal modes of neutron stars in massive scalar-tensor gravity". In: *EPL* 130.5 (2020), p. 50002. DOI: 10.1209/0295-5075/130/50002. arXiv: 2001.09117 [gr-qc].

[548] H. Sotani. "Scalar gravitational waves from relativistic stars in scalar-tensor gravity". In: *Phys. Rev. D* 89.6 (2014), p. 064031. DOI: 10.1103/PhysRevD.89.064031. arXiv: 1402.5699 [astro-ph.HE].

[549] D. Gerosa, U. Sperhake, and C. D. Ott. "Numerical simulations of stellar collapse in scalar-tensor theories of gravity". In: *Class. Quant. Grav.* 33.13 (2016), p. 135002. DOI: 10.1088/0264-9381/33/13/135002. arXiv: 1602.06952 [gr-qc].

[550] U. Sperhake et al. "Long-lived inverse chirp signals from core collapse in massive scalar-tensor gravity". In: *Phys. Rev. Lett.* 119.20 (2017), p. 201103. DOI: 10.1103/PhysRevLett.119.201103. arXiv: 1708.03651 [gr-qc].

[551] R. Rosca-Mead et al. "Core collapse in massive scalar-tensor gravity". In: *Phys. Rev. D* 102.4 (2020), p. 044010. DOI: 10.1103/PhysRevD.102.044010. arXiv: 2005.09728 [gr-qc].

[552] P. Brax et al. "Unified description of screened modified gravity". In: *Phys. Rev. D* 86 (4 2012), p. 044015. DOI: 10.1103/PhysRevD.86.044015. URL: https://link.aps.org/doi/10.1103/PhysRevD.86.044015.

[553] L. Hui, A. Nicolis, and C. Stubbs. "Equivalence Principle Implications of Modified Gravity Models". In: *Phys. Rev. D* 80 (2009), p. 104002. DOI: 10.1103/PhysRevD.80.104002. arXiv: 0905.2966 [astro-ph.CO].

[554] J. Sakstein et al. "Towards Strong Field Tests of Beyond Horndeski Gravity Theories". In: *Phys. Rev. D* 95.6 (2017), p. 064013. DOI: 10.1103/PhysRevD.95.064013. arXiv: 1612.04263 [gr-qc].

[555] J. Sakstein. "Astrophysical tests of screened modified gravity". In: *Int. J. Mod. Phys. D* 27.15 (2018), p. 1848008. DOI: 10.1142/S0218271818480085. arXiv: 2002.04194 [astro-ph.CO].

[556] J. Wang, L. Hui, and J. Khoury. "No-Go Theorems for Generalized Chameleon Field Theories". In: *Phys. Rev. Lett.* 109 (2012), p. 241301. DOI: 10.1103/PhysRevLett.109.241301. arXiv: 1208.4612 [astro-ph.CO].

[557] P. Brax et al. "Detecting dark energy in orbit: The cosmological chameleon". In: *Phys. Rev. D* 70 (12 2004), p. 123518. DOI: 10.1103/PhysRevD.70.123518. URL: https://link.aps.org/doi/10.1103/PhysRevD.70.123518.

[558] P. Brax, C. van de Bruck, and A.-C. Davis. "Swampland and screened modified gravity". In: *Phys. Rev. D* 101.8 (2020), p. 083514. DOI: 10.1103/PhysRevD.101.083514. arXiv: 1911.09169 [hep-th].

[559] C. Burrage and J. Sakstein. "Tests of Chameleon Gravity". In: *Living Rev. Rel.* 21.1 (2018), p. 1. DOI: 10.1007/s41114-018-0011-x. arXiv: 1709.09071 [astro-ph.CO].

[560] H. Desmond and P. G. Ferreira. "Galaxy morphology rules out astrophysically relevant Hu-Sawicki $f(R)$ gravity". In: *Phys. Rev. D* 102.10 (2020), p. 104060. DOI: 10.1103/PhysRevD.102.104060. arXiv: 2009.08743 [astro-ph.CO].

[561] M. Pernot-Borràs et al. "Constraints on chameleon gravity from the measurement of the electrostatic stiffness of the MICROSCOPE mission accelerometers". In: (Jan. 2021). arXiv: 2102.00023 [gr-qc].

[562] J. S. Read et al. "Constraints on a phenomenologically parametrized neutron-star equation of state". In: *Phys. Rev. D* 79 (12 2009), p. 124032. DOI: 10.1103/PhysRevD.79.124032. URL: https://link.aps.org/doi/10.1103/PhysRevD.79.124032.

[563] H. T. Cromartie et al. "Relativistic Shapiro delay measurements of an extremely massive millisecond pulsar". In: *Nature Astron.* 4.1 (2019), pp. 72–76. DOI: 10.1038/s41550-019-0880-2. arXiv: 1904.06759 [astro-ph.HE].

[564] A. G. Riess et al. "Cosmic Distances Calibrated to 1% Precision with Gaia EDR3 Parallaxes and Hubble Space Telescope Photometry of 75 Milky Way Cepheids Confirm Tension with ΛCDM". In: *Astrophys. J. Lett.* 908.1 (2021), p. L6. DOI: 10.3847/2041-8213/abdbaf. arXiv: 2012.08534 [astro-ph.CO].

[565] T. Minamidani et al. "Dense Clumps in Giant Molecular Clouds in the Large Magellanic Cloud: Density and Temperature Derived from ^{13}CO(J = 3-2) Observations". In: *Astron. Journal* 141.3, 73 (Mar. 2011), p. 73. DOI: 10.1088/0004-6256/141/3/73. arXiv: 1012.5037 [astro-ph.GA].

[566] D. Alic et al. "Efficient implementation of finite volume methods in Numerical Relativity". In: *Phys. Rev.* D76 (2007), p. 104007. DOI: 10.1103/PhysRevD.76.104007. arXiv: 0706.1189 [gr-qc].

[567] C. Bona, L. Lehner, and C. Palenzuela-Luque. "Geometrically motivated hyperbolic coordinate conditions for numerical relativity: Analysis, issues and implementations". In: *Phys. Rev.* D72 (2005), p. 104009. DOI: 10.1103/PhysRevD.72.104009. arXiv: gr-qc/0509092 [gr-qc].

[568] C. Bona et al. "Symmetry-breaking mechanism for the Z4 general-covariant evolution system". In: *Phys. Rev. D* 69 (6 2004), p. 064036. DOI: 10.1103/PhysRevD.69.064036. URL: https://link.aps.org/doi/10.1103/PhysRevD.69.064036.

[569] S. Valdez-Alvarado et al. "Dynamical evolution of fermion-boson stars". In: *Phys. Rev.* D87.8 (2013), p. 084040. DOI: 10.1103/PhysRevD.87.084040. arXiv: 1210.2299 [gr-qc].

[570] C. Bona et al. "New Formalism for Numerical Relativity". In: *Physical Review Letters* 75 (July 1995), pp. 600–603. DOI: 10.1103/PhysRevLett.75.600. eprint: gr-qc/9412071.

[571] S. Valdez-Alvarado et al. "Dynamical evolution of fermion-boson stars". In: *Phys. Rev. D* 87 (8 2013), p. 084040. DOI: 10.1103/PhysRevD.87.084040. URL: https://link.aps.org/doi/10.1103/PhysRevD.87.084040.

[572] A. Bernal et al. "Multi-state Boson Stars". In: *Phys. Rev.* D81 (2010), p. 044031. DOI: 10.1103/PhysRevD.81.044031. arXiv: 0908.2435 [gr-qc].

[573] G. Raposo et al. "Anisotropic stars as ultracompact objects in General Relativity". In: *Phys. Rev. D* 99.10 (2019), p. 104072. DOI: 10.1103/PhysRevD.99.104072. arXiv: 1811.07917 [gr-qc].

[574] J. A. Font. "Numerical Hydrodynamics in General Relativity". In: *Living Reviews in Relativity* 3.1 (2000), p. 2. ISSN: 1433-8351. DOI: 10.12942/lrr-2000-2. URL: https://doi.org/10.12942/lrr-2000-2.

[575] D. Radice, L. Rezzolla, and T. Kellerman. "Critical phenomena in neutron stars: I. Linearly unstable nonrotating models". In: *Classical and Quantum Gravity* 27.23 (2010), p. 235015. DOI: 10.1088/0264-9381/27/23/235015. URL: https://doi.org/10.1088/0264-9381/27/23/235015.

[576] M. Thierfelder, S. Bernuzzi, and B. Brügmann. "Numerical relativity simulations of binary neutron stars". In: *Phys. Rev. D* 84 (4 2011), p. 044012. DOI: 10.1103/PhysRevD.84.044012. URL: https://link.aps.org/doi/10.1103/PhysRevD.84.044012.

[577] J. A. Font et al. "Three-dimensional general relativistic hydrodynamics. 2. Long term dynamics of single relativistic stars". In: *Phys. Rev. D* 65 (2002), p. 084024. DOI: 10.1103/PhysRevD.65.084024. arXiv: gr-qc/0110047.

[578] H. M. Vaeth and G. Chanmugam. "Radial oscillations of neutron stars and strange stars". In: *aap* 260.1-2 (July 1992), pp. 250–254.

[579] *Advanced LIGO anticipated sensitivity curves : LIGO document T0900288-v3*. https://dcc.ligo.org/LIGO-T0900288/public.

[580] S. Hild et al. "Sensitivity Studies for Third-Generation Gravitational Wave Observatories". In: *Class. Quant. Grav.* 28 (2011), p. 094013. DOI: 10.1088/0264-9381/28/9/094013. arXiv: 1012.0908 [gr-qc].

[581] P. Amaro-Seoane et al. "Laser Interferometer Space Antenna". In: *arXiv e-prints*, arXiv:1702.00786 (Feb. 2017), arXiv:1702.00786. arXiv: 1702.00786 [astro-ph.IM].

[582] A. Nishizawa et al. "Probing non-tensorial polarizations of stochastic gravitational-wave backgrounds with ground-based laser interferometers". In: *Phys. Rev. D* 79 (2009), p. 082002. DOI: 10.1103/PhysRevD.79.082002. arXiv: 0903.0528 [astro-ph.CO].

[583] N. Yunes and X. Siemens. "Gravitational-Wave Tests of General Relativity with Ground-Based Detectors and Pulsar Timing-Arrays". In: *Living Rev. Rel.* 16 (2013), p. 9. DOI: 10.12942/lrr-2013-9. arXiv: 1304.3473 [gr-qc].

[584] E. Newman and R. Penrose. "An Approach to gravitational radiation by a method of spin coefficients". In: *J. Math. Phys.* 3 (1962), pp. 566–578. DOI: 10.1063/1.1724257.

[585] M. Boyle and A. H. Mroue. "Extrapolating gravitational-wave data from numerical simulations". In: *Phys. Rev. D* 80 (2009), p. 124045. DOI: 10.1103/PhysRevD.80.124045. arXiv: 0905.3177 [gr-qc].

[586] N. T. Bishop and L. Rezzolla. "Extraction of Gravitational Waves in Numerical Relativity". In: *Living Rev. Rel.* 19 (2016), p. 2. DOI: 10.1007/s41114-016-0001-9. arXiv: 1606.02532 [gr-qc].

[587] C. Reisswig and D. Pollney. "Notes on the integration of numerical relativity waveforms". In: *Classical and Quantum Gravity* 28.19, 195015 (Oct. 2011), p. 195015. DOI: 10.1088/0264-9381/28/19/195015. arXiv: 1006.1632 [gr-qc].

[588] J. D. Bekenstein. "Transcendence of the law of baryon-number conservation in black hole physics". In: *Phys. Rev. Lett.* 28 (1972), pp. 452–455. DOI: 10.1103/PhysRevLett.28.452.

[589] J. D. Bekenstein. "Novel "no-scalar-hair" theorem for black holes". In: *Phys. Rev. D* 51.12 (1995), R6608. DOI: 10.1103/PhysRevD.51.R6608.

[590] S. Hod. "Onset of spontaneous scalarization in spinning Gauss-Bonnet black holes". In: *Phys. Rev. D* 102.8 (2020), p. 084060. DOI: 10.1103/PhysRevD.102.084060. arXiv: 2006.09399 [gr-qc].

[591] D. D. Doneva et al. "Black hole scalarization induced by the spin: 2+1 time evolution". In: *Phys. Rev. D* 102.10 (2020), p. 104027. DOI: 10.1103/PhysRevD.102.104027. arXiv: 2008.07391 [gr-qc].

[592] D. D. Doneva et al. "Spin-induced scalarization of Kerr black holes with a massive scalar field". In: *Eur. Phys. J. C* 80.12 (2020), p. 1205. DOI: 10.1140/epjc/s10052-020-08765-3. arXiv: 2009.03774 [gr-qc].

[593] H.-J. Kuan, D. D. Doneva, and S. S. Yazadjiev. "Dynamical formation of scalarized black holes and neutron stars through stellar core collapse". In: (Mar. 2021). arXiv: 2103.11999 [gr-qc].

[594] D. D. Doneva and S. S. Yazadjiev. "Beyond the spontaneous scalarization: New fully nonlinear dynamical mechanism for formation of scalarized black holes". In: (July 2021). arXiv: 2107.01738 [gr-qc].

[595] C. Deffayet and F. Larrouturou. "Domain walls without a potential". In: *Phys. Rev. D* 103.3 (2021), p. 036010. DOI: 10.1103/PhysRevD.103.036010. arXiv: 2009.00404 [hep-th].

[596] P. Brax, J. A. R. Cembranos, and P. Valageas. "K-essence scalar dark matter solitons around supermassive black holes". In: *Phys. Rev. D* 101.6 (2020), p. 063510. DOI: 10.1103/PhysRevD.101.063510. arXiv: 2001.06873 [astro-ph.CO].

[597] J. Barranco et al. *Horndeski stars*. 2021. arXiv: 2108.01679 [gr-qc].

[598] R. C. Bernardo, J. Celestial, and I. Vega. "Stealth black holes in shift symmetric kinetic gravity braiding". In: *Phys. Rev. D* 101.2 (2020), p. 024036. DOI: 10.1103/PhysRevD.101.024036. arXiv: 1911.01847 [gr-qc].

[599] C. Charmousis et al. "Perturbations of a rotating black hole in DHOST theories". In: *Class. Quant. Grav.* 36.23 (2019), p. 235008. DOI: 10.1088/1361-6382/ab4fb1. arXiv: 1907.02924 [gr-qc].

[600] C. de Rham and J. Zhang. "Perturbations of stealth black holes in degenerate higher-order scalar-tensor theories". In: *Phys. Rev. D* 100.12 (2019), p. 124023. DOI: 10.1103/PhysRevD.100.124023. arXiv: 1907.00699 [hep-th].

[601] A. L. Madureira. *Numerical Methods and Analysis of Multiscale Problems*. SpringerBriefs in Mathematics. Springer International Publishing, 2017. ISBN: 978-3-319-50866-5, 978-3-319-50864-1.

[602] D. Hilditch. "An Introduction to Well-posedness and Free-evolution". In: *Int. J. Mod. Phys. A* 28 (2013). Ed. by V. Cardoso et al., p. 1340015. DOI: 10.1142/S0217751X13400150. arXiv: 1309.2012 [gr-qc].

[603] Y. Foures-Bruhat. "Theoreme d'existence pour certains systemes derivees partielles non lineaires". In: *Acta Mat.* 88 (1952), pp. 141–225. DOI: 10.1007/BF02392131.

[604] Y. Choquet-Bruhat and R. P. Geroch. "Global aspects of the Cauchy problem in general relativity". In: *Commun. Math. Phys.* 14 (1969), pp. 329–335. DOI: 10.1007/BF01645389.

[605] H. Ringström. *The Cauchy problem in general relativity*. 1st ed. QC 20120127. 2009, p. 294. ISBN: 978-3-03719-053-1.

[606] T. Delsate, D. Hilditch, and H. Witek. "Initial value formulation of dynamical Chern-Simons gravity". In: *Phys. Rev. D* 91.2 (2015), p. 024027. DOI: 10.1103/PhysRevD.91.024027. arXiv: 1407.6727 [gr-qc].

[607] G. Papallo. "On the hyperbolicity of the most general Horndeski theory". In: *Phys. Rev. D* 96.12 (2017), p. 124036. DOI: 10.1103/PhysRevD.96.124036. arXiv: 1710.10155 [gr-qc].

[608] G. Papallo and H. S. Reall. "On the local well-posedness of Lovelock and Horndeski theories". In: *Phys. Rev. D* 96.4 (2017), p. 044019. DOI: 10.1103/PhysRevD.96.044019. arXiv: 1705.04370 [gr-qc].

[609] L. Bernard, L. Lehner, and R. Luna. "Challenges to global solutions in Horndeski's theory". In: *Phys. Rev. D* 100.2 (2019), p. 024011. DOI: 10.1103/PhysRevD.100.024011. arXiv: 1904.12866 [gr-qc].

[610] H. Witek, L. Gualtieri, and P. Pani. "Towards numerical relativity in scalar Gauss-Bonnet gravity: $3+1$ decomposition beyond the small-coupling limit". In: *Phys. Rev. D* 101.12 (2020), p. 124055. DOI: 10.1103/PhysRevD.101.124055. arXiv: 2004.00009 [gr-qc].

[611] F.-L. Julié and E. Berti. "$d+1$ formalism in Einstein-scalar-Gauss-Bonnet gravity". In: *Phys. Rev. D* 101.12 (2020), p. 124045. DOI: 10.1103/PhysRevD.101.124045. arXiv: 2004.00003 [gr-qc].

[612] M. Salgado. "The Cauchy problem of scalar tensor theories of gravity". In: *Class. Quant. Grav.* 23 (2006), pp. 4719–4742. DOI: 10.1088/0264-9381/23/14/010. arXiv: gr-qc/0509001.

[613] M. Salgado et al. "Hyperbolicity of scalar-tensor theories of gravity". In: *Phys. Rev. D* 77 (2008), p. 104010. DOI: 10.1103/PhysRevD.77.104010. arXiv: 0801.2372 [gr-qc].

[614] A. D. Kovács. "Well-posedness of cubic Horndeski theories". In: *Phys. Rev. D* 100.2 (2019), p. 024005. DOI: 10.1103/PhysRevD.100.024005. arXiv: 1904.00963 [gr-qc].

[615] A. D. Kovács and H. S. Reall. "Well-Posed Formulation of Scalar-Tensor Effective Field Theory". In: *Phys. Rev. Lett.* 124.22 (2020), p. 221101. DOI: 10.1103/PhysRevLett.124.221101. arXiv: 2003.04327 [gr-qc].

[616] A. D. Kovács and H. S. Reall. "Well-posed formulation of Lovelock and Horndeski theories". In: *Phys. Rev. D* 101.12 (2020), p. 124003. DOI: 10.1103/PhysRevD.101.124003. arXiv: 2003.08398 [gr-qc].

[617] W. E. East and J. L. Ripley. "Evolution of Einstein-scalar-Gauss-Bonnet gravity using a modified harmonic formulation". In: *Phys. Rev. D* 103.4 (2021), p. 044040. DOI: 10.1103/PhysRevD.103.044040. arXiv: 2011.03547 [gr-qc].

[618] W. E. East and J. L. Ripley. "Dynamics of spontaneous black hole scalarization and mergers in Einstein-scalar-Gauss-Bonnet gravity". In: (May 2021). arXiv: 2105.08571 [gr-qc].

[619] O. Sarbach, E. Barausse, and J. A. Preciado-López. "Well-posed Cauchy formulation for Einstein-æther theory". In: *Class. Quant. Grav.* 36.16 (2019), p. 165007. DOI: 10.1088/1361-6382/ab2e13. arXiv: 1902.05130 [gr-qc].

[620] J. L. Ripley and F. Pretorius. "Gravitational collapse in Einstein dilaton-Gauss–Bonnet gravity". In: *Class. Quant. Grav.* 36.13 (2019), p. 134001. DOI: 10.1088/1361-6382/ab2416. arXiv: 1903.07543 [gr-qc].

[621] M. Bezares et al. "K-dynamics: well-posed initial value 1+1 evolutions in K-essence". In: (Aug. 2020). arXiv: 2008.07546 [gr-qc].

[622] P. Figueras and T. França. "Gravitational Collapse in Cubic Horndeski Theories". In: *Class. Quant. Grav.* 37.22 (2020), p. 225009. DOI: 10.1088/1361-6382/abb693. arXiv: 2006.09414 [gr-qc].

[623] J. Cayuso, N. Ortiz, and L. Lehner. "Fixing extensions to general relativity in the nonlinear regime". In: *Phys. Rev. D* 96.8 (2017), p. 084043. DOI: 10.1103/PhysRevD.96.084043. arXiv: 1706.07421 [gr-qc].

[624] G. Allwright and L. Lehner. "Towards the nonlinear regime in extensions to GR: assessing possible options". In: *Class. Quant. Grav.* 36.8 (2019), p. 084001. DOI: 10.1088/1361-6382/ab0ee1. arXiv: 1808.07897 [gr-qc].

[625] J. Chagoya et al. "Galileons and strong gravity". In: *JCAP* 10 (2014), p. 055. DOI: 10.1088/1475-7516/2014/10/055. arXiv: 1407.7744 [hep-th].

[626] M. Okounkova et al. "Numerical binary black hole mergers in dynamical Chern-Simons gravity: Scalar field". In: *Phys. Rev. D* 96.4 (2017), p. 044020. DOI: 10.1103/PhysRevD.96.044020. arXiv: 1705.07924 [gr-qc].

[627] M. Okounkova, M. A. Scheel, and S. A. Teukolsky. "Evolving Metric Perturbations in dynamical Chern-Simons Gravity". In: *Phys. Rev. D* 99.4 (2019), p. 044019. DOI: 10.1103/PhysRevD.99.044019. arXiv: 1811.10713 [gr-qc].

[628] M. Okounkova et al. "Numerical binary black hole collisions in dynamical Chern-Simons gravity". In: *Phys. Rev. D* 100.10 (2019), p. 104026. DOI: 10.1103/PhysRevD.100.104026. arXiv: 1906.08789 [gr-qc].

[629] M. Okounkova et al. "Numerical relativity simulation of GW150914 beyond general relativity". In: *Phys. Rev. D* 101.10 (2020), p. 104016. DOI: 10.1103/PhysRevD.101.104016. arXiv: 1911.02588 [gr-qc].

[630] H. Witek et al. "Black holes and binary mergers in scalar Gauss-Bonnet gravity: scalar field dynamics". In: *Phys. Rev.* D99.6 (2019), p. 064035. DOI: 10.1103/PhysRevD.99.064035. arXiv: 1810.05177 [gr-qc].

[631] H. O. Silva et al. "Dynamical Descalarization in Binary Black Hole Mergers". In: *Phys. Rev. Lett.* 127.3 (2021), p. 031101. DOI: 10.1103/PhysRevLett.127.031101. arXiv: 2012.10436 [gr-qc].

[632] A. Pound, E. Poisson, and B. G. Nickel. "Limitations of the adiabatic approximation to the gravitational self-force". In: *Phys. Rev. D* 72 (2005), p. 124001. DOI: 10.1103/PhysRevD.72.124001. arXiv: gr-qc/0509122.

[633] C. M. Will and M. Maitra. "Relativistic orbits around spinning supermassive black holes. Secular evolution to 4.5 post-Newtonian order". In: *Phys. Rev. D* 95.6 (2017), p. 064003. DOI: 10.1103/PhysRevD.95.064003. arXiv: 1611.06931 [gr-qc].

[634] J. T. Gálvez Ghersi and L. C. Stein. "Numerical renormalization group-based approach to secular perturbation theory". In: (June 2021). arXiv: 2106.08410 [hep-th].